

FUSED CONJUGATED STRUCTURES FOR ORGANIC ELECTRONICS

A THESIS SUBMITTED TO
THE GRADUATE SCHOOL OF NATURAL AND APPLIED SCIENCES
OF
MIDDLE EAST TECHNICAL UNIVERSITY

BY

ŞEVKI CAN CEVHER

IN PARTIAL FULFILLMENT OF THE REQUIREMENTS
FOR
THE DEGREE OF DOCTOR OF PHILOSOPHY
IN
CHEMISTRY

SEPTEMBER 2019

Approval of the thesis:

FUSED CONJUGATED STRUCTURES FOR ORGANIC ELECTRONICS

submitted by **ŞEVKI CAN CEVHER** in partial fulfillment of the requirements for the degree of **Doctor of Philosophy in Chemistry Department, Middle East Technical University** by,

Prof. Dr. Halil Kalıpçılar
Dean, Graduate School of **Natural and Applied Sciences**

Prof. Dr. Cihangir Tanyeli
Head of Department, **Chemistry**

Prof. Dr. Ali Çırpan
Supervisor, **Chemistry, METU**

Prof. Dr. Levent Toppare
Co-Supervisor, **Chemistry, METU**

Examining Committee Members:

Prof. Dr. Atilla Cihaner
Che. Eng. and App. Chem., Atılım University

Prof. Dr. Ali Çırpan
Chemistry, METU

Prof. Dr. Yasemin Udum Aslan
Technical Sciences Vocational Schools, Gazi University

Assoc. Prof. Dr. İrem Erel Göktepe
Chemistry, METU

Assoc. Prof. Dr. Görkem Günbaş
Chemistry, METU

Date: 13.09.2019

I hereby declare that all information in this document has been obtained and presented in accordance with academic rules and ethical conduct. I also declare that, as required by these rules and conduct, I have fully cited and referenced all material and results that are not original to this work.

Name, Surname: Şevki Can Cevher

Signature:

ABSTRACT

FUSED CONJUGATED STRUCTURES FOR ORGANIC ELECTRONICS

Cevher, Şevki Can
Doctor of Philosophy, Chemistry
Supervisor: Prof. Dr. Ali Çırpan
Co-Supervisor: Prof. Dr. Levent Toppare

September 2019, 197 pages

In the first application, to investigate the organic light emitting diode device performances three different polymers were synthesized in which fused phenantroimidazole ring was combined with benzotirazole based polymeric backbone. P1 incorporated electroluminescent device exhibited superior performance. The highest luminance efficiency for P1 based device was 3.01 cd/A with a luminance value of 140,180 cd/m². In the second part, monomer M1 was synthesized and functionalized from ketone (M1) to oxime (M2) and enamine (M3) for laccase based catechol biosensors. Laccase immobilized by crosslinking with glutaraldehyde on bare polymer coated galssy carbon electrode. M1 based electrode exhibited superior performance linear range between 0.005-0.175 mM with detection limit of 9.86 µM without need of any additional support material. In the final part, four similar polymers were synthesized where the effect of chalcogens or effect of electron donating/withdrawing ability of substituents were investigated separately. PO gave the highest power conversion efficiency among others with a value of 4.72 %. Hence preliminary studies of polymers exhibited promising properties for efficient solar cells. Two more polymers were synthesized to enlarge the absorption of conjugated polymers to infrared region. Optical band gaps of polymers were calculated from absorption on set values of 870 and 760 nm as 1.42 and 1.63 eV respectively for

PIQBDT and PIQCAR. The last study covered the synthesis of polymeric material, which can covalently bond to plasmonic nanoparticles. In this way morphological distribution of plasmonic nanoparticles could be in close proximity to polymer in solar cells.

Keywords: Fused molecules, conjugated polymers, biosensor, OLED, solar cell

ÖZ

ORGANİK ELEKTRONİKLER İÇİN KAYNAŞIK KONJÜGE YAPILAR

Cevher, Şevki Can
Doktora, Kimya
Tez Danışmanı: Prof. Dr. Ali Çırpan
Ortak Tez Danışmanı: Prof. Dr. Levent Toppare

Eylül 2019, 197 sayfa

İlk uygulamada, organik ışık saçan diyotlarda kullanılmak üzere fenanthroimidazol ile birleştirilmiş benzotriazol tabanlı polimerik zincire sahip üç farklı polimer sentezlenmiştir. P1 ile üretilmiş elektroluminans cihazı üstün özellikler göstermiştir. 3,02 eV ile en yüksek bant aralığına sahip P1 tabanlı cihaz en yüksek 3,01 cd/A luminans verimi ile 140.180 cd/m² luminans değerine sahip olmuştur. İkinci kısımda, lakkas tabanlı katekol biyosensörü için monomer M1 sentezlemiş olup ketondan (M1) oksime (M2) ve enamine (M3) fonksiyonellendirilmiştir. Enzim immobilizasyonu gluteraldehit ile üzeri çıplak elektrokimyasal polimer kaplı camsı karbon elektrotta çapraz bağlanmıştır. M1 tabanlı polimer herhangi bir yardımcı maddeye ihtiyaç duymadan 0.005-0.175 mM doğrusal aralığı ve 9.86 µM saptama sınırı gibi üstün özelliklere sahip olmuştur. Son bölümde, kalkojenlerin ve ayrıca electron itici/çekici grupların etkilerini incelemek amacıyla güneş pillerinde kullanılacak dört farklı polimer sentezlenmiştir. PO diğerlerine kıyasla en yüksek güç çevirim verimi % 4.72'ye ulaşmıştır. Polimerlerin ön araştırma sonuçları güneş hücreleri için gelecek vaad eden sonuçlar göstermiştir. Bunlardan ayrı iki farklı konjüge polimerler daha absorpsiyon aralıklarını kızıl ötesi bölgeye genişletmek amacıyla sentezlenmiştir. Optik bant aralıkları konjüge polimerlerin sırasıyla PIQBDT ve PIQCAR'ın absorpsiyon eğrilerindeki başlangıç (onset) değerleri olan 870 ve 760 nm kullanılarak

1,42 ve 1,63 eV olarak hesaplanmıştır. Son çalışma ise plasmonik nanoparçacıklara kovalent olarak bağlanabilecek polimerlerin sentezini kapsamaktadır. Bu sayede plasmonik nanoparçacıkların güneş hücreleri içindeki morfolojik dağılımını polimerin yakın çevresinde bulunmasını sağlayacaktır.

Anahtar Kelimeler: kaynaşık moleküller, konjüge polimerler, biyosensör, OLED, güneş pili

To my family,

ACKNOWLEDGEMENTS

First, I am grateful to my supervisor Prof. Dr. Ali ırpan for his eternal patience, expertise, endless care. Moreover, I am glad for the opportunities that are given by him.

I would like to thank also my co-advisor Prof. Dr. Levent Toppare for his support, valuable suggestions and discussions.

Words are intimately meaningless to express my feelings, pleasure and gratefulness to Duygu Keleş for her entire friendship, care and support.

I would like to present my gratitude to my family. They always support and believe in me to achieve success.

For their friendship, Ali Can zelađlayan, Ezgi Demircan, Buket Zaifođlu, Bengisu orakı, Metin Karayılan, I owe for their support in any circumstances

I am also grateful to Prof. Dr. Yasemin Udum Aslan, Assoc. Prof. Dr. Grkem Gnbaş, Assoc. Prof. Dr. Salih zubuku, Dr. Saniye Sylemez, Dr. Gnl Hızalan, Eda Alemdar and Aybke Bekmezci for their help in various studies.

I would like to express my gratitude to Prof. Dr. Halil İbrahim nal for his wise advices.

Finally, I would like to thank TUBITAK for their support throughout the project 118z738.

TABLE OF CONTENTS

ABSTRACT	v
ÖZ	vii
ACKNOWLEDGEMENTS	x
TABLE OF CONTENTS	xi
LIST OF TABLES	xviii
LIST OF FIGURES	xx
LIST OF ABBREVIATIONS	xxix
LIST OF SYMBOLS	xxxiii
CHAPTERS	
1. OUTLOOK	1
2. FUSED STRUCTURES IN ORGANIC LIGHT EMITTING DIODES	3
2.1. Organic Electronics	3
2.2. Properties of Organic Electronic Materials	4
2.3. Basics of Electronic Process in Conjugated Structures	9
2.3.1. Excited States	12
2.3.1.1. Soliton	12
2.3.1.2. Polaron	13
2.3.1.3. Bipolaron	15
2.3.1.4. Exciton	15
2.3.2. Charge and Energy Transfer	18
2.3.2.1. Excitation Energy Transfer	19
2.4. Polymer Light Emitting Diodes: Devices and Materials	21
2.4.1. Device Configuration of PLEDs	21

2.4.1.1. Substrate	22
2.4.1.2. Anode.....	23
2.4.1.3. Hole Transport/Injection layer.....	23
2.4.1.4. Emissive Layer	24
2.4.1.5. Electron Transport/Injection Layer.....	24
2.4.1.6. Cathode	24
2.4.2. Elementary Processes of PLEDs	25
2.4.2.1. Charge Injection.....	26
2.4.2.2. Carrier Transport	27
2.4.2.3. Carrier Recombination.....	28
2.4.2.4. Photon Emission	29
2.4.2.5. Photon Extraction	29
2.5. Characterizations of PLEDs.....	29
2.5.1. Current Density vs Applied Voltage Characteristics (<i>J-V</i>).....	29
2.5.2. Electroluminescence (EL) Spectra	30
2.5.3. Current Density vs Applied Voltage vs Luminescence Characteristics (<i>J-V-L</i>).....	31
2.5.4. Commission International de l'Eclairage (CIE) Coordinates.....	31
2.6. Aim of This Project.....	32
2.7. Experimental	33
2.7.1. Synthesis.....	36
2.7.1.1. 3-(1-(4-Hexylphenyl)-1H-phenanthro[9,10- <i>d</i>]imidazol-2-yl)phenol (I)	36
2.7.1.2. 2-(3-((10-Bromodecyl)oxy)phenyl)-1-(4-hexylphenyl)-1H-phenanthro[9,10- <i>d</i>]imidazole (II)	36

2.7.1.3.	2-(3-((10-(4,7-Dibromo-2H-benzo[<i>d</i>][1,2,3]triazol-2-yl)decyl)oxy)phenyl)-1-(4-hexylphenyl)-1H-phenanthro[9,10- <i>d</i>]imidazole (IV).....	37
2.7.1.4.	2-(3-((10-(4,7-Di(thiophen-2-yl)-2H-benzo[<i>d</i>][1,2,3]triazol-2-yl)decyl)oxy)phenyl)-1-(4-hexylphenyl)-1H-phenanthro[9,10- <i>d</i>]imidazole (V)	38
2.7.1.5.	2-(3-((10-(4,7-Bis(5-bromothiophen-2-yl)-2H-benzo[<i>d</i>][1,2,3]triazol-2-yl)decyl)oxy)phenyl)-1-(4-hexylphenyl)-1H-phenanthro[9,10- <i>d</i>]imidazole (VI).....	38
2.7.1.6.	Synthesis of polymer P1	39
2.7.1.7.	Synthesis of Polymer P2	40
2.7.1.8.	Synthesis of Polymer P3	41
2.7.2.	Electrochemical and Spectroelectrochemical Properties	41
2.7.3.	Fabrication of PLEDs	42
2.8.	Results and Discussions	42
2.8.1.	Optical Properties	42
2.8.1.1.	Further Insight to Optical Properties.....	44
2.8.2.	Electrochemical Properties	47
2.8.3.	Spectroelectrochemical Properties.....	49
2.8.4.	Kinetic Studies.....	51
2.8.5.	Characterization of PLEDs	53
2.9.	Conclusion.....	57
3.	FUSED STRUCTURES FOR BIOSENSOR APPLICATIONS.....	59
3.1.	Biosensors	59
3.2.	Basic Principals of Biosensors	61

3.3. Types of Biosensors	61
3.3.1. Electrochemical Biosensors	62
3.3.1.1. Amperometric Biosensors	63
3.3.1.2. Potentiometric Biosensors	64
3.3.1.3. Conductimetric Biosensors	64
3.3.2. Piezoelectric Biosensors	65
3.3.3. Thermal Biosensors	66
3.3.4. Photometric Biosensors	67
3.4. Sensing Mechanism of Enzymatic Biosensors	68
3.5. Immobilization Techniques of Biological Materials	68
3.5.1. Covalent Bonding	70
3.5.2. Adsorption	71
3.5.3. Crosslinking	71
3.5.4. Entrapment	71
3.6. Importance of Phenolic Compounds	72
3.7. Catechol	72
3.8. Laccase as Polyphenol Oxidase (PPO)	73
3.8.1. Catalytic Cycle of Laccase	74
3.9. Aim of the Study	75
3.10. Experimental	75
3.10.1. Synthesis of Monomers	75
3.10.1.1. 6,9-Dibromo-11 <i>H</i> -indeno[2,1- <i>b</i>]quinoxalin-11-one (I)	76
3.10.1.2. 6,9-Bis(4-hexylthiophen-2-yl)-11 <i>H</i> -indeno[2,1- <i>b</i>]quinoxalin-11-one (M1)	76

3.10.1.3. (E)-6,9-Bis(4-hexylthiophen-2-yl)-11-hydrazono-11 <i>H</i> -indeno[2,1- <i>b</i>]quinoxaline (M2)	77
3.10.1.4. (E)-6,9-Bis(4-hexylthiophen-2-yl)-11 <i>H</i> -indeno[2,1- <i>b</i>]quinoxalin-11-one oxime (M3).....	77
3.10.2. Biosensor Materials	78
3.11. Fabrication and Amperometric Measurements of the Biosensor and Electrochemical Characterization of the Polymers (PM1, PM2 and PM3)	79
3.12. Optimization of experimental variables	82
4. FUSED STRUCTURES FOR ORGANIC SOLAR CELLS	89
4.1. Organic Solar Cells	89
4.2. Organic Solar Cells Device Architectures.....	90
4.2.1. Single Layer.....	90
4.2.2. Bilayer.....	91
4.2.3. Three-Layer Solar Cell	92
4.2.4. Stacked Organic Solar Cells	93
4.2.5. Tandem Organic Solar Cells.....	94
4.2.6. Bulk Heterojunction Solar Cells Device Configuration	94
4.2.6.1. The Substrate.....	95
4.2.6.2. The Active Layer.....	96
4.2.6.3. The Top Contact.....	97
4.2.6.4. Operating Principle of Bulk Heterojunction Solar Cells	97
4.3. Characterization of Organic Solar Cells.....	99
4.3.1. First Generation Model.....	99
4.3.2. Second Generation Model	101
4.4. Photovoltaic Performance	103

4.5. Features of Fused Structures	104
4.5.1. Band Gap Engineering and Related Parameters.....	104
4.5.2. Morphology Engineering and Related Parameters.....	108
4.6. Aim of This Study.....	109
4.7. Benzo-2,1,3-chalcogenadiazoles.....	113
4.7.1. Experimental	113
4.7.1.1. Synthesis.....	114
4.7.1.2. Investigation of Optical and Electronic Properties	116
4.7.1.3. OSC Device Fabrication	116
4.7.2. Results and Discussions	117
4.7.2.1. Optical Properties	117
4.7.2.2. Electronic Properties.....	119
4.7.2.3. Photovoltaic	121
4.7.3. Conclusion.....	125
4.8. Low Band Gap Polymers	125
4.8.1. Synthesis.....	125
4.8.1.1. 6,9-Bis(5-bromo-4-hexylthiophen-2-yl)-11H-indeno[1,2- <i>b</i>]quinoxalin-11-one	126
4.8.1.2. PIQBDT	126
4.8.1.3. PIQCAR.....	127
4.8.2. Optical and Electronic Properties.....	127
4.8.3. Conclusions and Future Studies	129
4.9. Fused Structures with Plasmonic Nanoparticles.....	130
4.9.1. Materials and Methods	131

4.9.1.1. Synthesis of 4,7-dibromobenzo[<i>c</i>][1,2,5]oxadiazole-5,6-diol (4):...	132
4.9.1.2. Synthesis of 4,7-dibromo-5,6-bis(8-bromooctyloxy)benzo[<i>c</i>][1,2,5]oxadiazole (5b)	132
4.9.1.3. Synthesis of 5,6-bis(8-bromooctyloxy)-4,7-di(thiophen-2-yl)benzo[<i>c</i>][1,2,5]oxadiazole (6b).....	133
4.9.2. Discussions and Future Studies	133
4.10. Conclusions	134
5. STUDIES IN THIS THESIS	137
5.1. Summary of the Thesis	137
5.2. Other Studies	138
REFERENCES.....	141
CURRICULUM VITAE	193

LIST OF TABLES

TABLES

Table 2.1. Summary of electrochemical and spectroelectrochemical studies of P1, P2 and P3 (61). This article was published in Synthetic Metals, 244, Şevki Can Cevher, Duygu Keles, Gonul Hizalan, Levent Toppare, Ali Cirpan, Alkyl-end phenanthroimidazole modification of benzotriazole based conjugated polymers for optoelectronic applications, 1-9, Copyright Elsevier, 2018	51
Table 2.2. L, a, b values of colors at different states (61). This article was published in Synthetic Metals, 244, Şevki Can Cevher, Duygu Keles, Gonul Hizalan, Levent Toppare, Ali Cirpan, Alkyl-end phenanthroimidazole modification of benzotriazole based conjugated polymers for optoelectronic applications, 1-9, Copyright Elsevier, 2018.	51
Table 2.3. Summary of kinetic studies (61). This article was published in Synthetic Metals, 244, Şevki Can Cevher, Duygu Keles, Gonul Hizalan, Levent Toppare, Ali Cirpan, Alkyl-end phenanthroimidazole modification of benzotriazole based conjugated polymers for optoelectronic applications, 1-9, Copyright Elsevier, 2018	52
Table 2.4. Photoluminescence and electroluminescence properties of polymers (61). This article was published in Synthetic Metals, 244, Şevki Can Cevher, Duygu Keles, Gonul Hizalan, Levent Toppare, Ali Cirpan, Alkyl-end phenanthroimidazole modification of benzotriazole based conjugated polymers for optoelectronic applications, 1-9, Copyright Elsevier, 2018	56
Table 3.1. Electrochemical and optical properties monomers M1, M2, and M3 and their electrochemically produced polymers.	80
Table 3.2. Comparison of analytical parameters of other laccase biosensors in literature	87
Table 4.1. Optical and electronic properties of four polymers.	121

Table 4.2. Polymer Solar Cell Performances	123
Table 4.3. Optical and electronic properties of PIQCAR and PIQBDT.	129

LIST OF FIGURES

FIGURES

Figure 2.1. Conjugated molecular structures	7
Figure 2.2. Several different geometries of conjugated molecules	9
Figure 2.3. Energy band structures of metal, semiconductor, and insulator. The Fermi level is simply defined as the hypothetical energy level at which an orbital is exactly half-filled.	10
Figure 2.4. Schematic illustration neutral, negatively charged and positively charged solitons whose allowed transitions are indicated by solid arrows.	13
Figure 2.5. Schematic illustration of positive polaron (above). Positive and negative polarons whose allowed transitions are indicated by solid arrows (below).	14
Figure 2.6. Schematic representation of positive bipolaron	15
Figure 2.7. Illustrations of Frenkel and Wannier excitons	17
Figure 2.8. Device architecture of OLED	22
Figure 2.9. Working principle of PLEDs.....	25
Figure 2.10. Operational information of PLEDs	26
Figure 2.11. Current density vs applied voltage vs luminescence characteristics (J-V-L) diagram of red PLED device, luminescent working device is inside (61). This article was published in Synthetic Metals, 244, Şevki Can Cevher, Duygu Keles, Gonul Hizalan, Levent Toppare, Ali Cirpan, Alkyl-end phenanthroimidazole modification of benzotriazole based conjugated polymers for optoelectronic applications, 1-9, Copyright Elsevier, 2018.	31
<i>Figure 2.12.</i> The CIE chromaticity diagram. The curve inside the diagram represents the colors of blackbody radiation corresponding to the correlated color temperature.	32
Figure 2.13. Synthetic pathway of P1, P2 and P3. a) NH ₄ OAc, acetic acid, b) 1,10-dibromodecane, K ₂ CO ₃ , acetone, c) 4,7-dibromobenzotriazole, K ₂ CO ₃ , THF, d) 2-	

tributyltinthiophene, Pd(PPh₃)₂Cl₂, THF, e) NBS, CHCl₃, f) 2M K₂CO₃, N(C₆H₁₃)₄Br, Pd(PPh₃)₂Cl₂, bromobenzene, benzenboronic acid, THF g) Pd(PPh₃)₂Cl₂, bromobenzene, 2-tributyltinthiophene, THF.....35

Figure 2.14. a) Photoluminescence spectra for copolymer P1–P3 solutions and for films under excitation wavelength of 284 nm b) photoluminescence spectra (close-up view of the blue region) c) photoluminescence spectra for copolymer P1–P3 solutions and for films (excitation wavelengths were set according to absorption λ_{\max} values).(61) This article was published in Synthetic Metals, 244, Şevki Can Cevher,

Duygu Keles, Gonul Hizalan, Levent Toppare, Ali Cirpan, Alkyl-end phenanthroimidazole modification of benzotriazole based conjugated polymers for optoelectronic applications, 1-9, Copyright Elsevier, 2018.....44

Figure 2.15. Chemical structures of molecules (61). This article was published in Synthetic Metals, 244, Şevki Can Cevher, Duygu Keles, Gonul Hizalan, Levent Toppare, Ali Cirpan, Alkyl-end phenanthroimidazole modification of benzotriazole based conjugated polymers for optoelectronic applications, 1-9, Copyright Elsevier, 2018.....45

Figure 2.16. Emission spectra of solutions (0.42 g/L) of a) BTz, Imz-OH and BTz-Imz, b) BTz, TBTzT and TBTzT-Imz (61). This article was published in Synthetic Metals, 244, Şevki Can Cevher, Duygu Keles, Gonul Hizalan, Levent Toppare, Ali Cirpan, Alkyl-end phenanthroimidazole modification of benzotriazole based conjugated polymers for optoelectronic applications, 1-9, Copyright Elsevier, 201846

Figure 2.17. Emission spectra of TBzT and TBTzT-Imz a) 280 nm excitation wavelength, b) 420 nm excitation wavelength of thin films. (400 nm excitation wavelength for solutions) (61). This article was published in Synthetic Metals, 244, Şevki Can Cevher, Duygu Keles, Gonul Hizalan, Levent Toppare, Ali Cirpan, Alkyl-end phenanthroimidazole modification of benzotriazole based conjugated polymers for optoelectronic applications, 1-9, Copyright Elsevier, 201847

Figure 2.18. Single scan cyclic voltammograms of polymers in 0.1 M TBAPF₆/ACN electrolyte solution at 100 mV/s scan rate, a) P1, b) P2, c) P3 (61). This article was

published in Synthetic Metals, 244, Şevki Can Cevher, Duygu Keles, Gonul Hizalan, Levent Toppare, Ali Cirpan, Alkyl-end phenanthroimidazole modification of benzotriazole based conjugated polymers for optoelectronic applications, 1-9, Copyright Elsevier, 2018 49

Figure 2.19. Electronic absorption spectra and their original corresponding colors in oxidation and reduction states of polymers in 0.1 M TBAPF₆/ACN solution, a) P1, b) P2, and c) P3 (61). This article was published in Synthetic Metals, 244, Şevki Can Cevher, Duygu Keles, Gonul Hizalan, Levent Toppare, Ali Cirpan, Alkyl-end phenanthroimidazole modification of benzotriazole based conjugated polymers for optoelectronic applications, 1-9, Copyright Elsevier, 2018 50

Figure 2.20. Percent transmittance change of P1 (a), P2 (b) and P3 (c) between neutral and oxidized states (61). This article was published in Synthetic Metals, 244, Şevki Can Cevher, Duygu Keles, Gonul Hizalan, Levent Toppare, Ali Cirpan, Alkyl-end phenanthroimidazole modification of benzotriazole based conjugated polymers for optoelectronic applications, 1-9, Copyright Elsevier, 2018. 53

Figure 2.21. The energy band diagrams of the constructed devices (61). This article was published in Synthetic Metals, 244, Şevki Can Cevher, Duygu Keles, Gonul Hizalan, Levent Toppare, Ali Cirpan, Alkyl-end phenanthroimidazole modification of benzotriazole based conjugated polymers for optoelectronic applications, 1-9, Copyright Elsevier, 2018. 54

Figure 2.22. Electroluminescence spectra of the P1, P2 and P3 based PLEDs (61). This article was published in Synthetic Metals, 244, Şevki Can Cevher, Duygu Keles, Gonul Hizalan, Levent Toppare, Ali Cirpan, Alkyl-end phenanthroimidazole modification of benzotriazole based conjugated polymers for optoelectronic applications, 1-9, Copyright Elsevier, 2018. 55

Figure 2.23. Current density-voltage-luminance characteristics of the a) P1, b) P2 and c) P3 based OLEDs (61). This article was published in Synthetic Metals, 244, Şevki Can Cevher, Duygu Keles, Gonul Hizalan, Levent Toppare, Ali Cirpan, Alkyl-end phenanthroimidazole modification of benzotriazole based conjugated polymers for optoelectronic applications, 1-9, Copyright Elsevier, 2018. 56

Figure 3.1. Biosensor device.....	60
Figure 3.2. Typical biosensors and components	62
Figure 3.3. Electrochemical biosensor	63
Figure 3.4. Piezoelectric biosensor.	65
Figure 3.5. Thermal biosensor	66
Figure 3.6. Photometric biosensor	67
Figure 3.7. Immobilization techniques	70
Figure 3.8. Synthetic pathway of monomers (a: Br ₂ , HBr; b: NaBH ₄ , EtOH; c: Ninhydrin, PTSA, EtOH; d: n-BuLi, SnBu ₃ Cl, THF; e: Pd(PPh ₃) ₂ Cl ₂ , toluene; f: Hydrazine monohydrochloride, Hydrazine hydrate, NEt ₃ , THF; g: Hydroxylammonium chloride, NEt ₃ , THF.....	76
Figure 3.9. Electrochemical polymerization of M1 (a), M2 (c), M3 (e) and single scan voltammogram of PM1 (b), PM2 (d), PM3 (f) in DCM: ACN (5: 95) solution containing 0.1 M TBAPF ₆ on graphite electrode.....	81
Figure 3.10. Spectroelectrochemical absorption spectrum of electrochemically polymerized M1 (a), M2 (d), M3 (g), visual appearance and L, a and b values of electrochemically polymerized M1 (b), M2 (e), M3 (h), kinetic performances of electrochemically polymerized M1 (c), M2 (f), M3 (i)	82
Figure 3.11. Effect of cycle number on biosensor response (Measurements were carried out at -0.3 V vs silver wire and 50 mM sodium acetate buffer in the presence of 0.125 mM catechol under ambient conditions. Error bars show the standard deviation (±SD) of three measurements).	83
Figure 3.12. Effect of enzyme amount on biosensor response (Measurements were carried out at -0.3 V vs silver wire and 50 mM sodium acetate buffer in the presence of 0.125 mM catechol under ambient conditions. Error bars show the standard deviation (±SD) of three measurements.....	84
Figure 3.13. Effect of pH on biosensor response (Measurements were carried out at -0.3 V vs silver wire and 50 mM sodium acetate buffer in the presence of 0.125 mM catechol under ambient conditions. Error bars show the standard deviation (±SD) of three measurements).....	85

Figure 3.14. Calibration curve for catechol (in 50 mM acetate buffer, pH 5.5, 25 °C, - 0.3 V).....	86
Figure 4.1. Device architecture of single layer OSCs	91
Figure 4.2. Device architecture of bilayer OSCs.....	92
Figure 4.3. Device architecture of BHJ OSCs.....	92
Figure 4.4. Device architecture of three-layer OSCs.....	93
Figure 4.5. Device architecture of stacked OSCs	93
Figure 4.6. Device architecture of tandem OSCs	94
Figure 4.7. Detailed device architecture of BHJ OSCs	95
Figure 4.8. Operational processes of BHJ OSCs.....	98
Figure 4.9. The equivalent electrical circuit of a single solar cell.	100
Figure 4.10. R_{sh} and R_s in the equivalent circuit of a single solar cell	101
Figure 4.11. The two-diode model as an equivalent electrical circuit.....	102
Figure 4.12. The reverse 3-diode model.....	103
Figure 4.13. Photovoltaic performance from J-V curve.....	103
Figure 4.14. Illustration of aromatic and quinoidal form	105
Figure 4.15. Chemical structures of PTR based polymers	106
Figure 4.16. Chemical structures of PTDBD based polymers.....	107
Figure 4.17. Chemical structures of PTAT-3 and PTB-8.....	107
Figure 4.18. Chemical structures of PS, PSe, PO, PF and literature polymer.....	110
Figure 4.19. Indeno[1,2-b]quinoxalin containing polymers	111
Figure 4.20. Representative distribution of ordinary and modified nanoparticles ..	112
Figure 4.21. Synthesis of monomers: a) $SOCl_2$, DCM, NEt_3 , b) AcOH, DCM, Br_2 c) HNO_3 , AcOH d) $SnCl_2 \cdot 2H_2O/EtOH:HCl$ e) SeO_2 , AcOH, EtOH f) NaN_3 , n-Bu ₄ NBr, toluene, PPh_3	114
Figure 4.22. Polymerization reaction: a) $Pd(PPh_3)Cl_2$, toluene; end cap: 2-tributyltinthiophene, 2-bromothiophene	114
Figure 4.23. Electronic structure of constructed devices and literature polymer. ...	117
Figure 4.24. A thin film (a) and solution (b) Uv-Vis spectrum of polymers.....	118
Figure 4.25. Carbazole copolymers of benzothiadiazole derivatives	119

Figure 4.26. Single scan cyclic voltammograms of polymers PF, PO, PS, and PSe in 0.1 M TBAPF ₆ /ACN electrolyte solution at 100 mV/s scan rate.	120
Figure 4.27. J-V curves of polymer OSCs	123
Figure 4.28. IPCE curves of polymer OSCs	124
Figure 4.29. Synthetic pathways of low bandgap polymers	126
Figure 4.30. Uv-vis spectra of low bandgap polymers	128
Figure 4.31. Single scan cyclic voltammogram of PIQCAR ad PIQBDT.....	129
Figure 4.32. An example of the chemical structures of modified polymers	131
Figure 4.33. Synthetic pathways of monomers	132
Figure 5.1. Alkyl chain modification of BTz polymers.	138
Figure 5.2. Colours of modified super capacitor on different voltages. Reproduced with permission from J. Electrochem. Soc., 162 (14) A2807 (2015) Copyright 2015.	139
Figure 5.3. Conducting polymers containing polypeptide and ferrocene side chains as ethanol biosensors. Polym. Chem., 2014,5, 6295-6306 Reproduced by permission of The Royal Society of Chemistry (RSC) on behalf of the Centre National de la Recherche Scientifique (CNRS) and the RSC.	139
Figure 5.4. Left: preparation of PIP/CF555/anti-CD44 bioconjugate. Right: Imaging of HaCaT and U87-MG cells via fluorescence microscopy. Images were obtained after treatment of the cell with PIP monomer (A), PIP/anti-CD44 (B) and PIP/CF555/anti-CD44 (C1 and C2) for 2 h at 37 °C and 5.0% CO ₂ atmosphere, under humidity. Photos of A, B and C1 were taken with UV filter of fluorescence set up. Photos of C2 were taken with red filter of fluorescence set up with 100x magnification. All scale bars are 10 mm . RSC Adv., 2015,5, 83361-83367 Modified by permission of The Royal Society of Chemistry (RSC) on behalf of the Centre National de la Recherche Scientifique (CNRS) and the RSC.	140
Figure 5.5. Polymers for solar cell applications. This article was published in Polymer, 133, Özge Azeri, Ece Aktas, Cagla Istanbuluoglu, Serife O.Hacioglu, Sevki Can Cevher, Levent Toppare, Ali Cirpan, Efficient benzodithiophene and	

thienopyrroledione containing random polymers as components for organic solar cells, 60–67, Copyright Elsevier (2017).	140
Figure 0.1. FTIR spectra of 2-(3-((10-(4,7-dibromo-2H-benzo[d][1,2,3]triazol-2-yl)decyl)oxy)phenyl)-1-(4-hexylphenyl)-1H-phenanthro[9,10-d]imidazole (IV) (ATR).....	169
Figure 0.2. FTIR Spectra of 2-(3-((10-(4,7-di(thiophen-2-yl)-2H-benzo[d][1,2,3]triazol-2-yl)decyl)oxy)phenyl)-1-(4-hexylphenyl)-1H-phenanthro[9,10-d]imidazole (VI) (ATR).	169
Figure 0.3. FTIR spectrum of monomer M1 (ATR).....	170
Figure 0.4. FTIR spectrum of monomer M2 (ATR).....	170
Figure 0.5. FTIR spectrum of monomer M3 (ATR).....	170
Figure 0.6. Stacked FTIR spectrum of monomers M1, M2 and M3 (ATR).....	171
Figure 0.7. FTIR spectrum of polymers PS (ATR).	171
Figure 0.8. FTIR spectrum of polymers PSe (ATR).	171
Figure 0.9. FTIR spectrum of polymers PO (ATR).....	172
Figure 0.10. FTIR spectrum of polymers PF (ATR).	172
Figure 0.11. Stacked FTIR spectrum of polymers PS, PSe, PO and PF (ATR).....	172
Figure 0.12. FTIR spectrum of PIQCAR (polymer C) (ATR).	173
Figure 0.13. FTIR spectrum of PIQBDT (polymer B) (ATR).	173
Figure 0.14. Stacked FTIR spectrum of PIQCAR (polymer C) and PIQBDT (polymer B) (ATR).....	173
Figure 0.15. ¹ H NMR spectrum of 1,2-dimethoxy-4,5-dinitrobenzene (in CDCl ₃). 174	
Figure 0.16. ¹³ C NMR spectrum of 1,2-dimethoxy-4,5-dinitrobenzene (in CDCl ₃).	174
Figure 0.17. ¹ H NMR spectrum of 5,6-dimethoxybenzo[c][1,2,5]selenadiazole (in CDCl ₃).	175
Figure 0.18. ¹³ C NMR spectrum of 5,6-dimethoxybenzo[c][1,2,5]selenadiazole (in CDCl ₃).	175
Figure 0.19. ¹ H NMR spectrum of 4,7-Dibromo-5,6-dimethoxybenzo[c][1,2,5]selenadiazole (in CDCl ₃).....	176

Figure 0.20. ^{13}C NMR spectrum of 4,7-Dibromo-5,6-dimethoxybenzo[c][1,2,5]selenadiazole (in CDCl_3).....	176
Figure 0.21. ^1H NMR spectrum of 5,6-dimethoxybenzo[c][1,2,5]thiadiazole (in CDCl_3).....	177
Figure 0.22. ^{13}C NMR spectrum of 5,6-dimethoxybenzo[c][1,2,5]thiadiazole (in CDCl_3).....	177
Figure 0.23. ^1H NMR spectrum of 4,7-Dibromo-5,6-dimethoxybenzo[c][1,2,5]thiadiazole (in CDCl_3).....	178
Figure 0.24. ^{13}C NMR spectrum of 4,7-Dibromo-5,6-dimethoxybenzo[c][1,2,5]thiadiazole (in CDCl_3).....	178
Figure 0.25. ^1H NMR spectrum of 5,6-dimethoxybenzo[c][1,2,5]oxadiazole (in CDCl_3).....	179
Figure 0.26. ^{13}C NMR spectrum of 5,6-dimethoxybenzo[c][1,2,5]oxadiazole (in CDCl_3).....	179
Figure 0.27. ^1H NMR spectrum of 4,7-dibromo-5,6-dimethoxybenzo[c][1,2,5]oxadiazole (in CDCl_3).....	180
Figure 0.28. ^{13}C NMR spectrum of 4,7-dibromo-5,6-dimethoxybenzo[c][1,2,5]oxadiazole (in CDCl_3).....	180
Figure 0.29. ^1H NMR spectrum of P1 (in CDCl_3).....	181
Figure 0.30. ^1H NMR spectrum of P2 (in CDCl_3).....	181
Figure 0.31. ^1H NMR spectrum of P3 (in CDCl_3).....	182
Figure 0.32. ^1H NMR spectrum of PO (in CDCl_3).....	182
Figure 0.33. ^1H NMR spectrum of PS (in CDCl_3).....	183
Figure 0.34. ^1H NMR spectrum of PSe (in CDCl_3).....	183
Figure 0.35. ^1H NMR spectrum of PF (in CDCl_3).....	184
Figure 0.36. TGA result of P1.....	184
Figure 0.37. TGA result of P2.....	185
Figure 0.38. TGA result of P3.....	185
Figure 0.39. TGA result of PO.....	186
Figure 0.40. TGA result of PF.....	186

Figure 0.41. TGA result of PS	187
Figure 0.42. TGA result of PSe	187
Figure 0.43. TGA result of PIQCAR.....	188
Figure 0.44. TGA result of PIQBDT	188
Figure 0.45. DSC result of P1.....	189
Figure 0.46. DSC result of P2.....	189
Figure 0.47. DSC result of P3.....	189
Figure 0.48. DSC result of PO.....	190
Figure 0.49. DSC result of PF	190
Figure 0.50. DSC result of PS	191
Figure 0.51. DSC result of PSe.....	191
Figure 0.52. DSC result of PIQCAR	192
Figure 0.53. DSC result of PIQBDT	192

LIST OF ABBREVIATIONS

ABBREVIATIONS

OLED	organic light emitting diode
OPV	organic photovoltaic
Alq3	tris(8-hydroxyquinolato) aluminum
PPV	poly(<i>p</i> -phenylene vinylene)
PE	polyethylene
HOMO	highest occupied molecular orbital
LUMO	lowest unoccupied molecular orbital
VB	valence band
CB	conductance band
<i>t</i> -PE	trans polyethylene
PICT	photoinduced charge transfer
D	donor
A	acceptor
PIET	photoinduced electron transfer
FRET	fluorescence- resonance energy transfer
PLED	polymer light emitting diode
PEDOT:PSS	poly(3,4-ethylenedioxythiophene)-poly(styrenesulfonate)
ITO	indium tin oxide
FTO	fluorine doped tin oxide

AZO	aluminum doped zinc oxide
TCO	transparent conductive oxides
CVD	chemical vapor deposition
HTL	hole transport layer
ETL	electron transport layer
TADF	thermally activated delayed phosphorescent
<i>J-V</i>	current density vs applied voltage
<i>J-V-L</i>	current density vs applied voltage vs luminance
EL	electroluminescence
CIE	Commission International de l'Eclairage
OLED	organic light emitting diode
EQE	external quantum efficiency
BTz	4,7-dibromo-2-(10-bromodecyl)-2H-benzo[<i>d</i>][1,2,3]triazole)
TTBTzT	2-(10-bromodecyl)-4,7-di(thiophen-2-yl)-2H-benzo[<i>d</i>][1,2,3]triazole
NMR	nuclear magnetic resonance
TMS	trimethyl silyl
FTIR	fourier transform infrared
RID	refractive index detector
TGA	thermo-gravimetric analysis
DSC	differential scanning calorimeter
HRMS	high resolution mass spectrometer
PDI	polydispersity index

Mn	number average molecular weight
Mw	weight average molecular weight
GPC	gel permeation chromatography
CE	counter electrode
WE	working electrode
RE	reference electrode
CV	cyclic voltammeter
TBAPF ₆	tetrabutylammonium hexafluorophosphate
ACN	acetonitrile
SCE	standard calomel electrode
PL	photoluminescence
USD	United States dollar
HIV	human immunodeficiency virus
SARS-CoV	severe acute respiratory syndrome coronavirus
OCP	organic conjugated polymer
DNA	deoxyribonucleic acid
β -HCG	β -human chorionic gonadotropin
PQQGDH	pyrroloquinoline quinone glucose dehydrogenase
L-DOPA	levodopa 1-3,4-dihydroxyphenylalanine
IUPAC	International Union of Pure and Applied Chemistry
PPO	polyphenol oxidase
CNT	carbon nanotube

OSC organic solar cell

NIR near infrared

LIST OF SYMBOLS

SYMBOLS

Φ_w	work function
ΔE_e	injection barrier for electron
Φ_{wc}	work function of cathode
A	electron affinity
ΔE_h	injection barrier for hole
I	ionization potential
δ	chemical shift
J	coupling constant
λ_{max}	maximum wavelength
E_{ox}^{onset}	oxidation onset potential
E_{red}^{onset}	reduction onset potential
L	luminance
a	hue
b	saturation
pH	power of hydrogen
K_{sp}	solubility product
K_d	dissociation constant

CHAPTER 1

OUTLOOK

This Ph.D. thesis covers three different application areas of organic electronics; organic light emitting diodes, biosensors and organic solar cells.

In the first chapter, syntheses and characterizations of alkyl-end fused phenanthroimidazole containing conjugated moiety with benzotriazole based conjugated polymeric backbone were performed. In general, fused phenanthroimidazole emits deep blue light and fused structures have an ability to alter the morphology of active layer thus performance of the device. Combinations of phenanthroimidazole with benzotriazole conjugated polymeric backbone were investigated to reveal the effect of fused structures in organic light emitting diodes.

In the second part, laccase based catechol biosensor was constructed with three different electrochemically polymerized fused conjugated monomers. These three monomer differentiates with each other in terms of their functional groups. Ketone, oxime, and enamine functionalities were investigated for biosensor performances for catechol sensing in wastewater. Functional groups are important parameters to manage (i) electronic structure, (ii) morphology, (iii) interactions between enzyme and both analyte (catechol) and substrate (in this particular case electrochemically polymerized monomer on indium tin oxide coated glass, working electrode). To investigate the different functionalities on the biosensor performance; ketone, oxime, and enamine-functionalized monomers were used to construct laccase based catechol biosensors.

In the final part, conjugated organic polymers were investigated for organic solar cell performances. There will be three different study:

i) To increase the solar cell performance of previously known literature polymer four different polymer were synthesized. Bandgap engineering to adjust the HOMO and LUMO energy levels of the conjugated polymers as well as the optical absorption characteristics, two different approach were utilized. The first one is the single atom replacement in the derivatives of benzochalcogenodiazole moiety from oxygen to selenium. The second one is the modification of benzothiadiazole with electron withdrawing/donating (F/OCH₃) substituents. Both approaches not only affect the energetic levels of the polymers but also have great impact on morphology that is also crucial for efficient solar cells.

ii) To extend the absorption of polymers to infrared region, fused conjugated polymers were synthesized.

iii) To control the effect of plasmonic nanoparticles on conjugated polymers in organic solar cells, synthesis of thiol modified polymers were performed. Those polymers have an ability to covalently bond to the plasmonic gold nanoparticles. The distribution of nanoparticles in the bulk heterojunction solar cells could be controlled in such a way that existence of nanoparticles closer than ever in other studies.

CHAPTER 2

FUSED STRUCTURES IN ORGANIC LIGHT EMITTING DIODES

2.1. Organic Electronics

In 1977, the discovery of the metallic properties of iodine vapor doped polyethylene had pioneered the remarkable progress in the electronic and optical applications (1). Conjugated polymers/small molecules are precious material that they can possess both the optical and the electronic properties of metal and at the same time mechanical features with processing benefits of plastics. The key advantages of organic materials stem from their unique properties such as low cost, large area applicability, ease of tuning the optical and the electronic properties via fine chemical modifications, mechanical flexibility, versatility of chemical synthesis so on so forth (2). These organic materials currently are under enormous development for use in organic electronics, which covers but not limited to organic light emitting diodes (OLEDs) (3–6), sensors: biosensors (7), gas sensors (8, 9), metal ion sensors (10), lasers (11), organic photovoltaics (OPVs) (12–17), super capacitors (18, 19), carbon dioxide reduction (20, 21).

In the 1950s, researchers found that polycyclic organic aromatic materials like perylene compound can form 0.12 S/cm semiconducting charge transfer complex salt with iodine (22). In the 1960s, the discovery of electroluminescence of molecular crystals led intensive investment to organic electronics (23, 24). During the 1970s, besides molecular crystals, a second important type of organic semiconductors have taken a stage after successful synthesis of conjugated polymers whose conductivity can be controlled over the range of insulating to metallic (1). This led eventually a new research field awarded by Nobel Prize in Chemistry in 2000.

Real world application of organic optoelectronics has started by Tang and VanSlyke in 1987 (25). They were working at Kodak Company and using a thin film of tris(8-hydroxyquinolinato) aluminum namely Alq₃, an organic light emitting diode (OLED) device was successfully fabricated. Soon after, poly(*p*-phenylene vinylene) (PPV) has been emerged by Friend and coworkers at the Cavendish Laboratory in Cambridge (26). In today's world, organic electronics in particularly OLEDs have reached a new era and solid steps toward to commercialization of mobile phones, displays, televisions, and white light illuminations have been made.

Great effort has been done for developing the organic electronics and extensive collaborations of chemists, engineers and physicists will be needed for large scale production. Beside device fabrication techniques, the fundamental way to high performance devices is creating the novel material with optimal properties (2, 27–30). Hence, a better understanding of the intrinsic properties such as the nature of electronic excitation, charge transport and carriers phenomena raise a major challenge (2). Unfortunately, the nature of complex electronic processes is in generally “too abstract” for synthetic chemists to understand; although, there are various comprehensive reviews, books and papers on theoretical and experimental studies of organic electronics. Thereafter, the fundamental properties of organic electronics will be discussed from a chemist perspective.

2.2. Properties of Organic Electronic Materials

As compared with metals and inorganic semiconductors, delocalization of outer shell electrons over a bunch of atoms is suppressed by the nature of intermolecular interactions in organic semiconductors. These interactions can be classified into two main types (2):

- ☞ Nonpolar organic solids: weak van der Waals interactions are the dominant forces to held molecules together.
- ☞ Polar organic solids: Both weak van der Waals and relatively strong ionic bonding exist in these type of materials. Organic charge transfer

complexes, and radical ion salts can be a good example where opposite charges can be located the different side of the molecules. Intrinsically the ionic bond of polar organic solids is weaker than that of inorganics due to larger molecular radius than an atom.

A common property of the wide variety of organic semiconductors is possessing a π -conjugated electronic structure. The alternating single and double bond allows the delocalization of π -electrons over the contiguous sp^2 -hybridized carbons or atoms that have available p_z -orbitals. The main parameter to tune the optoelectronic properties of organic material is the conjugation system, which can be modified via feasible chemical synthesis.

Organic solids in general are classified into two main groups. These are conjugated small molecules and conjugated polymers according to their molecular weight. Chromophore can be defined as the conjugated moiety of a molecule and conjugated small molecules contain one or a few of conjugated moiety. Conjugated polymers can be regarded as an assembly of weakly coupled chromophores of only a few tens of short conjugation (30).

The crucial difference lies in crystallinity between conjugated small molecules and polymers while processing the thin film. Small molecules tend to form ordered arrays of crystals when they are deposited onto a surface by sublimation or chemical vapor deposition. On the other hand, as thin film formation of conjugated polymers is achieved by solution processing as spin coating or with printing techniques, generally amorphous morphology is obtained. Since intrinsic or dynamic defects often interrupt the delocalization of π -electrons, the performance of polymers devices is highly sensitive to the way the film formed.

Trans-polyethylene as the simplest conjugated polymer has an alternating single and double carbon-carbon bonds in its backbone. Whereas bare *trans*-polyethylene shows characteristics of insulators, its conductivity can be enhanced by chemical redox process (1). This extraordinary behavior of conjugated *trans*-polyethylene can be

regarded as a milestone in the timeline of organic electronics and it was awarded by Nobel Prize for Chemistry to Heeger, MacDiarmid and Shrikawa in 2000.

As *trans*-polyethylene, poly-aromatic hydrocarbons and their derivatives show similar properties. Because polyacene, a subclass of poly-aromatic hydrocarbons, has a simple linear structure, well defined conjugation, highly ordered crystal structures in solid state and well-studied optical and electronic properties; they are frequently regarded as a model for investigation in molecular and solid state physics.

There are various geometries to derive the molecular structures of conjugated moieties seen in Figure 2.1, linear: anthracenes, pentacene, ladder-type: poly-para-phenylene, geometric shapes: sheet-like coronene, ball-like fullerene and more.

To extend the variation one can introduce the heteroatom either inside (polythiophenes) or outside (polyanilines) of the aromatic ring. One of the special heteroatomic macrocycles is the class that includes phthalocyanines or porphyrins type materials which can make a complex with metals (31, 32).

Previously researchers mainly have been focused on the backbone of the polymer by introducing varieties of electron-donating or withdrawing substituents. These modifications not only alter the optical and electronic properties of material to desired level but also may enhance their processibilities in solution phase. It is worth noting here that an interesting strategy usage of bulky side groups can reduce the formation of non-emitting interchain aggregates.

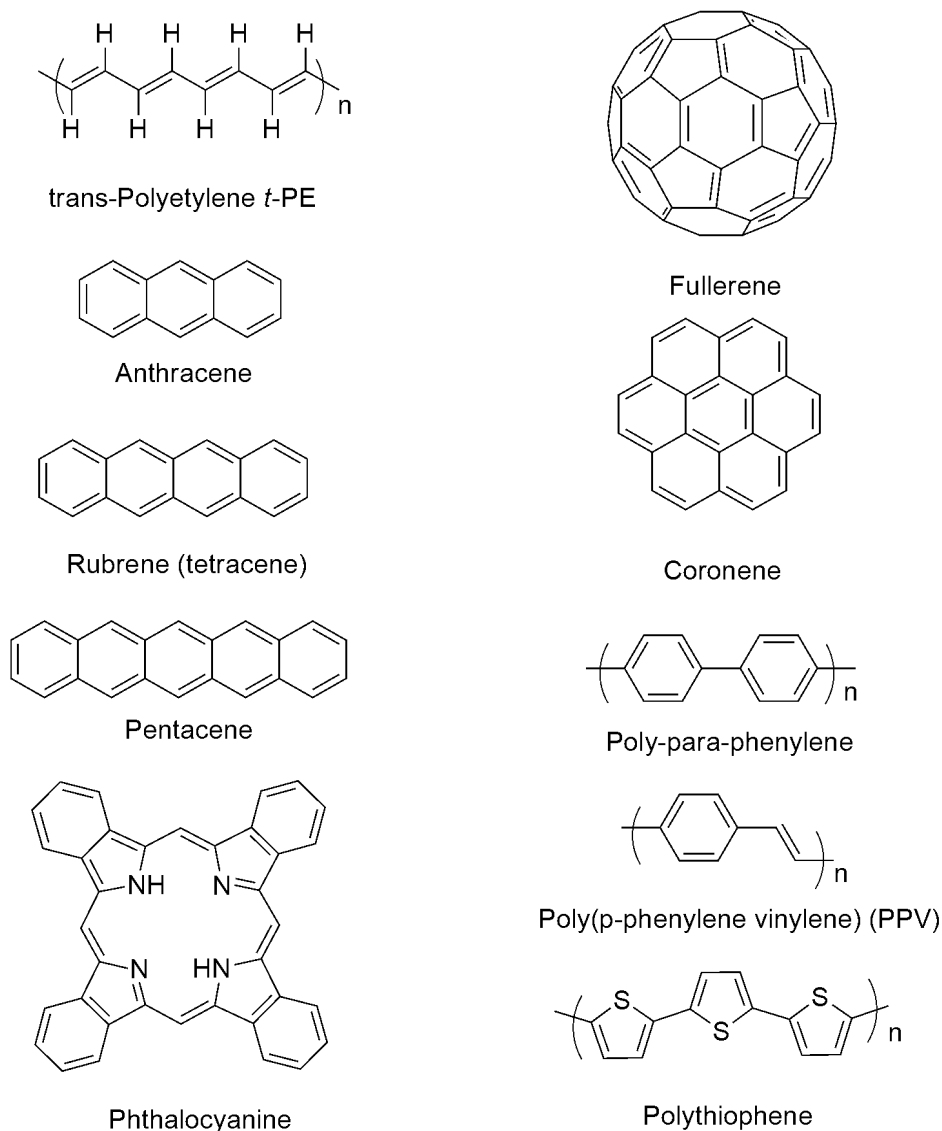


Figure 2.1. Conjugated molecular structures

One more important factor is the intermolecular forces for the optical and electronic properties. Depending on the usage, for example, π - π stacking is generally beneficial for charge transport and advantageous for field effect transistors; however, π - π stacking may quench the emissive excited state in electroluminescent devices (33). Other intermolecular forces can be listed as hydrogen bonding, hydrophilicity/hydrophobicity, electrostatic forces also direct the way of aggregation or assembly of the molecules in thin film morphology. One of the hot topics in this field is that the

role of intermolecular attraction during the thin film formation and its effect on the device performance. Molecular geometries of molecules or polymers have diverse effects on intermolecular attractions. From the simplest geometry linear polyethylene (PE) to two dimensional (2-D) planar phthalocyanines and even more complicated structures shown in Figure 2.2, such as star-shaped (34), tree-shaped dendrimers (35) and spiro structures (36) as well as 3-D structures have significant effect on conjugation and conformational disorder. Thus, assembling behaviors alter the solid state of the compound and greatly influence the thin film properties.

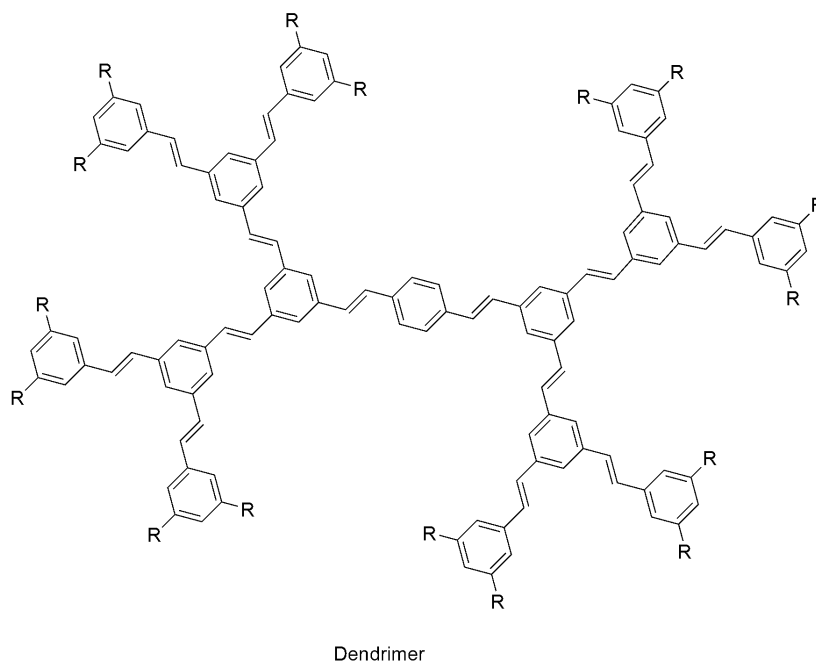
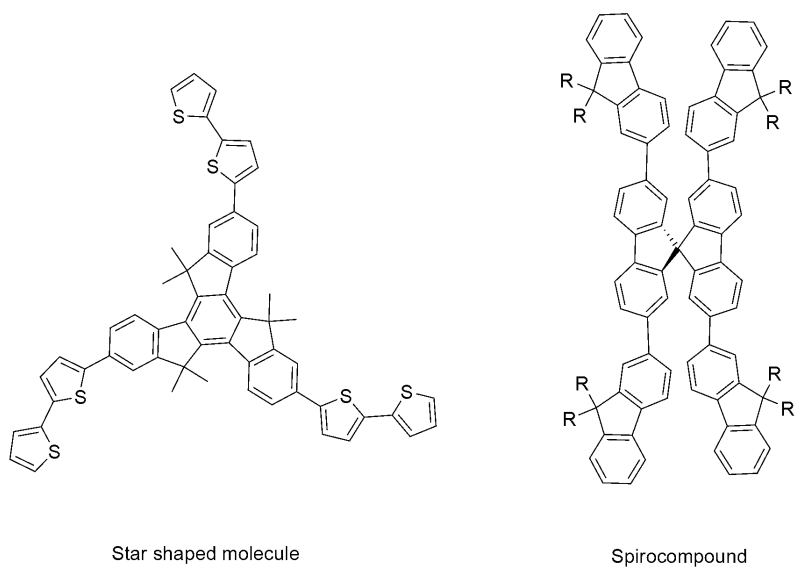


Figure 2.2. Several different geometries of conjugated molecules

2.3. Basics of Electronic Process in Conjugated Structures

In this section, (i) complex molecular system possessing various electronic and vibrational states and transitions; (ii) energy and charge transport phenomenon which can be multistep and have complex dynamics will be interpreted. There would be more sophisticated explanations from mathematicians and/or physicists; however, this

thesis covers the description of the basic information of organic electronics from a point view of a chemist.

Description of the energy band is a good point to start. In the solid form of material, atoms/molecules influence each other. Outer shell electrons are attracted by neighboring nuclei of atoms/molecules. Thus, their electronic structures are altered. This refers to the splitting of orbitals and redistribution of the energy levels. For many atoms/molecules, the complex structure of electronic interactions in solids ends up with continuous bands of energy. At this stage the first and crucial difference occurs between insulators/semiconductors and conductors. For insulator/semiconductor there is an energy gap where there is no electron orbital exists between filled and empty bands. In organic materials commonly filled orbitals named as Highest Occupied Molecular Orbital (HOMO) and empty orbitals named as Lowest Unoccupied Molecular Orbital (LUMO). In contrast, conductors has no gap between Valence Band (VB) and Conductance Band (CB). There is a hypothetical energy level, exactly half-filled, between filled and empty orbitals. According to characteristics of material whether n-type or p-type, it can shift to unfilled orbital or filled orbital, respectively (Figure 2.3).

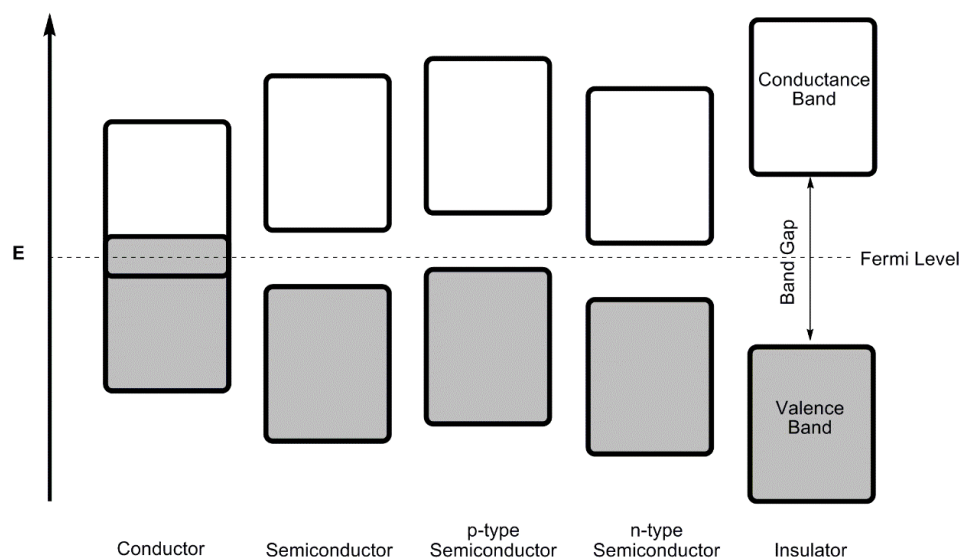


Figure 2.3. Energy band structures of metal, semiconductor, and insulator. The Fermi level is simply defined as the hypothetical energy level at which an orbital is exactly half-filled.

Overlapping VBs and CBs of metals supply these materials good conductivity even at a low temperature, whereas for inorganic solids like silicon thermoactivated electrons from VB into CB result in a bunch of mobile “free” electron which is responsible for semiconductivity. On the other hand, insulators have wide bandgap that is too large for thermoexcitation and therefore they cannot conduct electricity.

Plastics and rubbers known as the first commercial polymers have saturated carbon backbone and are good examples of insulators. On the other hand, conjugated polymers have alternating single and double bonds and since they have a π -conjugated backbone, they can possess semiconducting properties. In a specific case in which *t*-PE has a uniform C-C bond length throughout the backbone and if there is an unpaired electron on each carbon, then degenerate π -orbitals will be half-filled. Under these circumstances, *t*-PE behaves like a 1-D metal. Unfortunately, above mentioned structure is unstable and polymer favors alternating single and double bonds. Luckily, charge carriers can be generated upon chemical modifications, oxidation or reduction of the polymeric backbone. By this way, the conductivity of *t*-PE can be tuned from insulating to metallic character.

Conjugated polymers have been widely used since their semiconducting properties had been discovered by Alan J. Heeger, Alan G. MacDiarmid and Hideki Shirakawa in 1977 (1). From that time, interest in the scientific community has continuously increased. Promising electronic properties of π -conjugated polymers also show good mechanical properties like typical polymers. Moreover, polymeric materials with high conductance close to copper with enhanced mechanical properties comparable with steel have been produced (37). Conjugated polymers have been used for various applications in electrochromics, organic light emitting diodes (OLEDs), photovoltaic devices, thin film transistors, electrochemical transistors, and most recently in bio-applications such as biosensors, in-vitro diagnostics, and drug delivery.

2.3.1. Excited States

There are various types of excited states-charged or neutral- depending on the molecular structure of the conjugated polymers and extend of doping. These excited states are considered as quasiparticles (38) in order to investigate their interactions with surroundings, rather than pure electronic states. This is particularly useful for disturbed motion of electron by other electrons and nuclei, because it mainly behaves as an electron but with a different mass. Then it termed as an “electron quasiparticle” but for convenience simply called as electron. Solitons, polarons, bipolarons, and excitons are the terms to describe the various types of excitations whose chemical nature and characteristics will be described next.

2.3.1.1. Soliton

Previously mentioned *t*-PE possesses unique degenerate ground state and every carbon atom has one electron in p_z orbital to form a π -bond (39, 40). If the number of carbon atoms in the conjugation of *t*-PE is odd, then one unpaired electron remains on the backbone. This unpaired electron is a boundary element between two segments with opposite orientations and can move up to 14 carbons length (38) and it was claimed that for polyphenylenevinylenes (PPVs) average conjugation length (30) is around 10 nm. It can be turned into a positive or negative charge upon oxidation or reduction, respectively. Radical or charge associated with boundary is named as a soliton. Soliton can propagate without deformation and dissipation as solitary waves.

Existence of soliton results in localized electronic level at the mid gap (Figure 2.4):

- ☞ Neutral solution → half occupied
- ☞ Positively charged solution → empty
- ☞ Negatively charged soliton → doubly occupied.

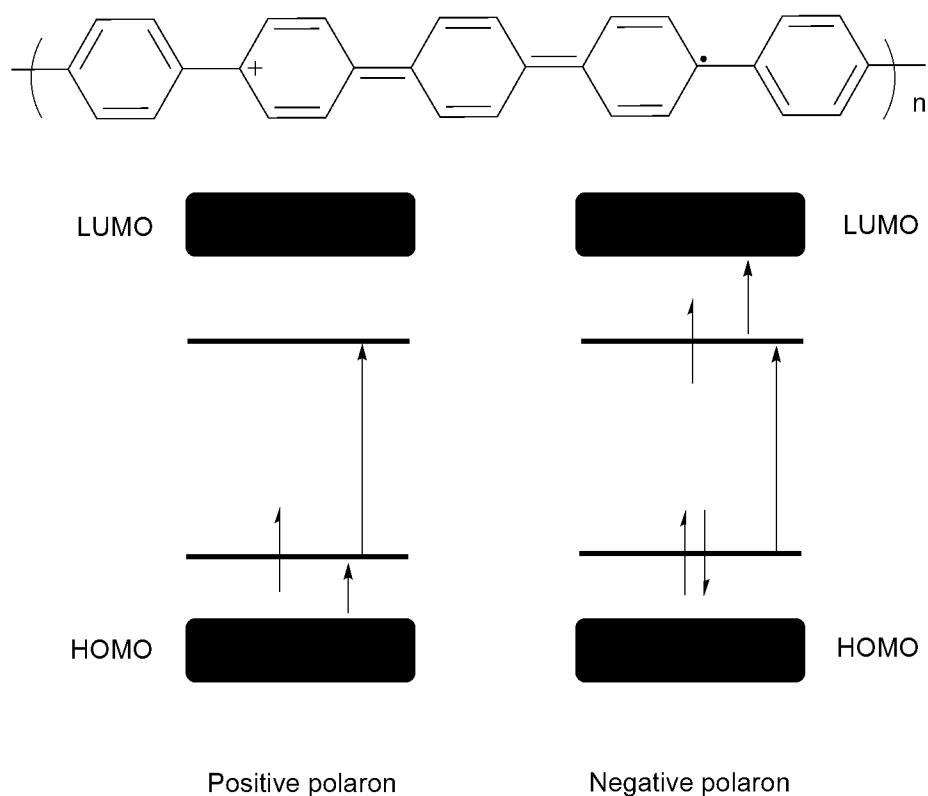


Figure 2.4. Schematic illustration neutral, negatively charged and positively charged solitons whose allowed transitions are indicated by solid arrows.

With increasing the doping level, overlapping of the soliton states at mid gap results in soliton band. Soliton only exists in π -conjugated structures with a degenerate ground state like *t*-PE and one of the primary elements of charge transport because it can spread over several atoms.

2.3.1.2. Polaron

Many conjugated molecules or polymers for example polythiophene possesses a nondegenerate ground state, unlike *t*-PE. The transition between aromatic and quinoid form with higher total energy (39) enables the main charged excitations, radical ions strongly bound with the lattice distortion. These charged excitations can be divided into two (Figure 2.5):

- ☞ Positive polarons: radical cations
- ☞ Negative polarons: radical anions

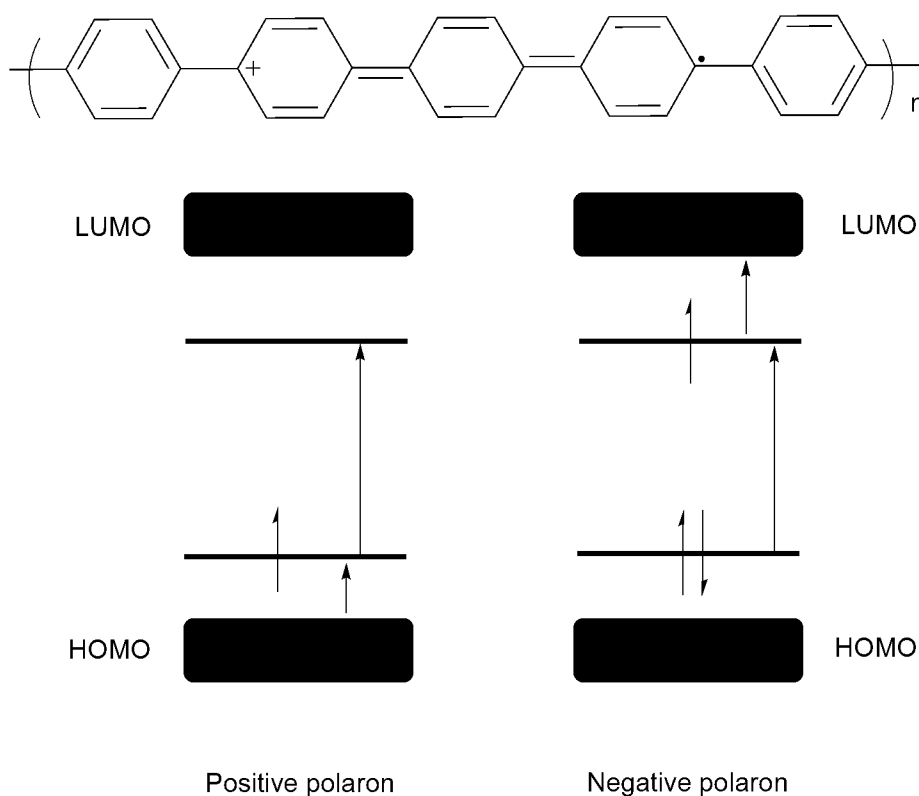


Figure 2.5. Schematic illustration of positive polaron (above). Positive and negative polarons whose allowed transitions are indicated by solid arrows (below).

Chemical/electrochemical redox reactions or photoinduced charge transfer are responsible for polaron formation. The local lattice distortion tends to localize the charge; therefore, upshift of HOMO and downshift of LUMO are observed. For two different cases, there are two possible transitions (solid arrows) can be seen. Although the valence band and conductance band remain filled and empty, respectively. Similar to a soliton, polaron can also propagate along with the conjugation. It is also possible if the acceptor chain has similar lattice distortion like donor (Marcus model), polaron can jump from donor to acceptor moieties. In the working principle of OLEDs holes and electrons are injected through respective electrodes and recombination of these positive and negative polarons may result in a general singlet or by the help of phosphorescent guest triplet excited states which can then emit light.

2.3.1.3. Bipolaron

Bipolaron is a couple of the same charges in lattice distortion. Further doping extents or high charge capacity differentiates bipolarons from polarons. Combination of two polarons with the same sign create a bipolaron (negative/positive) and this indicates that repulsion of the same charges in the confinement is less than the energy gained by the interaction with the lattice (39). Stronger lattice relaxation around two charges enables a stronger shift of HOMO and LUMO. Because bipolaron has no half-filled orbital, one electronic transition (solid arrow) can be seen in Figure 2.6. Hence, it can be distinguished from polaron simply by using spectroscopic methods.

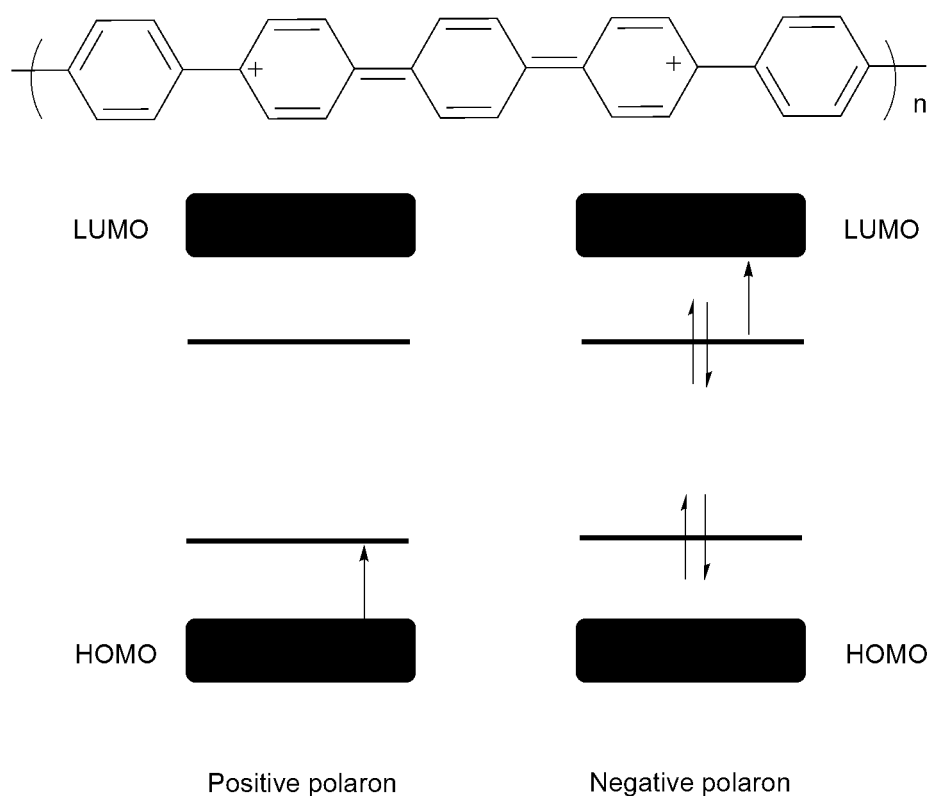


Figure 2.6. Schematic representation of positive bipolaron

2.3.1.4. Exciton

The neutral excitations generated following absorption which will be the course of organic solar cells or recombination of an electron and a hole which is crucial for

OLEDs are classified as excitons. In particular, excitons are divided into 3 major types according to their binding energies (38):

- ☉ Frenkel excitons: The most tightly bound (1 eV) exciton is the Frenkel type (Figure 2.7). This strong attraction of the hole and the electron results in a small radius of Frenkel excitons and generally, similar to a molecular excited state, they are located on the same molecule. Because Frenkel excitons are analogous to molecular excited states, they have well-defined spin states. Moreover, their diffusion in thin film solid states can be interpreted by Förster and Dexter models.
- ☉ Wannier-Mott excitons: Small binding energies of Wannier-Mott excitons enable to treat the electron and hole as two individual quasiparticles (Figure 2.7). These quasiparticles (negative polaron and positive polaron) are bound loosely by the same lattice distortion and can also be classified as neutral bipolarons. In contrast to Frenkel type, Wannier-Mott excitons have delocalization and small binding energy enables it to easily be separated. Also, rapid singlet-triplet exchange occurs. This Wannier-Mott type is generated usually in inorganic semiconductors and dissociation is very rapid at room temperature.
- ☉ Charge transfer excitons: This is the intermediate one between Wannier-Mott and Frenkel. According to lattice distortion, separated but still tightly bound charge transfer excitons can either be delocalized or localized. Analogous to charge transfer states, charge transfer excitons can be observed in donor-acceptor molecules where donor holds the hole and acceptor holds the electron.

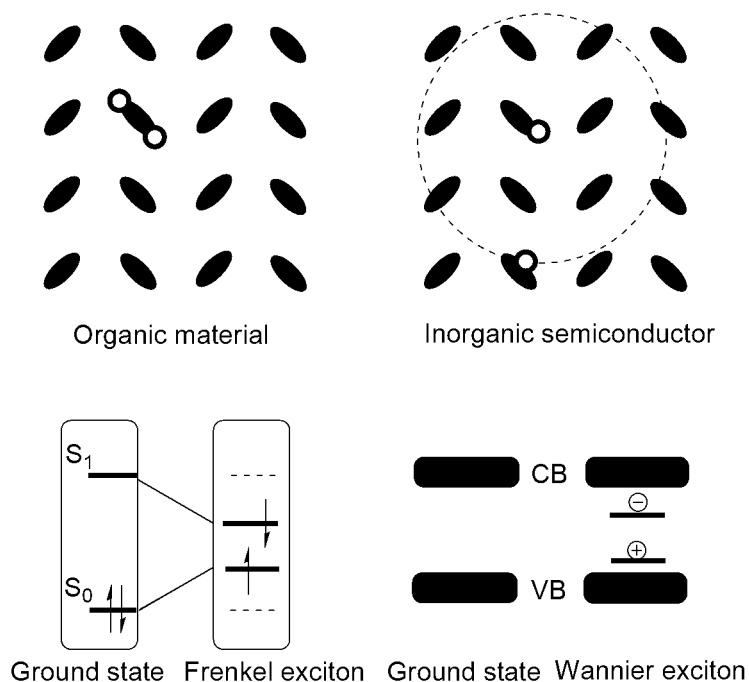


Figure 2.7. Illustrations of Frenkel and Wannier excitons

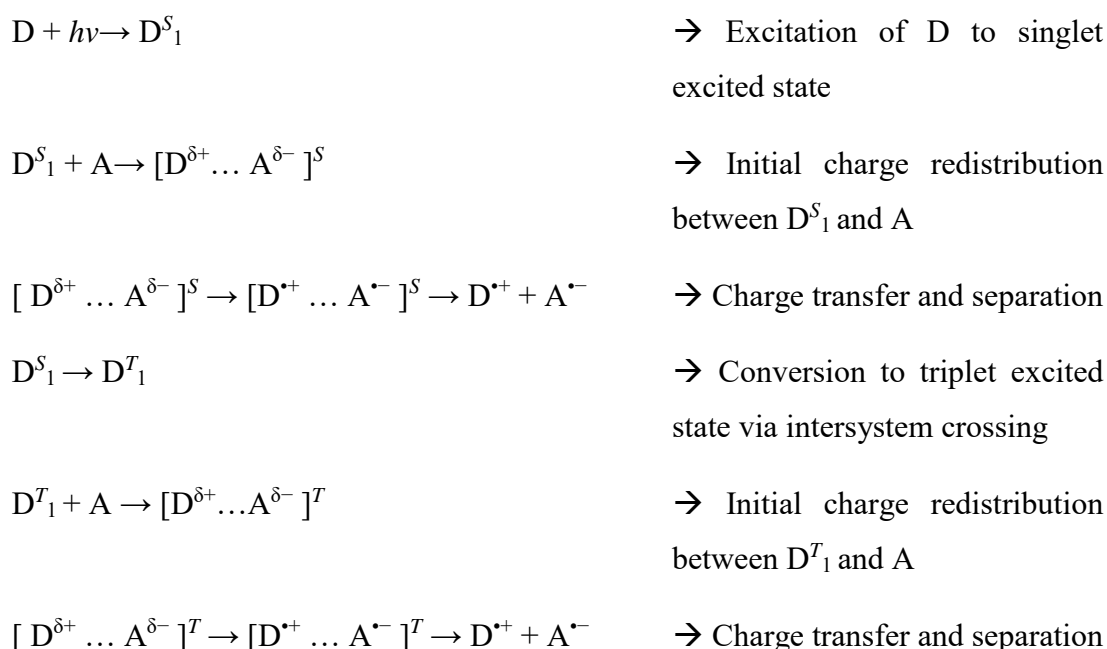
The debate concerning the intrinsic properties of primary excitations of conjugated polymer (41, 42) is whether they are Frenkel type, Wannier-Mott type, charge polarons or anything else? The answer is important for various applications such as for OLEDs. If the primary excitations are Frenkel type then, injected electrons and holes can generate triplet (spin multiplicity of three) and singlet (spin multiplicity one) states. Unless a phosphorescence mechanism is applied, only the latter one with the probability (theoretical efficiency) of 25% will recombine radiatively. However, theoretical efficiency can approach 100% if the primary excitations are charge polarons. In solar cell devices, the working principle will be explained in detail later but Frenkel excitons need to diffuse to donor-acceptor interface to dissociate into free charges. However, free charge carriers are formed locally because Wannier-Mott excitons tend to dissociate rapidly. One of the most important factor to identify the nature of the primary excitons is binding energy. According to the photoconductivity spectrum and electroabsorption measurements, polydiethylenes have been found to have an exciton with about 0.5 eV binding energy. However, photoconductivity of

PPV and its soluble derivatives began at the onset of optical absorption that is binding energy is less than 0.1 eV, although about 0.4 eV was found from other experimental techniques. Nowadays, it is generally thought that the lowest energy excitations are neutral Frenkel excitons in π -conjugated organic polymers.

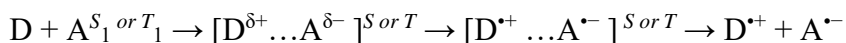
2.3.2. Charge and Energy Transfer

Following excitation, in general one of the two electrons at HOMO gain energy to jump to LUMO or higher. Owing to the high energy of the excited electron, it can be donated or because HOMO is now half-occupied, it can accept an electron. Such a light driven process is named as photoinduced charge transfer (PICT). Generation of excimer or exciplex is a particular case in which charge density is slightly redistributed over two constituents. Yet, in PICT complete transfer occurs between two distinct moieties, for example, atoms or molecules. At this point, photoinduced electron transfer, where electron providing moiety is named as donor (D) and electron receiving moiety is named as acceptor (A), gets attention.

In principle, either triplet or singlet excited state of D donates an electron to A, if A has a lower-lying empty energy level than the excited state of D.



In some cases; however, electron transfer occurs between ground states of D and excited A:



From this approach, excitation of A generates a vacancy at HOMO of A and this can be filled by electrons of D. At the end a new vacancy is created at HOMO of D. The term for such a vacancy is hole and during the process the generated hole at A is transferred to D. In this case HOMO of D should be higher than that of A.

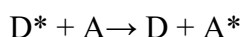
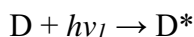
It is important to mention that electronically excited state is a kind of a bound electron-hole pair. Returning of this pair to the ground state is termed recombination and this is crucial for properly functioning organic electronics. In an organic system, PIET (Photoinduced electron transfer) can occur if D and A are sufficiently close that molecular orbitals of D and A become overlapped, namely short-range interactions. Long-range electron transfer may also take place if there is a bridging link-molecule between D and A.

2.3.2.1. Excitation Energy Transfer

Under certain circumstances, an excited D can transfer energy to A, typically emitting shorter wavelengths which overlap with the absorption of A.



In this way quenching the fluorescence of excited D will be observed. Fluorescence/phosphorescence of A can be observed if energy transfer is completed by excitation of D.



In a natural process, excitation energy transfer is a ubiquitous phenomenon. Especially, photosynthetic processes transfer the solar light energy by absorption of light-harvesting complexes and then energy is transferred to the photosynthetic reaction center. By the help of this transfer solar energy can be converted into chemical energy. Also, it is important for OLEDs; high band gap host material is often blended with low bandgap acceptor material. By this way, excitons can be transferred to emitting dopant materials. Two general approaches are described for energy transfer in conjugated organics, Förster and Dexter transfer (43).

2.3.2.1.1. Förster Model

This type of energy transfer is classified as a long range resonant dipole-dipole interaction. This interaction is much like two swings on a common supporting beam (43). Since the exchange is between similar dipole resonance frequencies, Förster energy transfer is often named as -fluorescence- resonance energy transfer (FRET). It is noteworthy to emphasize that reabsorption of fluorescence of D by A is a different process than this energy transfer.

FRET requires spectral overlap. That is the absorption spectrum of A and emission spectrum of D coincide. The extent of FRET depends on the distance between D and A, the extent of overlap. Generally, up to 10 nm FRET can be observed, because it does not require close contact of A and D.

This distance-dependence of FRET enables scientists to estimate/measure the distance between covalently labeled D and A sites of biological macromolecules(43). However, this approximation is misleading (44) when D and A are in close or linked by bridging.

2.3.2.1.2. Dexter Model

In contrast to FRET, Dexter energy transfer happens as short as 0.5-1.0 nm, which is the range of van der Waals distance. In Dexter (43) type energy transfer, similar to bimolecular reactions, overlapping of molecular orbitals is required. This is so crucial

that electron exchange is restricted only in the overlap region. As the overlap decays exponentially over distance, Dexter energy transfer decreases rapidly.

Since Dexter is involved in simultaneous two-electron exchange, triplet energy transfer can happen without intersystem crossing. This is one important mechanistic difference between Dexter and FRET, that is FRET require spin-flip for triplet transfer. FRET is usually used to define the mechanism of singlet energy transfer and Dexter is used to define the mechanism of triplet energy transfer (44).

In the solution phase, D and A must be close enough to generate electron exchange. For this particular case, Dexter is diffusion controlled; however, FRET can exceed the diffusion limit. On the other hand, in thin film solid state of D doped with a small amount of A, both Dexter and FRET come in action, principally. That is a superposition of both mechanisms depending on both the time and distance after excitation.

2.4. Polymer Light Emitting Diodes: Devices and Materials

Polymer light emitting diodes (PLEDs) are devices that they are simply generating light from electric current. As compared to older brother inorganic light emitting diodes, PLEDs not only have various advantages but also distinct drawbacks. Both of these characteristics of PLEDs will be mentioned throughout this section.

2.4.1. Device Configuration of PLEDs

PLEDs are the devices that organic light emitting material is sandwiched between two electrodes (Figure 2.8). Practically, at least one electrode should be transparent to let the light coming out of the device. Under applied voltage, electrons and holes are injected through respectively cathode and anode. The cathode is made of low work function materials, and the anode is a bilayer anode: poly(3,4-ethylenedioxythiophene)-poly(styrenesulfonate) (PEDOT:PSS) on indium tin oxide (ITO). Both electrons and holes from respective electrodes move to the opposite direction towards the recombination zone where organic active material is there, and

they combine to form excitons which eventually emit light. Depending on the choice of materials which should have high conductivity, highly efficient electroluminescence, good thermal and chemical stability as well as low turn-on voltage or low power consumption; different requirements should be employed by various layers of PLEDs.

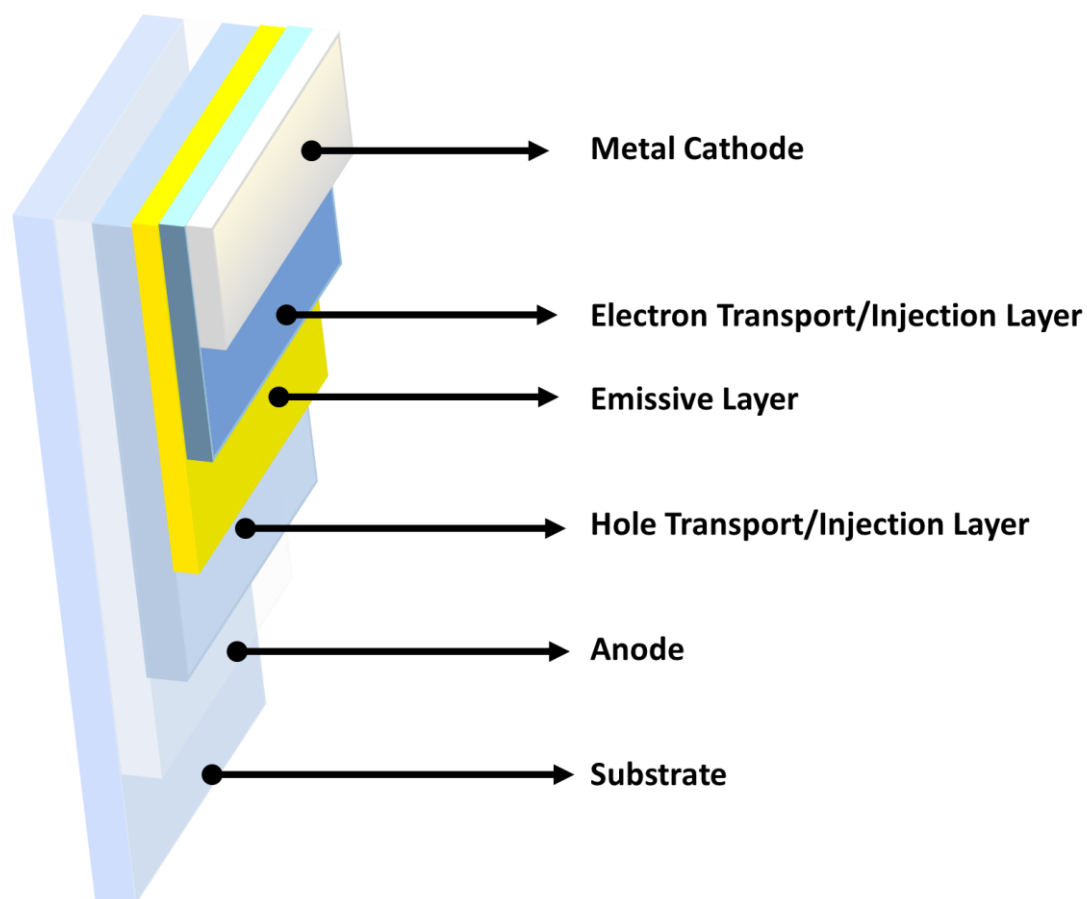


Figure 2.8. Device architecture of OLED

2.4.1.1. Substrate

An indispensable part of PLEDs is responsible for the passage of photon emitted by active material in the device. Therefore, it requires to be highly transparent. It also has properties of low roughness, scratch proof, rigidity and smooth surface (45). Generally, glass is used for its high glass transition temperature. Instead, the

transparent metal foil can also be used. To gain a flexible property to PLEDs, clear sheet of plastics-PET- can be used.

2.4.1.2. Anode

The anode material must be transparent and highly conductive for high performance PLEDs. The conductivity, transparency and work function of the anode are altered with different manufacturing techniques of deposition and surface treatment (45–47). Conventionally, ITO is used because it has high conductivity, high work function as $\Phi_W = 4.5$ to 5.1 eV to inject holes easily, satisfactory transparency in the visible region (90%) and excellent adhesion to the substrate. High chemical stability of ITO, however, is deteriorated by the migration of tin and oxygen into organic material which affects the performance of the PLEDs over time. Moreover, the high refractive index of ITO compared to organic material results in blocking the high percentage of generated photons from the device. There are several other materials are under investigation to find alternatives as fluorine doped tin oxide (FTO), aluminum doped zinc oxide (AZO), and other transparent conductive oxides (TCO) (48–50). FTO is a good replacement because of its low cost production and lowered sensitivity of surface cleaning methods (51). However, high leakage current is observed. AZO shows excellent transparency and various thin film fabrication methodologies such as chemical vapor deposition (CVD), pulsed-laser deposition and magnetron sputtering can be advantageous (52). Several highly transparent TCOs, for example, $\text{Ga}_{0.12}\text{In}_{1.88}\text{O}_3$, $\text{Ga}_{0.08}\text{In}_{1.28}\text{Sn}_{0.64}\text{O}_3$, $\text{Zn}_{0.5}\text{In}_{1.5}\text{O}_3$, and $\text{Zn}_{0.46}\text{In}_{0.88}\text{Sn}_{0.66}\text{O}_3$, were studied by Cui et al(53). It was found that organic light emitting diodes with these materials showed superior performance than that of ITO based ones. However, high turn-on voltage was an undesirable outcome.

2.4.1.3. Hole Transport/Injection layer

Hole transport/injection layer contains low ionization potential materials. Low ionization potential combined with low electron affinity and high hole mobility

enables the materials to accept and transport the positively charged carriers (54, 55). It helps to lower the charge injection barrier.

2.4.1.4. Emissive Layer

For practical purposes, materials with various colored emitter in the visible region are between HTL and ETL, hole transport layer and electron transport layer, respectively. Selection of color mainly depends on the energy difference between HOMO and LUMO as recombination occurs radiatively. Besides adjusting the desired color, solubility, solution viscosity, compatibilities of solvent and substrate also depend on the chemical structure of the polymer. Altering the conjugated backbone of the polymer, side groups, conjugation length/molecular weight, molecular orientation such as structural rigidity or regularity are some of the factors to fine-tune the properties of materials to be used in PLEDs. Long and proper working performance is obtained when high glass-transition-temperature organic materials are used. High processability of polymeric materials used in PLEDs does not require vacuum process to cast. Instead, ink-jet printing, doctor blade casting, spin coating techniques can be used to manufacture low cost PLEDs.

2.4.1.5. Electron Transport/Injection Layer

In general, mobility of hole is greater than the that of electrons in PLEDs. To balance the charges, which are to be recombined to emit light, injection of holes is needed to be blocked through the electron transport layer. High electron affinities combined with high ionization potentials usually beneficial for accepting and transporting electrons. It also plays an important role to prevent the leakage of charge and its accumulation at the interface between cathode and electron transport.

2.4.1.6. Cathode

To minimize the energy barrier to inject electron efficiently, low work function $\Phi_w \approx 2.9$ to 4.0 eV materials must be used. As the low work function cathode materials,

for example, Ca, K, Li, there occurs extra conditions needed to be considered; corrosion and high chemical reactivity with organics.

Some alloys of magnesium and aluminum or aluminum with variety of insulating layers as MgO, NaCl, Al₂O₃, are widely used (56–58). LiF and CsF show extraordinary performance due to their thermodynamic stabilities. Bilayered cathode exhibits better performance to inject electron hence higher electroluminescence in PLEDs. Thus, LiF/Al and CsF/Al have been widely used in PLEDs.

2.4.2. Elementary Processes of PLEDs

In general, 5 consecutive steps (Figure 2.9) are described for working principles of PLEDs:

- ④ Charge injection
- ④ Charge transport
- ④ Recombination into a neutral excited state
- ④ Emission of light
- ④ Transport of light out of the device

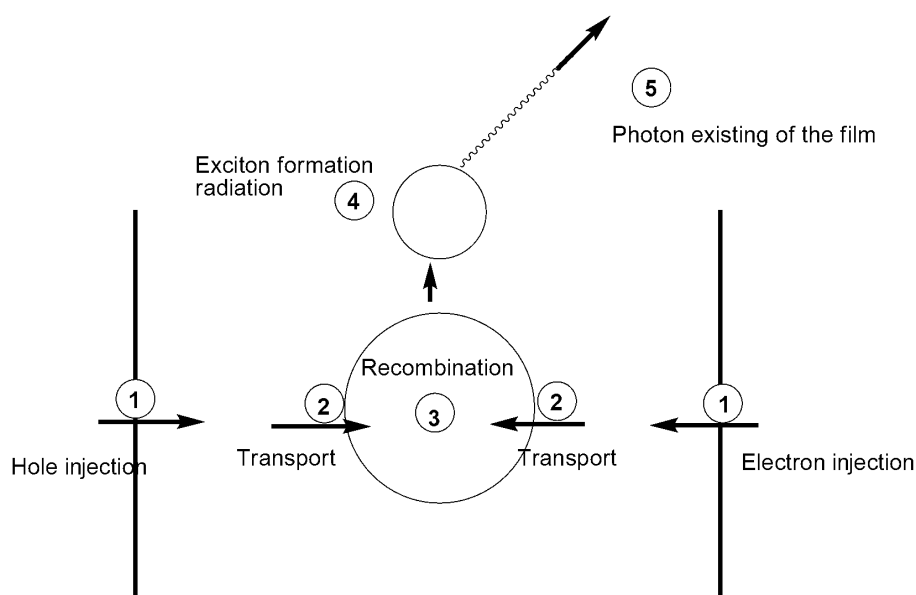


Figure 2.9. Working principle of PLEDs

2.4.2.1. Charge Injection

To operate the PLEDs charges must be injected because the equilibrium concentration of carriers in organic-active- the material is sufficiently low. There are two mechanisms for injection of charge:

- ☞ Proceeding over the interface barrier by thermionic emission:

Injection barrier for the electron: $\Delta E_e = \Phi_{Wc} - A$ (Φ_{Wc} : work function of the cathode, A: electron affinity of organic material)

Injection barrier for the hole: $\Delta E_h = I - \Phi_{Wa}$ or tunneling. (Φ_{Wa} : work function of the anode, I: ionization potential of organic material)

- ☞ Through tunneling

Working principle of PLEDs is quite different from inorganic conventional light emitting diodes. Because charge carrier concentration is sufficiently as low as $\sim 10^{14}$ - 10^{15} cm^{-3} , built-in field caused by the difference between the high work function of anode and low work function of cathode sweeps out any residual carriers introduced by impurities (58). Thus, rigid band model shown in Figure 2.10 can be approximated where there is negligible band bending for PLEDs.

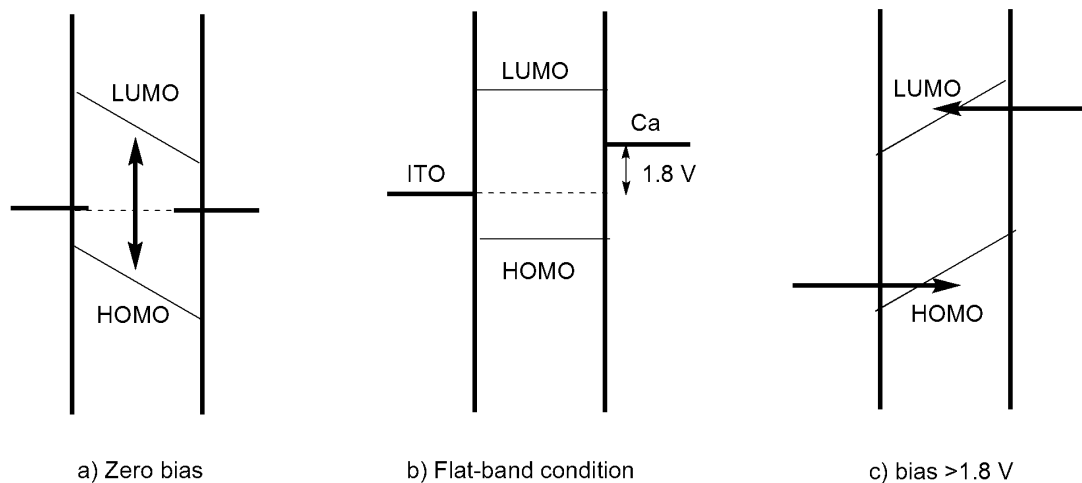


Figure 2.10. Operational information of PLEDs

Zero bias results in that common Fermi level move across the device (58).

When the voltage comes to the edge of minimum requirement to inject charges, flat-band condition occurs. This is the difference in the work function of anode and cathode. In the ideal case, at this voltage electroluminescence turns on (58).

When a forward bias is applied, through the triangular barriers which can be seen in the Figure 2.10 charge carriers are injected. Holes and electrons can combine to form excitons for electroluminescence. As the potential is increased; thus, the Fermi level of cathode is raised relative to anode, barrier thickness is decreased. The primary process is the tunneling of charges through the barrier by Fowler-Nordheim field emission. That is, tunneling electrons from the cathode to LUMO of active material, holes from anode to HOMO of active material. In the special case where the temperature is high and the barriers are small, then thermionic emission over the barriers can also occur. Strength of the electric field is important for Fowler-Nordheim tunneling so that the thickness of polymer is to be thin for the high electric field at low voltages (58).

If energy bands of active material are well matched with electrodes, the barrier is then small. In that condition current that passes through the device is not limited by injection. Space-charge limited hole current arises due to the screenings of the population of holes created near the anode. Also, electron transport is limited by the defects-traps, due to disorderliness of polymer.

2.4.2.2. Carrier Transport

After charges are injected, electrons are injected through cathode and holes are injected through the anode, they must be transported to a zone where they recombine. The general belief is that transport is maintained via a hopping mechanism between localized states, namely polarons and bipolarons.

One intrinsic property of conjugated polymers is that they have typically low hole mobility, i.e. 10^{-7} - 10^{-3} cm²/ (V.s) (58) and 1 to 2 order magnitude lower for electron mobility. The fact behind this is the disorder in the amorphous or polycrystalline phase of organic active material. Due to the usual charge injection from the metallic

electrode is not as efficient as the injection from ITO, asymmetrically imbalanced carrier concentration reduces the efficiency of PLEDs.

There are two general models in PLEDs for an explanation of carrier hopping:

- ❖ Polaron model; strong interactions of localized charge carriers between host neighboring guest molecules via molecular vibrations leads to a significant relaxation of the host around the carrier. Simply carrying this relaxation to adjacent molecule/polymer, a charge carrier can move along with it. Certainly, the energy of the electron carrier is lowered below the LUMO level and energy of the hole carrier raised above the HOMO level due to this relaxation or stabilization.
- ❖ Disorder model; charge carrier coupling with molecular modes is assumed to be weak and therefore the activation energy reflects the static disorder of the hopping sites. In contrast to deformation energy, energetic disorder energy of polaron model is small. The change in molecular conformation occurs while charge injection leads to disorder around this position. Energy difference of this disorderliness is fundamental to distinguish disorder or polaron model. It is widely accepted that charge carrier exists as polarons rather than free electrons and holes, although there is generally better agreement between disorder model and charge transport measurements.

2.4.2.3. Carrier Recombination

For conjugated polymers, the typical dielectric constant is small. Attractive forces between electron and hole are larger than energy at room ~operating- temperature ($>kT$) and Coulomb screening is not efficient. These facts lead the scientists to believe that the recombination process in PLEDs is Langevin recombination; since trap-assisted nonradiative recombination controls the current. Langevin type is independent of the applied field according to well-studied molecular crystals.

2.4.2.4. Photon Emission

Generally, π -conjugated polymers are made up of light elements like C, H, O, S and so on so forth. Spin-orbit coupling, thus, is inefficient. Well-classified neutral excited states are singlet and triplet excited states. Higher spin states usually come to the stage at sufficiently high energies as the splitting energy difference between singlet and triplet is typically 1 eV. The ratio of injected charges to emitted photons is termed quantum yield of electroluminescence and it is proportional to $(\eta_s + 3\eta_t)/4$; where η_s is quantum yield of fluorescence coming from singlet emission and η_t is quantum yield of phosphorescence coming from triplet emission. Thus, scientists recently have been investigating various strategies such as usage of phosphorescent iridium doped organometallic compounds or thermally activated delayed phosphorescent (TADF) materials to enhance the quantum yield of the devices. The former one is simply enhancing the spin-orbit coupling because it contains heavy iridium atom and the later one is some more complex strategy to reduce the singlet-triplet splitting energy.

2.4.2.5. Photon Extraction

Non-textured and disordered morphology of light emitting active layer results in isotropic emission inside the thin film. That is almost Lambertian emission pattern occurs outside the device (59). This behavior is indeed beneficial for display application because luminance is independent of the angle view.

2.5. Characterizations of PLEDs

Basic performances of PLEDs are tested by current density vs applied voltage characteristics (J - V), current density vs applied voltage vs luminance characteristics (J - V - L), and spectral distribution of electro luminance (EL) and Commission International de l'Eclairage (CIE) coordinates.

2.5.1. Current Density vs Applied Voltage Characteristics (J - V)

The J - V characteristics of PLEDs create a curve that is obtained due to applying a potential difference between two electrodes; hence, current passes through the device.

In practice, before the barrier voltage is reached there should be no current generated. After that voltage, further an increase in voltage results in a rise of current similar to an ordinary conductor. Cut-in voltage is termed to a point at which the current starts to flow through the device. In general, the luminance value of 1 cd/m^2 is standardized to find the power-on voltage of the device. Power-on voltage should be ideally as low as possible. Although inorganic semiconductors as Schottky-barrier or $p-n$ junction device have typically equal or lower operational voltage than their band gaps, PLEDs start to illuminate at much higher voltages than their bandgaps. Because $J-V$ characteristics depend on the electric field, the operating voltage is reduced as the thickness decreased. However, thickness has a little minor effect on turn-on voltage, the required voltage to reach the flat band condition (60).

A log-log conversion of $J-V$ curve also can be interpreted to find valuable information. three main regions induce different characteristics of the individual device. In the first region, where no light emission is observed, the current obeys the Ohmic law. This Ohmic current is intrinsically observed by thermally activated residual free charges. In this zone, the concentration of these charges is higher than that of the injected ones. In the second zone, space charge density approaches a level that the device starts to generate light. Primarily, a substantial amount of these charges fill the trap centers at which recombination occurs non-radiatively. In the third zone, all traps are filled. Thus, the current changes its behavior from trapped space charge limited to trap free space charge limited.

2.5.2. Electroluminescence (EL) Spectra

Electroluminescence spectra are taken to reveal spectral information of emitted light out of the device. Characteristic wavelengths of the conjugated polymer are revealed with accordance to applied operational voltage.

2.5.3. Current Density vs Applied Voltage vs Luminescence Characteristics (J-V-L)

The J-V-L curve is an output of combined characteristics of all current density, bias voltage and electroluminescence (Figure 2.11). It is seen that, as the driven voltage is increased, both electroluminescence and current density increases.

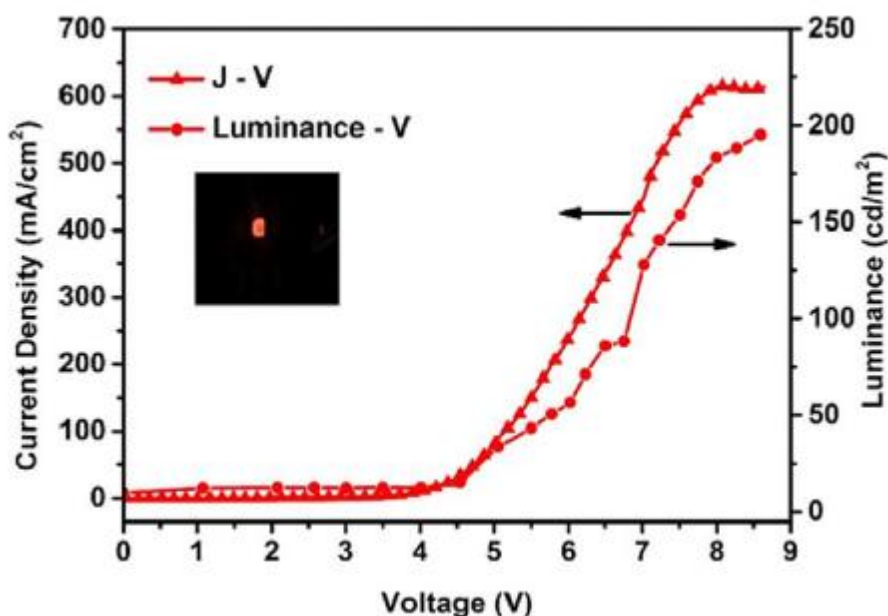


Figure 2.11. Current density vs applied voltage vs luminescence characteristics (J-V-L) diagram of red PLED device, luminescent working device is inside (61). This article was published in Synthetic Metals, 244, Şevki Can Cevher, Duygu Keles, Gonul Hizalan, Levent Toppare, Ali Cirpan, Alkyl-end phenanthroimidazole modification of benzotriazole based conjugated polymers for optoelectronic applications, 1-9, Copyright Elsevier, 2018.

2.5.4. Commission International de l'Eclairage (CIE) Coordinates

CIE describes how human see the color in terms of a numbered code, which can be seen in Figure 2.12 Any color by using the coding system of CIE can be described in terms of three primary colors (62, 63). The shift in the whole range of brightness and the entire operation process is if between 0.005 and 0.01 then the device is said to be properly efficient. However, recently involved new concept of tunable white OLEDs is one of the exceptional methodologies where the color changes following voltage (64).

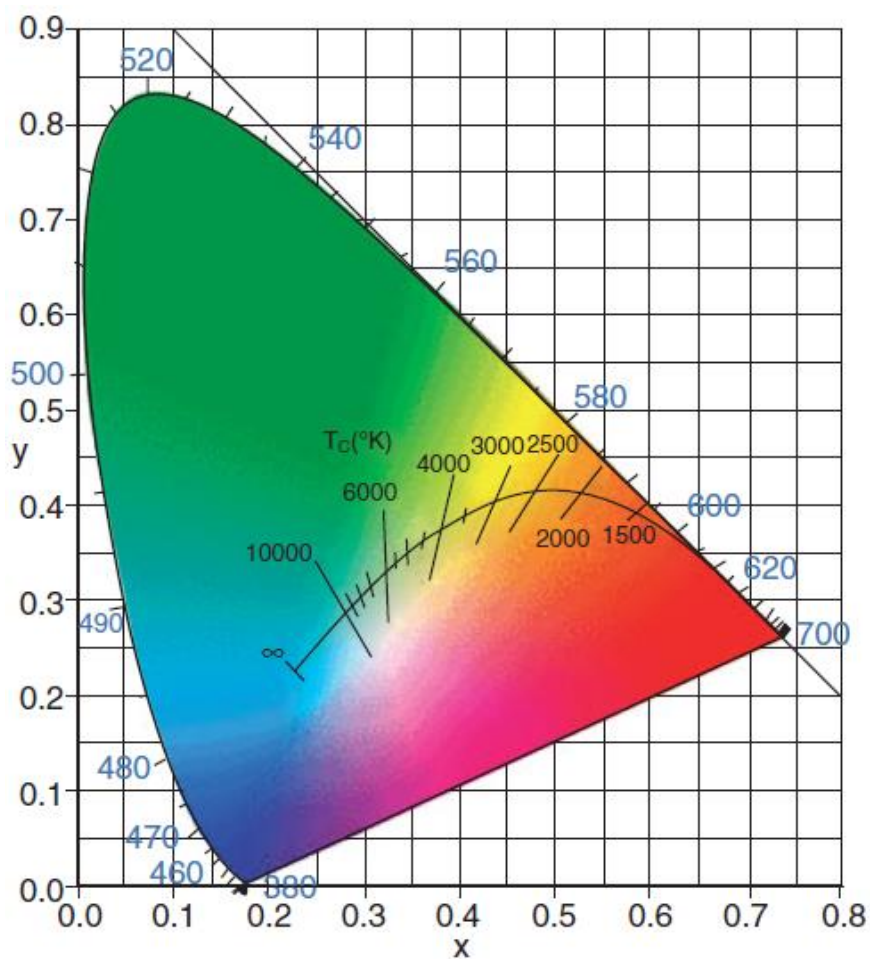


Figure 2.12. The CIE chromaticity diagram. The curve inside the diagram represents the colors of blackbody radiation corresponding to the correlated color temperature.

2.6. Aim of This Project

2-Component (65–67) or 3-component (68, 69) combinations of high performance red, green, yellow and blue colored emitters have been used to produce white OLEDs. In this regard, phenanthroimidazole based molecules, typically emit deep blue or sky blue, were generally preferred for their excellent thermal stability, and compatible optical and electronic properties (70–73). Combining electron withdrawing and donating units, phenanthroimidazole based molecules did not change the blue colored emission significantly to any other primary color (74). Strong fluorescence ability of

phenanthroimidazole based molecules makes them a good candidate for OLEDs. Generally, high fluorescence quantum yields result in high EQE for OLEDs.

On the other hand, when a multi component OLED device is aimed, one should consider the energy/charge transfer. Inter/intramolecular transfers may ruin or enhance the properties under investigation. For example, primary colors (red, green, blue) or two complementary colors (blue and yellow) can be used to produce white color OLEDs. However, prevalent and unavoidable energy transfer overwhelmingly dominates the emission of the lower band gap component (75). There are yet countable examples in which energy transfer could not be observed in solution (76) or both in solution and in thin film form (77).

In this study, benzotriazole based conjugated polymers were synthesized where their alkyl-ends were modified with blue emitting phenanthroimidazole. In this way, two different components were attached via an alkyl spacer. Synthesized polymers were anticipated as being capable of dual emission. Effect of imidazole ring attached via alkyl-spacer to the conjugated polymer backbone was investigated in terms of the optical, electronic and as well as optoelectronic properties.

2.7. Experimental

All chemicals were purchased from Sigma Aldrich and used without further purification unless otherwise mentioned. Tetrahydrofuran was distilled over benzophenone/sodium just before usage. Palladium catalyzed reactions were performed under argon atmosphere. SiO₂ column filler was used as a stationary phase in column chromatography. Synthetic pathway of the polymers were given in Figure 2.13. Tributyl(thiophen-2-yl)stannane (78) and 4,7-dibromo-2H-benzo[*d*][1,2,3]triazole (79) (III) were synthesized according to the previous methodologies. BTz and TBTzT were synthesized according to previously published recipes via changing alkyl chain to 1,10-dibromodecane (BTz 4,7-dibromo-2-(10-bromodecyl)-2H-benzo[*d*][1,2,3]triazole) (80), TBTzT (2-(10-bromodecyl)-4,7-di(thiophen-2-yl)-2H-benzo[*d*][1,2,3]triazole) (81). ¹H and ¹³C NMR spectra were

recorded on a Bruker Spectrospin Avance DPX-400 Spectrometer with TMS as the internal reference proved structures of organic molecules. Thermo Scientific Nicolet FTIR- IS10 was used for recording IR data. Shimadzu RID-20A, calibrated against polystyrene standards, was used to investigate the molecular weights of the polymers. Pyris 1 TGA Thermogravimetry Analyzer and Perkin Elmer Diamond DSC Differential Scanning Calorimeter were used to investigate thermal properties of the polymers. High-resolution mass analyses (HRMS) of the monomers were recorded on Waters SYNAPT MS System to confirm the monomer synthesis.

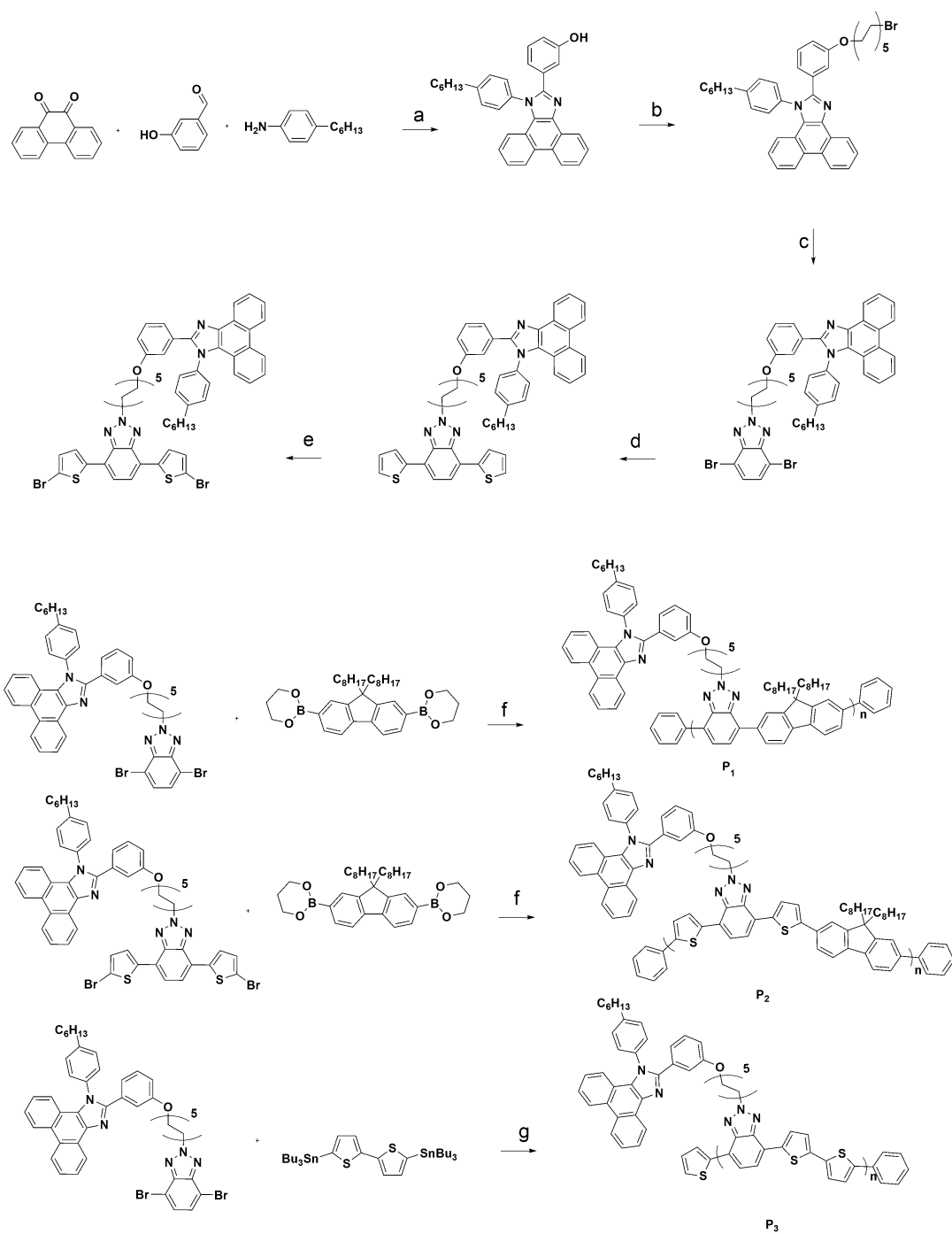


Figure 2.13. Synthetic pathway of P1, P2 and P3. a) NH_4OAc , acetic acid, b) 1,10-dibromodecane, K_2CO_3 , acetone, c) 4,7-dibromobenzotriazole, K_2CO_3 , THF, d) 2-tributyltinthiophene, $\text{Pd}(\text{PPh}_3)_2\text{Cl}_2$, THF, e) NBS, CHCl_3 , f) $2\text{M K}_2\text{CO}_3$, $\text{N}(\text{C}_6\text{H}_{13})_4\text{Br}$, $\text{Pd}(\text{PPh}_3)_2\text{Cl}_2$, bromobenzene, benzeneboronic acid, THF g) $\text{Pd}(\text{PPh}_3)_2\text{Cl}_2$, bromobenzene, 2-tributyltinthiophene, THF.

2.7.1. Synthesis

2.7.1.1. 3-(1-(4-Hexylphenyl)-1H-phenanthro[9,10-*d*]imidazol-2-yl)phenol (I)

Phenanthrene-9,10-dione (0.99 g, 23.8 mmol), 3-hydroxybenzaldehyde (0.58 g, 4.76 mmol), ammonium acetate (1.83 g), 4-hexylaniline (1.69 g, 9.52 mmol) were mixed in 30 mL acetic acid and the solution was refluxed overnight. After cooling, the solution was poured in ice water mixture (300 mL) and the precipitate was collected by filtration. Precipitate was dissolved in acetone (50 mL) and addition of water (10-25 mL) to acetone solution yielded the solid product and used without further purification (1.85 g, 83%). ¹H NMR (400 MHz, CDCl₃) δ (ppm): 8.73 (d, *J* = 7.9 Hz, 1H), 8.66 (d, *J* = 8.4 Hz, 1H), 8.61 (d, *J* = 8.3 Hz, 1H), 7.65 – 7.57 (m, 2H), 7.55 (t, *J* = 7.6 Hz, 1H), 7.42 (t, *J* = 7.7 Hz, 1H), 7.31 – 7.20 (m, 4H), 7.15 (d, *J* = 7.1 Hz, 1H), 7.08 (d, *J* = 8.3 Hz, 1H), 6.91 (t, *J* = 7.9 Hz, 1H), 6.71 (dd, *J* = 8.1, 2.1 Hz, 1H), 6.63 (d, *J* = 7.6 Hz, 1H), 2.67 (t, *J* = 7.6 Hz, 2H), 1.69 – 1.57 (m, 2H), 1.35 – 2.28 (m, 6H), 0.85 (t, *J* = 6.8 Hz, 3H). ¹³C NMR (101 MHz, CDCl₃) δ (ppm): 151.67, 144.89, 136.41, 135.57, 129.99, 129.30, 129.08, 128.66, 128.38, 127.94, 127.53, 126.73, 126.29, 125.67, 125.04, 124.02, 123.17, 122.88, 122.69, 120.98, 120.69, 117.79, 117.15, 35.64, 31.68, 31.06, 28.77, 22.65, 14.11.

2.7.1.2. 2-(3-((10-Bromodecyl)oxy)phenyl)-1-(4-hexylphenyl)-1H-phenanthro[9,10-*d*]imidazole (II)

3-(1-(4-Hexylphenyl)-1H-phenanthro[9,10-*d*]imidazol-2-yl)phenol (1.20 g) were dissolved in 30 mL of acetone. 1,10-Dibromodecane (2.40 g) and potassium carbonate (0.66 g) were introduced into solution, respectively. Reaction was set to refluxed overnight. After cooling, solvent was removed under reduced pressure and then the extraction with chloroform (150 mL)/water (100 mL) was performed. Organic phase was collected and dried over magnesium sulfate and the solvent was removed under reduced pressure. After purification of the crude product via column chromatography with chloroform, product II was obtained (1.54 g, 88%). ¹H NMR (400 MHz, CDCl₃) δ (ppm): 8.81 (d, *J* = 7.9 Hz, 1H), 8.65 (d, *J* = 8.4 Hz, 1H), 8.59 (d, *J* = 8.3 Hz, 1H),

7.64 (t, $J = 7.5$ Hz, 1H), 7.57 – 7.50 (m, 1H), 7.42 – 7.35 (m, 1H), 7.33 – 7.25 (m, 4H), 7.16 – 7.03 (m, 5H), 6.78 – 6.73 (m, 1H), 3.71 (t, $J = 6.5$ Hz, 2H), 3.30 (t, $J = 6.8$ Hz, 2H), 2.72 – 2.61 (m, 2H), 1.82 – 1.69 (m, 2H), 1.69 – 1.57 (m, 4H), 1.38 – 1.18 (m, 18H), 0.84 (t, $J = 8.8$ Hz, 3H). ^{13}C NMR (101 MHz, CDCl_3) δ (ppm): 158.82, 150.78, 144.83, 136.28, 130.07, 129.27, 129.15, 128.80, 128.27, 128.20, 127.27, 126.22, 125.59, 124.86, 124.08, 123.12, 122.82, 121.73, 120.94, 116.15, 114.71, 67.92, 35.72, 34.06, 32.85, 31.73, 31.29, 29.51, 29.42, 29.39, 29.25, 28.89, 28.80, 28.20, 26.08, 22.69, 14.16.

2.7.1.3. 2-(3-((10-(4,7-Dibromo-2H-benzo[*d*][1,2,3]triazol-2-yl)decyl)oxy)phenyl)-1-(4-hexylphenyl)-1H-phenanthro[9,10-*d*]imidazole (IV)

Compound II (1.54 g, 2.23 mmol) and compound III (0.62g, 2.23 mmol) were dissolved in tetrahydrofuran (60 mL) and potassium carbonate (0.35 g, 2.50 mmol) was added and the mixture was refluxed overnight. Cooling of the solution was followed by removal of the solvent under reduced pressure. Extraction with chloroform (150 mL)/water (100 mL) was performed and collected organic phase was dried over magnesium sulfate. After removing the solvent under reduced pressure column chromatography chloroform-hexane (v/v: 1/2) was performed to obtain product IV (660 mg, 33%). ^1H NMR (400 MHz, CDCl_3) δ (ppm): 8.78 (dd, $J = 8.0$, 1.1 Hz, 1H), 8.65 (d, $J = 8.4$ Hz, 1H), 8.59 (d, $J = 8.3$ Hz, 1H), 7.63 (dd, $J = 11.0$, 4.0 Hz, 1H), 7.57 – 7.50 (m, 1H), 7.40 (ddd, $J = 9.9$, 5.8, 2.5 Hz, 1H), 7.35 – 7.22 (m, 6H), 7.15 – 7.03 (m, 5H), 6.77 (ddd, $J = 9.4$, 5.8, 1.9 Hz, 1H), 4.81 (t, $J = 7.4$, 2H), 3.72 (t, $J = 6.5$ Hz, 2H), 2.68 (t, $J = 6.8$, 2H), 1.94 – 1.83 (m, 2H), 1.62 (d, $J = 13.9$, 2H; d, $J = 6.2$ Hz, 2H), 1.35 – 1.16 (m, 18H), 0.84 (t, $J = 6.9$, 3H). ^{13}C NMR (101 MHz, CDCl_3) δ (ppm): 158.81, 150.82, 145.94, 144.79, 137.26, 136.33, 131.98, 131.81, 131.71, 130.04, 129.23, 129.12, 128.81, 128.23, 128.21, 127.78, 127.28, 127.22, 126.19, 125.52, 124.80, 124.05, 123.14, 123.09, 122.75, 121.69, 120.92, 116.07, 114.76, 112.98, 101.72, 67.91, 49.82, 35.70, 31.70, 31.49, 31.26, 29.42, 29.35, 29.32, 29.21, 29.02, 28.86, 26.34, 26.03, 22.66, 14.13. IR $\nu_{\text{max}}/\text{cm}^{-1}$: 591, 676, 695, 718, 724, 753, 803, 858, 954, 1018, 1194, 1238, 1260, 1307, 1347, 1380, 1451, 1465,

1485, 1514, 1600, 2852, 2921, 2962. Melting point of compound IV : 67.4 °C. HRMS (ESI): Calc:885.2512, found: 885.2521

2.7.1.4. 2-(3-((10-(4,7-Di(thiophen-2-yl)-2H-benzo[d][1,2,3]triazol-2-yl)decyl)oxy)phenyl)-1-(4-hexylphenyl)-1H-phenanthro[9,10-d]imidazole (V)

Compound IV (250 mg, 0.28 mmol) and tributyltin thiophene (420 mg, 112 mmol) were dissolved in tetrahydrofuran (20 mL) and the solution was bubbled with argon gas for 20 min. After introducing the bistriphenylpalladium dichloride (10% mole) temperature was set to reflux. Reaction was carried out overnight. After cooling of the solution, the solvent was removed under reduced pressure and extraction with chloroform (100 mL)/water (50 mL) was performed. Organic phase dried over magnesium sulfate and the solvent was removed under reduced pressure. Column chromatography was performed hexane-chloroform (v/v 1/1) in order to obtain V (186 mg, 73%). ¹H NMR (400 MHz, CDCl₃) δ (ppm): 8.80 (dd, *J* = 7.9, 1.0 Hz 1H), 8.66 (d, *J* = 8.3 Hz, 1H), 8.60 (d, *J* = 8.3 Hz, 1H), 7.99 (dd, *J* = 3.6, 1.1 Hz, 2H), 7.64 (t, *J* = 7.5 Hz, 1H), 7.57 – 7.51 (m, 1H), 7.51 (s, 2H), 7.40 (ddd, *J* = 8.3, 6.8, 1.4 Hz 1H), 7.32 – 7.22 (m, 6H), 7.15 – 7.01 (m, 7H), 6.75 (dt, *J* = 7.0, 2.5 Hz, 1H), 4.71 (t, *J* = 7.2 Hz, 2H), 3.69 (t, *J* = 6.5 Hz, 2H), 2.70 – 2.62 (m, 2H), 2.15 – 2.05 (m, 2H), 1.64 – 1.54 (m, 5H), 1.38 – 1.13 (m, 18H), 0.86 – 0.81 (m, 3H). ¹³C NMR (101 MHz, CDCl₃) δ (ppm): 158.82, 150.83, 144.78, 142.10, 139.97, 137.29, 136.34, 131.71, 130.03, 129.26, 129.12, 128.81, 128.25, 128.23, 128.10, 127.31, 127.24, 126.97, 126.18, 125.55, 124.80, 124.07, 123.59, 123.17, 123.11, 122.76, 121.70, 120.94, 116.09, 114.73, 67.91, 56.84, 35.70, 31.70, 31.25, 30.05, 29.48, 29.38, 29.36, 29.23, 29.03, 28.87, 26.59, 26.04, 22.66, 14.13.

2.7.1.5. 2-(3-((10-(4,7-Bis(5-bromothiophen-2-yl)-2H-benzo[d][1,2,3]triazol-2-yl)decyl)oxy)phenyl)-1-(4-hexylphenyl)-1H-phenanthro[9,10-d]imidazole (VI)

Compound V (186mg) was dissolved in 50 mL chloroform and the reaction flask covered with aluminum foil. N-bromosuccinimide was added pinch by pinch. After completion of the reaction (almost 7 h), extraction with chloroform/water (100

mL/100mL) was performed. Organic phase collected and condensed by a rotary evaporator. Crude product was purified by column chromatography chloroform: ethyl acetate: hexane (v/v/v 3/1/20). (142 mg, 65%) ^1H NMR (400 MHz, CDCl_3) δ (ppm): 8.79 (dd, $J = 7.9, 0.8$ Hz, 1H), 8.67 (d, $J = 8.4$ Hz, 1H), 8.61 (d, $J = 8.3$ Hz, 1H), 7.69 – 7.62 (m, 3H), 7.60 – 7.51 (m, 1H), 7.46 – 7.38 (m, 1H), 7.37 (s, 2H), 7.34 – 7.24 (m, 4H), 7.16 – 6.99 (m, 7H), 6.77 (ddd, $J = 7.2, 5.7, 2.0$ Hz, 1H), 4.70 (t, $J = 7.1$ Hz, 2H), 3.71 (t, $J = 6.5$ Hz, 2H), 2.72 – 2.55 (m, 2H), 2.13 – 2.03 (m, 2H), 1.67 – 1.52 (m, 4H), 1.41 – 1.10 (m, 18H), 0.84 (t, $J = 7.0$ Hz, 3H). ^{13}C NMR (101 MHz, CDCl_3) δ (ppm): 158.81, 150.82, 144.77, 141.71, 141.23, 137.29, 136.34, 131.71, 130.87, 130.01, 129.26, 129.10, 128.80, 128.24, 128.22, 127.30, 127.22, 126.91, 126.17, 125.51, 124.78, 124.06, 123.17, 123.09, 122.98, 122.77, 122.20, 121.69, 120.93, 116.06, 114.76, 114.72, 113.18, 67.91, 56.90, 35.70, 31.69, 31.25, 30.00, 29.45, 29.36, 29.33, 29.21, 28.97, 28.86, 26.55, 26.03, 22.65, 14.11. IR $\nu_{\text{max}}/\text{cm}^{-1}$: 614, 675, 629, 724, 753, 792, 825, 871, 970, 1046, 1080, 1113, 1138, 1159, 1208, 1234, 1282, 1326, 1380, 1430, 1453, 1482, 1501, 1514, 1542, 1574, 16001, 2026, 2161, 2851, 2922, 3034. Melting point of compound V: 72.3 °C. HRMS (ESI):Calc: 1049.2211, Found: 1049.2218.

2.7.1.6. Synthesis of polymer P1

Compound IV (316 mg, 0.36 mmol), compound VII (200 mg, 0.36 mmol), tetrahexylammonium bromide (50 mg), potassium carbonate solution (2 M 5 mL) were mixed in tetrahydrofuran (10 mL) and the solution was degassed for 20 min with argon. After introducing 50 mg of bistrisphenylpalladium dichloride, temperature was set to reflux for 36 h. For the termination of the polymerization, phenyl boronic acid (0.72 mmol) and bromobenzene (1.44 mmol) were added consequently. After evaporation of the solvent by vacuum, crude polymer was precipitated in methanol (100 mL). Soxhlett extraction was performed with methanol, acetone, hexane, and chloroform, respectively. Chloroform part was condensed by the rotary evaporator and mixed with quadrasil and stirred for 3 hours. After column chromatography, the solvent was removed and remaining viscous liquid was precipitated in methanol

(100ml) to yield P1 (240 mg, 60%). GPC (CHCl₃): Mn= 28.1 kDa, Mw= 85.7 kDa PDI= 3.1 ¹H NMR: (400 MHz, CDCl₃) δ (ppm): 8.80 (d, *J* = 8.0 Hz, 1H), 8.68 (d, *J* = 8.4 Hz, 1H), 8.62 (d, *J* = 8.2 Hz, 1H), 8.11 (s, 2H), 8.02 (s, 2H), 7.84 (d, *J* = 7.7 Hz, 2H), 7.70 (s, 1H), 7.68 – 7.62 (m, 2H), 7.58 – 7.51 (m, 1H), 7.45 – 7.37 (m, 1H), 7.30 (q, *J* = 8.4 Hz, 4H), 7.17 – 7.01 (m, 5H), 6.77 (d, *J* = 7.4 Hz, 1H), 4.78 (s, 2H), 3.73 (t, *J* = 6.4 Hz, 2H), 2.74 – 2.62 (m, 2H), 2.18 (s, 2H), 2.09 – 2.01 (m, 4H), 1.70 – 1.58 (m, 6H), 1.41 – 1.22 (m, 18H), 1.06 (s, 22H), 0.84 (t, *J* = 9.1 Hz, 6H), 0.71 (t, *J* = 6.7 Hz, 9H). TGA: T_d 95% at 430 °C. DSC: No distinct thermal behavior was observed between 20 °C and 250 °C.

2.7.1.7. Synthesis of Polymer P2

135 mg of compound VI, 72 mg VII, tetrahexylammonium bromide (25 mg), 2 M 5 mL potassium carbonate solution were mixed in 10 mL tetrahydrofuran and degassed for 20 min with argon. After introducing 25 mg of bistrisphenylpalladium dichloride, temperature was set to reflux for 40 hours. For the termination of the polymerization, phenyl boronic acid and bromobenzene were added. After evaporating the solvent, crude polymer was precipitated in methanol (100 mL). Soxhlett extraction was performed with methanol, acetone, hexane, chloroform respectively. Chloroform was condensed by rotary evaporator and mixed with quadrasil and stirred for 3 hours. After column chromatography, the solvent was removed and remaining viscous liquid was precipitated in methanol (100 mL) to yield P2 (94 mg 57%). GPC (CHCl₃): Mn= 6.8 kDa, Mw= 12.7 kDa, PDI= 1.9. ¹H NMR: (400 MHz, CDCl₃) δ 8.88 (d, *J* = 8.4 Hz, 1H), 8.76 (d, *J* = 8.4 Hz, 1H), 8.70 (d, *J* = 8.3 Hz, 1H), 8.26 – 7.92 (m, 2H), 7.77 – 7.61 (m, 9H), 7.53 – 7.45 (m, 3H), 7.42 – 7.32 (m, 5H), 7.23 – 7.09 (m, 5H), 6.87 – 6.80 (m, *J* = 5.4 Hz, 1H), 4.89 (s, 2H), 3.79 (t, *J* = 6.3 Hz, 2H), 2.83 – 2.67 (m, 2H), 2.25 (s, 2H), 2.08 (s, 2H), 1.71 (s, 4H), 1.57 (s, 8H), 1.35 (s, 18H), 1.10 (s, 22H), 0.87 (dd, *J* = 21.7, 10.9 Hz, 6H), 0.79 (t, *J* = 5.8 Hz, 9H). TGA: T_{decomposition} 95% at 420 °C. DSC: No distinct thermal behavior was observed between 20 °C and 250 °C.

2.7.1.8. Synthesis of Polymer P3

Compound VIII (200 mg, 0.27 mmol) and compound IV (239 mg, 0.27 mmol) were mixed in tetrahydrofuran (10 mL) and the solution was bubbled with argon for 20 min. After addition of 50 mg of bistrisphenylpalladium dichloride catalyst, the mixture was refluxed for 36 h. Termination of the polymerization was achieved via addition of stanyllated thiophene (0.54 mmol) and bromobenzene (1.08 mmol). After evaporating the solvent by vacuum, crude polymer was precipitated in methanol (100 mL). Soxhlett extraction was performed with methanol, acetone, hexane, and chloroform, respectively. Since silica traps polymer P3, quadrasil treatment was not applied. Chloroform portion was condensed by rotary evaporator and the product was precipitated in methanol (100 mL) to yield P3 (195 mg 81%). Low solubility decreased the quality of characterization of the polymer: GPC (CHCl₃): Mn= 4.8 kDa Mw= 13.5 kDa PDI= 2.8. ¹H NMR: (400 MHz, CDCl₃) δ (ppm): 8.79 (s, 1H), 8.60 (s, 2H), 7.95 (s, 1H), 7.56 (s, 6H), 7.29 (s, 5H), 7.06 (s, 5H), 6.77 – 6.73 (m, 2H), 4.77 (s, 2H), 3.70 (s, 2H), 2.65 (s, 2H), 2.10 (s, 2H), 1.60 (s, 12H), 1.35 – 1.1 (m, 38H), 0.81 (s, 9H). TGA: T_d95% at 350 °C. DSC: No distinct thermal behavior was observed between 20 °C and 250 °C.

2.7.2. Electrochemical and Spectroelectrochemical Properties

Cyclic voltammetry is a key technique for the investigation of redox potentials of conjugated polymers. To achieve this aim, Gamry 600 potentiostat was used with three-electrode system, which consists of a counter electrode (CE), a working electrode (WE) and a reference electrode (RE). They were immersed in a supporting electrolyte and a solvent mixture to provide ionic conductivity. In this study, polymer film coated on ITO, platinum and silver wires were used as WE, CE, RE, respectively. For this purpose, polymers were dissolved in chloroform (5 mg/mL) and solutions were spray coated on ITO coated glasses. For spectroelectrochemistry and kinetic studies, Varian Cary 5000 UV-Vis spectrophotometer was used. By this way changes in absorption spectra were observed during doping process. Spectroelectrochemistry

studies also allow observing the formation of polaron and bipolaron bands. Optical contrasts and switching times were calculated from kinetic studies.

2.7.3. Fabrication of PLEDs

For the characterization of electroluminescence behaviors of the polymers, PLEDs were fabricated with the device structure of ITO/ PEDOT:PSS/ Polymer /LiF /Al. ITO coated glass substrates were cleaned with detergent, deionized water, isopropyl alcohol in ultrasonic bath subsequently. Substrates were dried with N₂ gun. Right after drying process, oxygen plasma cleaning was carried out to improve the wettability of the surface. Approximately 40 nm thick PEDOT:PSS (Heraeus V P Al 4083) layer was spin coated under ambient atmosphere. Substrates were dried at 120°C for 15 minutes to remove residual water. Polymer solutions were prepared with a concentration of 1.5% in chloroform and spin coated inside a glove box. Thicknesses of the active layers were 100 nm, 97 nm and 87 nm for P1, P2 and P3, respectively. Calcium and aluminum electrodes were evaporated at low pressure (10⁻⁶ mbar). Current density vs voltage (*J-V*) analyses were performed using Keithley 2400. Luminance, electroluminescence and chromaticity studies were carried out using fiber optic cable embedded in Maya spectrophotometer. *J-V* and luminance vs voltage characteristics were tested simultaneously.

2.8. Results and Discussions

2.8.1. Optical Properties

The photophysical behavior of polymers are shown in Figure 2.14. 284 nm excitation was performed in order to see blue light emission of polymers as given in Figure 2.14a. Although P3 gave the dominant blue emission in thin film, P1 and P2 gave trace amount of blue emission both in thin film form and in solution (Figure 2.14.b). However, strong blue light emission of P3 indicates that interaction between phenanthroimidazole and polymer backbone was minimized. In literature, there are several examples for such an observation where emission of highly energetic region was suppressed by intra/intermolecular energy transfer. Jin et al. demonstrated that

energy transfer occurred at thin film of dendron-jacketed electrophosphorescent copolymers, although there was no indication of energy transfer in solution form (76). In another study (82) by Ner et al., emission of acceptor moiety at 593 nm was enhanced while the emission of donor moiety at 450 nm was quenched as the acceptor concentration increases. Moreover, changing concentration of donor acceptor ratio, color was changed from blue to orange. The photoluminescence spectra for copolymer P1–P3 solutions and for thin films excited at absorption maxima are shown in Figure 2.14.c. Solution based emission λ_{max} values of P1, P2 and P3 were located at 466, 530 and 587 nm, respectively. The PL spectra of all polymer films showed a red shift (15 nm for P1, 67 nm for P2, and 66 nm for P3) and some broadening of the emission bands in comparison to their solution spectra. These large shifts can be attributed to increased stacking of thiophene π -bridged P2 and P3. This enhanced stacking can be seen further in the red/infrared region of thin film P2 and P3 fluorescence spectra. Moreover, as going from P1 to P3 band gap of polymers decreased and the polymer emissions were shifted to lower energy regime. Fine-tuning of the emission of polymers were achieved.

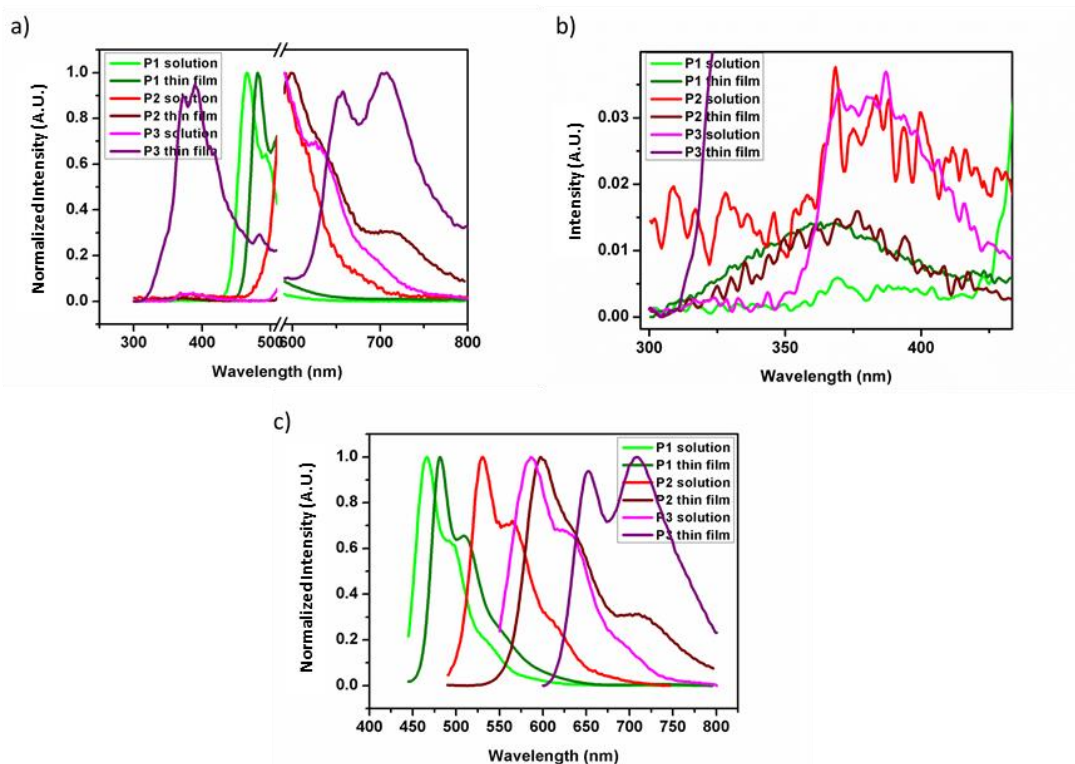


Figure 2.14. a) Photoluminescence spectra for copolymer P1–P3 solutions and for films under excitation wavelength of 284 nm b) photoluminescence spectra (close-up view of the blue region) c) photoluminescence spectra for copolymer P1–P3 solutions and for films (excitation wavelengths were set according to absorption λ_{max} values). (61) This article was published in Synthetic Metals, 244, Şevki Can Cevher, Duygu Keles, Gonul Hizalan, Levent Toppare, Ali Cirpan, Alkyl-end phenanthroimidazole modification of benzotriazole based conjugated polymers for optoelectronic applications, 1-9, Copyright Elsevier, 2018

2.8.1.1. Further Insight to Optical Properties

Structures of molecules, discussed in terms of their optical properties, can be seen in Figure 2.15.

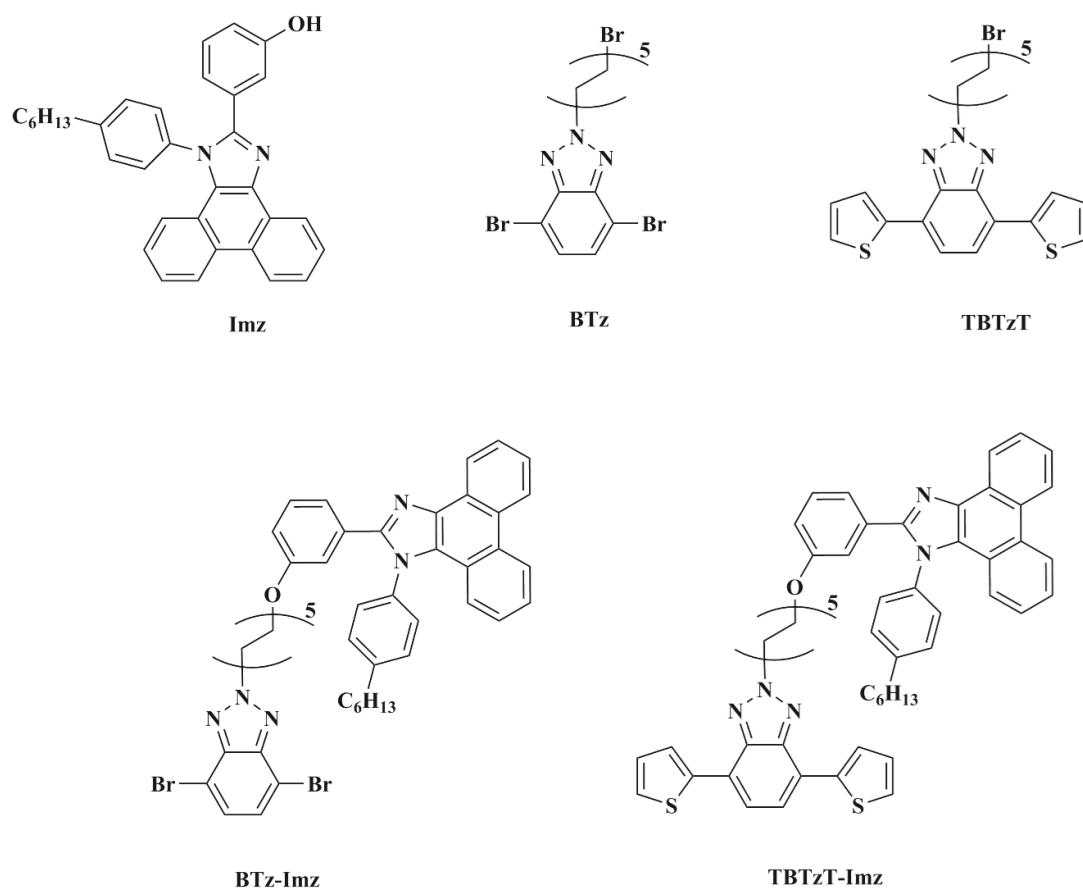


Figure 2.15. Chemical structures of molecules (61). This article was published in *Synthetic Metals*, 244, Şevki Can Cevher, Duygu Keles, Gonul Hizalan, Levent Toppare, Ali Cirpan, Alkyl-end phenanthroimidazole modification of benzotriazole based conjugated polymers for optoelectronic applications, 1-9, Copyright Elsevier, 2018

As expected, BTz has no fluorescence. BTz-Imz and Imz-OH have characteristics of blue color emissions at λ_{\max} 388 nm and 387 nm. Introducing alkyl chain to hydroxyl group did not have any distinct effect on the fluorescence as seen in Figure 2.16.a. Thus, it can be referred that blue light emission is directly related with the imidazole ring attached to benzotriazole.

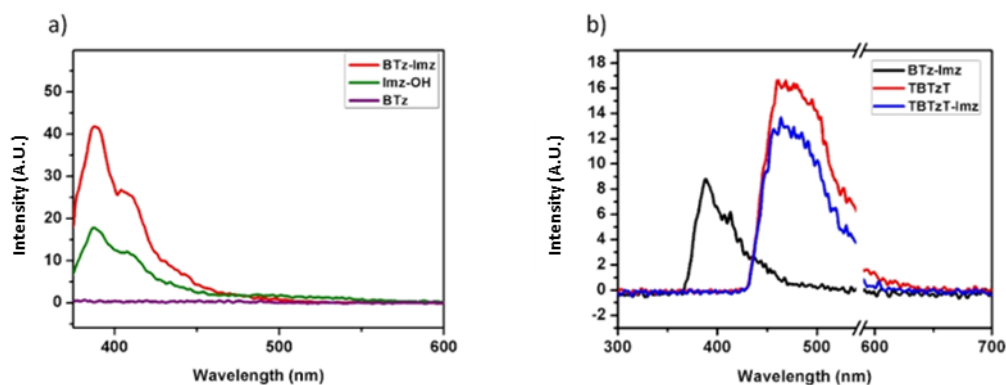


Figure 2.16. Emission spectra of solutions (0.42 g/L) of a) BTz, Imz-OH and BTz-Imz, b) BTz, TBTzT and TBTzT-Imz (61). This article was published in *Synthetic Metals*, 244, Şevki Can Cevher, Duygu Keles, Gonul Hizalan, Levent Toppare, Ali Cirpan, Alkyl-end phenanthroimidazole modification of benzotriazole based conjugated polymers for optoelectronic applications, 1-9, Copyright Elsevier, 2018

In Figure 2.16. emission features of BTz-Imz, TBTzT, TBTzT-Imz were compared. As depicted in PL spectra, in the case of TBTzT, TBTzT-Imz energy transfer from imidazole unit to the backbone was achieved; thus, emission from imidazole was diminished.

Normalized fluorescence spectra of TBzT and TBTzT-Imz in solution and as thin film forms were presented in Figure 2.17.a. (excited at 280 nm). Maximum emissions were observed at 462 and 464 nm for solutions of TBTzT and TBTzT-Imz, respectively. Thin film emissions were red shifted due to aggregations in solid form. Emission spectra of the TBTzT and TBTzT-Imz thin films were centered at 509 and 515 nm, respectively.

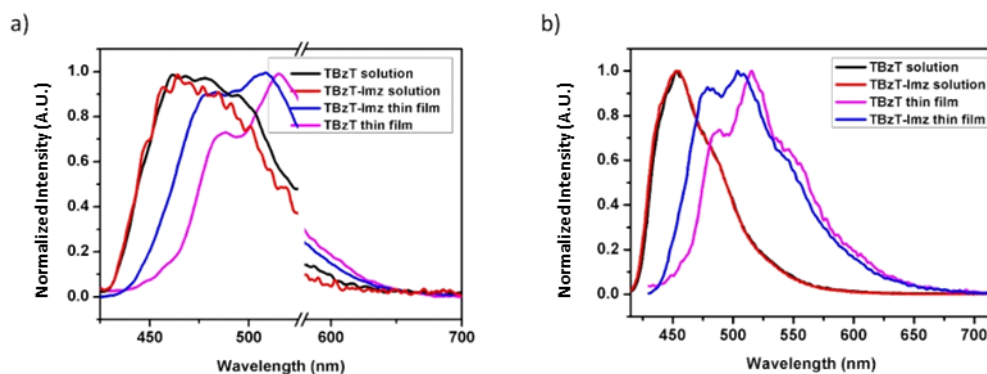


Figure 2.17. Emission spectra of TBzT and TBTzT-Imz a) 280 nm excitation wavelength, b) 420 nm excitation wavelength of thin films. (400 nm excitation wavelength for solutions) (61). This article was published in Synthetic Metals, 244, Şevki Can Cevher, Duygu Keles, Gonul Hizalan, Levent Toppare, Ali Cirpan, Alkyl-end phenanthroimidazole modification of benzotriazole based conjugated polymers for optoelectronic applications, 1-9, Copyright Elsevier, 2018

Emission spectra at 420 nm and 400 nm excitation wavelengths for TBzT and TBTzT-Imz in thin films and solutions were given in Figure 2.17.b. 463 nm peak stands for λ_{max} for both molecules in solution. However, there is a slight difference observed in thin film emissions. 504 nm and 515 nm emission λ_{max} were measured for TBzT and TBTzT-Imz, respectively. Imidazole ring played an important and interesting role where emission λ_{max} in thin films were shifted to the blue region by 10 nm. Fused planar structures which are attached to the main chain, not only enhances the high energy emission band in the solid state but also introduce a bathochromic shift.

2.8.2. Electrochemical Properties

All CV measurements were performed in an electrolyte solution of 0.1 M solution of TBAPF₆ in ACN with 100 mV/s scan rate under nitrogen atmosphere.

All polymers exhibit both p- and n-doping characters as given in Figure 2.18. Doping and dedoping potentials are 1.60 V/1.16 V for P1, 0.98 V/0.71 V and 1.27 V/1.06 V for P2 and 1.00 V/0.58 V for P3 during p-doping. Differences in oxidation potentials can be attributed to electron density differences in polymer backbones. P2 has a lower oxidation potential compared to P1, since P2 contains electron donating thiophene π -

bridge. Due to higher electron donating ability of bithiophene with respect to fluorene, P3 has lower oxidation potential (81).

Ambipolar features of the polymers enable to calculate the highest occupied molecular orbital (HOMO) and the lowest unoccupied molecular orbital (LUMO) energy levels using corresponding onset potentials according to equations $\text{HOMO} = - (4.75 + E_{\text{ox}}^{\text{onset}})$ and $\text{LUMO} = - (4.75 + E_{\text{red}}^{\text{onset}})$ (taking NHE as 4.75 eV versus vacuum level). Table 1.1. demonstrates the electronic features of the polymers.

HOMO and LUMO levels are calculated as -5.97 eV/-2.95 eV for P1, -5.43 eV/-3.04 eV for P2 and -5.39 eV/-3.38 eV for P3. Comparing P2 with P1, adding thiophene to the polymer backbone causes an increase in HOMO level and a decrease in LUMO level resulting in a lower bandgap. This situation was observed in another study; Kaya et al. synthesized benzotriazole and fluorene containing alternating polymers and their HOMO and LUMO energy levels are very close to HOMO and LUMO energy levels of P1 and P2 in this study (83). These results also showed that the replacement of fluorene with bithiophene in donor part causes to high lying HOMO and low lying LUMO since fluorene is a weaker donor unit compared to bithiophene. Using HOMO and LUMO levels, electronic band gaps were calculated as 3.02 eV, 2.39 eV and 2.01 eV for P1, P2, and P3, respectively.

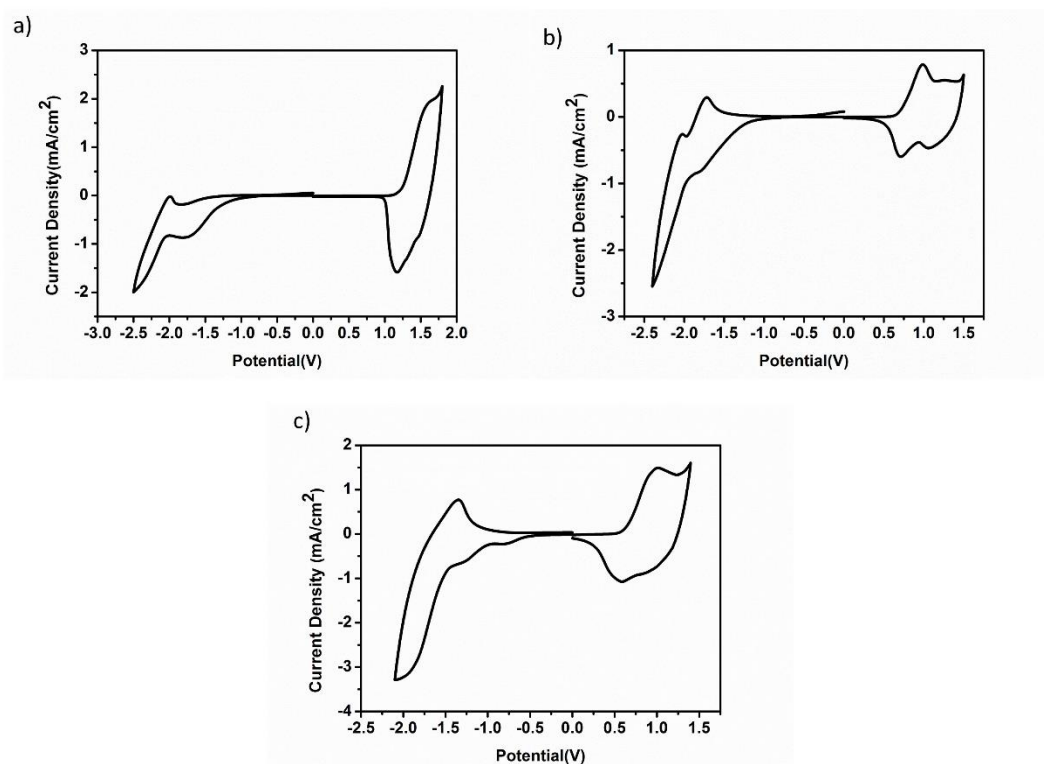


Figure 2.18. Single scan cyclic voltammograms of polymers in 0.1 M TBAPF₆/ACN electrolyte solution at 100 mV/s scan rate, a) P1, b) P2, c) P3 (61). This article was published in Synthetic Metals, 244, Şevki Can Cevher, Duygu Keles, Gonul Hizalan, Levent Toppare, Ali Cirpan, Alkyl-end phenanthroimidazole modification of benzotriazole based conjugated polymers for optoelectronic applications, 1-9, Copyright Elsevier, 2018

2.8.3. Spectroelectrochemical Properties

To investigate the optical properties of conjugated polymers, spectroelectrochemistry studies were performed upon applied potentials. For these studies, 0.1 M TBAPF₆/ACN medium was used with a three-electrode system consisting of the polymer film coated on ITO, platinum and silver wires.

During stepwise oxidation, the color change was observed and the absorption spectra were recorded for each oxidation state (Figure 2.19). π - π^* transitions of P1, P2, and P3 were observed at 410 nm, 458 nm and 535 nm, respectively, in thin film spectra. Due to the differences in their λ_{\max} values, they reveal different colors and corresponding L, a, b values were reported in Table 1.2. Upon doping, the changes in color were observed and new absorption bands were formed. While polaron bands

were generated around at 610 nm, 680 nm and 740 nm, bipolaron bands were around at 1950 nm, 1500 nm and 1470 nm for P1, P2, and P3, respectively. Optical band gaps are calculated from neutral state spectra using $\lambda_{\text{max}}^{\text{onset}}$ values as, 2.62 eV, 2.22 eV and 1.89 eV for P1, P2, and P3, respectively. Creation of free charges during cyclic voltammetry studies resulted in higher electronic band gaps than that of optical calculated in spectroelectrochemistry part (84).

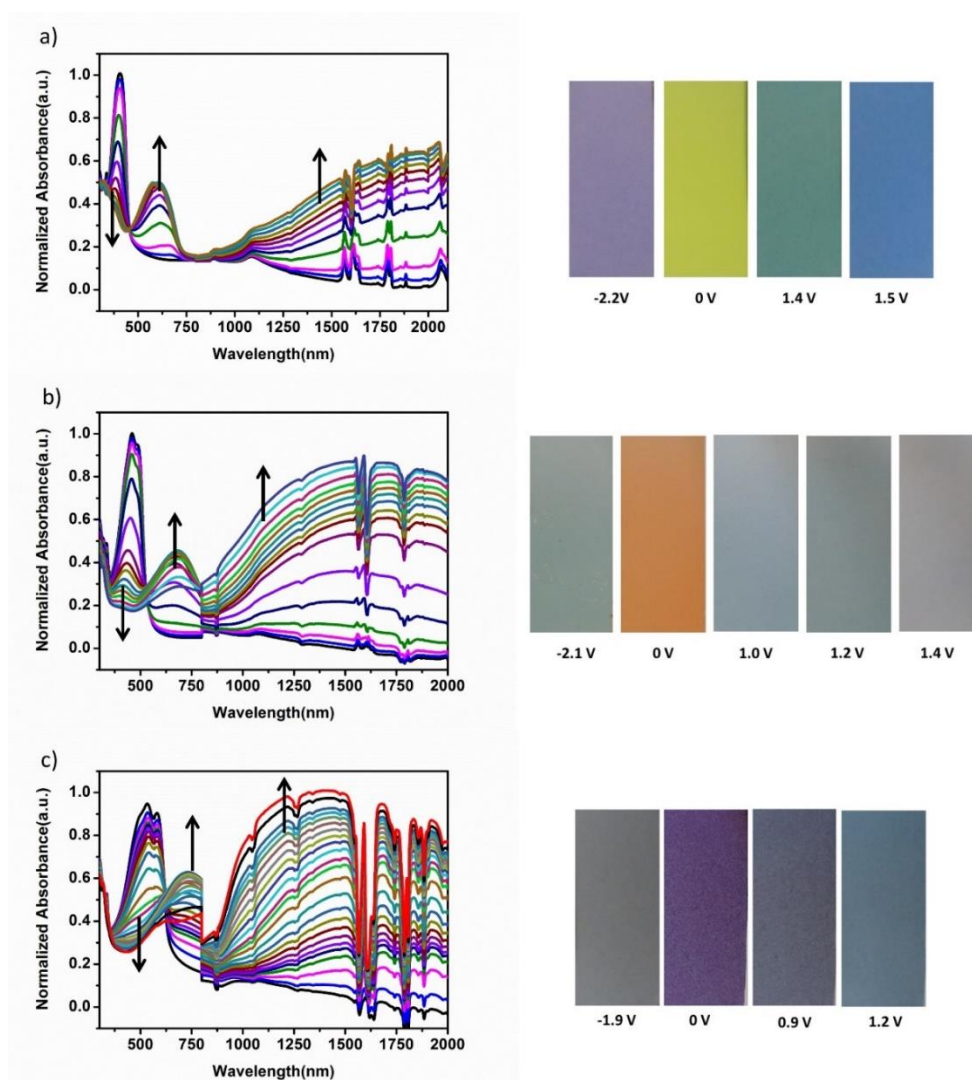


Figure 2.19. Electronic absorption spectra and their original corresponding colors in oxidation and reduction states of polymers in 0.1 M TBAPF₆/ACN solution, a) P1, b) P2, and c) P3 (61). This article was published in *Synthetic Metals*, 244, Şevki Can Cevher, Duygu Keles, Gonul Hizalan, Levent Toppare, Ali Cirpan, Alkyl-end phenanthroimidazole modification of benzotriazole based conjugated polymers for optoelectronic applications, 1-9, Copyright Elsevier, 2018

Table 2.1. Summary of electrochemical and spectroelectrochemical studies of P1, P2 and P3 (61). This article was published in *Synthetic Metals*, 244, Şevki Can Cevher, Duygu Keles, Gonul Hizalan, Levent Toppare, Ali Cirpan, Alkyl-end phenanthroimidazole modification of benzotriazole based conjugated polymers for optoelectronic applications, 1-9, Copyright Elsevier, 2018

<i>Polymer</i>	$E_{p-doping}$ (V)	$E_{n-doping}$ (V)	<i>HOMO</i> (eV)	<i>LUMO</i> (eV)	E_g^{op} (eV)	E_g^{el} (eV)
P1	1.60	-2.47	-5.97	-2.95	2.62	3.02
P2	0.98/1.27	-2.39	-5.43	-3.04	2.22	2.39
P3	1.00	-2.07	-5.39	-3.38	1.89	2.01

Table 2.2. *L*, *a*, *b* values of colors at different states (61). This article was published in *Synthetic Metals*, 244, Şevki Can Cevher, Duygu Keles, Gonul Hizalan, Levent Toppare, Ali Cirpan, Alkyl-end phenanthroimidazole modification of benzotriazole based conjugated polymers for optoelectronic applications, 1-9, Copyright Elsevier, 2018.

<i>Polymer</i>	<i>Potential</i>	<i>L</i>	<i>a</i>	<i>b</i>
P1	0 V	74	-14	57
	1.4 V	53	-16	0
	1.5 V	50	-3	-31
	-2.2 V	55	9	-17
P2	0 V	61	20	35
	1.0 V	62	-4	-6
	1.2 V	55	-5	-2
	1.4 V	60	0	1
	-2.1 V	63	-5	1
P3	0 V	35	17	-21
	0.9 V	38	2	-9
	1.2 V	46	-6	-10
	-1.9 V	45	0	-1

2.8.4. Kinetic Studies

Fast switching time and high optical contrast are desired for electrochromic applications. Percent transmittance change between the neutral and oxidized states is

defined as the optical contrast. Switching time is the time needed for switching between neutral and oxidized states. For the kinetic studies, the same three-electrode system as described in spectroelectrochemistry was constructed and the spectra were recorded during applying a square-wave potential with 5 s time intervals. Kinetic performance can be seen in Figure 2.20 and the results were summarized in Table 2.3.

Table 2.3. *Summary of kinetic studies (61). This article was published in Synthetic Metals, 244, Şevki Can Cevher, Duygu Keles, Gonul Hizalan, Levent Toppare, Ali Cirpan, Alkyl-end phenanthroimidazole modification of benzotriazole based conjugated polymers for optoelectronic applications, 1-9, Copyright Elsevier, 2018*

<i>Polymer</i>	<i>Wavelength (nm)</i>	<i>% T</i>	<i>Switching Time (s)</i>
P1	410	45	1.5
	610	22	0.2
	1950	49	0.2
P2	458	50	1.8
	680	22	0.6
	1500	61	0.4
P3	535	42	0.4
	740	19	0.7
	1470	64	1.1

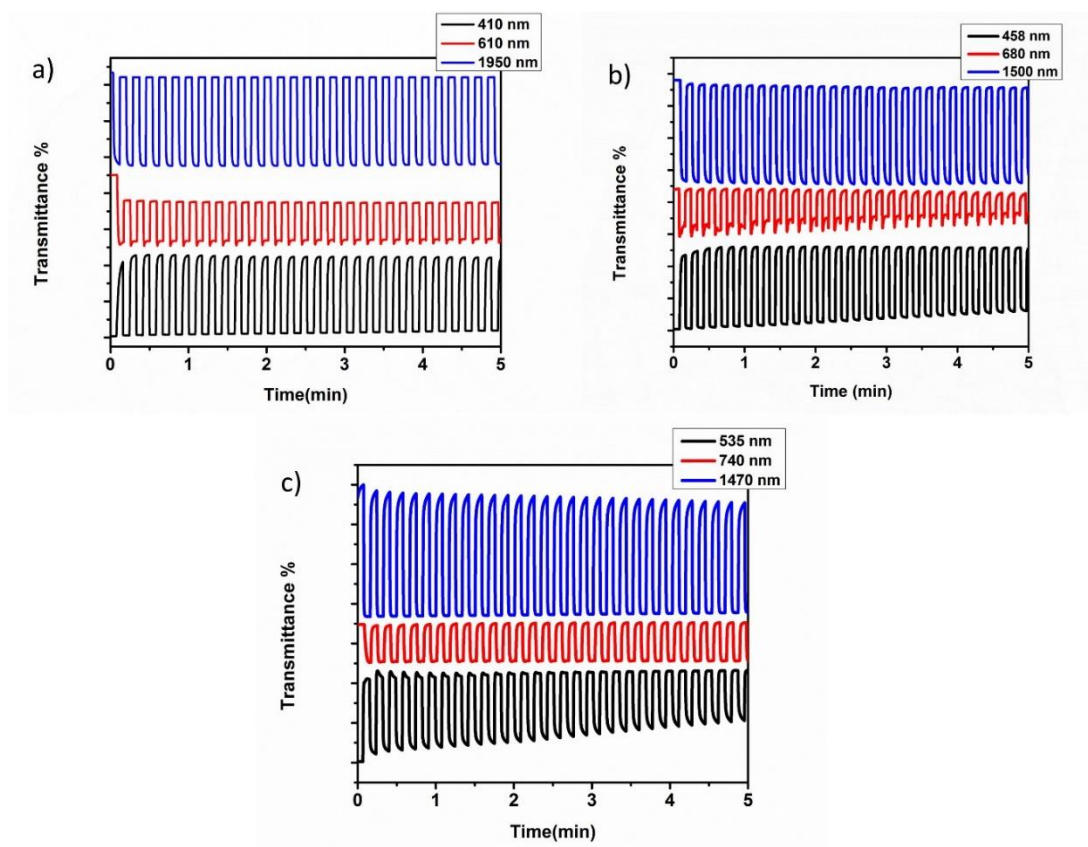


Figure 2.20. Percent transmittance change of P1 (a), P2 (b) and P3 (c) between neutral and oxidized states (61). This article was published in *Synthetic Metals*, 244, Şevki Can Cevher, Duygu Keles, Gonul Hizalan, Levent Toppare, Ali Cirpan, Alkyl-end phenanthroimidazole modification of benzotriazole based conjugated polymers for optoelectronic applications, 1-9, Copyright Elsevier, 2018.

2.8.5. Characterization of PLEDs

Electroluminescence properties of the P1, P2 and P3 based OLEDs were investigated with the device structure of ITO/ PEDOT:PSS/ polymer /LiF /Al. Energy band diagram of the devices was depicted in Figure 2.21.

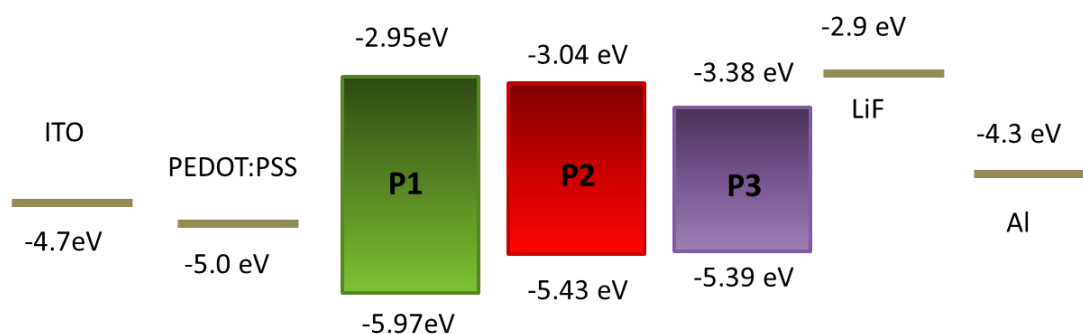


Figure 2.21. The energy band diagrams of the constructed devices (61). This article was published in *Synthetic Metals*, 244, Şevki Can Cevher, Duygu Keles, Gonul Hizalan, Levent Toppare, Ali Cirpan, Alkyl-end phenanthroimidazole modification of benzotriazole based conjugated polymers for optoelectronic applications, 1-9, Copyright Elsevier, 2018.

Maximum EL intensity was obtained at 482 nm for P1 based device corresponding to CIE coordinates of 0.2295, 0.4646. (CIE L, a, b: 33.8, -42.5, 9.1) P2 based device gave the peak intensity at 590 nm which corresponds to CIE coordinates of 0.5446, 0.4485. (CIE L, a, b: 16.9, 11.7, 28.5). Maximum EL intensity was at 641 nm for P3 based device corresponding to CIE coordinates of 0.4737, 0.3012 (CIE L, a, b: 0.4, -1.2, 0.1) as depicted in Figure 2.22. With the incorporation of electron rich thiophene units to the polymer backbone, PL of the polymers and EL for the devices are red shifted. PL and EL characteristics were summarized in Table 2.4. Similar EL and PL characteristics prove that photoexcitation and electrical excitation produces the same emitting species, PL and EL processes have similar mechanism and recombination center.

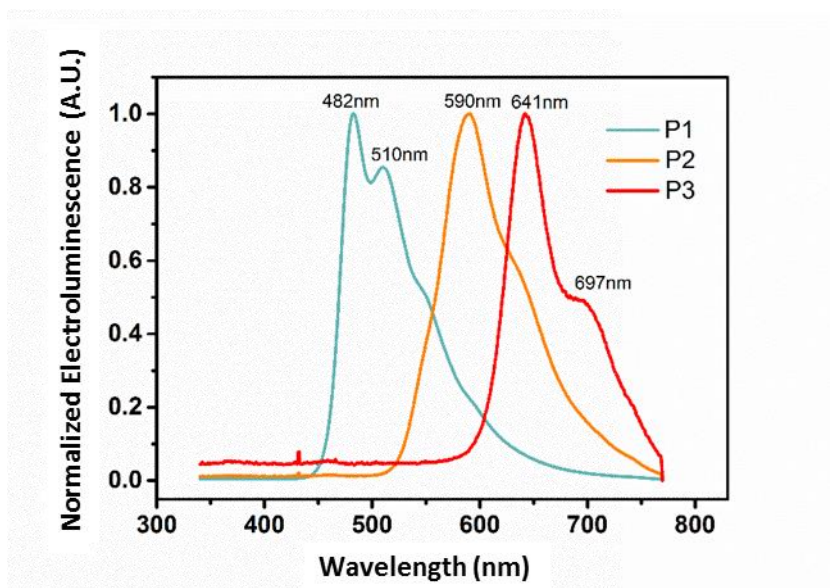


Figure 2.22. Electroluminescence spectra of the P1, P2 and P3 based PLEDs (61). This article was published in *Synthetic Metals*, 244, Şevki Can Cevher, Duygu Keles, Gonul Hizalan, Levent Toppare, Ali Cirpan, Alkyl-end phenanthroimidazole modification of benzotriazole based conjugated polymers for optoelectronic applications, 1-9, Copyright Elsevier, 2018.

The current density vs. voltage and luminance vs. voltage characteristics of P1, P2 and P3 based electroluminescent devices were presented in Figure 2.23. Above the turn on voltage, current density and luminance values increase exponentially, obeying diode characteristics.

Luminance-voltage characteristics were investigated and luminance values were determined as 14180 cd/m² for P1 and 11440 cd/m² for P2 and 195 cd/m² for P3 incorporated electroluminescent device. The turn-on voltage of the electroluminescent devices mainly depends on the bandgap of the emissive polymer and work function of the electrodes (60). P1 based device exhibited the highest turn on voltage among the polymers which is a result of the wide bandgap of this polymer.

In Table 2.4., photoluminescence, electroluminescence characteristics, maximum luminance values and CIE coordinates are summarized. P2 incorporated device exhibited 1.61 cd/A luminance efficiency at a bias of 9.5 V with a luminance of 9301 cd/m². The highest luminance efficiency for P1 based device was 3.01 cd/A at 9.5 V at a luminance value of 1665 cd/m².

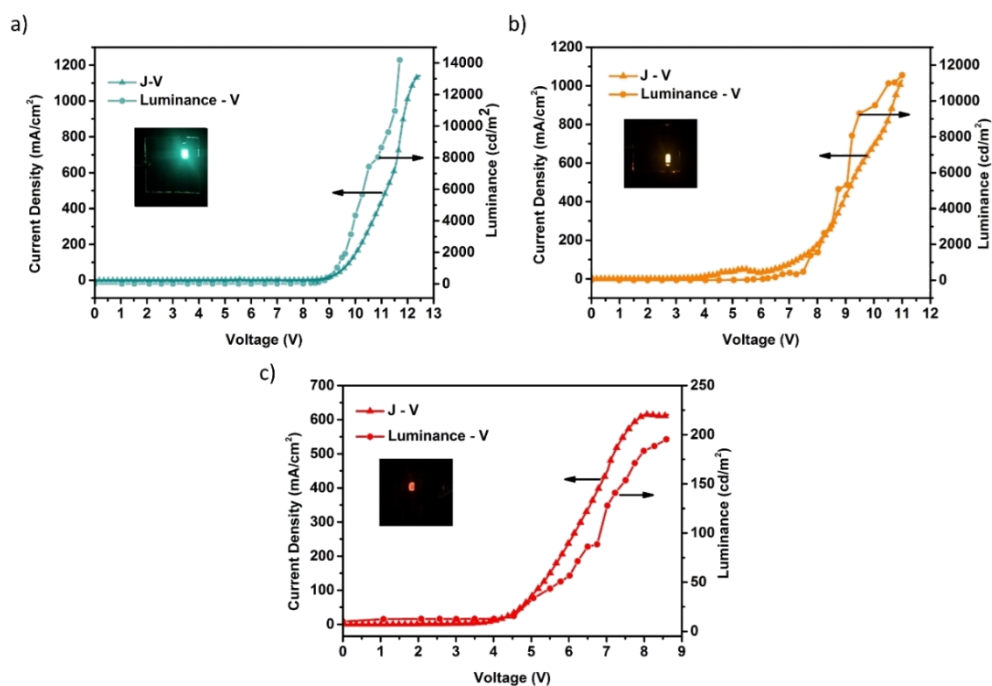


Figure 2.23. Current density-voltage-luminance characteristics of the a) P1, b) P2 and c) P3 based OLEDs (61). This article was published in *Synthetic Metals*, 244, Şevki Can Cevher, Duygu Keles, Gonul Hizalan, Levent Toppare, Ali Cirpan, Alkyl-end phenanthroimidazole modification of benzotriazole based conjugated polymers for optoelectronic applications, 1-9, Copyright Elsevier, 2018.

Table 2.4. Photoluminescence and electroluminescence properties of polymers (61). This article was published in *Synthetic Metals*, 244, Şevki Can Cevher, Duygu Keles, Gonul Hizalan, Levent Toppare, Ali Cirpan, Alkyl-end phenanthroimidazole modification of benzotriazole based conjugated polymers for optoelectronic applications, 1-9, Copyright Elsevier, 2018

Polymer	PL λ_{max} Solution (nm)	PL λ_{max} thin film (nm)	EL λ_{max} (nm)	CIE coordinates (x,y)	Max Luminance (cd/m ²)	Max Luminance efficiency (cd/A)
P1	466-492	481-509	482-510	0.2295, 0.4646	14180	3.01
P2	530-564	597	590	0.5446, 0.4485	11440	1.61
P3	587-628	653-709	641-697	0.4737, 0.3012	195	0.032

2.9. Conclusion

Benzotriazole based alkyl-end phenanthroimidazole modified conjugated polymers were synthesized and published in Synthetic Metals Journal (61). Investigation of photoluminescence properties revealed that only P3 in thin film form showed the emission of both phenanthroimidazole and the conjugated polymer backbone. For the rest, energy transfer occurred between phenanthroimidazole and conjugated polymer backbone; thus, emission in the blue region was diminished. Optical/ electronic band gaps of polymers were 2.62/ 3.02, 2.22/ 2.39, and 1.89/ 2.01 eV for P1, P2, and P3, respectively. OLED's were fabricated by using these polymers as active materials. The highest luminance value of 14180 cd/m² was achieved with P1 based device. While photoluminescence of P3 emitted blue/red light in the thin film form (excited at 284 nm), electroluminescence spectrum showed dominant red light emission.

CHAPTER 3

FUSED STRUCTURES FOR BIOSENSOR APPLICATIONS

3.1. Biosensors

Sensors have surrounded the daily life of human being. Comfort of these sensors is so intriguing that research and development of various type of sensors have been raised exponentially. Publications and the capital spent for their investigation are obvious truism (85–87). Sensors spread over enormous number of areas e.g.; sensors of temperature (88–90), gas (91–93), motion (94–96), light (97–99), tactile (100–102) and so on so forth. As temperature responsive sensors are beneficial for the development of thermometers and light sensitive sensors can be examples of infrared television remote controls as well as motion sensors are good candidates for home security systems and tactile sensors for touch screen devices such as smartphones and laptops. Dexterous combination of recognition of biological macromolecule and electronics opens a new concept of biosensors. Expeditious progress and development of material science and environmental concerns of our recent decades, have brought the advancements of biosensors to today's one of the top research fields.

Principally, biosensors are analytical devices that sense biological analytes. Integration of bio-receptor, analyte specific material: enzyme, antibody; and transducers, responsible for biochemical signal production as biochemical reaction happens, can generate meaningful electrical signal that can be fetched by the detector. A device configuration of biosensor can be seen in Figure 3.1. An estimated market research on biosensors gives a value of 31.5 billion USD by 2024 (103). The motivation underneath this interest simply relies on the needs of quantification and exploitation of bio-elements in the course of environmental concerns (104), clinical purposes (105–107), investigation of food quality (108), and defence (109).

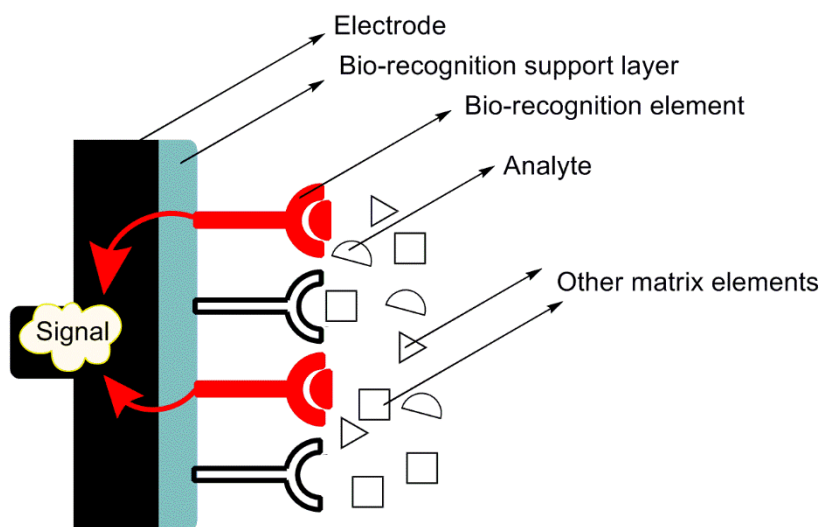


Figure 3.1. Biosensor device

Beside conventional methods like chromatographic analysis techniques, biosensors serve economic and robust way of analyzing in complex matrices. The real advantage of biosensors is being highly specific for a selected target chemical entity without the necessity of chemical/physical separation of analyte from its interfering surroundings. Practically, biosensors as sensors are supposed not to depend on parameters like pH, pressure and temperature to acquire reproducible, precise and reliable results. However, the dependence of such parameters of biomolecule that is under investigation needs an advanced knowledge in distinct fields. The field of chemical physics helps to understand the process that converting the biochemical response into an electrical signal. The field micro-electronics are associated with the device configuration/circuit required to maintain the process at a scale of micro to utmost pico molar concentration according to recent technology.

“Biosensor” was termed by Clark and co-workers in a study to develop glucose oxidase-enzyme based glucose sensing device (110). Ease of modification to sense various kind of biological species, biosensors have been revolutionized to detect complex biological elements like insulin (111), virus (112), pathogens (113), neurotransmitters (114), hormones (115) and more. Combined properties of early detection, on-site and real-time operation modes reveal the importance of biosensors

for human life, in particularly sensing the menacing diseases like Hendra, HIV, SARS-CoV, etc (116–118).

The performance of biosensor depends on several parameters (109) which include but not limited to; limit of detection, linear range, selectivity, sensitivity and reproducibility. Beside performance of a biosensor, response time, storage and stability are important factors. Various type of materials has been used to construct biosensors such as magnetic nanoparticles (119), inorganic semiconductors (120), metal oxide nanofibers (121), carbon nanomaterials (122) and organic conjugated polymers (OCPs) (114). Among them OCPs have superior characteristics such as tunable electrical conductivity, unique chemical (biocompatibility (123)) and electronic properties (facile electron transfer (124)), environmental tolerance(125), facile and wide range of synthesis especially corrosion-free (126). Due to the fact that they can efficiently transfer the electron as biochemical reaction happens, OCPs have been utilized extensively as transducer the intermediate layer between biological analyte and electronic circuit. In the literature, many of the biosensing systems were created using OCPs and showed superior sensor (127–129).

3.2. Basic Principals of Biosensors

Ordinarily, bio-recognition element is immobilized on the transducer. Therefore, the surface of transducer gains ability to form specific interaction with the target analyte. Specified binding molecules often cause conformational change in immobilized bio-recognition element. Monitoring this biochemical change and transducing it into a meaningful electrochemical, thermometric, optical or piezoelectric signal, in accordance with their combined bioreceptors (130), allows the quantification of analyte under investigation.

3.3. Types of Biosensors

According to the type of sensing the biochemical/physicochemical signal, in general biosensors can be divided into four main categories: electrochemical, piezoelectric, thermal, and optical (Figure 3.2).

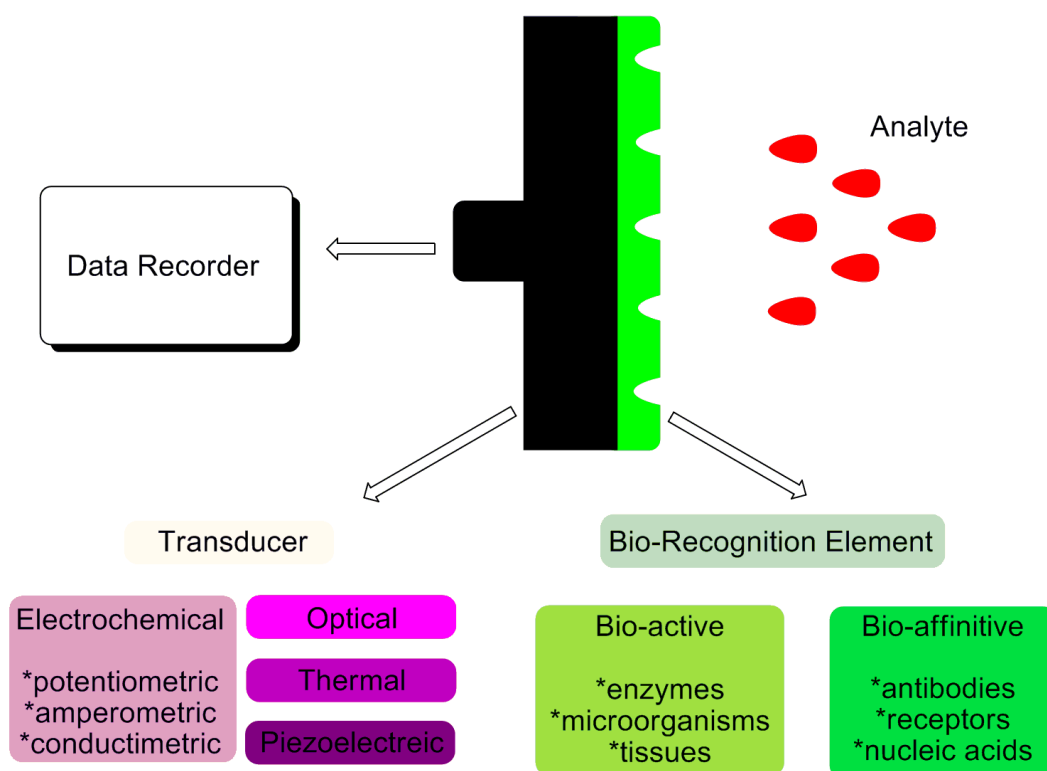


Figure 3.2. Typical biosensors and components

3.3.1. Electrochemical Biosensors

In this category, bio-recognition elements are generally matrix-bound structured and coupled with electrochemical transducer (Figure 3.3). Beside common bio-recognition elements enzymes, antigens antibodies and also micro-organisms can also be used (131–134).

Essential feature of electrochemical biosensors is the correlation of the amount of electrons, which are produced or consumed during biochemical reaction, with the amount/concentration of target analyte (135). Moreover, the change in electrical characteristics can also be associated with the rate of production or consumption of biological molecules (136).

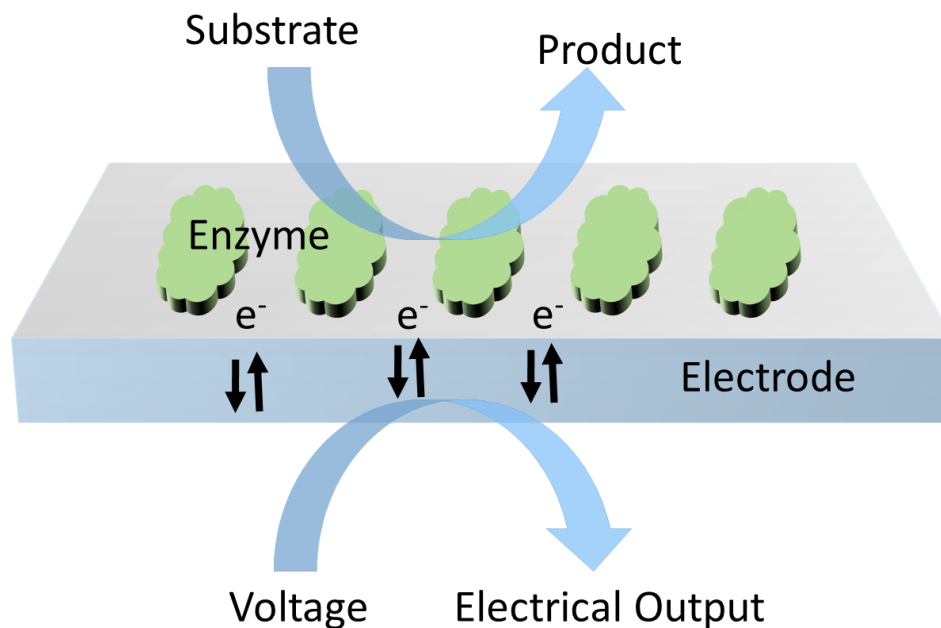


Figure 3.3. Electrochemical biosensor

There are three different methodologies to monitor the electrochemical process; probing the generated current in amperometric biosensors, probing the charge or potential accumulation in potentiometric biosensors and probing the conductivity in conductometric biosensors.

3.3.1.1. Amperometric Biosensors

Being a common approach, amperometry processes are fast and facile. Amperometric biosensor depends on measuring the current generated by electrochemical redox reaction vs time upon applied steady potential. Potential difference between electrodes promotes the efficient electron transfer. Thus, the resulting current is directly proportional to the concentration of redox active materials over a range of linear applied potential. As a result of these facts, amperometric biosensors hold a leading position.

3.3.1.2. Potentiometric Biosensors

Potentiometry is a kind of electrometric analytical method in which the several physicochemical quantities such as acidity (pH), solubility product (K_{sp}), dissociation constant (K_d) can be estimated (137). Another potential is the usage of potentiometry in sensing applications where the potential is measured in accordance with the cumulative electrical charges on dielectric layer (138). Potentiometric biosensors are chosen for their important characteristics like; inherent selectivity, no consumption of analyte, simple instrumental setup and logarithmic signal response (138).

Unfortunately, potentiometric biosensors where enzymes are immobilized on OCP layer are rarely used, in contrast to common amperometric ones, though several advantages of potentiometric polypyrrole based glucose oxidase biosensor over amperometric one have been demonstrated (139).

Potentiometric biosensors are utilized with ion selective electrodes which are used as working electrodes. The most important properties of ion selective electrodes is permselective ion conductive property. Their working principle depends on the accumulation of charges resulting in generation of potential difference and negligible current flow. Transformation of recognition process by bioreceptors, provides an outgoing analytical signal.

3.3.1.3. Conductimetric Biosensors

When biochemical reaction produces charges causing to alter the conductance of medium, conductimetry can be used for analytical investigation. To provide analytical information, conductimetric biosensors thereof measures the conductance which varies with the concentration of charged moieties. Due to the deviation of concentration of charged moieties caused by enzymatic reactions, conductimetric biosensors generally utilized with enzymes (140). On the other hand, enzyme-based conductimetric biosensors have limitation as mutable ionic background of various samples and necessity for consideration of minor deviation of conductivity due to the deviation of ionic strength (141, 142).

3.3.2. Piezoelectric Biosensors

Sauerbrey found that a change in the resonance frequency of a resonator can be directly related to the mass placed on it (143). This idea has opened a new era for the invention of piezoelectric materials and applications. It then gave a birth to a marvellous application area of biosensors seen in Figure 3.4 where biomolecule is immobilized onto a functional surface. Allowing the label-free recognition of piezoelectric biosensors can be thought more than a mere mass biosensor. They also influenced by the surface charge, interfacial phenomena, surface roughness and viscoelastic properties of biological molecules. These inner nature properties of piezoelectric biosensors lead to invention of a powerful tool to examine the morphological change in cell, in which the biosensor is adhered to liposomes proteins and cell (144).

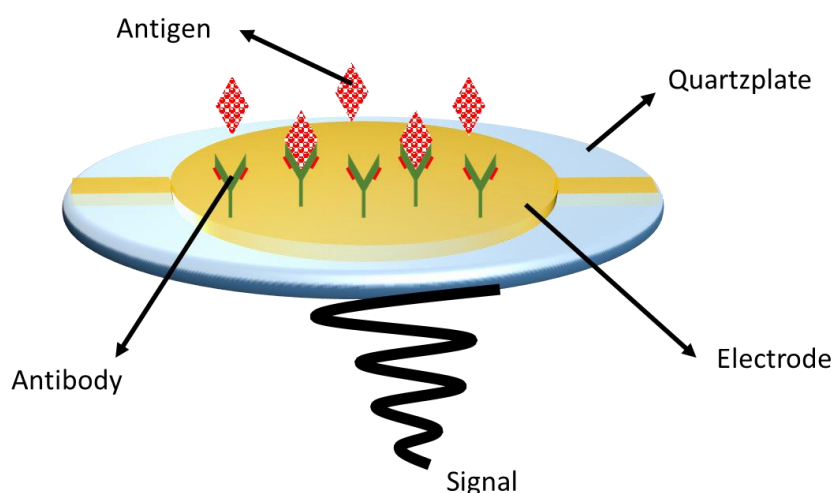


Figure 3.4. Piezoelectric biosensor.

Principally, the electrical signal is produced depending on the mass, size and chemical and physical structure of analyte which causes vibration of piezo material at a certain resonant frequency (87). As the mass of binding element increases usually, the vibration frequency decreases. Although piezoelectric biosensors have not taken great attention, they can be classified as second class of electrochemical biosensors (136).

Various piezoelectric biosensors were developed to detect Caffeine, HS, CO, NH₃ (145, 146).

3.3.3. Thermal Biosensors

Although providing weak sensitivity and imprecise heat change, thermal biosensors can be used to determine the biological molecules. In general, enzymatic biochemical reactions possess exothermic entity with an enthalpy of more or less 80 kJ/mole (147). This heat evolution or for some cases heat absorption as biochemical reaction processes is proportional to enthalpy and amount of respective products (148).

The change in temperature is monitored by thermistor. Augmented sensitivity and limit of detection can be obtained by steady enthalpy change (149). Simple device configuration has been demonstrated in Figure 3.5 that biochemical reaction is monitored by measuring the enthalpy (most clearly heat) change during the course of reaction. Major advantages of calorimetric determination are stability, and augmented sensitivity. Moreover, ability to be miniaturized, they can easily be incorporated with microfluidics.

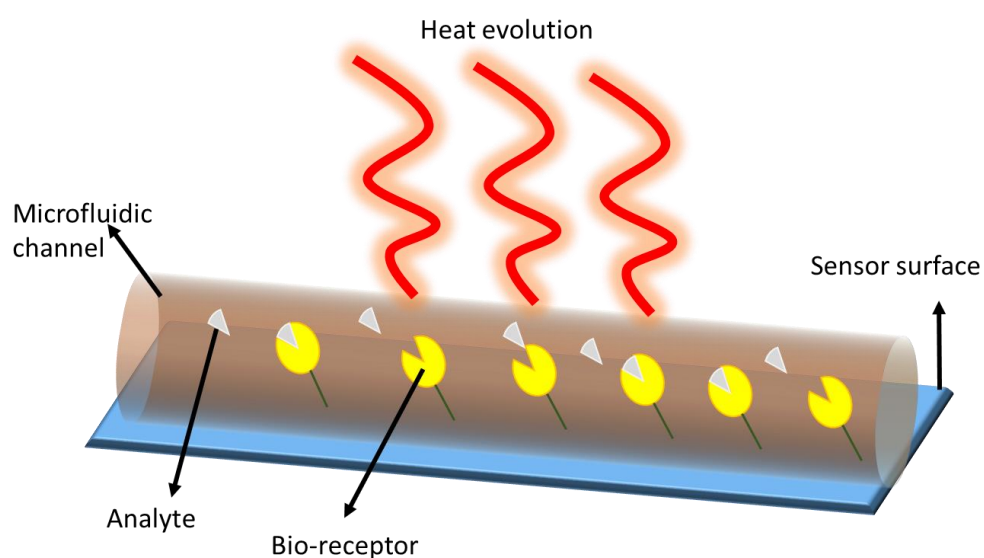


Figure 3.5. Thermal biosensor

Electroactive materials generally interfere the glucose detection in clinical/blood samples; however, electro active and optical interferences do not fluctuate the calorimetric signals. Recent advance of combination calorimetry with pyrroloquinoline quinone glucose dehydrogenase (PQQGDH), the obtained calorimetric biosensor exhibited linear range between 0.009 to 100 mM for glucose (150).

3.3.4. Photometric Biosensors

Photometric biosensors simply monitor and relate the change in optical parameters such as absorption, transmission, luminescence (chemi-, bio-, photo-), surface plasmon resonance of analyte as the biochemical reactions undergo (151). For example, the frequency change due to the formation excited state is investigated in a chemiluminescence based biosensor. Wide variety of photometric measurement techniques and optical wave guide can be coupled with (152, 153). Photometric biosensor seen in Figure 3.6. can be given as an example for chloroform (limit of detection= 9.22 ppm) biosensor in which polyaniline-dioctyl sodium sulfosuccinate film coated on fiber bragg grating (154). Another example is that alkaline vapor-which can be formed upon spoilage of fish-sensitive optical sensors based aniline and ortho-phenylenediamine containing biosensors changes its color in accordance to pH (155).

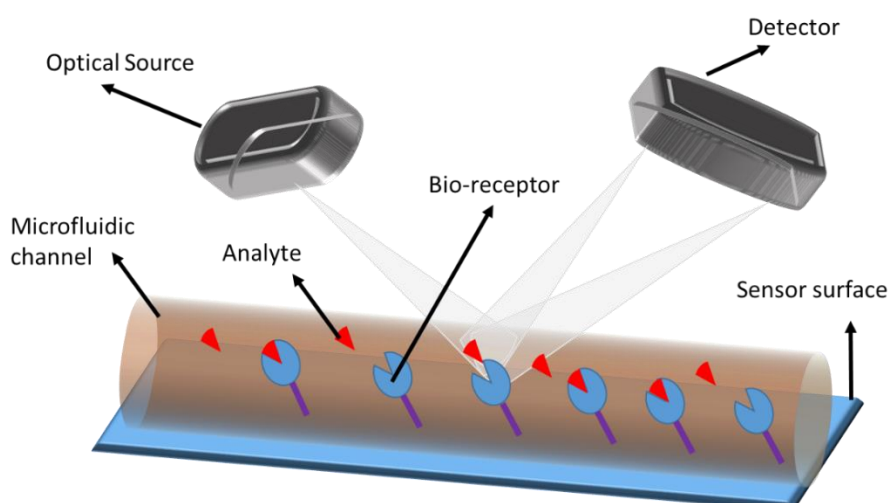


Figure 3.6. Photometric biosensor

3.4. Sensing Mechanism of Enzymatic Biosensors

There are different types of mechanism explained for each of enzymatic biosensors, immunosensors and genosensors. In this text, only enzymatic biosensors will be covered.

Enzymes, possessing 3D orbicular structure of long chains of amino acid, have ability to accelerate the biochemical reactions (156, 157). In 1958 Daniel Koshland and previously 100 years ago Emil Fischer, introduced and demonstrated the principles of lock and key model of enzymatic reaction (158, 159). Enzymes have affinity to get substrate-analyte/reactant into the right conformation which consequently breakdown into product. The interaction with substrate and enzyme is maintained by the distinct region called active site of enzyme. The rest is responsible for conformational form.

There are four main steps for operational principle of enzymatic biosensors where enzymes are immobilized onto working electrode surface:

- ☞ Diffusion of analyte from the bulk solution to immobilized enzyme electrode
- ☞ Happening of biochemical reaction
- ☞ Formation of product and consequent transportation to transducer
- ☞ Measuring the formation of product with the aid of a transducer (160).

3.5. Immobilization Techniques of Biological Materials

Preservation of its integrity is essentially important to maintain biological activity of enzymes as being attached to any surface. Thus, immobilization of these biomolecules on host materials, i.e. organic conjugated polymer coated electrode, is crucial for biosensors. Activity of a biosensor depends on various factors like (161, 162):

- ☞ Material: surface area, biocompatibility, electron transfer efficiency, porosity
- ☞ Immobilization method: deviation of biomolecule from its original form, biological activity, decaying or desorption of biomolecule over biosensor.

Although immobilization is important for a properly working biosensor, issues related with the conformational change, mass transfer limitations, denaturation of

biomolecule, caused by the immobilization methodology, lower the performance of biosensor (163). Better performances can be exhibited by proper orientation of biomolecules to expose their active site.

A number of materials for immobilization host materials, for example magnetic hydrogels, sol-gels, resins and clays; however, biocompatibility, synthesis and poor response are main limitations for these host materials (162, 164–167). Important advancement has been obtained by organic conjugated polymers, which enhance the response time and compatibility due to the fact that organic conjugated polymers function as 3D host matrix to keep biomolecule active for a prolonged time. Moreover, porosity, high electron transfer rate and better signal transduction properties of organic conjugated polymers make them an excellent candidate for immobilization platform (168, 169). This 3D matrix also prevents the leaching out integrated enzyme of the matrix and permeability of this matrix retains the active site of enzyme accessible (170).

Biocompatibility in neutral aqueous solution is crucial for in vivo biomedical applications. On the other hand, the physical and electronic properties of organic conjugated polymers are also essential for a certain application where conductivity is needed above pH of 4 (171, 172). However, one should bear in mind that stability/property concerns of organic conjugated polymers in ambient conditions like oxygen, redox reactant (173).

Immobilization simply refers to the fixation of an enzyme molecule to a solid support. The immobilized enzyme has several advantages over the free one:

- ☉ Multiple/repetitive usage
- ☉ Enhanced stability
- ☉ Ease of separation of enzyme and product/reactant
- ☉ Low cost enzyme catalyzed production

There are four main categories represented in Figure 3.7 to define the immobilization of enzyme onto the organic conjugated polymer surface, while retaining the catalytic activity of enzyme, covalent bonding, adsorption, crosslinking, and entrapment.

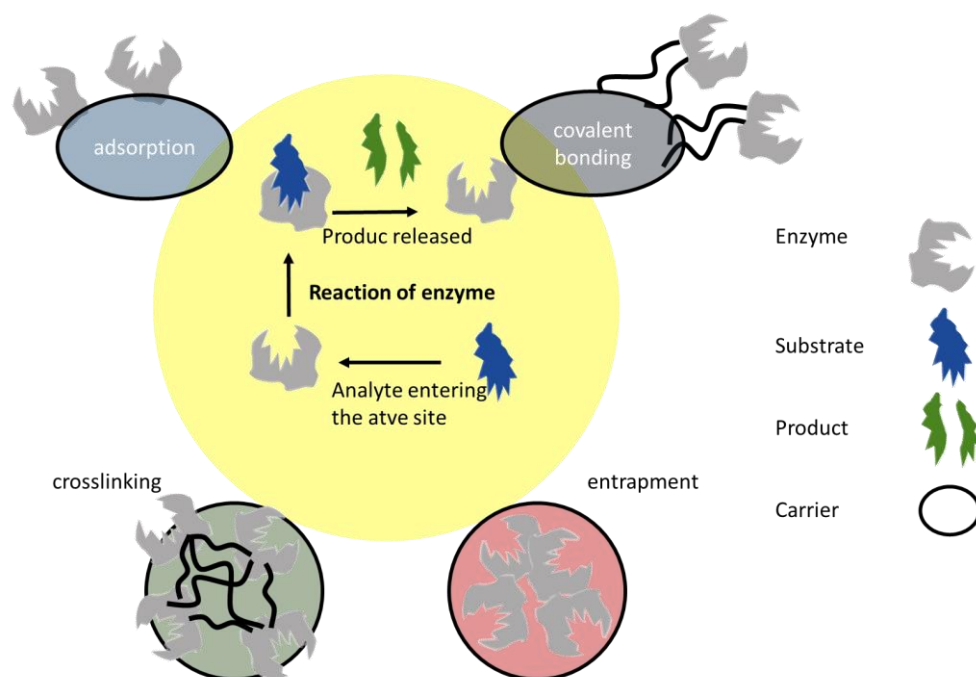


Figure 3.7. Immobilization techniques

3.5.1. Covalent Bonding

This is the most commonly used and the oldest technique for immobilization. Immobilization was obtained by chemical reaction where enzyme covalently bonded to water-insoluble host. The covalent bond is formed between the functional groups of host surface and enzyme surface results in robust immobilization. As the binding force (covalent bond) is strong enough to prevent leakage of enzyme from the host surface, even in high ionic strength solution or substrate has minimal affect (174). However, immobilization conditions are complex and less mild adsorption. Covalent bonding has high risk to alter the conformational change and/or blocking the active site of enzyme so that consequent activity lost may occur.

3.5.2. Adsorption

Physical adsorption of enzyme onto substrate is established via interactions of Van der Waals, ionic and hydrogen bond (175). Physical adsorption is simple and cheap among the other methods. It is accomplished by facile adjustment of pH, temperature and ionic strength with suitable carrier. This noninvasive method retains the activity of enzyme at supreme due to the fact that there is minimal or no conformational deformation. However, weak binding force usually results in leakage of enzyme.

3.5.3. Crosslinking

Crosslinking is a support-free immobilization technique in which enzymes are crosslinked to form enormous 3D structure. This can be achieved by physical or chemical methods (176). Bi-functional or multi-functional crosslinking agent like glutaraldehyde allows the fabrication of membranous sheet of enzymes. Crosslinking of enzymes to each other makes some of enzymes inevitably behaves as a support, this method is both redundantly expensive and insufficient. Moreover, multilayer formation decreases the activity and increases the diffusional barrier, deterioration of active site of enzyme and poor stabilities are major bottlenecks associated with crosslinking method (177, 178). However, conjugation of crosslinking with other method/s can be regarded as the best way to use crosslinking. Hence, stabilization of adsorbed enzymes further eliminates the leakage problems (179, 180).

3.5.4. Entrapment

Localization of enzyme into a lattice and/or cavity while retaining the activity unaffected. Localization can be accomplished by ionic interaction for micelle-microcapsule or lattice structures for electrochemical entrapment. Electrochemical entrapment, where the electrochemically growing polymeric 3D structure traps the enzyme solution in close proximity the electrode, has superior advantages such as one step simple entrapment, accurate control over film thickness, high reproducibility. This method has limited application due to the necessity of water-soluble monomer and possible blemishing of enzyme because of the applied potential (181, 182).

3.6. Importance of Phenolic Compounds

One ubiquitous compound in nature phenolics lower the market value of food item due to cause browning as well as exhibit antioxidant characteristics. Phenolic compounds fight against cancer and heart related diseases. As in the case of L-DOPA, neurotransmitters can contain phenolic compounds (183, 184). Breakdown of some biomolecules like tannins, lignins and humic materials produce phenolics. Although there is copious amount of beneficial phenolic compounds, there are plenty of hazardous chemicals. These hazardous phenolics are used in or wasted from industrial effluents, chemical (especially paper, paint and textile) and pharmaceutical industry. Global production reached and may exceed the annual value of 50 ktons (185). Industrial waste of phenolic compounds contaminate water reservoirs so as the nutrients and thus environment (186–188). Biologically safe limit of phenolics is 1 ppm above which it is highly toxic. Thus, it is extremely vital to monitor and control their concentration for aquatic life (189, 190). Moreover, some phenolic compounds are in the class of endocrine disrupting chemicals. According to a study done by European Union, almost half of the 11 highest priority elements of 118 endocrine disrupting compounds are phenolics. Thus, the future of living creatures is desperate, gloom and doom if there should not be taken any precaution to contamination of this phenolic compounds to environment, in particularly natural water (191, 192) due to their insufficient elimination and consequent release (193–195).

3.7. Catechol

Catechol (IUPAC name: 1,2-dihydroxybenzene) is a derivate of phenolic compounds. As phenolics do have, catechol has high toxicity and low degradability properties (196, 197). Abundantly used industrial raw and processed chemical catechol hold an importance for chemical (photography, dye and cosmetic) and pharmaceutical industries (198). In addition, it exists in teas, foods (vegetables and fruits) and tobaccos as an intermediate compound. Yet it acts as a neurotransmitter to regulate the blood pressure and metabolism as well as used as biological indicator for several

diseases (199). It inhibits the replication of DNA, and causes the chromosomal aberration (200). Moreover, advancement of the composting technology in municipal solid waste management system generally results in direct or by-product pollutant (201). Hence, there is an emergency to establish rapid and efficient quantitative determination of catechol.

3.8. Laccase as Polyphenol Oxidase (PPO)

PPO is produced in almost every living creature range from the smallest microorganisms to animals and as well as plants (202, 203). Prosthetic copper and utilization of molecular oxygen catalyze two major reactions.

- ☉ Cresolase activity: incorporation of hydroxyl group at ortho position of monophenol to obtain *o*-diphenolic material.
- ☉ Catecholase activity: converting the *o*-diphenolic material into quinone, which is polymerized to form pigments: red, brown and black (204–206).

Based on substrate selectivity and reaction mechanism, PPOs are divided into three main types (207, 208):

- ☉ Tyrosinase: catalyzes both monophenol and diphenols. It is present in higher cluster organisms (plants, animals and fungi) but not common for others.
- ☉ Catechol oxidase: it is ubiquitous in nature. It catalyzes diphenolic compounds due the absence of catalytic activity of hydroxylase.
- ☉ Laccase: it has *p*-hydroxylation activity as well.

Laccases can also be divided into three main segments according to the spectroscopic and functional properties of copper atom. Copper mediated reactions are classified as:

- ☉ Copper type 1: Electron is captured and transferred through a copper atom.
- ☉ Copper type 2: Molecular oxygen is activated by this type of copper atom.
- ☉ Copper type 3: Oxygen is uptaken by this of copper atom.

3.8.1. Catalytic Cycle of Laccase

Catalytic cycle of laccase mechanism starts from the primary electron acceptor type 1 copper atom via reduction of Cu^{2+} into Cu^+ by reducing substrate; thus, substrate is one-electron oxidized. Typically, type 1 copper exhibits an intense absorption at 600 nm so that enzyme solution resembles light blue color. Type 2 copper atom forms a trinuclear copper cluster with two type 3 copper atoms. The distance between the sites where type 2 and type 3 copper atoms are present is 4 Å, whereas the distance between the site occupied by type 1 copper and trinuclear copper center is 12 Å (209). By extracting the electron and transferring it to trinuclear copper site, conversion of resting-fully oxidized- form of laccase to 4 e⁻ reduced-fully reduced- form is achieved. 4 substrate molecules are required to be oxidized to fully reduce- 4 e⁻ reduction- the laccase (210, 211). Rate determining step is the electron transfer from copper type 1 atom to trinuclear site (212). 2-steps dioxygen reduction process occurs through a formation bound oxygen intermediates. Molecular oxygen first binds to the trinuclear site and consequent rapid transfer of two electrons occurs. Thus, first peroxide intermediate is formed. The peroxide intermediate bridges between the type 3 coppers and type 2 copper, although the configuration has not been fully understood, followed by a rapid 1 e⁻ transfer from type 1 copper. Thus, the peroxide intermediate decays to an oxy radical and release of water molecule is followed up by 2 e⁻ reductive cleavage of O-O bond (213, 214). 1 e⁻ transfer from the type 2 copper atom facilitates the slow decay of the intermediate which can be accelerated by decreasing pH and protonation from a neighboring carboxylic acid functionalities. In the last step 4 present copper atoms are in oxidized form and O^{2-} is released as a second water molecule. The reoxidation of type 2 copper atom correlates with the decay of the intermediate in which the first water molecule is released and the second water molecule remains bound and slowly exchanged with the bulk (215).

3.9. Aim of the Study

In this study, an amperometric laccase sensor was developed to detect catechol in water samples. Laccase was used as a model enzyme during amperometric biosensing experiments. The need of additives such as metal nanoparticles or carbon nanotubes to enhance the signal was aimed by introducing three different functional groups (ketone (M1), enamine (M2), and oxime (M3)) on the conjugated backbone of polymer. Since the most effective sensor was created by PM1, laccase was immobilized on the PM1 coated electrode surface for further experiments. Pristine polymer coated sensor (PM1/Lac) is very efficient for catechol detection without needing any additional materials. The sensor showed superior performance when compared to the literature examples.

3.10. Experimental

3.10.1. Synthesis of Monomers

All chemicals were purchased from Sigma Aldrich except SiO₂ from Merck and used without further purification unless otherwise mentioned. Tetrahydrofuran and toluene was distilled over benzophenone/sodium just before usage. Palladium catalyzed reactions were performed under argon atmosphere. SiO₂ column filler was used as a stationary phase in column chromatography. Synthetic pathways of the polymers were given in Figure 3.8. Tributyl(thiophen-2-yl)stannane (78) and 4,7-dibromo-2H-benzo[*d*][1,2,3]triazole (79) (III) were synthesized according to the previous methodologies. Structures of BTz and TBTzT were synthesized according to previously published recipes via changing alkyl chain to 1,10-dibromodecane (BTz 4,7-dibromo-2-(10-bromodecyl)-2H-benzo[*d*][1,2,3]triazole) (80), TBTzT (2-(10-bromodecyl)-4,7-di(thiophen-2-yl)-2H-benzo[*d*][1,2,3]triazole) (81). Structures of organic molecules were proven by NMR recorded on a Bruker Spectrospin Avance DPX-400 Spectrometer with TMS as the internal reference.

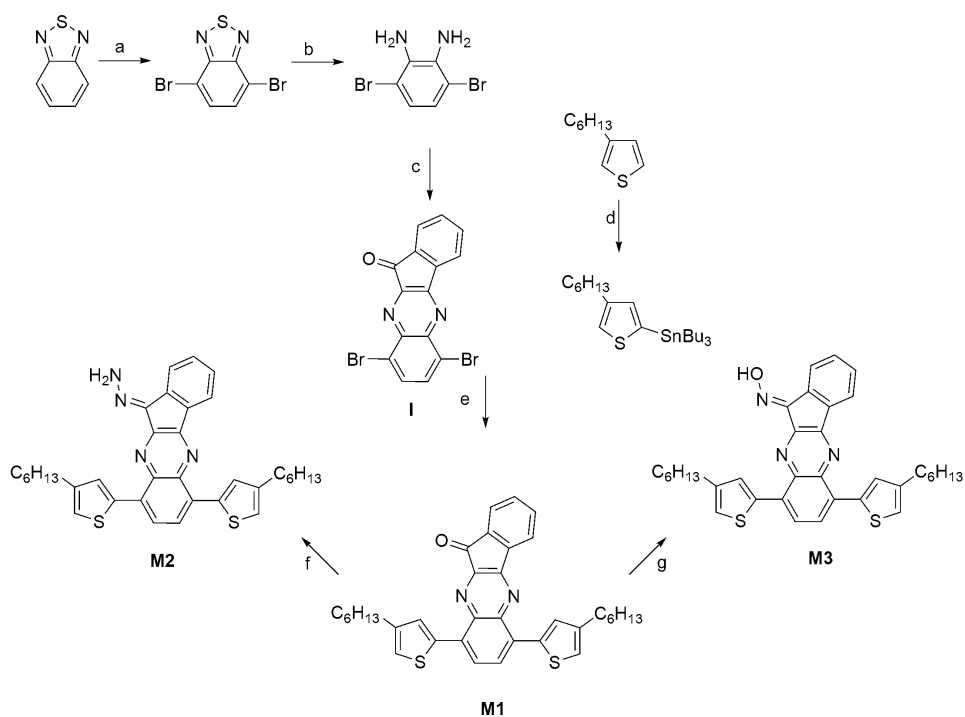


Figure 3.8. Synthetic pathway of monomers (a: Br₂, HBr; b: NaBH₄, EtOH; c: Ninhydrin, PTSA, EtOH; d: *n*-BuLi, SnBu₃Cl, THF; e: Pd(PPh₃)₂Cl₂, toluene; f: Hydrazine monohydrochloride, Hydrazine hydrate, NEt₃, THF; g: Hydroxylammonium chloride, NEt₃, THF.

3.10.1.1. 6,9-Dibromo-11*H*-indeno[2,1-*b*]quinoxalin-11-one (I)

3,6-Dibromobenzene-1,2-diamine (530 mg, 1.99 mmol), ninhydrin (355 mg, 1.99 mmol) and catalytic amount of PTSA (*p*-toluenesulfonic acid) (10% mol) were dissolved in ethanol (25 mL) and refluxed overnight. After cooling the mixture, precipitate was filtered and washed with cold ethanol (100-150 mL) and dried. There was no need for further purification of compound **I** (yellow solid, 0.668 mg, yield 86%).

3.10.1.2. 6,9-Bis(4-hexylthiophen-2-yl)-11*H*-indeno[2,1-*b*]quinoxalin-11-one (M1)

Compound **I** (0.668 mg, 1.71 mmol) and tributyl(4-hexylthiophen-2-yl)stannane (2.65 g, 5.79 mmol) were put in freshly distilled toluene (30 mL) and the solution was

bubbled with argon for 20 min. After catalytic amount of Pd(PPh₃)₂Cl₂ (7% mol) was introduced to the mixture, the overnight reaction temperature was set to reflux. As the reaction performs, undissolved yellow compound **I** was dissolved and color was turned into dark red. After the reaction was finished, controlled by TLC, reaction was cooled and extraction was done with water/dichloromethane (100/150 mL). Organic phase was collected and dried over MgSO₄, then solvent was removed under vacuum. Liquid residue was chromatographed and final **M1** product was obtained (dark red/black solid, 895 mg, 92%).

3.10.1.3. (E)-6,9-Bis(4-hexylthiophen-2-yl)-11H-indeno[2,1-*b*]quinoxaline (M2)

Hydrazine hydrate (50-60%) solution (0.26 mL, 3.5 mmol) was added into a solution of **M1** (200 mg, 3.54 mmol) in THF (30 mL) and catalytic amount of AcOH (a few drops). The solution was refluxed overnight. Color was changed upon addition of hydrazine hydrate from dark red to orange. After cooling the reaction, the solvent was removed and extraction was performed with water/dichloromethane (80/150 mL). Organic phase collected and dried over MgSO₄ and then the solvent was removed under vacuum. Crude orange product was purified by column chromatography with hexane/ethylacetate (v/v, 4/1). First orange fraction was collected as **M2** (60 mg, yield 29%).

It should be noted that *Z*-isomer was assumed a major product, however, the formation of intramolecular hydrogen-bond between amine group and nitrogen atom on the pyrazine ring stabilizes the ring. Hence, the solubility was decreased. Therefore the first fraction coming from the column was attributed to *E*-isomer. Moreover NMR spectrum of each fraction had no distinct difference.

3.10.1.4. (E)-6,9-Bis(4-hexylthiophen-2-yl)-11H-indeno[2,1-*b*]quinoxalin-11-one oxime (M3)

Hydroxylamine solution (50%) (0.25 mL, 4.2 mmol) and hydroxylamine hydrochloride (25 mg, 3.60 mmol) were added into a solution of **M1** (200 mg, 3.54

mmol) in THF (30 mL) and trimethylamine (4-7 drops). The solution was refluxed overnight. Color was changed as the reaction proceeded from dark red to bright orange. After cooling the reaction, the solvent was removed and extraction was performed with water/dichloromethane (50/150 mL). Organic phase was collected and dried over MgSO₄ and then the solvent was removed under vacuum. Crude orange product was purified by column chromatography with hexane/ethylacetate (v/v, 3/1). First orange fraction was collected as **M3** (33 mg, yield 16%).

3.10.2. Biosensor Materials

Laccase (oxygen oxidoreductase, EC 1.10.3.2) (21.8 U/mg) from *Trametes versicolor* and glutaraldehyde (%50 wt in H₂O) were obtained from Sigma-Aldrich. Dichloromethane (DCM), acetonitrile (ACN), were purchased from Merck (Darmstadt, Germany) and directly used without further purification. By using 0.025 M Na₂HPO₄ from Merck (Darmstadt, Germany) and 0.025 M NaH₂PO₄ from Fluka Analytical (Germany), phosphate buffer solution (PBS) was prepared. As a substrate, 0.05 M catechol solution (from Sigma-Aldrich) was prepared at room temperature. All chemicals were of analytical reagent grade.

Electropolymerization with cyclic voltammetry studies was performed by using GAMRY Reference 600 (GAMRY Instruments Inc., Pennsylvania, USA). During all amperometric measurements PS Trace 5.5 potentiostat (Palm Instruments, Houten, and The Netherlands) was used. Three-electrode system was used in all electropolymerization studies and amperometric measurements. Graphite electrode (Ringsdorff Werke GmbH, Bonn, Germany, type RW001, 3.05 mm diameter and 13 % porosity) as a working electrode, and platinum electrode (Metrohm, Switzerland) as a counter electrode were used. Lastly, Ag wire were used as the pseudo-reference electrode. Amperometric measurements were recorded as average of three measurements and \pm SD. All measurements were performed at room temperature

3.11. Fabrication and Amperometric Measurements of the Biosensor and Electrochemical Characterization of the Polymers (PM1, PM2 and PM3)

First, bare graphite electrode was cleaned and polished using emery paper. PM1 coated surface was obtained using cyclic voltammetry technique. Electropolymerization of M1 (10^{-3} M) was performed in equimolar 0.1 M TBAPF₆ supporting electrolyte containing 5:95 (v/v) DCM:ACN solution with repeated scan intervals between 0.0 and 1.2 V versus Ag wire pseudo-reference electrode (Scan rate 100 mV/s). After electropolymerization, the polymer coated electrode was washed with distilled water in order to remove impurities. 5.0 μ L of laccase solution was immobilized on the polymer coated graphite electrode and after a while, glutaraldehyde solution (5.0 μ L, %1 in H₂O) was spread over to the electrode surface as a crosslinking agent. Then, prepared electrode was left to dry for 2 h at room temperature. At the end of 2 h, the electrode was washed with distilled water to rinse unbound enzyme molecules.

All amperometric measurements were performed in the reaction cell that is containing 10 mL sodium acetate buffer (50 mM, pH 5.5) solution at room temperature under stirring by applying -0.3 V constant potential. Before each measurement, buffer solution in reaction cell was refreshed. When current reached to the equilibrium, a certain amount of catechol was added into the sodium acetate buffer solution (reaction medium) and the change in current was monitored due to enzymatic reaction. This change was recorded as a biosensor response. All amperometric measurements were carried out at ambient conditions. Briefly, when the analyte is introduced into the reaction cell, immobilized Lac is oxidized by molecular oxygen and then, reduced again by phenolic substrates, acting as electron donors for the enzyme regeneration and then, the phenolic substrates are converted into quinone, phenoxy radicals, or both, and subsequently, these products can be reduced at the electrode surface (216).

Three different monomers were polymerized in the presence of ACN: DCM (95:5) in 0.1 M TBAPF₆ electrolyte-solvent system by scanning between 0.0 V and +1.4 V

potential for M1 and for the others 0.0 V and +1.2 V. As shown in Figure 3.9, the monomer oxidation potentials were found as 1.05 V, 1.06 V, and 1.00 V, respectively for M1, M2 and M3. Moreover, the polymer oxidation potentials were recorded as 0.34/1.15 V, 0.40/0.97 V and 0.55/1.12 V, respectively for electrochemically polymerized PM1, PM2 and PM3. Detailed electrochemical properties can be seen in Table 3.1. Although there was an absorption peak in low energy region of each electrochemically polymerized monomers, they were assumed charged species resulted in electrochemical process and the higher energetic region was taken for calculation of optical bandgap.

Table 3.1. *Electrochemical and optical properties monomers M1, M2, and M3 and their electrochemically produced polymers.*

<i>Material</i>	E_{ox} (V)	E_{red} (V)	E_{ox}^{onset} (V)	λ_{max} (nm)	E_g^{op} (eV)
M1	1.05	0.50	0.92	-	-
M2	1.06	0.59	0.96	-	-
M3	1.00	0.53	0.88	-	-
PM1	0.34	0.22	0.10	430	1.24
	1.15	0.79		580	
PM2	0.40	0.33	0.13	345	1.62
	0.97	0.83		545	
PM3	0.55	0.48	0.30	335	1.64
	1.12	0.93		535	

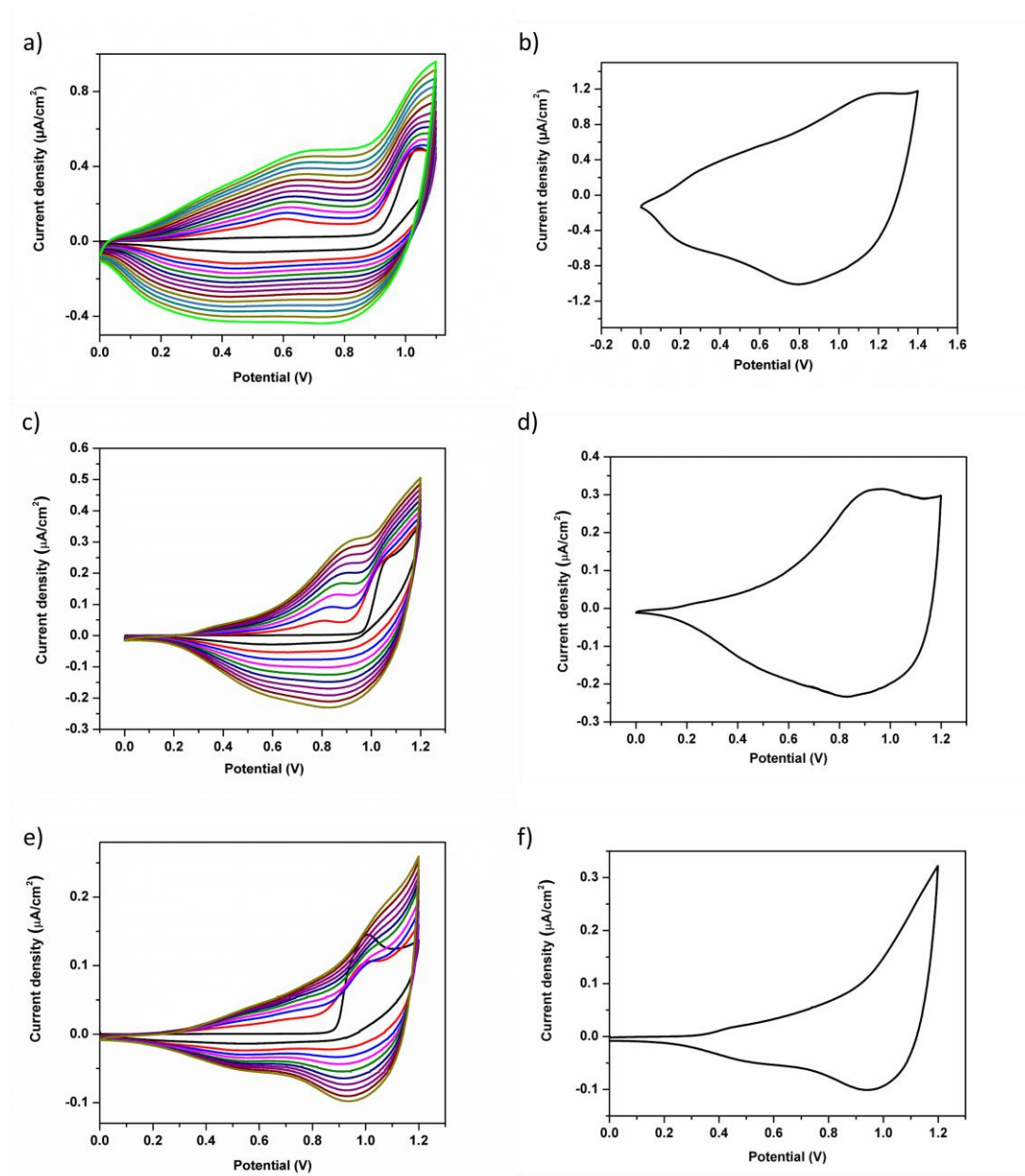


Figure 3.9. Electrochemical polymerization of M1 (a), M2 (c), M3 (e) and single scan voltammogram of PM1 (b), PM2 (d), PM3 (f) in DCM: ACN (5: 95) solution containing 0.1 M TBAPF₆ on graphite electrode.

In order to reveal electrochemical redox device feature, Uv-vis absorption spectra of polymers were taken for each increased potential as the polymer was oxidized systematically. As doing this, their colors were taken to reveal color parameters (L, a and b). These features were illustrated in Figure 3.10.

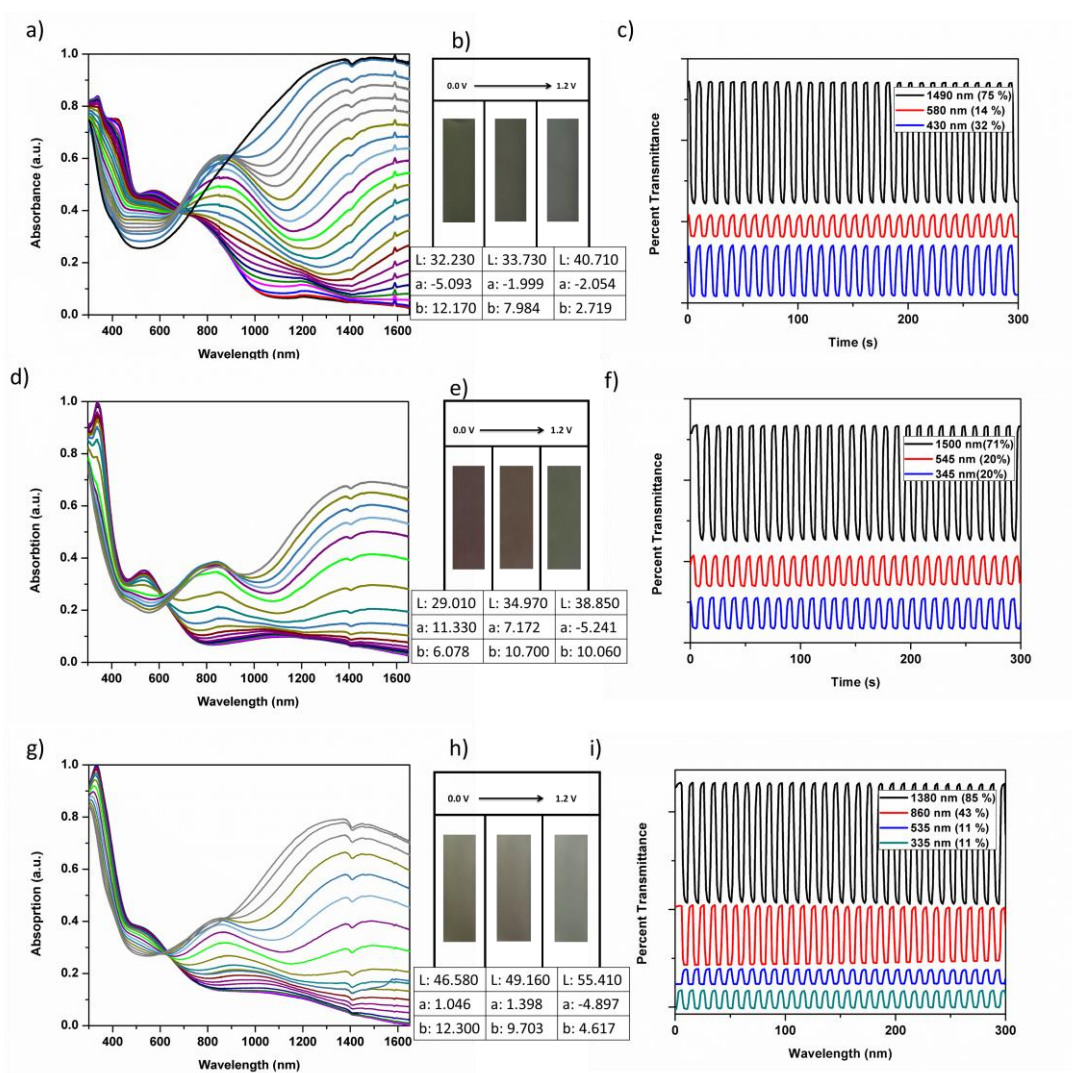


Figure 3.10. Spectroelectrochemical absorption spectrum of electrochemically polymerized M1 (a), M2 (d), M3 (g), visual appearance and L, a and b values of electrochemically polymerized M1 (b), M2 (e), M3 (h), kinetic performances of electrochemically polymerized M1 (c), M2 (f), M3 (i)

3.12. Optimization of experimental variables

Optimization studies have great importance to obtain sensitive biosensor. Parameters that affect the interaction between enzyme molecule and transducer should be optimized. Polymer thickness was determined by changing scan number during electropolymerization. As the polymer film gets too thick, the electron transfer between the enzyme and electrode may be hindered. On the other hand, unnecessarily thin polymer film cannot preserve features of good host. In order to optimize the

thickness of polymer layer, electrochemical polymerization was optimized in the manner of scan numbers like 5, 10, 20 and 40 scans. Response of prepared biosensors were measured by keeping other parameters constant and as shown in Figure 3.11, the highest signal was recorded with 10 scans.

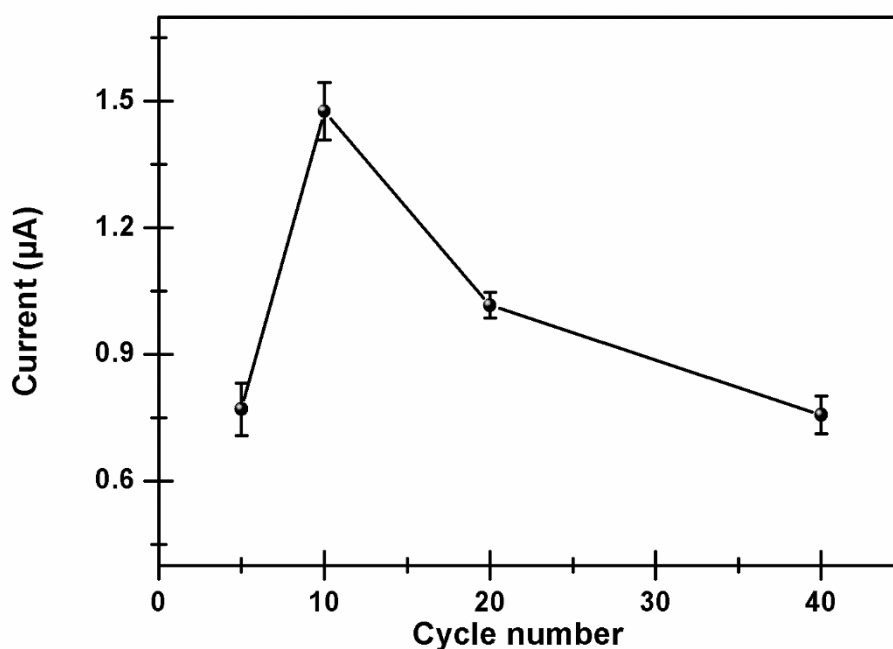


Figure 3.11. Effect of cycle number on biosensor response (Measurements were carried out at -0.3 V vs silver wire and 50 mM sodium acetate buffer in the presence of 0.125 mM catechol under ambient conditions. Error bars show the standard deviation (\pm SD) of three measurements).

Secondly, effect of amount of laccase was investigated to obtain optimum enzyme amount. Different amounts such as 4.36, 6.54, 10.9 and 13.08 Unit laccase were immobilized on polymer coated electrodes by keeping other parameters constant and optimum enzyme amount was recorded as 6.54 U laccase as shown in Figure 3.12.

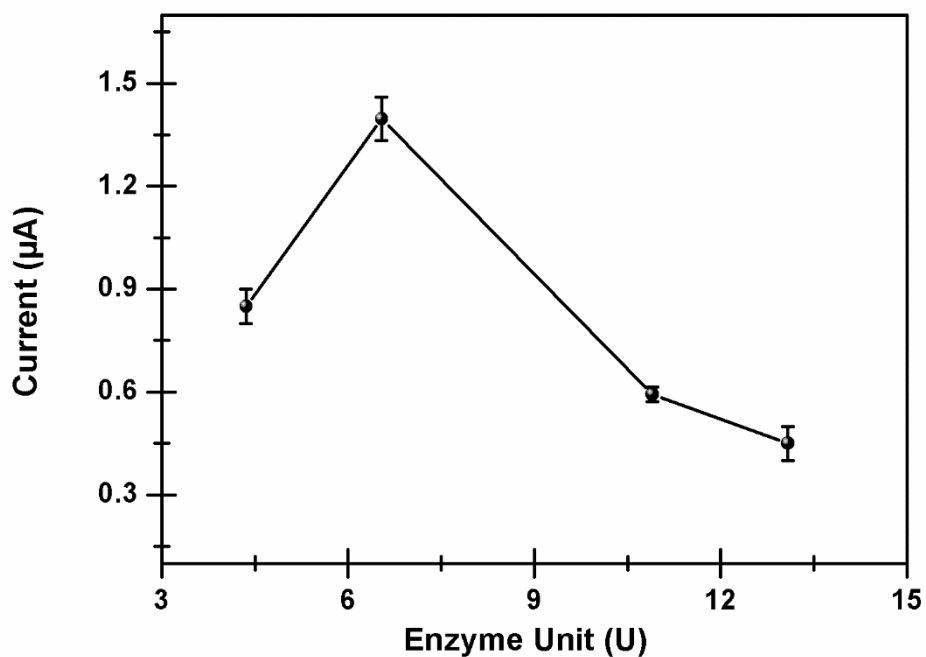


Figure 3.12. Effect of enzyme amount on biosensor response (Measurements were carried out at -0.3 V vs silver wire and 50 mM sodium acetate buffer in the presence of 0.125 mM catechol under ambient conditions. Error bars show the standard deviation (\pm SD) of three measurements

Finally, in order to enhance activity of enzyme, optimum pH was investigated between pH range of 4.5-7.5 by using 50 mM buffer solution. As shown in Figure 3.13, the best sensor performance was obtained with pH 5.5.

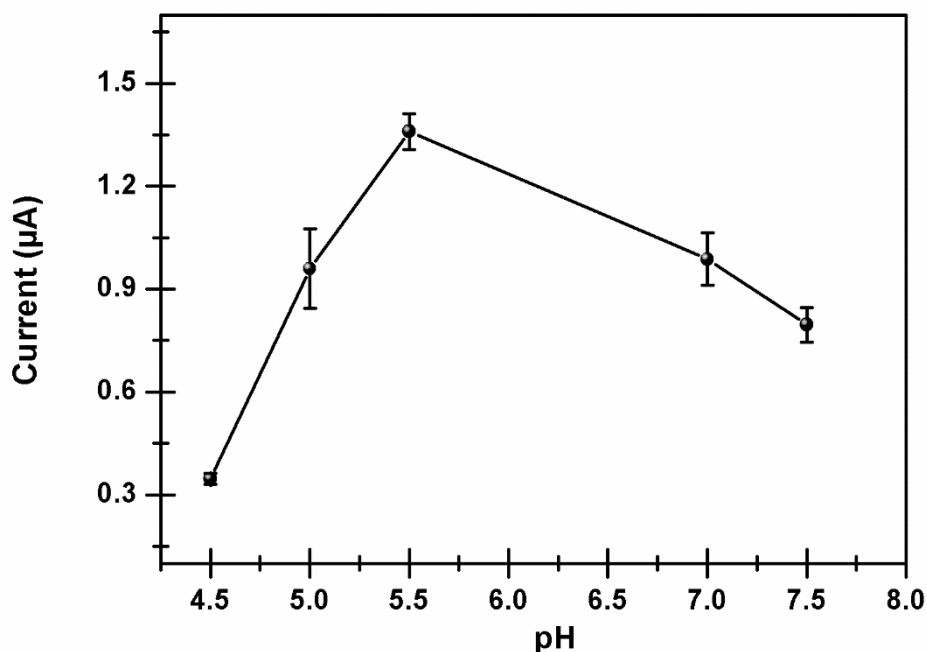


Figure 3.13. Effect of pH on biosensor response (Measurements were carried out at -0.3 V vs silver wire and 50 mM sodium acetate buffer in the presence of 0.125 mM catechol under ambient conditions. Error bars show the standard deviation (\pm SD) of three measurements).

3.3 Analytical Characterization

Calibration curve for pyrocatechol was constructed after all optimization studies were performed. Results revealed that linear range was in between 0.005-0.175 mM. Equation of calibration curve was found as $y=8.576x+0.276$ whose $R^2 = 0.994$ as shown in Figure 3.14. The limit of detection (LOD) was estimated according to equation $3S_b/m$, where S_b is the standard deviation of 3 measurements for the lowest concentration in the calibration curve, and m is the slope of the linear regression equation. The LOD and sensitivity values were calculated as 9.86 μ M and 153.6 μ A/mM.cm², respectively. The kinetic parameters found by various reactions catalyzed by immobilized enzymes while varying the concentrations of substrates at constant assay conditions. K_m is the measure of the affinity of the enzyme toward its substrate. K_M^{app} also refers to substrate concentration at V_{max} (217). Analytical parameters, K_M^{app} and I_{max} (instead of V_{max}) values for the amperometric biosensor

systems were calculated from the Lineweaver-Burk plot (217). Kinetic parameters (K_M^{app} and I_{max}) were calculated by using Michaelis–Menten enzyme kinetic and found as 0.018 mM and 1.16 μ A, respectively. Low K_M^{app} value indicates affinity of enzyme to its substrate. In Table 3.2, the comparison between constructed biosensors and previously reported studies were shown. Without any support material PM1 based catechol biosensor exhibited high sensitivity as 153.6 μ A/(mM.cm²) and low LOD value of 9.86 μ M. The moderate linear response range with high sensitivity of PM1 based laccase biosensor was comparably a better candidate for sensitive detection within a broad range between 0.005-0.175 mM.

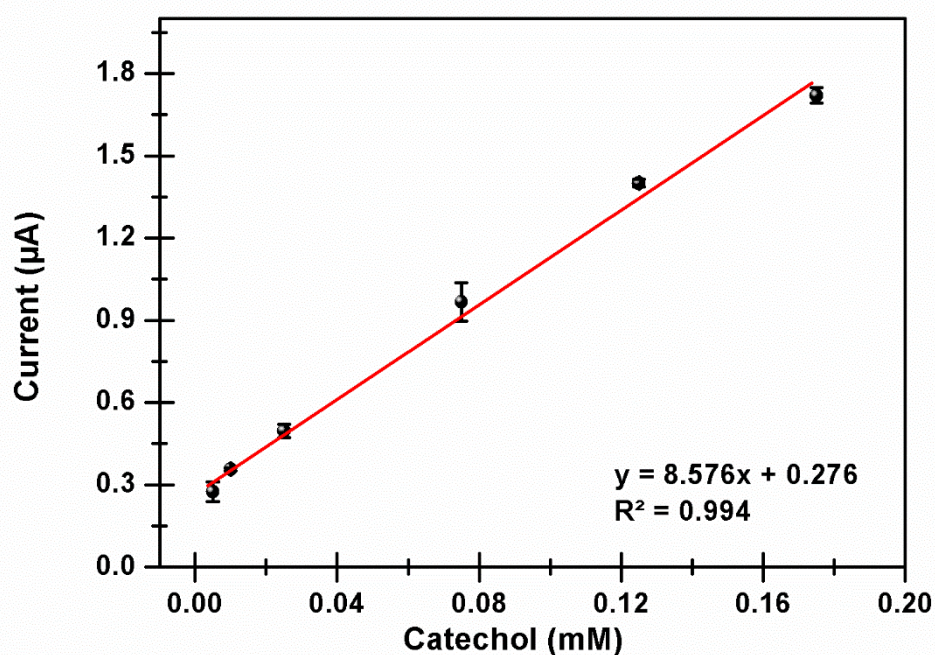


Figure 3.14. Calibration curve for catechol (in 50 mM acetate buffer, pH 5.5, 25 °C, - 0.3 V).

Table 3.2. Comparison of analytical parameters of other laccase biosensors in literature

Device	Linear Range (mM)	Detection Limit (μM)	Sensitivity ($\mu\text{A}/[\text{mM}\cdot\text{cm}^2]$)	K_m^{app} (mM)	Ref
MBTH/Nafion-SG/Lac.	0.500-8.000	330	NR	NR	(218)
Ant-PAA/Lac.	0.050-0.250	46	NR	NR	(219)
GC-rGO/GCE/Lac	0.0005-0.020	0.31	93	0.0934	(220)
Gold electrode/Lac	0.010-0.100	6	27.5	0.070	(221)
Cu/CNFs/Lac/Nafion/GCE	0.00995-9.760	1.18	33.1	0.0995	(222)
This work	0.005-0.175	9.86	153.6	0.018	

3.4. Conclusions

In this study, the best efficient catechol biosensor was constructed with the configuration of graphite electrode/PM1/Lac. The best sensor performance was obtained using only polymer without using any additional materials such as nanomaterials and nafion. There are multistep applications of similar methods for the preparation of laccase sensor in the literature. To the best of our knowledge, one step preparation of conducting polymer bilayer for catechol detection is rare in the literature and our results were very good when compared to the literature examples. Low K_M^{app} value as 0.018 mM corresponds to a high enzyme affinity toward the substrate. High sensitivity of $153.6 \mu\text{A}/(\text{mM}\cdot\text{cm}^2)$ and low LOD value of $9.86 \mu\text{M}$ within the broad range between 0.005 and 0.175 mM were superior characteristics of laccase based PM1 coated glassy carbon catechol biosensor. Further experiments will be also performed to investigate the interference effects of the substances in the water samples to the biosensor. This study was in preparation of publishing in the course of

newly designed polymer coated surface for laccase based catechol determination in water samples.

CHAPTER 4

FUSED STRUCTURES FOR ORGANIC SOLAR CELLS

4.1. Organic Solar Cells

Photovoltaic devices (PVs) are defined as the devices, which process sunlight energy and convert it into electrical power. Quantum theory is the mechanism behind the action of all types of PV devices. Light is composed of discrete packets of energy called photons. The photon energy is completely dependent on the frequency of the light. For the specific cases, the energy of photons is sufficient to excite electrons from valence band to conduction band in semiconductors. After excitation by a photon, the excited electrons (bound state) would quickly relax back to their ground state. Here before recombination occurs, if electrons and their positively charged vacancies called as holes and they are collected at opposite electrodes, then electrical current can be generated.

It is expected that various photovoltaic technologies will play an important role in the future because of their ability to directly convert sunlight into electricity. An urgent motivation for harvesting renewable and sustainable energy sources has resulted from the predictable shortage of fossil fuels and desiring of limiting CO₂ emissions. The widespread PV systems are based on traditional inorganic semiconductors, such as crystalline silicon; however, they are restrained by the relatively high cost.

Organic solar cells (OSCs) is a class of PVs. They are composed of organic semiconducting small molecules or polymers and convert incident sunlight into electrical energy. Significant differences between organic and inorganic photovoltaic devices are both physical principles of their operation and their methods of production. The following key advantages of OSC devices made them remarkable: low weight and flexibility of the PV modules, semitransparency, convenient integration into other

products, new market opportunities, like wearable PV, remarkably lower manufacturing costs compared to inorganic ones, low environmental impact (223).

The idea of organic solar cells dates back to the early 1950s (224). The imagination of the availability of organic materials as light absorbers comes from a simple observation. The plant photosynthetic systems use molecular systems to collect light and convert it into chemical energy. An important development in 1986 was made by Ching W. Tang, who published a 2-layer design showing a power conversion efficiency of approximately 1 % (225). Thermally evaporated two organic materials were composed of his devices. When one was absorbing light and generating an excited state as an electron donor, the other was pulling the electron acting as an acceptor. This donor-acceptor charge transfer principle would become a basis of organic solar cell designs. In 1992, the discovery of highly efficient photoinduced charge transfer between a semiconducting polymer and Buckminsterfullerene (C_{60}) by Sariciftci et al. was the another important development in the OSC history (226). This study was a pioneer for high-volume solution-processable organic solar cells. These two milestones contribute greatly to the development of successful OSC industry.

4.2. Organic Solar Cells Device Architectures

As a result of effort in increasing the efficiency of OSCs, different strategies have been applied for many years. For example, traveling of light to the longer distance in the active layer results in the higher percentage of absorbed photon towards higher efficiency (227). Therefore, improvements in OSCs structure have been a critical issue to make efficient OSCs.

4.2.1. Single Layer

The first OSCs were based on single layer type in which thermally evaporated molecular organic layers sandwiched between two metal electrodes as shown in Figure 4.1. Single layer cells are suffered from short exciton diffusion lengths and recombination of the excited charge carriers. This brings poor fill factor and low efficiency (228).

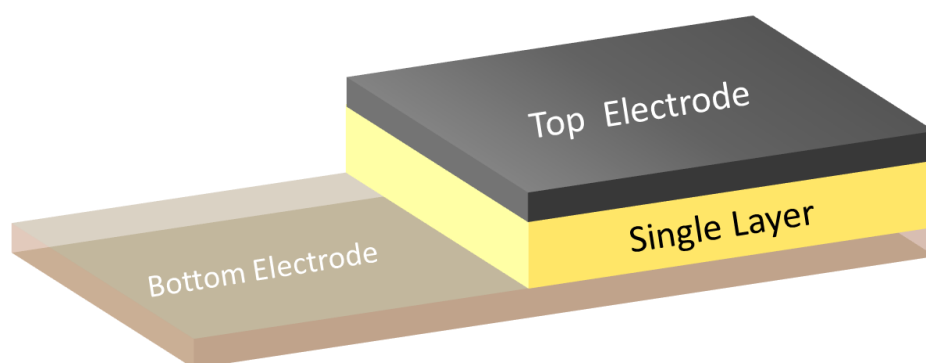


Figure 4.1. Device architecture of single layer OSCs

4.2.2. Bilayer

Introduction of an electron acceptor layer between the active material and the negative metal electrode generates two layer type OSCs (Figure 4.2). The advantage of this type on single layer one is improving both the exciton diffusion range and the poor shunt resistor. However, efficient exciton dissociation is still a critical problem in this design. Although the optimum length scale is in the range of the exciton diffusion length is typically known as a few tens of nanometers, the thickness of the active layer should be comparable to the penetration length (typically 80-200 nm) of the incident light. When charge carriers travel to their respective electrodes in pure n-type or p-type layers, the possibility of recombination are significantly increased (229). Since exciton dissociation caused by interfacial area is still a problem, bulk hetero-junction cell type is developed. As seen in Figure 4.3, electron donor and electron acceptor layers are in a mixture and wider interfacial area is obtained. This brings more efficient exciton dissociation and hence generation of polaron pairs anywhere in the bulk.

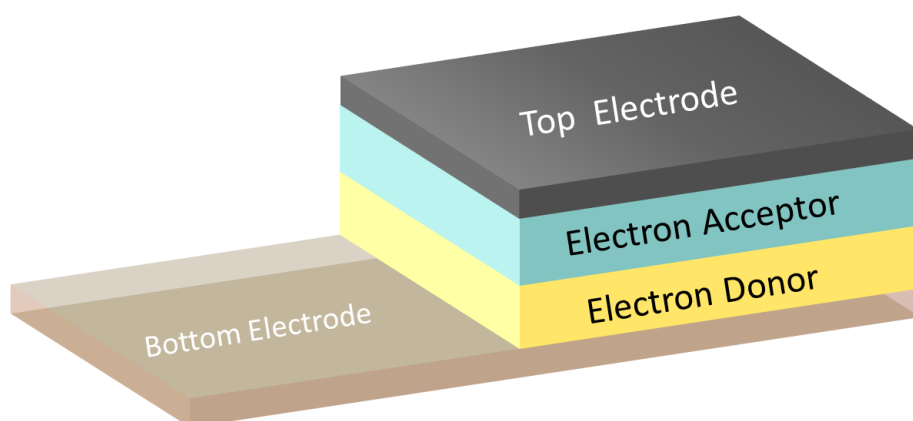


Figure 4.2. Device architecture of bilayer OSCs

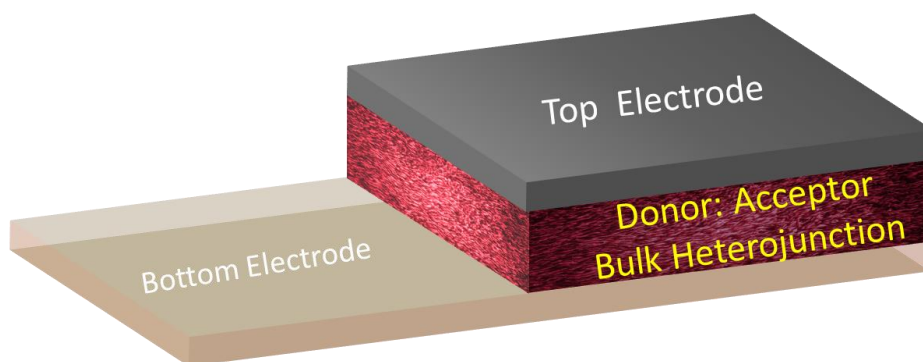


Figure 4.3. Device architecture of BHJ OSCs

4.2.3. Three-Layer Solar Cell

Addition of an intrinsic layer into the device structure (Figure 4.4) might cause the dissociation of excitons into free charges by the built-in electric field at the P-N junction. In this type, the purpose is increasing depletion region volume and effective light absorption area size. Due to the forming of intrinsic layer by co-evaporation of two different materials, its conductivity is reduced and the series resistance of devices increases. Moreover, the series resistance of the solar cell is inversely proportional to fill factor (FF), and thus increasing of intrinsic layer thickness would result in increasing of short-circuit current and decreasing of FF value. Therefore, the intrinsic

layer is a mixture of different materials that makes it easier for carriers in the intrinsic layer (228).

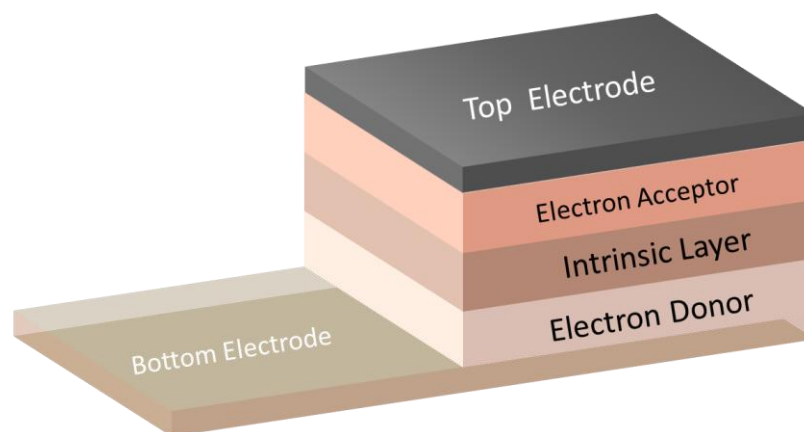


Figure 4.4. Device architecture of three-layer OSCs.

4.2.4. Stacked Organic Solar Cells

Figure 4.5 shows a more efficient structure which is achieved by stacking two cells on top of each other. Since two separate single PV cells are joined by a transparent electrode, the overall absorption width of the solar cell is increased. The fact that this stacked type is the sum of two single cells in series cause improving the open circuit voltage and the short circuit current (230).

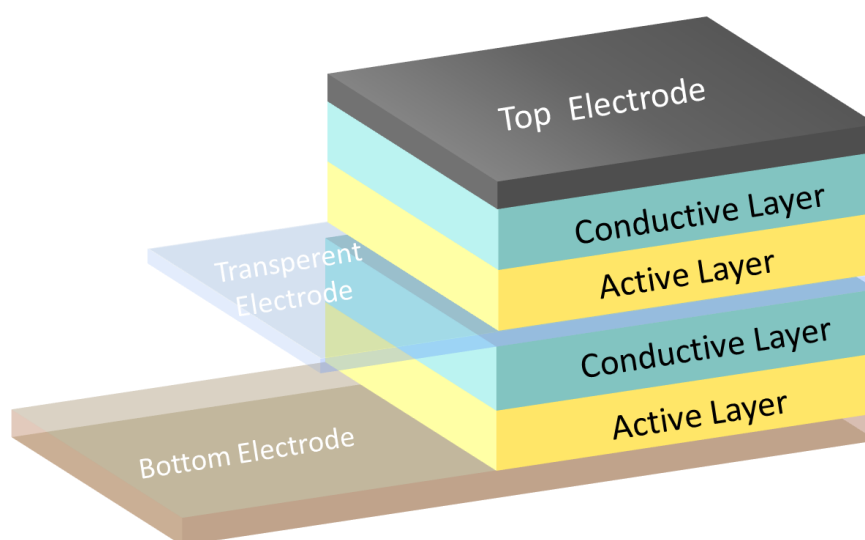


Figure 4.5. Device architecture of stacked OSCs

4.2.5. Tandem Organic Solar Cells

A tandem cell is generated as the improved version of the stacked cell because in this type different active materials are selected for different cells of the device as shown in Figure 4.6. Active polymers with different absorption characteristics are connected to provide a wider range of the PV spectrum and increase the photon absorption. When the light is not absorbed in the bottom device, it can be further absorbed on the top cell. In the case of using high and low bandgap materials, the light should first crash the absorber with the higher bandgap.

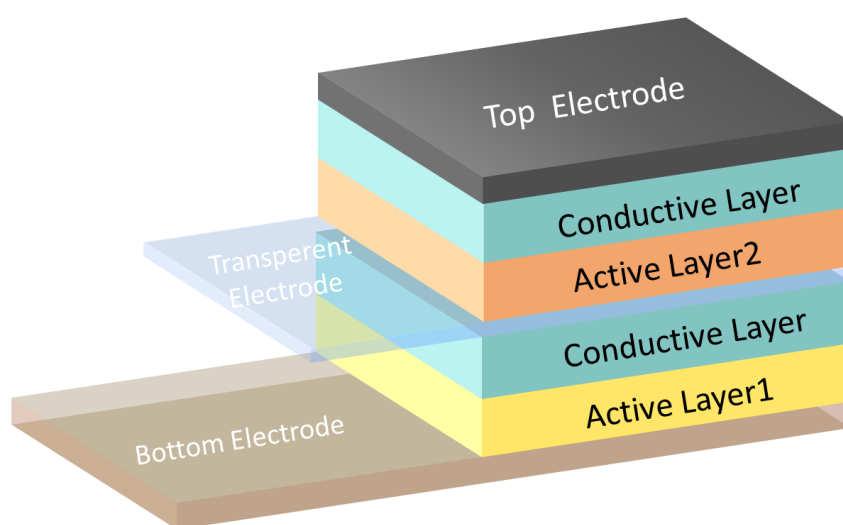


Figure 4.6. Device architecture of tandem OSCs

4.2.6. Bulk Heterojunction Solar Cells Device Configuration

In this thesis, the main interest was the construction of bulk heterojunction type organic solar cells. In this type, a layer of intermixed donor and acceptor moieties was sandwiched between two electrodes and recombination of excitons is reduced than that of single layered and simple bilayered solar cells. Thus, the performance of solar cells is greatly enhanced. Conventionally, transparent conductive oxide namely indium tin oxide (ITO) coated glass substrate has coated a layer of PEDOT:PSS. On top of that, sun absorbing active layer- donor acceptor mix- was coated. Then, a top

contact electrode was coated where in between a top contact and active layer a thin layer of LiF was inserted.

As OSCs possess the inverse operational principle of OLEDs where electrical current is converted into a light, OSCs converts light into electricity and general characteristics of the device are shaped according to absorb light and convert into electricity. Yet main purposes of materials like TCO, substrate, electrodes remain similar as in the case of OLEDs. The detailed device structure of bulk heterojunction OSCs can be seen in Figure 4.7.

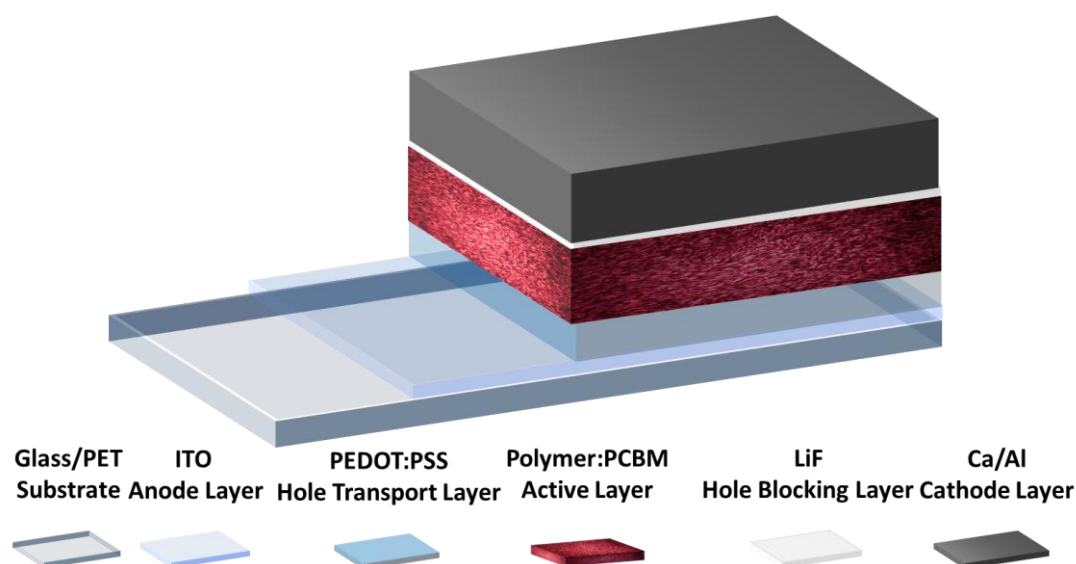


Figure 4.7. Detailed device architecture of BHJ OSCs

4.2.6.1. The Substrate

As a substrate, generally glass or plastic is used in the OSC device. Although glass is preferred in OSC research due to its low cost, stability, and extremely effective barrier properties, flexible plastic substrates such as poly (ethylene terephthalate) (PET), poly (ether sulfonate) (PES), and polycarbonate is used in the laboratory (231). Moreover, plastic substrates are more useful for solution processing high volume production via roll-to-roll methods.

Suitable substrates for organic PV devices should meet some conditions such as low-cost, chemical and thermal stability, mechanical and environmental stability, with good barrier properties to oxygen and water, and high optical transparency.

The substrate which is one of the electrodes in OSC is coated with a transparent conductive oxide (TCO). Due to demonstrating a good balance between transparency and conductivity, commonly indium-doped tin oxide (ITO) is chosen as TCO. Preparation technique and surface treatment/cleaning can vary the work function of ITO which is in the range of 3.7 and 5.1 eV (232). It is known that treatments with oxidizing agents such as oxygen plasma raise the work function (233).

Commonly, PEDOT:PSS, a polyethylenedioxythiophene doped with poly(styrene sulfonate) is coated on ITO electrode as additional layer in solution processed OSCs. The purpose of its application is to decrease the ITO surface roughness and provide a surface with a more defined work function (234).

4.2.6.2. The Active Layer

Active layer for solution-processed OSC devices is typically composed of a mixture of conjugated polymer and a small-molecule component, such as P3HT:PCBM. In the BHJ type cells, an interpenetrating network of donor and acceptor parts are cast on substrate. In the donor acceptor solution, changing of concentration, a solvent of the mixture, coating conditions would affect phase segregation between the donor and acceptor for charge generation (235). Creating of the high density of donor/acceptor interfaces on the nanoscale of 10–20 nm results in producing excitons by light absorption anywhere in the BHJ and increase the possibility of reaching the donor/acceptor interface to be dissociated and be transported without significant loss through recombination and collected by the electrodes.

When polymerization is achieved with controlled regioregularity, polymers are produced with repetition of one pattern and this leads to higher charge carrier mobilities. Existence of alkyl chain on the backbone affects the morphology of the active layer film and the mobility.

Controlling the phase separation during the film formation can improve the morphology of the BHJ blend. There are several parameters which affect the morphology of the BHJ blends such as solvent casting (viscosity, boiling point, interaction with substrate), donor: acceptor ratio, chemical additives, donor: acceptor concentration in solution, phase separation control by thermal and/or solvent annealing, the molecular structure of the materials.

Due to solubility of the donor and acceptor species in organic solvents and miscibility in each other is affected by their molecular structures, this directly plays a critical role in morphology. Moreover, solvent type affects both solubility and drying time during film forming. Post-fabrication with thermal annealing at high temperatures increases the crystallinity within the phase-separated networks which result to enhance charge transport to the electrodes and increase efficiency.

4.2.6.3. The Top Contact

The deposition of a top metal contact is a final step of OPV device fabrication. Generally, the application of the top electrode is achieved by vacuum deposition. Plastic foil precoated a metallic film (236) or a layer of conductive nanotubes (237) could be rarely used for this purpose. The top metal is commonly chosen according to its work function to achieve Ohmic contact with the typically an n-type active layer. It is known that the work function of metals is inversely proportional to its work function. Low work-function metals are reactive and can easily be exposed to environmental degradation. Therefore, more stable metals with high work function, e.g. aluminum, are often preferred as the top contact. Moreover, it is known that ultrathin LiF interlayer could be added on top of organic layer so that Al electrode gains low work function due to the formation of charge transferred species containing the Li⁺ cation during Al deposition.

4.2.6.4. Operating Principle of Bulk Heterojunction Solar Cells

As shown in Figure 4.8, the general working principle of bulk heterojunction solar cell commences with the absorption of light. Photoexcitation of the donor polymer

generates Coulombic bound electron hole pairs namely excitons. They diffuse to the interface of donor and acceptor. Before excitons recombine, they can be separated into free charge carriers as holes and electrons. These free charges can be collected at the respective electrodes by the help of internal electric field caused by the difference in the work function of anode and cathode. Thus electricity is generated at outer circuit.

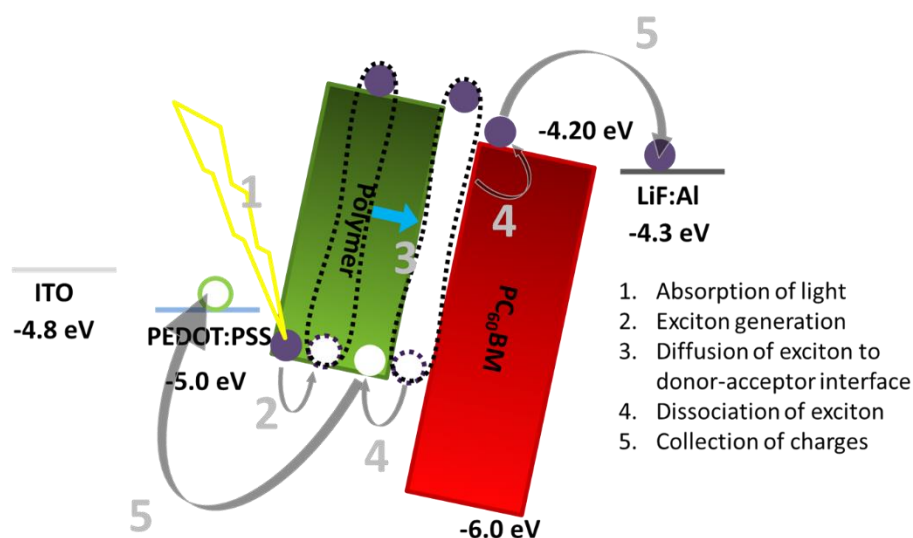


Figure 4.8. Operational processes of BHJ OSCs

Since the life time of exciton is short, the distance between 5 and 14 nm, it should be separated for efficient photocurrent generation (238–242). Bulk heterojunction solar cells form a bicontinuous network and create two channels to collect holes in the donor domain and electrons in the acceptor domain of donor acceptor matrix. These channels succeed in the efficient charge collection.

One of the major breakthroughs is the discovery of usage of fullerene:polymer composite for efficient charge transfer for bulk heterojunction solar cells (226). Low lying LUMO is thermodynamically favored to accept an electron from a donor (243). Triply degenerate LUMO provide unique negative charge stabilization up to six electrons. Fast kinetic photoelectron transfer on a time scale of 45 fs enables the charge separation quantum efficiency to become unity (244).

4.3. Characterization of Organic Solar Cells

J-V (short circuit current density vs voltage) and *P-V* (power vs voltage) curves are used to investigate the performance of solar cells and modules (245–249). Two different models have been employed to describe different characteristics. The first structural model describes the mechanism and impact of photovoltaic effect. Charge distribution, efficient depth of the cell and some more can be extracted by that model. The other model investigates the basic parameters for performance like current, voltage, power. Although there are various types of photovoltaic cells such as organics, inorganics, perovskites, dye-sensitized, multijunction solar cells and their physical structures, needs and functions are different from each other, almost any photovoltaic cell can be modeled as an electrical circuit. Yet this thesis slightly covers some of these models for brief introduction. Five key parameters; short circuit current J_{sc} , shunt resistance R_{sh} , series resistance R_s , open circuit voltage V_{oc} , and ideality factor A , are extracted (248, 250, 251). Besides them some important factors such as photocurrent generated in standard test conditions I_{ph} , dark current (leakage current) I_0 and cell temperature T are investigated (245, 252–254). The nature of using an electrical model enables to usage of electrical charge q (1.6×10^{-19} C) and Boltzmann constant K (1.38×10^{-23} J/K) (245). Some parameters can be extracted analytically/theoretically. Yet there is a need for experimental data for others like I_{ph} and A .

4.3.1. First Generation Model

Wafer-based crystalline silicon solar cells (p-n junction diode), which cover the 90 % of total solar cells, were described in a single diode model until 2013 (255).

In general, the characteristics of solar cells are determined by using the Shockley diode equation (256). This approach assumes a solar cell as a light sensor, which converts absorbed light into electric current. Also, there is an anti-parallel diode which manages the direction of the current which can be seen in Figure 4.9. Nonlinear current voltage

relation is obtained by the Kirchhoff law and used to evaluate implicit parameters (255).

$$I = I_{ph} - I_0 \left[\exp\left(\frac{V}{AV_T}\right) - 1 \right] \quad (1)$$

Where; V: bias voltage

I_0 : leakage current

I_{ph} : photocurrent

A: ideality factor

V_T : thermal voltage (257)

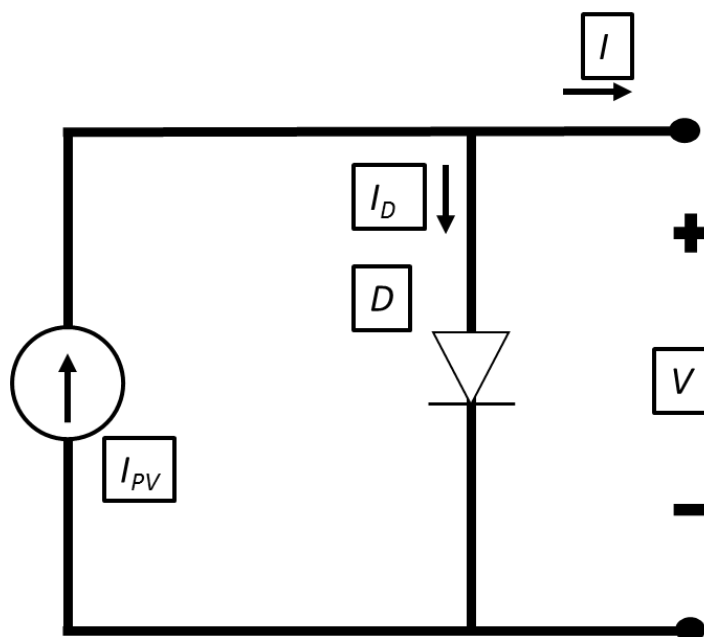


Figure 4.9. The equivalent electrical circuit of a single solar cell.

Besides these main five parameters, there are two hidden internal factors to affect the current such as bypass current between two junctions (Figure 4.10). A shunt resistor is the first one. It is caused by the malformation and anomalies in the p-n junction and reduces the current. The second one is the all-external resistance. Because it affects the output current due to the resistance of connections between solar cells and other

part of the electric system, it is represented as R_s (series resistance). So that Eq 1 is modified to Eq 2 (258).

$$I = I_{ph} - I_0 \left[\exp\left(\frac{V}{AV_T}\right) - 1 \right] - \frac{V_T + IR_s}{R_{sh}} \quad (2)$$

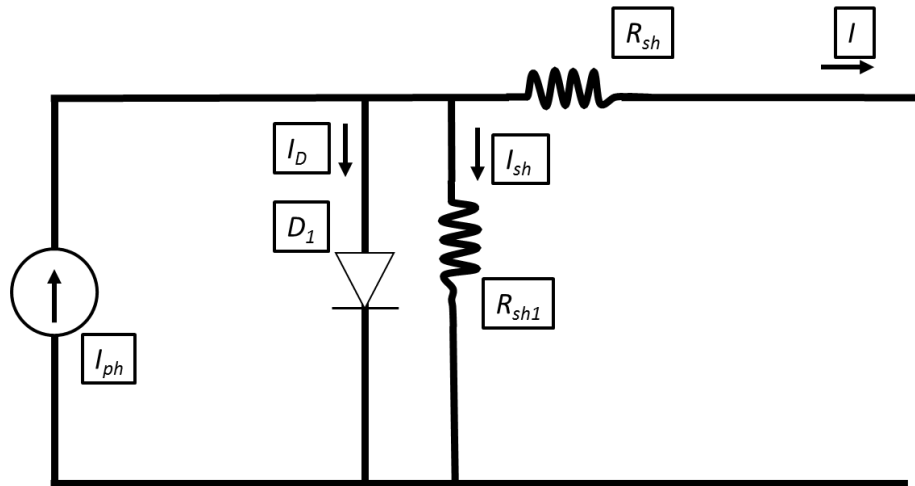


Figure 4.10. R_{sh} and R_s in the equivalent circuit of a single solar cell

The experimental results match well with the data provided the model (259). Yet it lacks the effect of time. Real world applications loss the current as time passes due to Joule heating.

4.3.2. Second Generation Model

Since the first generation model represents the ideal case, diffusion current and recombination current is inserted to an electrical circuit model for the second generation. Diffusion current due to the propagation of charge carriers is related to a decrease in output current as recombination of mobile charge carriers occurs (260). This two-diode model is shown in Figure 4.11.

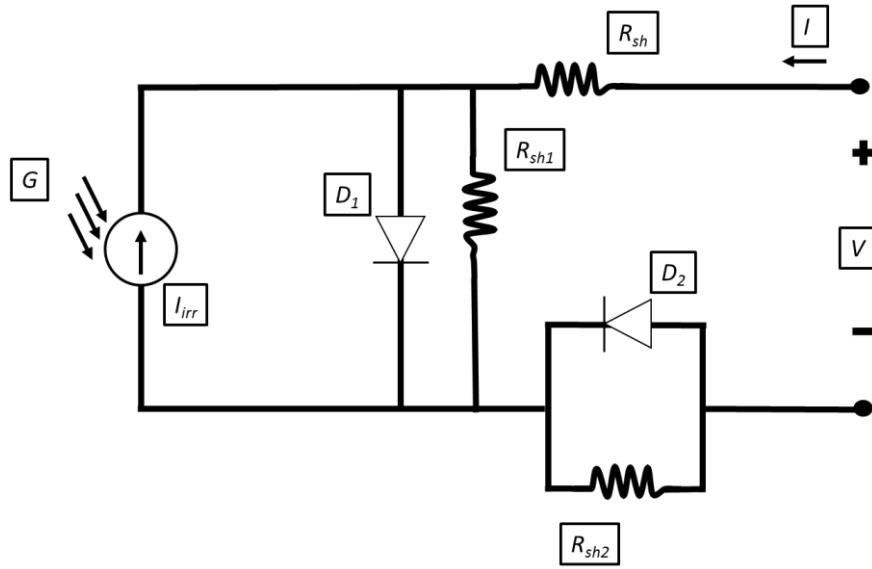


Figure 4.11. The two-diode model as an equivalent electrical circuit

For OSCs, the single or simple two-diode model is not suitable due to a strange characteristic of current voltage curves. The curve sometimes represents a kink (S-shape) (261) and it cannot be fitted to the model seen in Figure 4.11 (262). Within a limited voltage window, the reverse second diode model well matched with the experimental data. Yet its strong dependence on computation time and in forwarding bias causes to increase the current after the kink. The model represented with the Figure 4.12 precisely solves the problem for some limited cases where W is the Lambert function (263) and well fits to the experimental data (264). Moreover, considering the shunt resistance between D_2 and D_3 in the modified three diode model based on Figure 4.12 can give appropriate fit for OSCs. The Eq. 1 is then transformed into a complicated one as Eq. 3 (265):

$$I = \frac{V - \left[(I + I_{ph} + I_{01})R_{sh1} - A_1 V_T W \left(\frac{I_{01} R_{sh1}}{A_1 V_T} \exp \left(\frac{(I + I_{ph} + I_{01}) R_{sh1}}{A_1 V_T} \right) \right) \right]}{R_{sh2}} - I_{02} \left[\exp \left(V - \left[(I + I_{ph} + I_{01})R_{sh1} - A_1 V_T W \left(\frac{I_{01} R_{sh1}}{A_1 V_T} \exp \left(\frac{(I + I_{ph} + I_{01}) R_{sh1}}{A_2 V_T} \right) \right) \right] \right) - 1 \right] - I_{03} \left[\exp \left(V - \left[(I + I_{ph} + I_{01})R_{sh1} - A_1 V_T W \left(\frac{I_{01} R_{sh1}}{A_1 V_T} \exp \left(\frac{(I + I_{ph} + I_{01}) R_{sh1}}{A_3 V_T} \right) \right) \right] \right) - 1 \right] \quad (3)$$

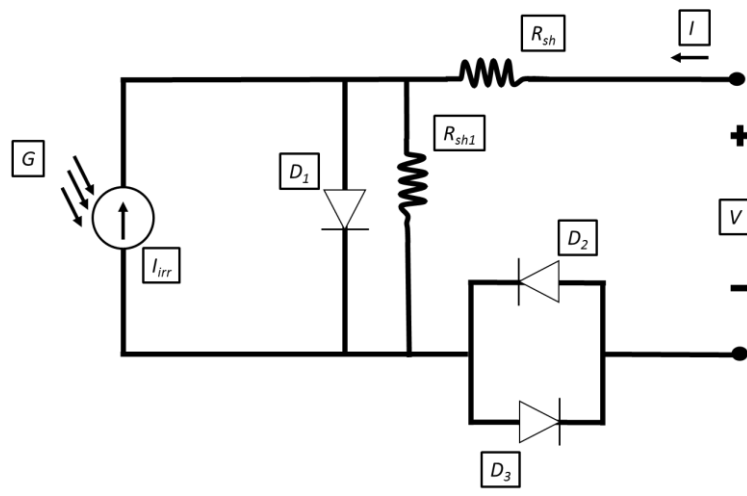


Figure 4.12. The reverse 3-diode model

4.4. Photovoltaic Performance

Since above mentioned calculation need expertise in theoretic calculations, being an experimental chemist and for the simplicity basic characteristics of solar cells were examined in this thesis such as J_{sc} (short circuit current density), V_{oc} (open circuit voltage), FF (fill factor), $\% \eta$ (% power conversion efficiency) (see Figure 4.13).

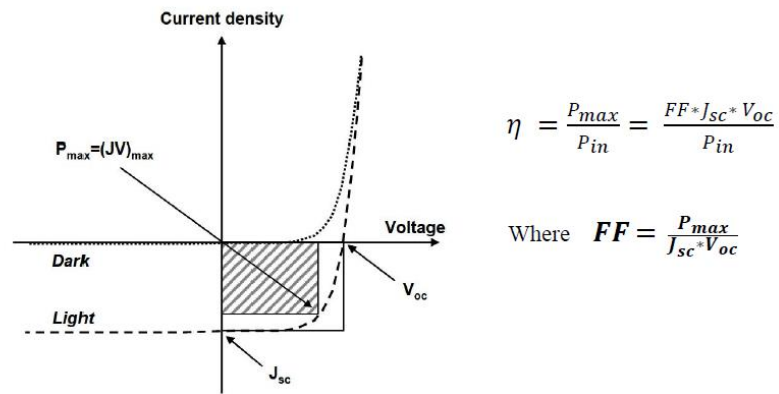


Figure 4.13. Photovoltaic performance from J-V curve.

The J_{sc} , found at a point where device generates zero bias, is directly related with the E_g , spectral coverage and absorption coefficient of a material to count the conversion of absorbed light into electrical current. Incomplete absorption, recombination mechanism, loss mechanism due to inappropriate donor-acceptor morphology are some of the parameters that affect negatively.

The V_{oc} is the maximum potential can be gathered from a device. It mainly depends on the difference between the work functions of electrodes. Yet, for a specific case where the energy levels of materials of the active layer are located within these ranges, then V_{oc} is limited to a value of energy difference between the HOMO level of the donor and the LUMO level of the acceptor material. Poor contacts or chemical interaction between electrodes and inner layers of the device and severe recombination processes can decrease the V_{oc} . FF is a parameter for a device to show how ideal the device operated. The ideal case is $FF=1$ where R_{sh} and R_{sh} are both neglected. To simply show the performance of a device, final parameter is maximum power conversion efficiency gathered from a device, which is denoted by η .

4.5. Features of Fused Structures

4.5.1. Band Gap Engineering and Related Parameters

As OSCs converting the sunlight directly into the electrical energy, absorption of sunlight holds the priority. AM 1.5 G is a simulation of sun light found at the surface of the earth, and for better performance the OSCs devices should absorb as much light as possible. A great portion of the light is gathered at visible and near infrared (NIR) regions. Thus, it is important to find and employ active materials possessing a low bandgap of 1.4 eV for successful absorption.

As the theoretical investigation by Shockley and Queisser reveals that the optimum bandgap for photovoltaics is around 1.3 eV (266). Several investigations were made with donor polymers; whose bandgaps are between 1.35 and 1.65 eV, to achieve more than 10 percent power conversion efficiencies (267). There is recently explored a new approach non-fullerene acceptors with an efficiency over 16% (268) for organic solar cells. Moreover, for tandem organic solar cells with an efficiency above 17% (269), and double bulk heterojunction solar cell configuration reveals the opportunity of over 25% up to 30% efficiencies (270). This thesis focuses on fullerene based bulk heterojunction OSCs. Since the need for low band gap material is important for all

abovementioned studies, one should consider the bandgap and energy levels of the newly designed small molecule/polymer for photovoltaic applications.

Several ways of decreasing the bandgap of the conjugated polymers have extensively investigated by scientists over the years. One important method is developing a D-A combination. An interesting consequence of this type of polymer is the existence of the quinoidal nature of the polymer backbone. Although it is not unique to those, it is shown as a common feature. Preference of adoption to quinoidal structure exhibits a lowered bandgap for certain polymers. Hence, quinoidal form enhances the planarity and therefore more efficient π -electron delocalization is achieved. For example, thiophene possesses a lower resonance energy 1.26 eV and benzene has higher resonance energy of 1.56 eV (Figure 4.14). Moreover, the higher degree of aromaticity of benzene causes the high bandgap of ca. 3.2 eV for polyphenylene whereas polythiophene possesses 2 eV bandgap with lower aromaticity. In the case of fusion of benzene with thiophene, the tendency of thiophene backbone is adopting the quinoidal form to keep the benzene aromatic due to its higher resonance energy. Competing aromaticity between different rings results in stabilization of the quinoidal form with a value of 2.4 kcal/mol (271) with respect to its aromatic form. Strong stabilization energy of benzene with respect to thiophene results in a low bandgap polymer about 1.1 eV (272). Similar effect was observed in other examples such as; polythieno[3,4-*b*]pyrazine (band gap= 0.95 eV) and poly(thieno[3,4-*b*]thiophene) (band gap= 0.8–0.9 eV) (273).

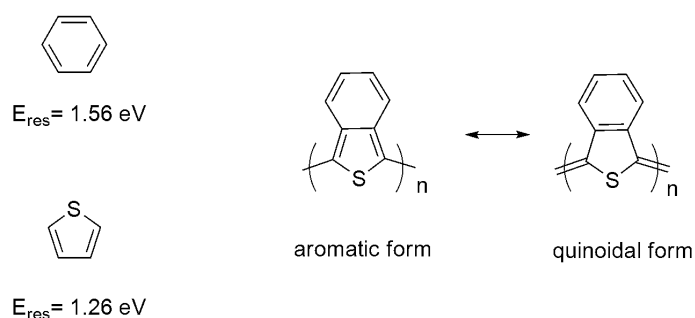


Figure 4.14. Illustration of aromatic and quinoidal form

It is not always a good way to obtain low bandgap polymers via fusion of aromatic rings together. In the study of Zhen and coworkers, a series of ladder-type benzodithiophene (BDT) structures were synthesized (274). It was found that increasing the number of fused BDT from five to nine rings (PTR5, PTR7, and PTR9 in Figure 4.15), LUMO level decreases and eventually goes beyond LUMO of acceptor moiety in the polymeric backbone. The intermolecular charge transfer between D and A was inhibited and less quinoidal character was observed. As a result, the polymer with highly fused structure exhibited a blue shift in the absorption and decreased power conversion efficiency.

In the light of these facts, monomer conjugation should be limited not to influence the energy penalty to favor the aromatic form instead of the one of quinoidal.

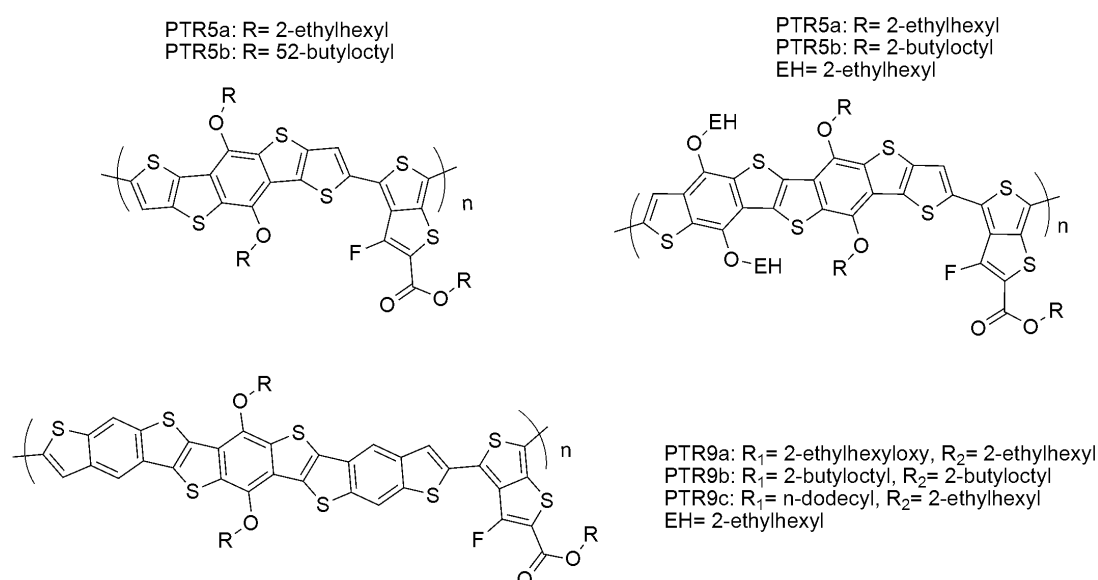
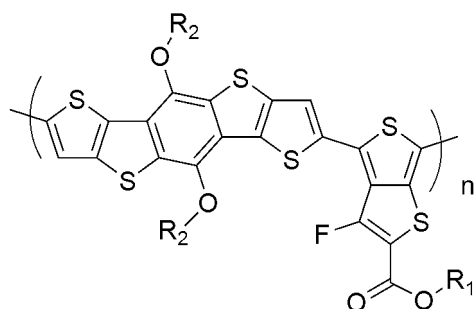


Figure 4.15. Chemical structures of PTR based polymers

A PTB7 analogue, PTDBD was synthesized to extend the BDT with two fused rings. It was aimed to enhance the delocalization of holes, which results in reduced Coulombic attraction of excitons. Thus, charge separation would be facilitated and OSC device performance would be enhanced. The fused molecules ensure the decrease in solution processability of polymers. Thus, inevitably the need of bulky side chains is popped up. However, the further increase of the bulkiness of the side

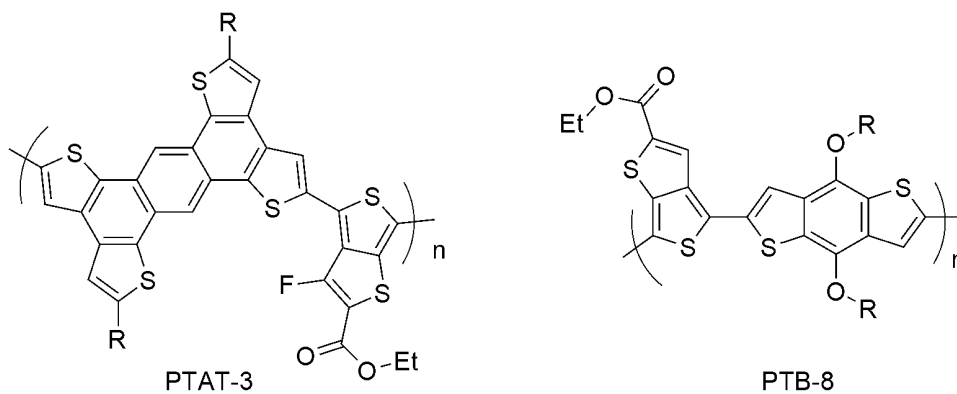
chain from PTDBD2 to PTDBD3 increased the distance of crystalline polymer domains (Figure 4.16). Thus, the decrease in charge transport properties reduces performance.



PTDBD2: R₁= 2-butyloctyl, R₂= 2-butylhexyl
 PTDBD3: R₁= 5,9-diethyl-7-tridecyl, R₂= 2-butylhexyl

Figure 4.16. Chemical structures of PTDBD based polymers

2-D conjugation is an important feature to enhance the intermolecular charge transport properties via π - π stacking. He and coworkers synthesized the PTAT-3 and PTB-8 with the same bulky alkyl chain (Figure 4.17) (275). Although the common drawback is poor solubility, the study revealed the consequence of the larger the conjugation the better the performance.



PTAT3 : R= 2-butyloctyl,
 PTB8: R= 2-butyloctyl

Figure 4.17. Chemical structures of PTAT-3 and PTB-8

4.5.2. Morphology Engineering and Related Parameters

Recently discovered non-fullerene acceptors have drawn serious attention (276–279) and also in particular for highly efficient (10.2%) semitransparent OSCs (280). Beside fullerenes drawbacks including, low absorptivity in the high energetic region, production and purification cost, relatively large voltage loss and morphology related stability issues; non-fullerene based acceptor possesses an ability to tune the absorption, energy levels and as well as morphological properties. Thus, non-fullerene acceptors are promising materials for the future of photovoltaics.

Although the necessity of the morphology of polymeric donor is vital for high performance OSCs, the morphology of acceptor (fullerene or non-fullerene) plays an important role. Thus, morphology should be tuned. Early investigations of perylene diimide (PDI) based non-fullerene acceptors revealed large coplanar molecules with high crystallinity. As a result of excessive aggregation in a solid state, phase separation has reached to the micrometer size (281). To decrease the intermolecular interactions and thus domain size, four PDI moieties were attached to a congested core. Although the small domain size obtained as highly twisted molecular structure inhibit the intermolecular π - π stacking, the twisting rate had inverse proportionality effect on device performance (282, 283).

Another study compared the differences between the tetramer of PDI with fused and non-fused non-fullerene acceptors (284). Beside electronic advantages of fusion such as better charge transport ability, higher electron mobility, upshifted LUMO level thus high V_{oc} , high short circuit current density because of enhanced absorptivity/absorption coefficient, morphology also had drastic effects on performance. Due to the ability of a generation of conformational isomers, fused TTB-PDI-4 was susceptible to deteriorate the intermolecular packing and charge transport network (285, 286). Whereas, fused FTTB-PDI-4 exhibited slightly larger coherence than the other one (1.5 vs 1.3 nm) and reasonably small domain size maximized the charge mobility; thus, the device performance was enhanced one more time. While the best

performance of un-fused PDI derivative was 7.11%, for the fused FTTB-PDI-4 it was increased to 10.58 % with the minimum V_{oc} loss 0.53 V among of best values of its time.

4.6. Aim of This Study

In this chapter, there are benches of polymers. These polymers consisting of fused structures in their polymeric backbone were synthesized and characterized for the photovoltaic applications.

In the first bench of polymers, donor BDT core was utilized with TPD and derivatives of benzo-2,1,3-chalcogenadiazoles to optimize optical and electronic properties of the literature polymer for enhanced power conversion efficiency. Fused BDT and TPD moieties were responsible for high performance OSCs, while derivatives of benzo-2,1,3-chalcogenadiazoles affect optical and electronic properties. As going down through the 6A periodic table elements, the effect of chalcogens was investigated. Altering the acceptor characteristics of benzochalcogen via one atom modification from O to Se, not only HOMO but also most dominantly LUMO of random conjugated polymers were aimed to be tuned. Differentiating the substituent directly bonded to the polymeric backbone, the effect of electron donating and electron withdrawing moieties was investigated. Chemical structures of polymeric compounds can be seen in Figure 4.18. Fine tuning of the energy levels as well as absorption profiles of the polymers were successfully achieved. Finally photovoltaic performances of four different polymers were investigated under AM 1.5 G illumination.

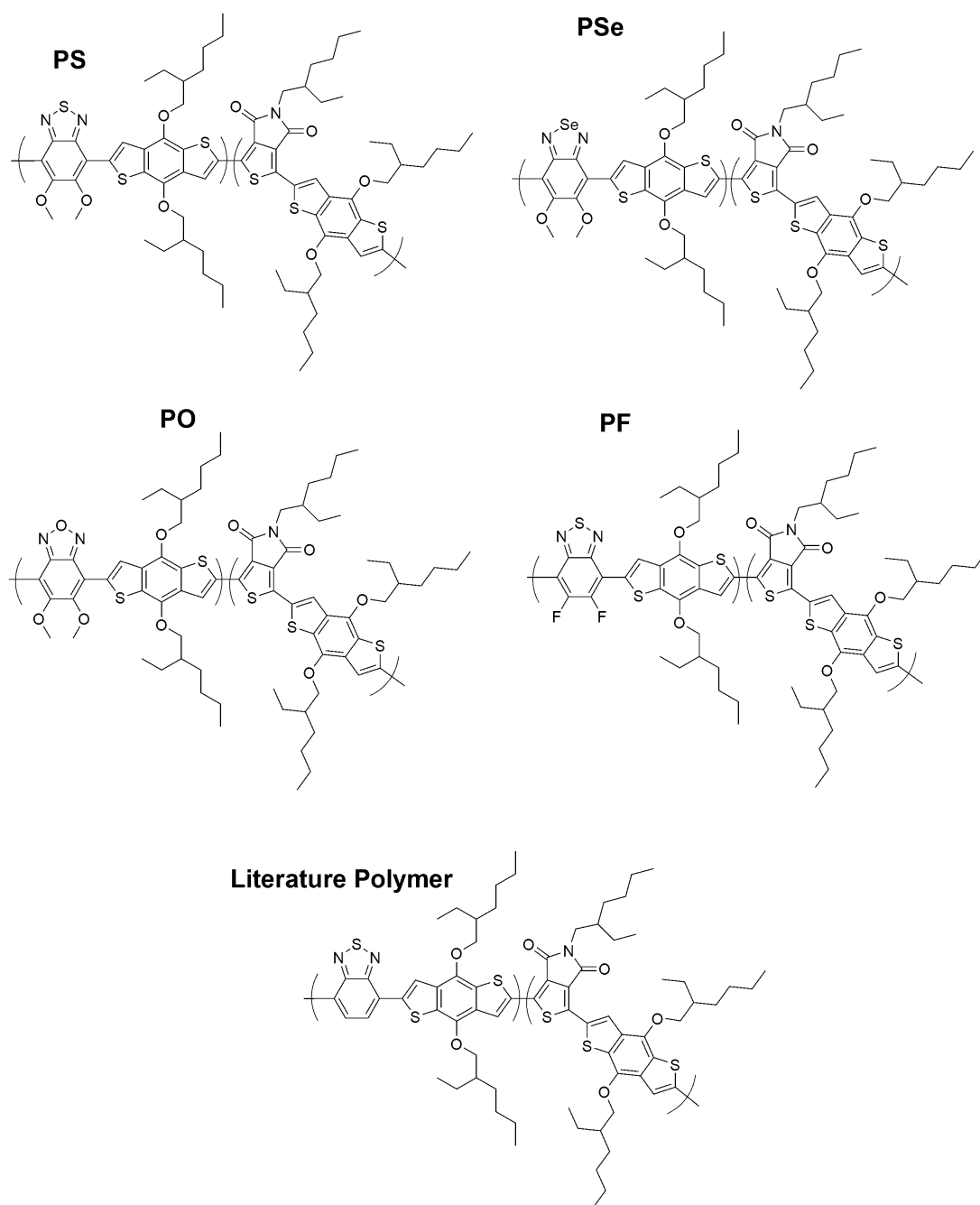


Figure 4.18. Chemical structures of PS, PSe, PO, PF and literature polymer

In the second part, highly fused 11H-indeno[1,2-*b*]quinoxalin-11-one containing polymers were synthesized (Figure 4.19). The literature polymer with long alkoxy substituted fused moiety was used for the first time and there is only a single application in literature for OSCs to the best of our knowledge (287). To decrease the

HOMO energy level of literature example, alkoxy solubility enhancing side groups were removed and to acquire the solution processable polymer, 3-hexylthiophene was incorporated. This π -bridge incorporation was also supposed to enhance the conjugation length to reduce the bandgap of the conjugated polymer. Two different polymers were synthesized with different donor moieties via palladium catalyzed coupling reactions. After optical and electronic features were investigated by Uv-vis spectrum and cyclic voltammetry studies, the polymers will be used as active materials in fabrication of OSC devices.

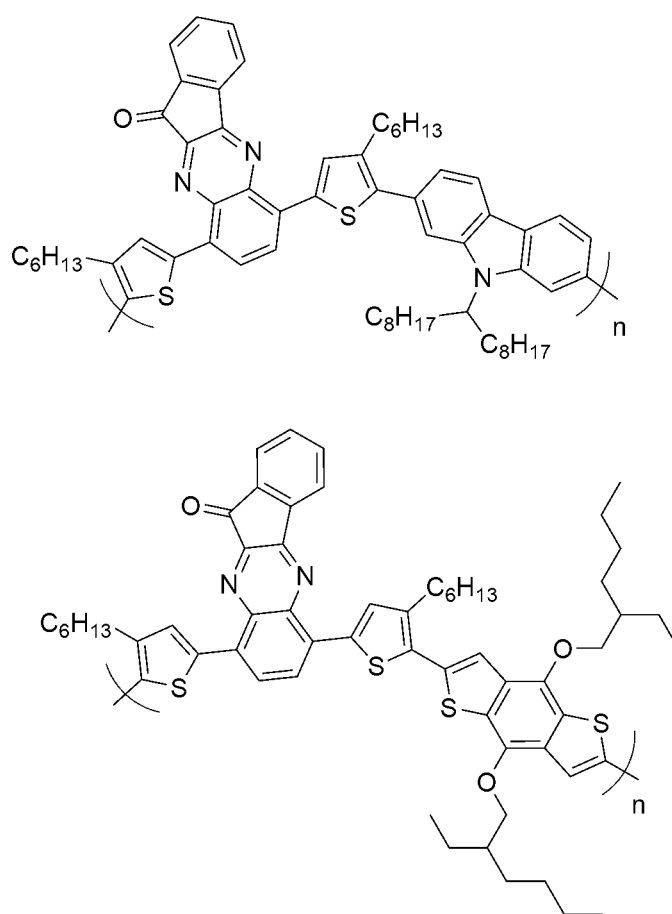


Figure 4.19. Indeno[1,2-*b*]quinoxalin containing polymers

In the third part; although the main interest is to benefit from the plasmonic effect of gold nanoparticles in OSCs, the polymers that were aimed to construct the device contains fused structures like BDT. In the course of TÜBİTAK 118Z738 project, a

trade-off between absorption of sunlight and carrier collection in OSCs can be coped with plasmonic metallic nanoparticles, i.e. gold nanoparticles, coupled to OSCs. Light trapping abilities of plasmonic gold nanoparticles enhance the absorption of light. The higher the absorption, the higher number of the generated excitons. Thus, higher rate of generation of free charges occurs. Consequently, improve the performance of the device in terms of power conversion efficiency. Literature examples of usage of plasmonic gold nanoparticles were dispersed randomly to any layer of the device. In this study, the sharp contrast to the literature plasmonic gold nanoparticles were aimed to attach covalently to the polymeric active material in the active layer of the device so that the degree of influence of plasmonic nanoparticles can be enhanced. To achieve this goal, the polymer was designed to have a free thiol functionality. These thiols can covalently bound to gold nanoparticles and dispersion of plasmonic gold nanoparticles were concentrated in close proximity to polymer.

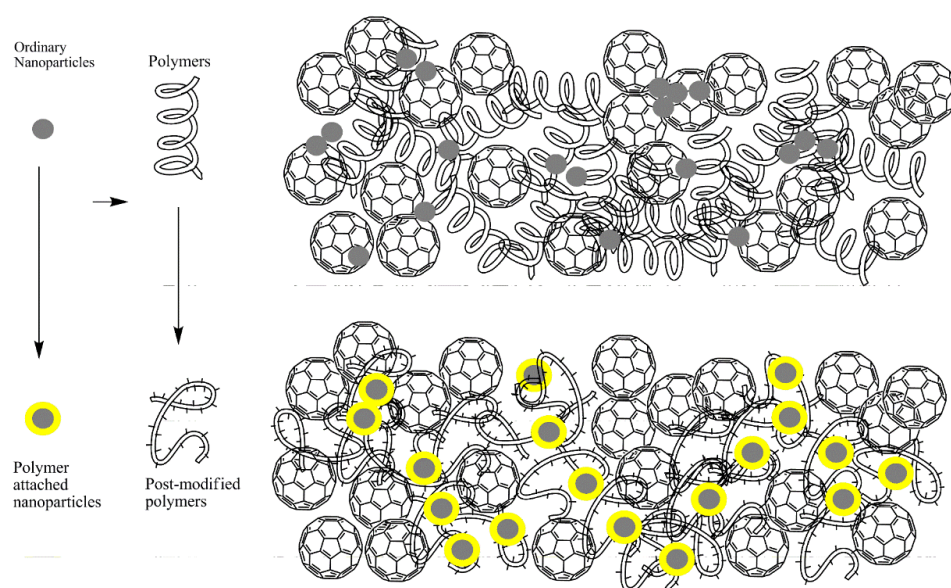


Figure 4.20. Representative distribution of ordinary and modified nanoparticles

4.7. Benzo-2,1,3-chalcogenadiazoles

4.7.1. Experimental

All chemicals were purchased from Sigma Aldrich and used without further purification unless otherwise mentioned. Tetrahydrofuran/toluene was distilled over benzophenone/sodium just before usage. Palladium catalyzed reactions were performed under argon atmosphere. SiO₂ column filler was used as the stationary phase in column chromatography. Synthetic pathway of monomers and polymers were given in Figure 4.21 and Figure 4.22 in respectively. 4,7-Dibromo-5,6-dimethoxybenzo[*c*][1,2,5]thiadiazole (288), 4,7-dibromo-5,6-dimethoxybenzo[*c*][1,2,5]oxadiazole (289), and 4,7-dibromo-5,6-difluorobenzo[*c*][1,2,5]thiadiazole (290) were synthesized according to the previous methodologies. NMR recorded on a Bruker Spectrospin Avance DPX-400 Spectrometer with TMS as the internal reference proved structures of organic molecules. Shimadzu RID-20A, calibrated against polystyrene standards in chloroform solvent, was used to investigate the molecular weights of the polymers. Pyris 1 TGA Thermogravimetry Analyzer and Perkin Elmer Diamond DSC Differential Scanning Calorimeter were used to investigate thermal properties of the polymers.

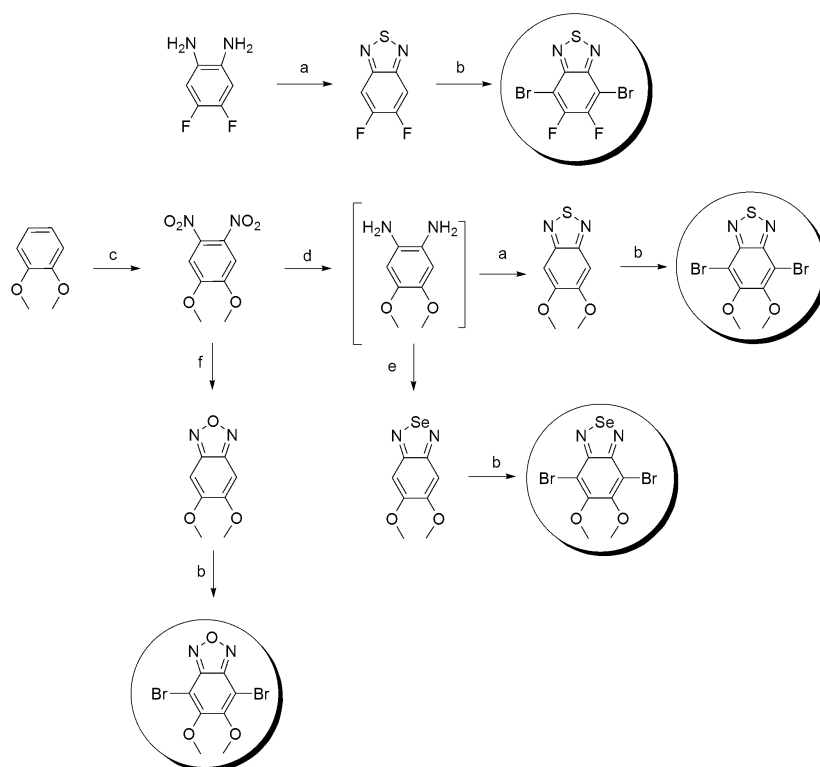


Figure 4.21. Synthesis of monomers: a) SOCl_2 , DCM, NEt_3 , b) AcOH, DCM, Br_2 c) HNO_3 , AcOH d) $\text{SnCl}_2 \cdot 2\text{H}_2\text{O}/\text{EtOH}:\text{HCl}$ e) SeO_2 , AcOH, EtOH f) NaN_3 , $n\text{-Bu}_4\text{NBr}$, toluene, PPh_3 .

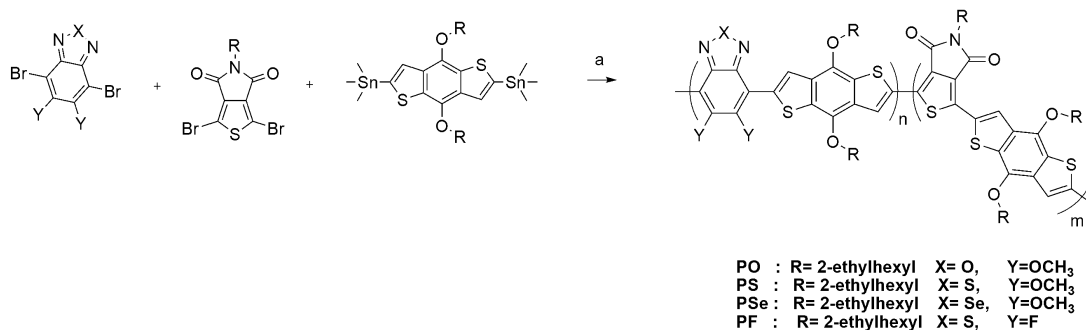


Figure 4.22. Polymerization reaction: a) $\text{Pd}(\text{PPh}_3)\text{Cl}_2$, toluene; end cap: 2-tributyltinthiophene, 2-bromothiophene

4.7.1.1. Synthesis

4.7.1.1.1. 4,7-Dibromo-5,6-dimethoxybenzo[*c*][1,2,5]selenadiazole

Similar synthetic procedures from 1,2-dimethoxy-4,5-dinitrobenzene were applied to the synthesis of 4,7-dibromo-5,6-dimethoxybenzo[*c*][1,2,5]selenadiazole where

instead of tetradecyloxy (291) alkoxy groups methoxy substituted selenadiazole core was considered (55%).

5,6-Dimethoxybenzo[*c*][1,2,5]selenadiazole: ^1H NMR (400 MHz, CDCl_3) δ (ppm): 6.93 (s, 2H), 3.92 (s, 6H). ^{13}C NMR (101 MHz, CDCl_3) δ (ppm): 157.24, 154.73, 99.05, 56.34.

4,7-Dibromo-5,6-dimethoxybenzo[*c*][1,2,5]selenadiazole: ^1H NMR (400 MHz, CDCl_3) δ (ppm): 3.98 (s, 6H). ^{13}C NMR (101 MHz, CDCl_3) δ (ppm): 154.83, 142.68, 107.80, 61.53.

4.7.1.1.2. Synthesis of polymer PS

1,3-dibromo-5-(2-ethylhexyl)-4H-thieno[3,4-*c*]pyrrole-4,6(5H)-dione (70 mg, 0.197 mmol, 1 eq), 4,7-dibromo-5,6-dimethoxybenzo[*c*][1,2,5]thiadiazole (84 mg, 0.197 mmol, 1 eq), and 2,6-bis(trimethylstannyl)-4,8-bis(2-ethylhexyloxy)benzo[1,2-*b*:4,5-*b'*]dithiophene (305 mg, 0.396 mmol, 2 eq) were dissolved in toluene (15 mL) under inert atmosphere. After 20 minutes of bubbling with nitrogen gas, $\text{Pd}(\text{PPh}_3)_2\text{Cl}_2$ (5% mol) was introduced and the reaction was refluxed for two days. After that, end cappers stannylated thiophene and bromo thiophene were put into reaction 4 eq and 8 eq, respectively for 6 h and overnight. The next day polymer was precipitated in methanol (100 mL). The obtained crude solid product was purified by Soxhlet extraction in the order of methanol, acetone, hexane, and chloroform. Chloroform portion was collected and 10-20 mg quadrasil was introduced and the mixture was stirred for 3 h. Then, the solution was filtered through a plug of silica and the solvent was removed under reduced pressure. The viscous polymer solution was precipitated in methanol (100 mL) and the solid polymer was obtained by filtration (yield 88%). GPC: $M_n=32.2$ kDa, $M_w=351.8$ kDa, PDI= 10.9. TGA: $T_d 95\%$ at 340 °C. DSC: No distinct thermal behavior was observed between 26 °C and 250 °C.

4.7.1.1.3. Synthesis of Polymer PO

Similar experimental procedure of PS was applied (yield 95%). GPC: $M_n=41.5$ kDa, $M_w=212.0$ kDa PDI= 5.1. TGA: T_d 95% at 330 °C. DSC: No distinct thermal behavior was observed between 26 °C and 250 °C.

4.7.1.1.4. Synthesis of Polymer PF

Similar experimental procedure of PS was applied (yield <25%). The low solubility of the polymer reduced the yield. There was a flake of polymer that cannot be dissolved in hot chlorobenzene. The reaction was repeated for a short polymerization period of 24 h yield was increased to 60%. Yet there was insoluble portion in soxhlet. GPC: $M_n= 37.0$ kDa, $M_w= 113.2$ kDa PDI= 3.1. TGA: T_d 95% at 345 °C. DSC: No distinct thermal behavior was observed between 26 °C and 250 °C.

4.7.1.1.5. Synthesis of Polymer PSe

Similar experimental procedure of PS was applied (84%). GPC: $M_n=40.5$ kDa, $M_w=579.8$ kDa PDI= 14.3. TGA: T_d 95% at 335 °C. DSC: No distinct thermal behavior was observed between 26 °C and 250 °C.

4.7.1.2. Investigation of Optical and Electronic Properties

Similar methods were used in the case of Chapter 1 to examine the optical and electronic properties of polymers.

4.7.1.3. OSC Device Fabrication

Device fabrication was first started by etching and cleaning the ITO surface. Then, PEDOT:PSS was spin coated. On its top active layer polymer:PC₇₁BM was spin coated. Under inert atmosphere and high vacuum, LiF and Al were deposited respectively. BHJ OSCs were fabricated with ITO/PEDOT:PSS/Polymer:PC₇₁BM/LiF/Al conventional device structure. The structure of the device and electronic levels were illustrated in Figure 4.23. The performance of OPVs was strongly affected by such processing parameters like blend

ratio, morphology regulatory additives and choice of solvent as well as the device structure-material used for anode, cathode and acceptor.

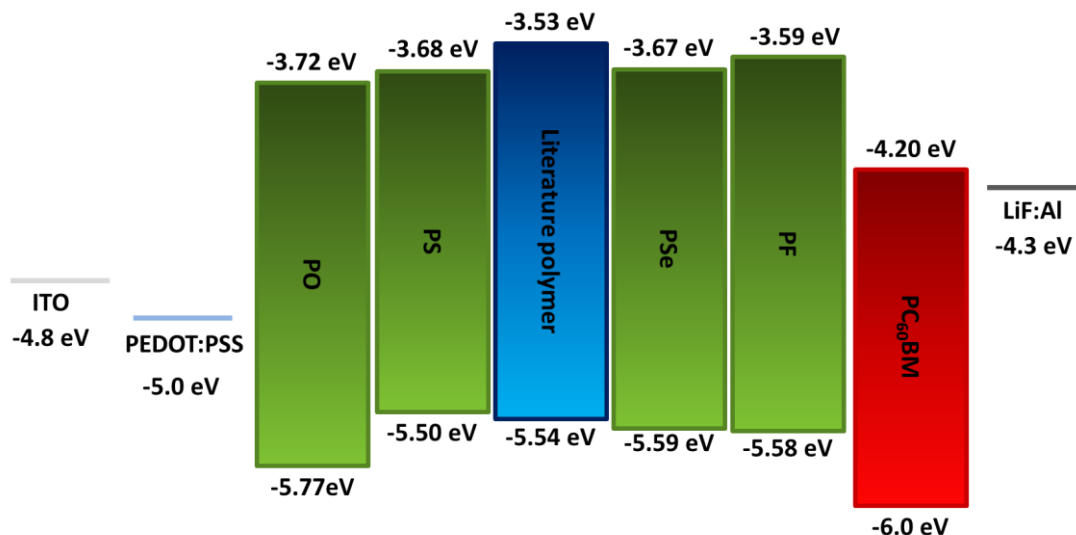


Figure 4.23. Electronic structure of constructed devices and literature polymer.

4.7.2. Results and Discussions

4.7.2.1. Optical Properties

The photophysical behavior of polymers can be shown in Figure 4.24. All four polymers demonstrated similar optical band gaps of ~ 1.7 - 1.8 eV in their thin film forms. In comparison to the literature polymer, there were only slight changes in optical features. Maximum absorptions were determined as 601, 610, 595 and 592 nm in thin films, respectively, for PO, PS, PSe and PF. The hypochromic shift was prominent for 16 nm for PO, 6 nm for PS and 5 nm for PF. This was attributed to the twisting of conjugated backbone so that effective conjugation length was decreased. However, regular molecular orientation as π - π stacking was indicated by 7 nm, bathochromic shift was observed for PF. Optical bandgaps in thin film of the polymers exhibit a bow like trend as going down in chalcogens. From PO to PS, optical bandgap was increased, while from PS to PSe, it was decreased. The lowest band gap was determined for PSe as 1.72 eV.

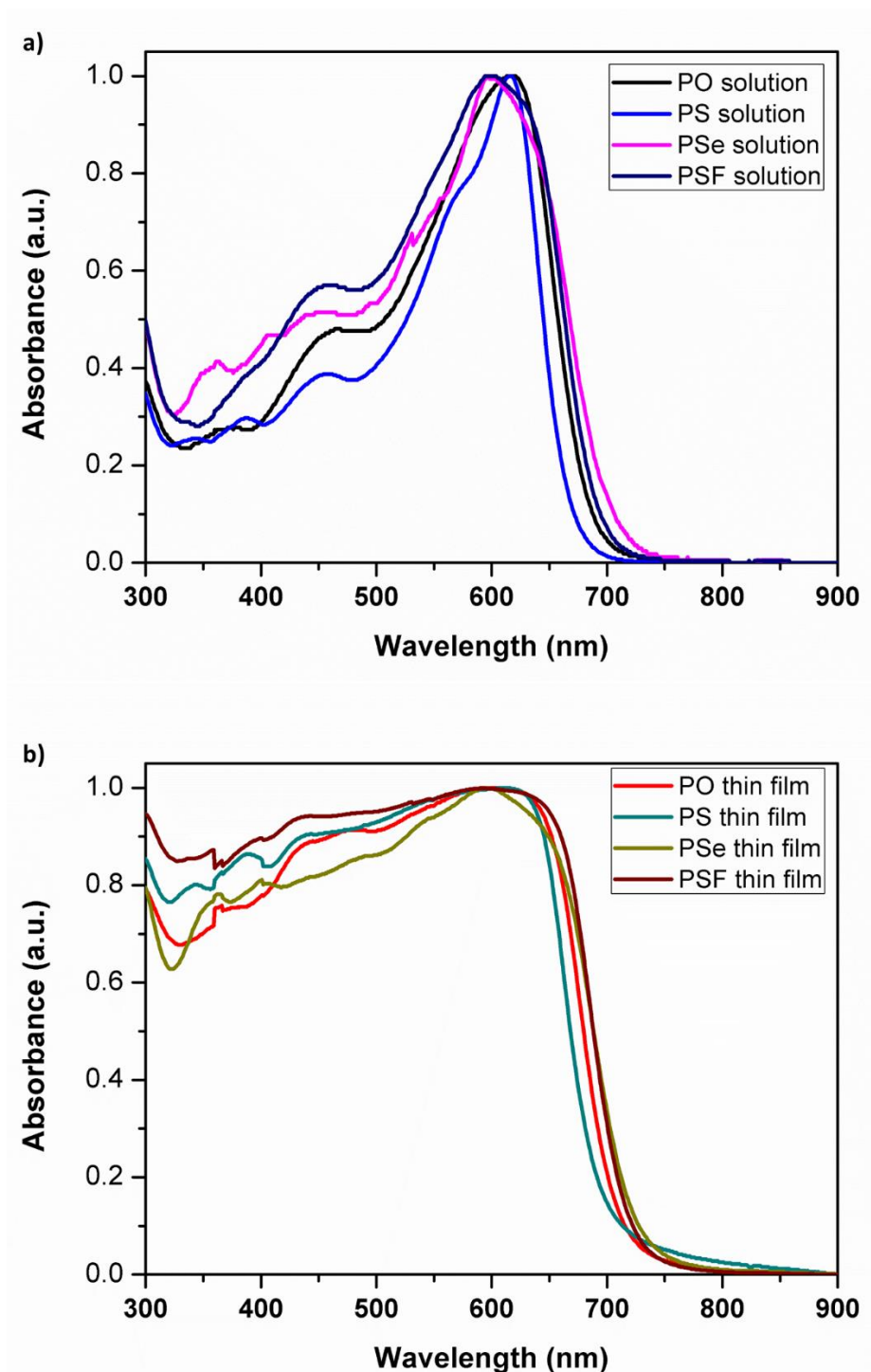


Figure 4.24. A thin film (a) and solution (b) Uv-Vis spectrum of polymers.

Moreover, while changing the substituents from electron withdrawing to electron donating moiety, attaching an electron withdrawing F element caused a slight

reduction in the optical bandgap with a value of 1.74 eV. To reduce the bandgap of these type of random polymers it was found that there was no straight pathway. Hence, there are tremendous parameters that affect the bandgap. Going down a group influence the electronic properties of the moiety yet the interaction with adjacent conjugated molecules, orbital overlapping and dihedral angle, molecular weight and morphologically the thin film orientation such as π - π stacking should also be considered. For example, polymers 1-4 seen in Figure 4.25 exhibited a strange feature (292–294). Base model polymer 1 exhibited 1.9 eV bandgap. While the polymer 2 with short alkoxy group exhibited lowered band gap of 1.82 eV, longer alkoxy derivative exhibited higher value of 1.99 eV. Moreover, when the substitution was performed by F atom, the bandgap was determined as 1.96 eV.

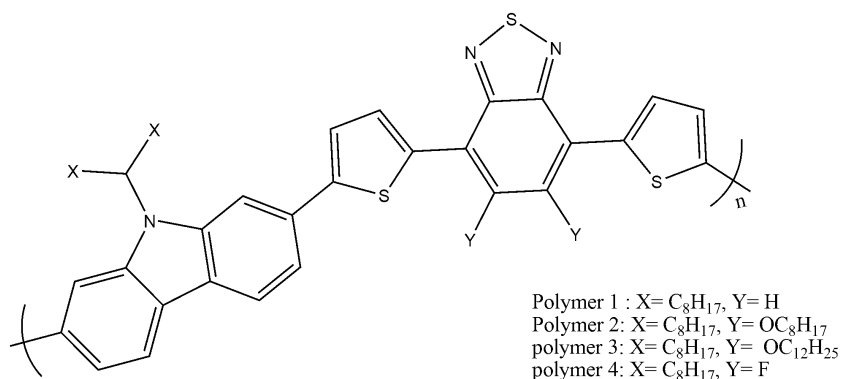


Figure 4.25. Carbazole copolymers of benzothiadiazole derivatives

4.7.2.2. Electronic Properties

Going down in 6A group elements, the bow like trend appeared for HOMO levels of PO, PS and PSe; -5.77 eV, -5.50 eV, -5.59 eV, respectively. Increasing of LUMO was expected as going from most electronegative atom O to least electronegative atom Se. However, there was no negligible change (0.01 eV difference) between HOMO of PS and PSe. It can be attributed to that influence of deep the LUMO level of PSe was mainly supported by thienopyrrolidone (TPD) moiety.

There should be a remarkable bathochromic shift resulted in a decrease in bandgap excepted when heavy Se atom was substituted (295). However, electronic bandgap

was found an intermediate value of 1.92 eV between PO and PS. Comparing the optical and electronic bandgaps of the polymers revealed that the latter is larger than the former one. This might have been caused by the generation of energy barrier while electrochemical redox was performed at the interface between the electrode and the polymer film surface. Previously, similar phenomena have been faced in the literature (296–298). Because of this reason, although the electronic bandgap of PSe is higher than PS, optical bandgap is lowered. Thus, introducing heavy atom was a simple and effective way of reducing the optical bandgap of the polymers and absorption profile is red shifted to longer wavelength (299, 300).

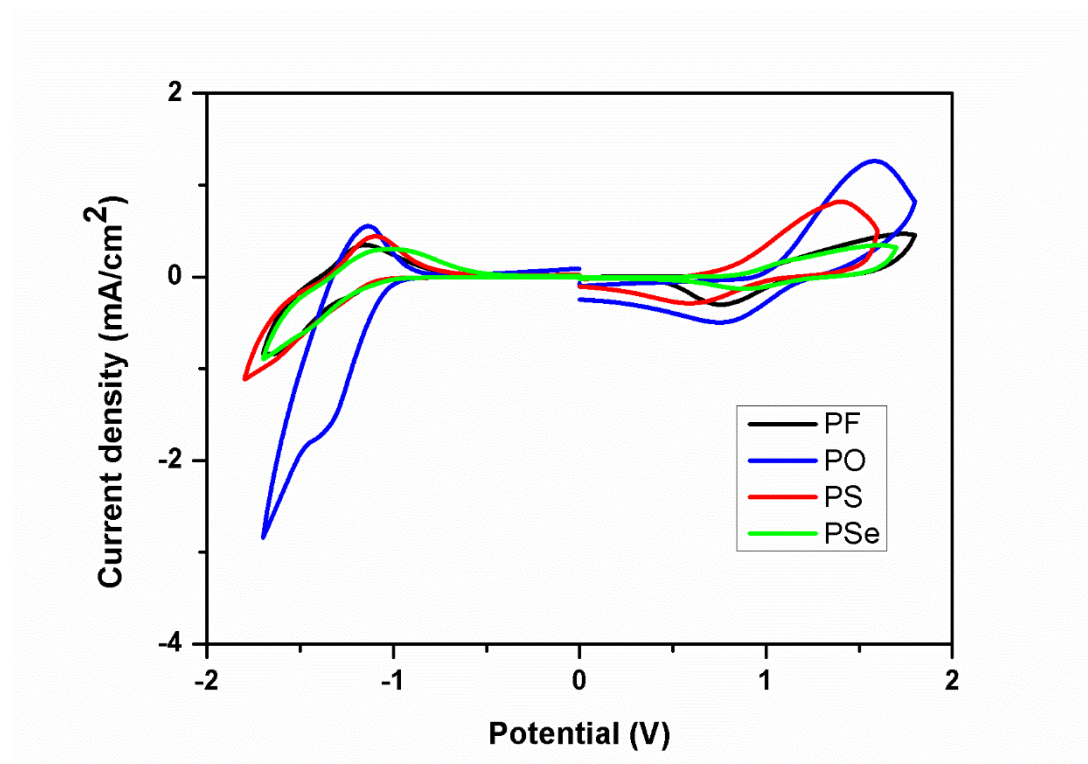


Figure 4.26. Single scan cyclic voltammograms of polymers PF, PO, PS, and PSe in 0.1 M TBAPF₆/ACN electrolyte solution at 100 mV/s scan rate.

Comparing the literature polymer, as expected, F substitution exhibited a stabilization of both HOMO and LUMO from -5.54 eV to -5.59 eV and from -3.53 eV to -3.67 eV, respectively. Electron donating alkoxy substitution while weakly destabilizing the HOMO level by 0.04 eV, stabilization of LUMO was observed by 0.15 eV. The higher

values of electronic band gaps of polymer than that of optical was attributed to the influence of charged species during cyclic voltammetry.

As an example, base model polymer 1 seen in Figure 4.25 possesses values of -5.5 eV for HOMO, -3.6 eV for LUMO, and 1.9 eV for bandgap. Modification of alkoxy group for polymer 2 destabilized both HOMO to -5.11 eV and LUMO to -3.29 eV (294). However, when longer chain was used as in the case of polymer 3, stabilization was performed for HOMO back to -5.60 eV and LUMO to -3.61 eV (293). Moreover, flourine atom substitution revealed no significant change in the electronic levels -5.54 eV and -3.58 eV for HOMO and LUMO, respectively (292). Therefore, electron withdrawing/donating ability of the substituent cannot solely be thought as the parameter to control the energy levels of the polymer. Both optical and electronic properties of four polymers can be seen in Table 4.1.

Table 4.1. *Optical and electronic properties of four polymers.*

<i>Polymer</i>	$E_{p-doping}$ (V)	$E_{n-doping}$ (V)	<i>HOMO</i> (eV)	<i>LUMO</i> (eV)	E_g^{op} (eV)	E_g^{el} (eV)
PO	1.59	-1.41	-5.77	-3.72	1.79	2.05
PS	1.41	-1.72	-5.50	-3.68	1.80	1.82
PSe	1.09/1.59	-1.57	-5.59	-3.67	1.72	1.92
PF	1.73	-1.63	-5.58	-3.59	1.74	1.99

4.7.2.3. Photovoltaic

The binding energy of the excitons is ~ 0.3 - 0.5 eV. LUMO energy level of the donor must be positioned higher than that of the acceptor (i.e., PC₇₁BM) by 0.3–0.5 eV for efficient photoinduced electron transfer from excited state of D to A (301–305). Thus, the driving forces ($-\Delta G$) for electron transfer from the excited states of polymers ($-\Delta G > 0.60$ eV) to PC₇₁BM are sufficient.

The difference between HOMO of D and LUMO of A is closely related to the V_{oc} value (267). While lowest lying HOMO of PO exhibited to highest V_{oc} of 0.87 V, the discrepancy of the rest may be explained by morphology of the active layer (306).

Solubility and molecular weight generally had great impact on the interface resistance and the nano- to micrometer scale morphology, resulting in a low V_{oc} , as well as J_{sc} and FF. As it can be seen in Table 4.2, the lowest FF was obtained from PSe which exhibited also the lowest power conversion efficiency. In a study where the effect of polymer molecular weight on the performance of OSCs was investigated, it was found that parameters like activation energy for carrier transport in the conjugated polymer, carrier concentration and recombination rate were identified to strongly influence the performance (307). Polymer with different molecular weights for example: low (~50 kDa), medium (~100 kDa), high (~200 kDa) and very high (~300 kDa) were investigated. As going low to high performances of OSCs were enhanced. Even though the charge carrier mobility of 300 kDa polymer was found the highest, it exhibited lower performance. The lowest recombination rate and the highest charge carrier concentration with the lowest activation energy for charge transport were found in 200 kDa based devices. FF values of low, medium, and high molecular weight polymer devices exhibited over 60% performance with the max 63% of 200 kDa. However, further increase in the molecular weight drastically decreases the FF to 51.6% and similar J_{sc} value with 300 kDa resulted in a decrease of power conversion efficiency from 9.57 % to 7.73 %. Therefore, the low FF values of PS and PSe were attributed to their undesirable high weight average molecular weights. Although there was no significant difference between PS and PSe, the difference between their photovoltaic performances was attributed to morphological incompatibility in the active layer. Irregularity in the surface morphology of PSe:PC₇₁BM might induce the inhomogenous surface contact between the cathode (Al) and the active layer, thereby accelerating charge recombination at the interface and lowering the V_{oc} value (306). Co-occurrences of qualitatively the highest R_s and the lowest R_{sh} that deviated further away from the ideality resulted in the lowest efficiency for PSe with 2.84 %.

Table 4.2. Polymer Solar Cell Performances

Polymer:PC ₇₁ BM Weight ratio	V _{oc} (V)	J _{sc} (mA/cm ²)	V _{MP} (V)	J _{MP} (mA/cm ²)	FF	PCE (%)
PO:PC ₇₁ BM (1:2)	0.87	9.74 (9.59)	0.69	6.87	0.557	4.72
PSe:PC ₇₁ BM (1:3)	0.75	9.38 (9.73)	0.50	5.66	0.405	2.84
PF:PC ₇₁ BM (1:2)	0.81	8.58 (8.57)	0.56	6.18	0.504	3.50
PS:PC ₇₁ BM (1:3)	0.80	11.44 (11.12)	0.56	7.42	0.459	4.20

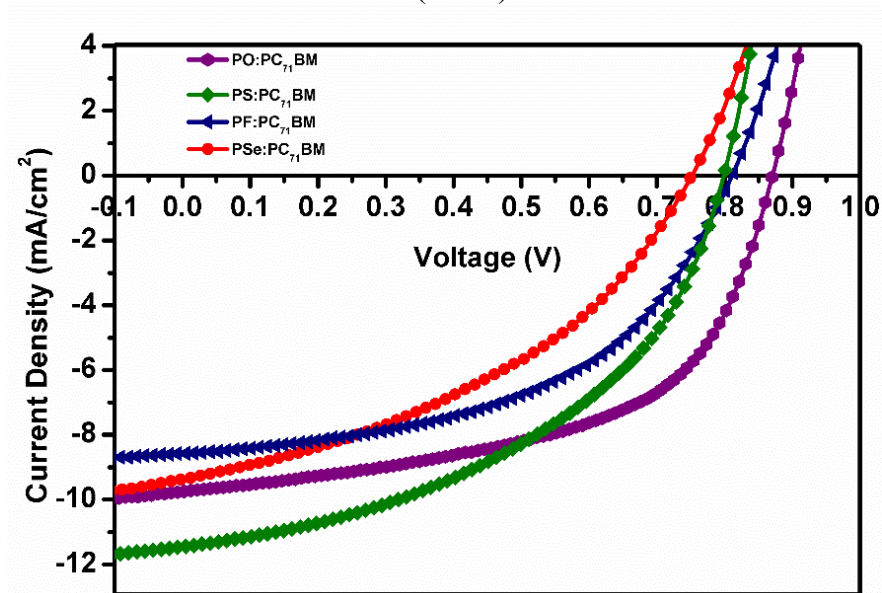


Figure 4.27. J-V curves of polymer OSCs

The weight ratio of the blend is an important parameter to be optimized. The difference between donor and acceptor units in terms of mobility of holes and electrons, respectively, plays a vital role for charge balance. By changing the ratio, this imbalance was modified to a content point for efficient charge collection as morphology changes. While the best performance was obtained by 1:3 ratio of Polymer:PC₇₁BM for PSe and PS, it was 1:2 for PF and PO (Figure 4.27). It was noted that while changing the ratio of Polymer:PC₇₁BM from 1:1.5 to 1:4, there was a little

change in hole mobility, the drastic increase in electron mobility increases the power conversion efficiency by decreasing R_s . However, a further increase in the blend ratio decreased the J_{sc} and EQE and this was attributed to the decreasing the absorber content in the active layer. Thus, active layer content is a crucial parameter that one should consider for efficient solar cells (308).

The best performances of the devices were optimized by changing parameters such as blend ratio of Polymer:PC₇₁BM, thickness, additives. Results can be seen in *Table 4.2*. The best performance of 4.72% power conversion efficiency was obtained by PO. The best performance PO based device exhibited the highest V_{oc} value of 0.87 V and FF value of 0.56, with moderate J_{sc} value of 9.74 mA/cm².

Incident photon to current efficiency measurements in Figure 4.28 showed that all devices with different polymers extracted electricity from incoming sunlight with moderate efficiency above 50%. The best EQE was extracted from PS based device around 65%. Low FF value of 0.46 for PS, which was resulted from high R_s , was suspicious for low efficiency with low V_{oc} .

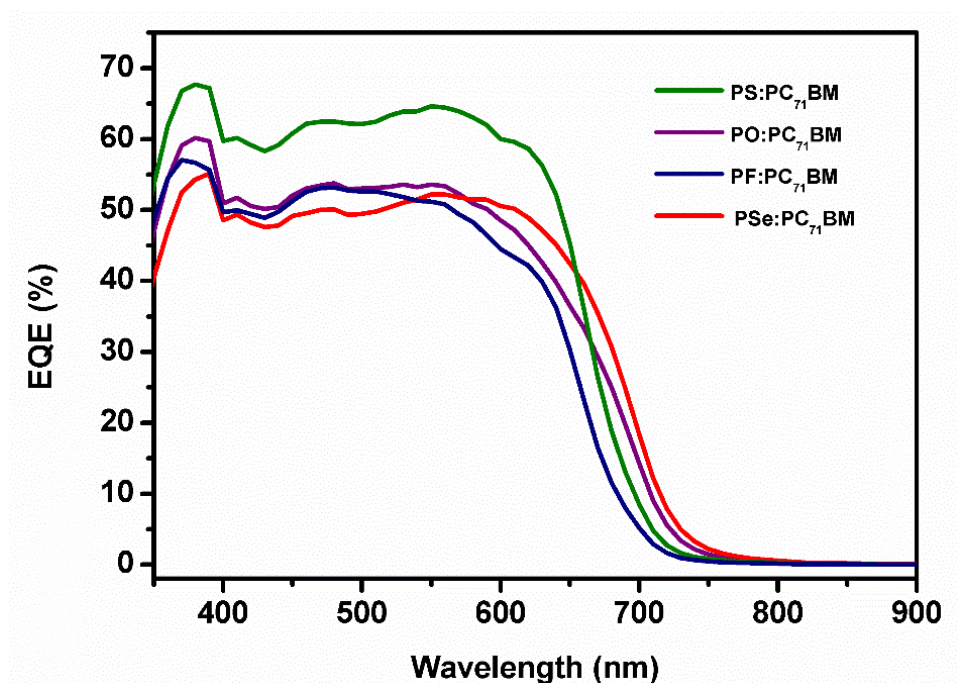


Figure 4.28. IPCE curves of polymer OSCs

4.7.3. Conclusion

Four novel benzochalcogenodiazole derivatives were used for random copolymerization of TPD and BDT. Investigations were made upon increasing the electronegativity of substituents or altering the periodic table group 6A elements from O atom to Se atom. As it was found that, there was no straightforward route to tune the bandgap and energy levels of random polymers, one should consider other parameters like a dihedral angle which has a great influence on conjugation length and consequently on bandgap. The lowest band gap PS exhibited superior IPCE results yet higher lying LUMO level than PO resulted in lower V_{oc} of 0.80 V. Because FF value of PS was beaten by that of PO with higher V_{oc} value, PO took the lead with the highest power conversion efficiency of 4.72 %. Changing electron withdrawing or electron donating side groups to the polymer resulted in lowered efficiencies. This can be attributed to high current collecting ability of literature polymer with respect to low J_{sc} values of PF and PS. Thus, changing the substituents in such random polymers to tune the bandgap and energy levels was found as not only crucial single parameters but also one had to consider the morphological structure of the active layer. To tune the morphology additive optimization will be performed and the effect of additives will be investigated using both power conversion efficiencies and morphological change.

4.8. Low Band Gap Polymers

4.8.1. Synthesis

Syntheses of 6,9-dibromo-11H-indeno[1,2-*b*]quinoxalin-11-one and 6,9-bis(4-hexylthiophen-2-yl)-11H-indeno[1,2-*b*]quinoxalin-11-one were performed as they was described in section 3.10. Synthetic pathways of low bandgap polymer can be seen in Figure 4.29.

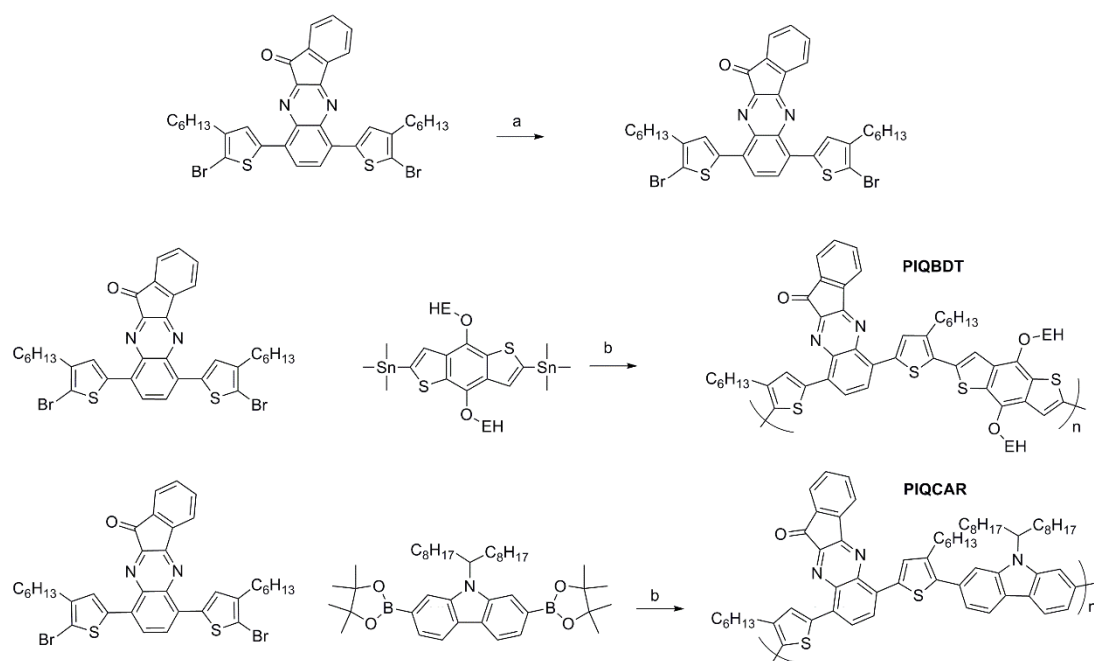


Figure 4.29. Synthetic pathways of low bandgap polymers

4.8.1.1. 6,9-Bis(5-bromo-4-hexylthiophen-2-yl)-11H-indeno[1,2-*b*]quinoxalin-11-one

6,9-Bis(4-hexylthiophen-2-yl)-11H-indeno[1,2-*b*]quinoxalin-11-one (380 mg, 0.67 mmol) was added in DCM (50 mL) at room temperature. The solution was stirred at dark and NBS (252 mg 1.42 mmol) was added in steps. After the reaction was performed overnight, saturated solution of NaHSO_{3(aq)} (10 mL) was added and extracted with DCM/water (100/50 mL). The organic phase was collected and dried over MgSO₄ and the solvent was removed under vacuum. The crude product was chromatographed (hexane/chloroform, v/v, 4/1) and a dark red solid was collected (380 mg, 78%).

4.8.1.2. PIQBDT

6,9-Bis(4-hexylthiophen-2-yl)-11H-indeno[1,2-*b*]quinoxalin-11-one (135 mg, 0.186 mmol), 2,6-bis(trimethylstannyl)-4,8-bis(2-ethylhexyloxy)benzo[1,2-*b*:4,5-*b'*]dithiophene (145 mg, 0.187 mmol) were dissolved in freshly distilled toluene (20

mL) and the solution was bubbled for 20 min. Then, Pd(PPh₃)₂Cl₂ (8% mol) was introduced and the reaction was refluxed for 2 days and the same procedure was applied as in section 2.7.1.6. The polymer was obtained as dark brown solid (149mg, 79%). GPC: M_n= 4.9 kDa, M_w= 8.8 kDa PDI= 1.8. TGA: T_d 95% at 350 °C. DSC: No distinct thermal behavior was observed between 26 °C and 250 °C.

4.8.1.3. PIQCAR

Similar procedure was applied to the synthesis of PIQCAR, where 6,9-bis(4-hexylthiophen-2-yl)-11H-indeno[1,2-b]quinoxalin-11-one (130 mg, 0.180 mmol) and 9-(heptadecan-9-yl)-2,7-bis(4,4,5,5-tetramethyl-1,3,2-dioxaborolan-2-yl)-9H-carbazole (118 mg, 0.180 mmol) were used. The dark brown polymer was obtained as solid (150 mg, 86%). GPC: M_n= 3.7 kDa, M_w= 6.2 kDa PDI= 1.7. TGA: T_d 95% at 403 °C. DSC: No distinct thermal behavior was observed between 26 °C and 250 °C.

4.8.2. Optical and Electronic Properties

In the Figure 4.30, the solution and the thin film absorption behaviors can be seen. The low energy transition was enhanced in the thin film absorption. This increase was caused by strong intermolecular π - π interaction due to promoted aggregated stacking. Such a solid film formation might be beneficial for OSCs to absorb more light in the red/IR region of the spectrum. PIQCAR in solution exhibited one major and two minor absorption peaks, 368 nm, 460 nm and 564 nm, respectively. Its thin film possessed a similar trend with enhanced absorption peaks red shifted to 390 nm, 480 nm, and 605 nm. The optical bandgap was calculated as 1.63 eV. Whereas PIQBDT, where stronger donor BDT was used, exhibited 444 nm absorption λ_{\max} with 602 nm shoulder in the solution phase. A thin film of PIQBDT similarly exhibited red shifted absorption to 484 nm absorption λ_{\max} with 658 nm shoulder. As expected, optical bandgap of PIQBDT was calculated by onset value of 870 nm as 1.42 eV, due to strong donor moiety BDT.

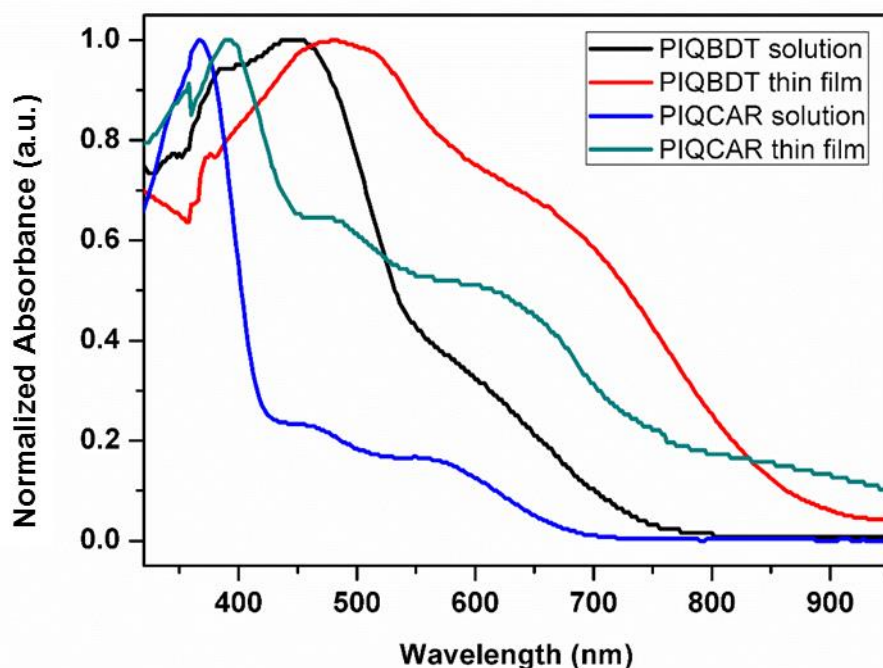


Figure 4.30. Uv-vis spectra of low bandgap polymers

Single scan cyclic voltammogram can be seen in Figure 4.31. Oxidation onset potentials were used to calculate HOMO energy levels of polymers of PIQCAR and PIQBDT, -5.80 eV and -5.62 eV, respectively. LUMO energy levels were estimated by considering the optical bandgap. LUMO of PIQCAR was found as -4.17 eV and that of PIQBDT was found as -4.20 eV. Strong donor property of BDT core resulted in both higher lying HOMO level of PIQBDT and lower bandgap of the polymer. Summary of the optical and electronic properties of the polymer can be seen in

Table 4.3.

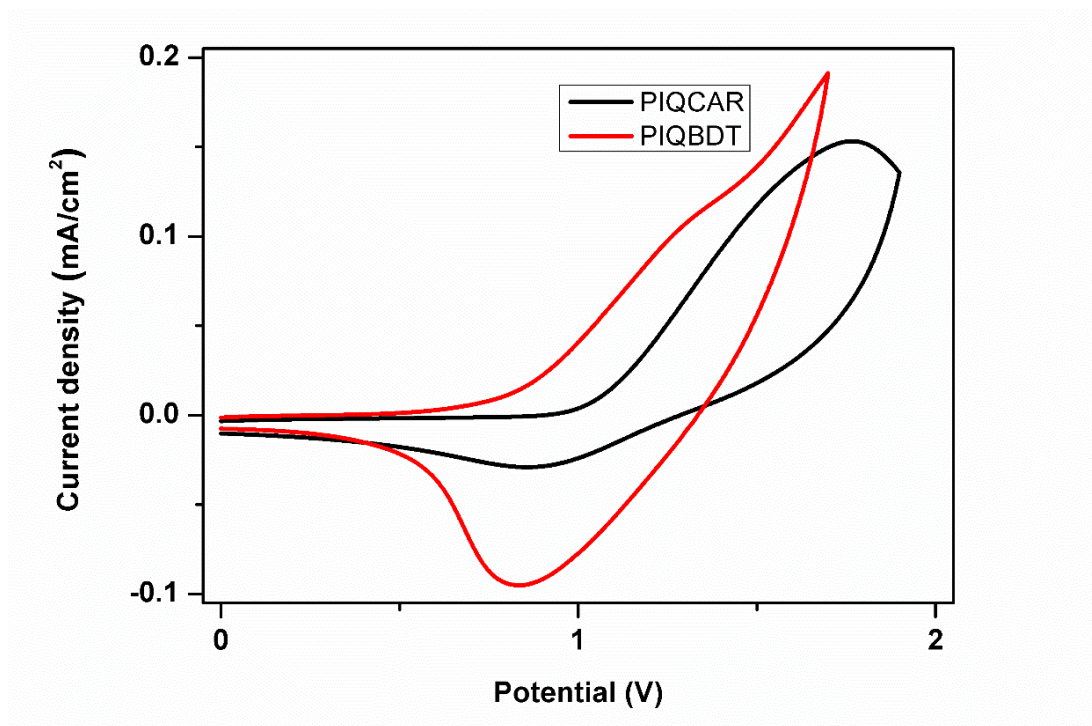


Figure 4.31. Single scan cyclic voltammogram of PIQCAR ad PIQBDT.

Table 4.3. Optical and electronic properties of PIQCAR and PIQBDT.

Material	E_{ox} (V)	E_{ox}^{onset} (V)	HOMO (eV)	LUMO (eV)*	λ_{max} (nm)	E_g^{op} (eV)
PIQCAR	1.74	1.05	-5.80	-4.17	368/460/564	1.63
PIQBDT	1.29	0.87	-5.62	-4.20	444/602	1.42

* Calculated from the optical bandgap ($LUMO = HOMO + (1241/\lambda_{onset})$)

4.8.3. Conclusions and Future Studies

In this part, fused indenoquinoxaline moiety was coupled with hexyl thiophene to enhance the solubility of the fused structure. Two different polymers were obtained by palladium catalyzed polymerizations with carbazole and benzodithiophene donor moieties, respectively, PIQCAR and PIQBDT. PIQBDT including strong donor moiety exhibited a bathochromic shift in both the absorption spectra of the thin film and the solution phase. Strong aggregation of the fused structure containing

copolymers of PIQCAR and PIQBDT could be deduced from the enhancement in the Uv-Vis absorption spectrum. It could be beneficial for charge transport properties in OSCs to enhance the performance of the devices. For future studies, these two different polymers will be used as an active material to construct OSC devices. Performance of devices will be investigated in parallel to their morphological behaviors in thin films. Morphology modifiers such as annealing and additive strategies will be used to alter the morphology of the active layer of polymer:PC₇₁BM composition so that the maximum performance of the device will be revealed.

4.9. Fused Structures with Plasmonic Nanoparticles

Design of this project was aimed to be supported by TUBITAK (118Z738). In this study, the aim was the incorporation of plasmonic gold nanoparticles covalently to the polymeric active material for organic solar cells. For this purpose, high performance literature polymers were taken as examples and chemically modified versions were aimed to be investigated. One example of the desired polymer in this project can be seen in Figure 4.32. Modification of polymers was aimed such a way that free thiol moieties can covalently bound to gold nanoparticles which were put together in the active layer of organic solar cells. Thus, the distribution of plasmonic gold nanoparticle was placed in close proximity to the light absorbing conjugated polymer. In this freshly accepted project, syntheses and characterizations of some core structures for the project aim were successfully performed.

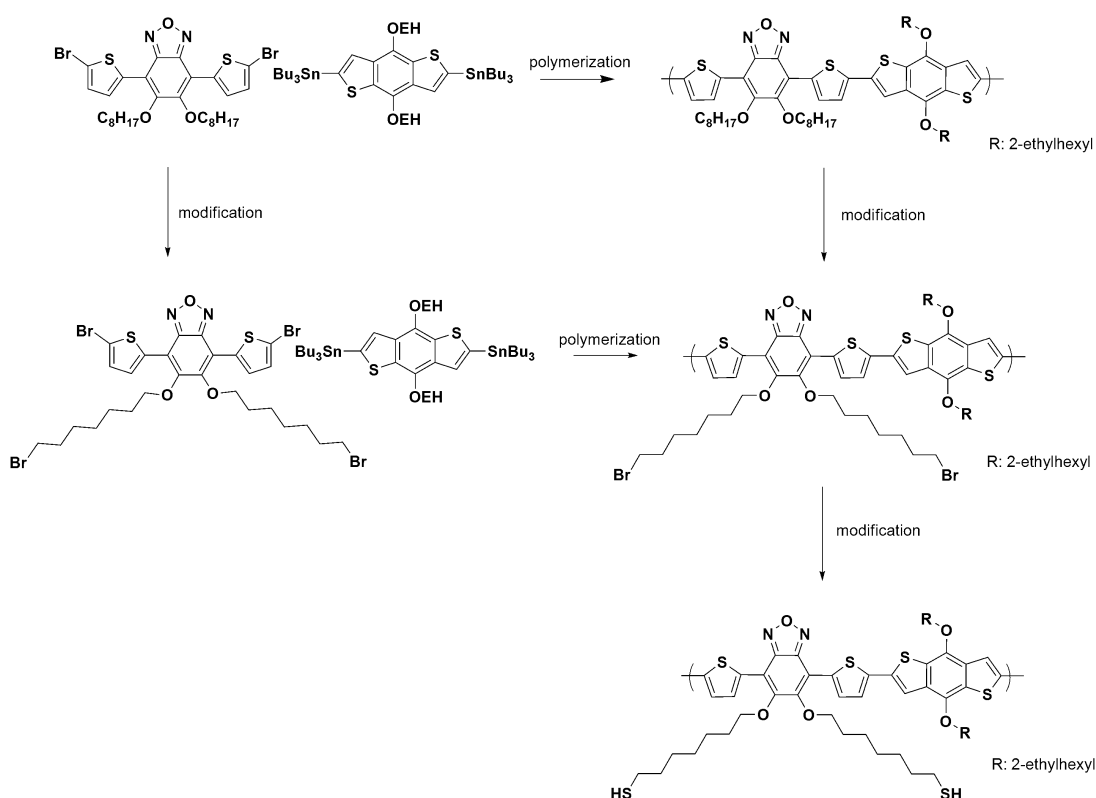


Figure 4.32. An example of the chemical structures of modified polymers

4.9.1. Materials and Methods

All chemicals were purchased from Sigma Aldrich, DCM was purchased from a local company and before usage, it was distilled. Toulene was distilled over Na/benzophenone and used freshly. SiO_2 column filler was used as the stationary phase in column chromatography. NMR recorded on a Bruker Spectrospin Avance DPX-400 Spectrometer with TMS as the internal reference was used to prove the structures of organic molecules. Synthetic pathway of the desired final product can be seen in Figure 4.33. Synthesis of 1, 2 and 3 numbered structures were explained previously in this chapter.

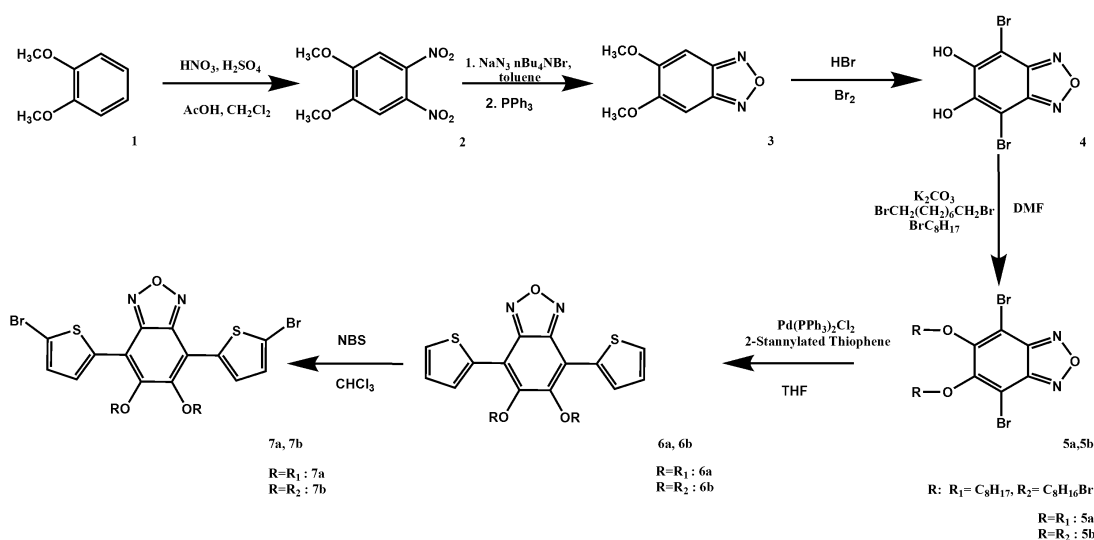


Figure 4.33. Synthetic pathways of monomers

4.9.1.1. Synthesis of 4,7-dibromobenzo[*c*][1,2,5]oxadiazole-5,6-diol (4):

There were two synthetic pathways. The first one can be seen in Figure 4.21 and for the second and the more convenient method is dividing this single step reaction into two parts: first the bromination of 4- and 7-positions and then hydrolysis of ether to alcohol.

Bromination was performed by molecular bromine in DCM/AcOH solution. Quantitative bromination of starting material was followed by hydrolysis in HBr/AcOH solution. Simply separating the solid, which was formed after precipitating it in excess water, gave target molecule 4.

4.9.1.2. Synthesis of 4,7-dibromo-5,6-bis(8-bromooctyloxy)benzo[*c*][1,2,5]oxadiazole (5b)

Compound 4 in DMF with K_2CO_3 and doubly brominated alkyl chain were reacted to obtain the target molecule 5b. Because there was a high probability to obtain polymeric compound, excess alkyl chain was used. The crude product was purified by column chromatography.

4.9.1.3. Synthesis of 5,6-bis(8-bromooctyloxy)-4,7-di(thiophen-2-yl)benzo[c][1,2,5]oxadiazole (6b)

Compound 5b and stannylated thiophene was dissolved in freshly distilled thiophene and bubbled for 20 min. After that period palladium catalyst was introduced and the reaction was refluxed overnight. The next day, solvent was removed and the extraction was performed with DCM/water. The organic phase was collected and dried over MgSO₄. The organic solvent was removed under reduced pressure and the crude product was separated by column chromatography.

4.9.2. Discussions and Future Studies

The initial steps for the synthesis of modified polymers were performed. The success of the last step was low due to unwanted side reaction of sp³ hybridized carbon interference. It was needed to optimize the condition of this reaction.

After successful synthesis of acceptor moieties, which have bromine or straight alkyl group functionalities, will be copolymerized with various donor moieties. Polymers were collected and purified by Soxhlet extraction. Additionally, some portion of the bromo modified polymer will be converted into the thiol functionality. Thus, the molecular weight of the bromine- and thiol-functional polymers will not effect device parameters. Each polymer was compared with each other to reveal the intrinsic properties on power conversion efficiencies. Hence, the success rate of the thiolation in post polymerization process would be another parameter that affects the performance of OSCs. Bromine atoms in the polymeric compound might act as a recombination center. Thus, the effect of ready to modification brom-alkyl end version of the polymer should also be investigated in the active layer of OSCs. After all of these characterizations, a combination of plasmonic gold nanoparticles with these thiol-modified/unmodified polymers was investigated using power conversion efficiency. The change in the efficiency will be correlated with the morphological distribution of gold nanoparticles; thus, AFM SEM images will be investigated carefully.

4.10. Conclusions

To sum up, three different studies have been carried out in this chapter and some are still in progress.

The first study revealed the effect of two different parameters. The first parameter was the single atom replacement in the benzochalcogenodiazole moiety in random copolymer through the chalcogens from O to Se atom. Going down in the group 6A elements, optical and electronic properties of the conjugated polymers were investigated. Moreover, the effect of these atoms was investigated for organic solar cell applications. The second parameter was the side group effect, where electron donating methoxy or electron withdrawing fluorine atom was investigated. The influence on electronic structure and optical properties were revealed. The best efficiency was achieved by PO which had among the highest FF factor and V_{oc} value with moderate J_{sc} . Although the PS exhibited superior performance in IPCE data, the low FF value was suspicious for its low efficiency. Further investigations will be performed to reveal the effect of the morphological change on power conversion efficiency and then the study will be ready for publication.

In the second study, two different fused indenoquinoxaline containing hexyl thiophene-bridged copolymers were synthesized. Hexylthiophenes not only act as a bridge but also enhanced the solubility of the fused core. Optical and electronic properties were investigated. UV-vis spectra of polymers revealed that strong intermolecular attractions of fused conjugated polymers created charge transfer states and optical band gap was reduced below 1 eV in the thin film form. However, the solutions of these polymers had bandgap of 1.63 and 1.42 eV, respectively for PIQCAR and PIQBDT. Because such stacking behaviors are important for charge mobility, these polymers with their broad absorption windows will be promising materials for organic solar cell applications. Further studies will be performed to reveal solar cells performances of these polymers.

In the final study, fused conjugated BDT containing conjugated polymers were synthesized in such a way that the polymer can covalently bound to the plasmonic gold nanoparticles via thiol functional groups. This attachment of plasmonic gold nanoparticles was aimed to enhance the absorption of the polymer to generate many excitons in the active layer of solar cells. For this purpose, chemical structure of conjugated acceptor was designed to couple fused BDT moiety. Synthesis of compound 6b was successfully achieved in the first couple months of 32-month termed TUBITAK 118Z738 numbered project. After successful synthesis and characterization of monomer, polymerization will be followed and the thiol modifications will be performed. After all, differently modified polymers were investigated for their solar cell performances. Then, plasmonic gold nanoparticles were introduced into the active layer and distribution of them will be controlled by thiol linkage to set gold nanoparticles to be in close proximity with the polymer. Randomly distributed:unmodified polymer and close proximity:modified polymer devices will be compared for their organic solar cell performances.

CHAPTER 5

STUDIES IN THIS THESIS

5.1. Summary of the Thesis

In this thesis, fused conjugated organic structures were utilized for three separate applications of organic electronics.

In the first application, OLEDs, phenanthroimidazole alkyl-end modified polymers were synthesized and were used as active materials for OLED construction. Fine modification of band gap were successfully achieved to lower the band gap via two different methodologies; i) usage of π -thiophene bridge, ii) usage of stronger donor. P1 was determined to be one the most efficient material with the highest luminance value of 14180 cd/m² among benzotriazole based OLEDs.

For biosensor application, three different functional groups oxime, enamine, and ketone were investigated for catechol determination in water samples. The most promising PM1 exhibited high performance without any additives such as Nafion or carbon nanotubes. Catechol biosensor of laccase based bare PM1 coated carbon electrode showed linear range between 5.0-175.0 mM with low K_M^{app} 18 mM. Interference effect will be further investigated for the substances in water samples.

The final application was OSCs. this chapter covered three different studies. In the first study, four different polymers were synthesized to optimize the energy levels thus optimize the power conversion efficiency of solar cells. Two different methodologies were applied: i) electron donating/withdrawing substituents, ii) single atom variation through the chalcogens from O to Se. The best performance obtained as 4.72 % from PO based device, due to both possessing lowest lying HOMO causing the highest V_{oc} of 0.87 V and highest FF value of 0.557. The second study covered the syntheses of two low bandgap fused conjugated polymers that absorbing the light in infrared

region. Bandgap of synthesized polymer in thin film forms were found as 1.63 and 1.42 eV, respectively PIQCAR and PIQBDT. Further investigation will be performed to reveal the solar cell characteristics of polymers. In the last study, to benefit more from the plasmonic effect on polymers in OSCs, plasmonic nanoparticle attachable conjugated polymers were designed. High performance polymers were selected as model polymers and through a simple thiol modification covalent bonding between nanoparticle and polymer was aimed. By this modification distribution of nanoparticles were aimed to be controlled in active layer. Syntheses of monomers were successfully achieved and further studies will be continued to obtain and characterize the polymers for OSCs.

5.2. Other Studies

Throughout my stay as visiting scholar at the Prof. Dr. Paul M. Lahti's lab in University of Massachusetts (Amherst, USA) effects of pendant groups of Benzotriazolevinyl-based polymers (pBTzV) on thin film morphology and on PCE were investigated. Branch alkyl chain showed fibrillary morphology whereas straight alkyl chain featured smooth surface morphology. Theoretical studies were supported with the experimental data and PCE of the synthesized polymers were found as 2.87% for *n*-alkyl and 1.47% for branched alkyl chain. It was concluded that pBTzV pendant chain-driven morphology variation seems likely to be a major determinant of bulk electronic behavior in the solid state, and thus, further solar performance increases may be possible with this family of polymers. This study was selected as a cover article (309).

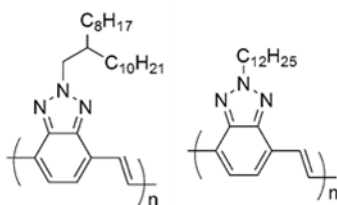


Figure 5.1. Alkyl chain modification of BTz polymers.

Utilization of benzotriazole and dithienothiophene containing polymer in a study in which super capacitor was modified. The instant capacity of the energy storage device, which was designed as all organic super capacitor, was determined by multi-electrochromic properties of the polymer which can be seen in Figure 5.2 (310).

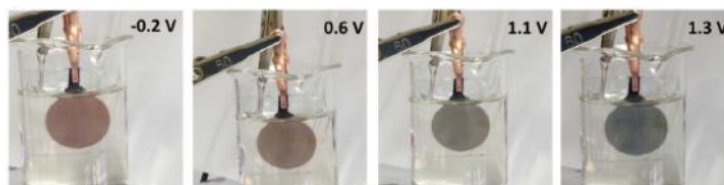


Figure 5.2. Colours of modified super capacitor on different voltages. Reproduced with permission from *J. Electrochem. Soc.*, 162 (14) A2807 (2015) Copyright 2015.

Moreover, I have been involved in synthesis of materials for biological applications such as glucose biosensors (311).

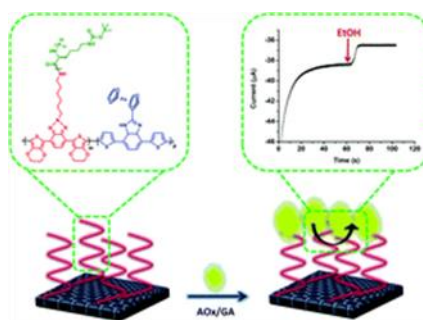


Figure 5.3. Conducting polymers containing polypeptide and ferrocene side chains as ethanol biosensors. *Polym. Chem.*, 2014,5, 6295-6306 Reproduced by permission of The Royal Society of Chemistry (RSC) on behalf of the Centre National de la Recherche Scientifique (CNRS) and the RSC.

A multi-functional fluorescent scaffold as a multicolour probe was designed and application in targeted cell imaging was successfully studied. This design offers multicolour cell images by emitting at dual wavelengths with no quenching in its fluorescent property. A fluorescent and alcohol-functionalized monomer, 3-(1*H*-phenanthro[9,10-*d*]imidazol-2-yl)phenol (PIP) and an antibody labelling kit (CF555) were merged on the same scaffold. The bioconjugated PIP/CF555/anti-CD44 was successfully used as a novel fluorescent bio-probe for targeted imaging of CD44 positive U87-MG cancer cells (312).

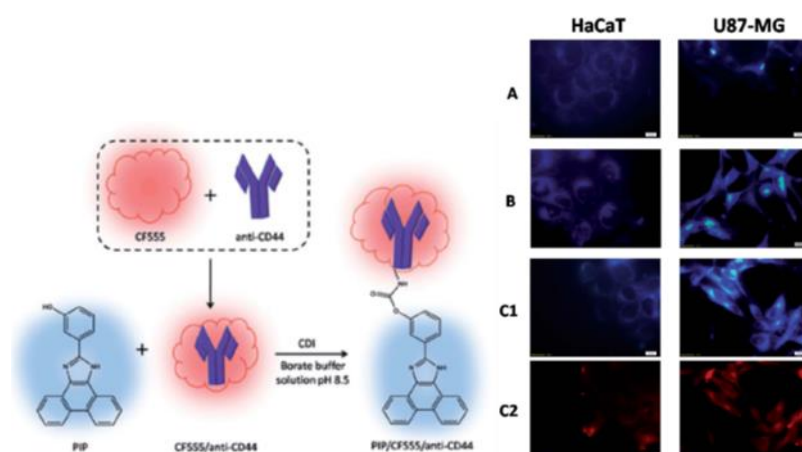


Figure 5.4. Left: preparation of PIP/CF555/anti-CD44 bioconjugate. Right: Imaging of HaCaT and U87-MG cells via fluorescence microscopy. Images were obtained after treatment of the cell with PIP monomer (A), PIP/anti-CD44 (B) and PIP/CF555/anti-CD44 (C1 and C2) for 2 h at 37 °C and 5.0% CO₂ atmosphere, under humidity. Photos of A, B and C1 were taken with UV filter of fluorescence set up. Photos of C2 were taken with red filter of fluorescence set up with 100x magnification. All scale bars are 10 μm. RSC Adv., 2015,5, 83361-83367 Modified by permission of The Royal Society of Chemistry (RSC) on behalf of the Centre National de la Recherche Scientifique (CNRS) and the RSC.

I have been also involved in various studies that covers the syntheses and investigations of the conjugated polymers in organic photovoltaics and some yet unpublished studies. (313–318)

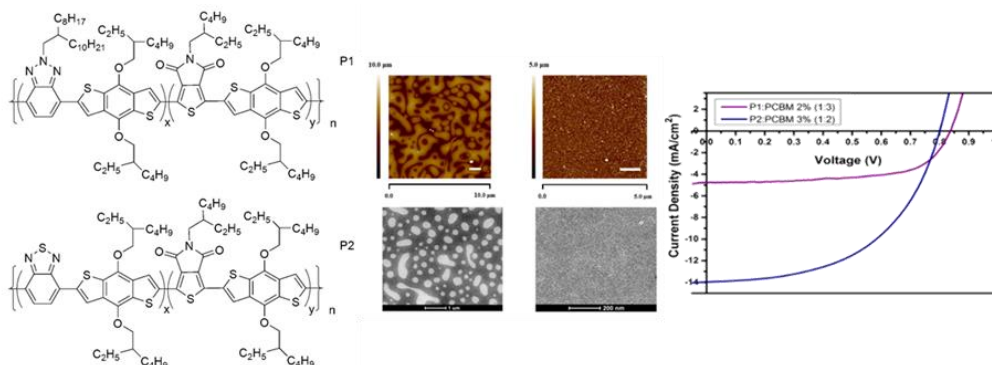


Figure 5.5. Polymers for solar cell applications. This article was published in Polymer, 133, Özge Azeri, Ece Aktas, Cagla Istanbuluoglu, Serife O.Hacioglu, Sevki Can Cevher, Levent Toppare, Ali Cirpan, Efficient benzodithiophene and thienopyrroledione containing random polymers as components for organic solar cells, 60–67, Copyright Elsevier (2017).

REFERENCES

1. C. K. Chiang, C. R. Fincher, Y. W. Park, A. J. Heeger, H. Shirakawa, E. J. Louis, S. C. Gau, A. G. MacDiarmid, Electrical Conductivity in Doped Polyacetylene. *Phys. Rev. Lett.* **39**, 1098–1101 (1977).
2. J.-L. Brédas, D. Beljonne, V. Coropceanu, J. Cornil, Charge-Transfer and Energy-Transfer Processes in π -Conjugated Oligomers and Polymers: A Molecular Picture. *Chem. Rev.* **104**, 4971–5004 (2004).
3. A. Cirpan, H. P. Rathnayake, P. M. Lahti, F. E. Karasz, Luminescence of fluorenes 2,7-conjugatively extended with pyrenylvinylene and pyrenylvinylene-phenylenevinylene. *J. Mater. Chem.* **17**, 3030–3036 (2007).
4. V. A. F. Deichmann, A. Cirpan, F. E. Karasz, L. Akcelrud, Photo- and electroluminescent properties of a π -conjugated copolymer containing 2,2'-bipyridyl units. *Polym. Int.* **56**, 252–257 (2007).
5. H. P. Rathnayake, A. Cirpan, Z. Delen, P. M. Lahti, F. E. Karasz, Optimizing OLED efficacy of 2,7-diconjugated 9,9-dialkylfluorenes by variation of periphery substitution and conjugation length. *Adv. Funct. Mater.* **17**, 115–122 (2007).
6. H. P. Rathnayake, A. Cirpan, F. E. Karasz, M. Y. Odoi, N. I. Hammer, M. D. Barnes, P. M. Lahti, Luminescence of molecular and block copolymeric 2,7-bis(phenylethenyl)-fluorenones; identifying green-band emitter sites in a fluorene-based luminophore. *Chem. Mater.* **19**, 3265–3270 (2007).
7. M. Kesik, H. Akbulut, S. Söylemez, Ş. C. Cevher, G. Hızalan, Y. Arslan Udum, T. Endo, S. Yamada, A. Çırpan, Y. Yağcı, L. Toppare, Synthesis and characterization of conducting polymers containing polypeptide and ferrocene side chains as ethanol biosensors. *Polym. Chem.* **5**, 6295–6306 (2014).
8. S. Pirsä, Chemiresistive gas sensors based on conducting polymers. *Mater. Sci. Eng. Concepts, Methodol. Tools, Appl.* **1–3**, 543–574 (2017).
9. A. Gusain, N. J. Joshi, P. V. Varde, D. K. Aswal, Flexible NO gas sensor based on conducting polymer poly[N-9'-heptadecanyl-2,7-carbazole-alt-5,5-(4',7'-di-2-thienyl-2',1',3'-benzothiadiazole)] (PCDTBT). *Sensors Actuators, B Chem.* **239**, 734–745 (2017).
10. A. K. Şahutoğlu, İ. Kaya, Synthesis and a new mercury (II)ion sensor application of conductive polymer containing rhodamine B. *React. Funct. Polym.* **141**, 50–57 (2019).
11. H. Xia, C. Hu, T. Chen, D. Hu, M. Zhang, K. Xie, Advances in Conjugated

- Polymer Lasers. *Polymers (Basel)*. **11**, 443–458 (2019).
12. S. Goker, G. Hizalan, E. Aktas, S. Kutkan, A. Cirpan, L. Toppare, 2,1,3-Benzooxadiazole, thiophene and benzodithiophene based random copolymers for organic photovoltaics: thiophene versus thieno[3,2-b]thiophene as π -conjugated linkers. *New J. Chem.* **40**, 10455–10464 (2016).
 13. D. Hazar Apaydin, D. Esra Yildiz, A. Cirpan, L. Toppare, Optimizing the organic solar cell efficiency: Role of the active layer thickness. *Sol. Energy Mater. Sol. Cells.* **113**, 100–105 (2013).
 14. C. Istanbuluoglu, S. Göker, G. Hizalan, S. O. Hacioglu, Y. A. Udum, E. D. Yildiz, A. Cirpan, L. Toppare, Synthesis of a benzotriazole bearing alternating copolymer for organic photovoltaic applications. *New J. Chem.* **39**, 6623–6630 (2015).
 15. E. Kaya, D. H. Apaydn, D. E. Yldz, L. Toppare, A. Cirpan, Solution processable benzotriazole and fluorene containing copolymers for photovoltaic applications. *Sol. Energy Mater. Sol. Cells.* **99**, 321–326 (2012).
 16. H. Unay, G. A. dos Reis Benatto, M. J. Beliatis, S. A. Gevorgyan, P. Kavak, S. Memiş, A. Cirpan, L. Toppare, E. A. Parlak, F. C. Krebs, High stability of benzotriazole and benzodithiophene containing medium band-gap polymer solar cell. *Sol. Energy Mater. Sol. Cells.* **174**, 433–444 (2018).
 17. Q. Zhang, A. Cirpan, T. P. Russell, T. Emrick, Donor-acceptor poly(thiophene-block-terylene diimide) copolymers: Synthesis and solar cell fabrication. *Macromolecules.* **42**, 1079–1082 (2009).
 18. R. Yuksel, S. Coskun, G. Gunbas, A. Cirpan, L. Toppare, H. E. Unalan, Silver nanowire/conducting polymer nanocomposite electrochromic supercapacitor electrodes. *J. Electrochem. Soc.* **164**, A721–A727 (2017).
 19. R. Yuksel, S. C. Cevher, A. Cirpan, L. Toppare, H. E. Unalan, All-Organic Electrochromic Supercapacitor Electrodes. *J. Electrochem. Soc.* **162**, A2805–A2810 (2015).
 20. H. Coskun, A. Aljabour, P. De Luna, D. Farka, T. Greunz, D. Stifter, M. Kus, X. Zheng, M. Liu, A. W. Hassel, W. Schöfberger, E. H. Sargent, N. S. Sariciftci, P. Stadler, Biofunctionalized conductive polymers enable efficient CO₂ electroreduction. *Sci. Adv.* **3**, 1–9 (2017).
 21. D. H. Apaydin, E. Tordin, E. Portenkirchner, G. Aufischer, S. Schlager, M. Weichselbaumer, K. Oppelt, N. S. Sariciftci, Photoelectrochemical Reduction of CO₂ Using Third-Generation Conjugated Polymers. *ChemistrySelect.* **1**, 1156–1162 (2016).
 22. H. Naarmann, in *Ullmann's Encyclopedia of Industrial Chemistry* (Wiley-VCH Verlag GmbH & Co. KGaA, Weinheim, Germany, 2000;

http://doi.wiley.com/10.1002/14356007.a21_429).

23. M. Pope, H. P. Kallmann, P. Magnante, Electroluminescence in Organic Crystals. *J. Chem. Phys.* **38**, 2042–2043 (1963).
24. W. Helfrich, W. G. Schneider, Recombination Radiation in Anthracene Crystals. *Phys. Rev. Lett.* **14**, 229–231 (1965).
25. C. W. Tang, S. A. VanSlyke, Organic electroluminescent diodes. *Appl. Phys. Lett.* **51**, 913–915 (1987).
26. J. H. Burroughes, D. D. C. Bradley, A. R. Brown, R. N. Marks, K. Mackay, R. H. Friend, P. L. Burns, A. B. Holmes, Light-emitting diodes based on conjugated polymers. *Nature*. **347**, 539–541 (1990).
27. M. Schwoerer, H. C. Wolf, *Organic Molecular Solids* (Wiley-VCH Verlag GmbH & Co. KGaA, Weinheim, 2007; <http://www.amazon.com/Organic-Molecular-Solids-Physics-Textbook/dp/3527405402>).
28. W. Brütting, *Physi[1] W. Brütting, Physics of Organic Semiconductors. Weinheim: Wiley-VCH Verlag GmbH & Co. KGaA, 2006.cs of Organic Semiconductors* (Wiley-VCH Verlag GmbH & Co. KGaA, Weinheim, 2006; <http://doi.wiley.com/10.1002/9783527654949%0Ahttp://doi.wiley.com/10.1002/3527606637>).
29. V. Agranovich, *Excitations in Organic Solids* (Oxford University Press, Oxford, 2005; <https://www.oxfordscholarship.com/10.1093/acprof:oso/9780199234417.001.0001/acprof-9780199234417>).
30. S. Mukamel, T. Sergei, T. Wagersreiter, V. Chernyak, Electronic Coherence and Collective Optical Excitations of Conjugated Molecules. *Science* (80-.). **277**, 781–787 (1997).
31. C. F. van Nostrum, R. J. M. Nolte, S. J. Picken, A. J. Schouten, Synthesis and Supramolecular Chemistry of Novel Liquid Crystalline Crown Ether-Substituted Phthalocyanines: Toward Molecular Wires and Molecular Ionoelectronics. *J. Am. Chem. Soc.* **117**, 9957–9965 (1995).
32. D. Holten, D. F. Bocian, J. S. Lindsey, Probing electronic communication in covalently linked multiporphyrin arrays. A guide to the rational design of molecular photonic devices. *Acc. Chem. Res.* **35**, 57–69 (2002).
33. S. Setayesh, A. C. Grimsdale, T. Weil, V. Enkelmann, K. Müllen, F. Meghdadi, E. J. W. List, G. Leising, Polyfluorenes with polyphenylene dendron side chains: Toward non-aggregating, light-emitting polymers. *J. Am. Chem. Soc.* **123**, 946–953 (2001).
34. Y. Sun, K. Xiao, Y. Liu, J. Wang, J. Pei, G. Yu, D. Zhu, Oligothiophene-

- functionalized truxene: Star-shaped compounds for organic field-effect transistors. *Adv. Funct. Mater.* **15**, 818–822 (2005).
35. P. L. Burn, S. C. Lo, I. D. W. Samuel, The development of light-emitting dendrimers for displays. *Adv. Mater.* **19**, 1675–1688 (2007).
 36. D. Katsis, Y. H. Geng, J. J. Ou, S. W. Culligan, A. Trajkovska, S. H. Chen, L. J. Rothberg, Spiro-linked ter-, penta-, and heptafluorenes as novel amorphous materials for blue light emission. *Chem. Mater.* **14**, 1332–1339 (2002).
 37. K. Akagi, M. Suezaki, H. Shirakawa, H. Kyotani, M. Shimomura, Y. Tanabe, Synthesis of polyacetylene films with high density and high mechanical strength. *Synth. Met.* **28**, D1–D10 (1989).
 38. H. Lin, F. Bai, Electronic Process in Organic Solids. *Org. Optoelectron.*, 1–42 (2013).
 39. J. L. Bredas, G. B. Street, Polarons, Bipolarons, and Solitons in Conducting Polymers. *Acc. Chem. Res.* **18**, 309–315 (1985).
 40. A. J. Heeger, S. Kivelson, J. R. Schrieffer, W.-P. Su, Solitons in conducting polymers. *Rev. Mod. Phys.* **60**, 781–850 (1988).
 41. N. S. Sariciftci, *Primary Photoexcitations in Conjugated Polymers: Molecular Exciton Versus Semiconductor Band Model* (WORLD SCIENTIFIC, 1998; <https://doi.org/10.1142/3299>).
 42. U. Rauscher, H. Bässler, D. D. C. Bradley, M. Hennecke, Exciton versus band description of the absorption and luminescence spectra in poly(p-phenylenevinylene). *Phys. Rev. B.* **42**, 9830–9836 (1990).
 43. J. R. Lakowicz, *Principles of Fluorescence Spectroscopy* (Springer US, Boston, MA, 2006; <http://link.springer.com/10.1007/978-0-387-46312-4>).
 44. F. Laquai, Y. S. Park, J. J. Kim, T. Basché, Excitation energy transfer in organic materials: From fundamentals to optoelectronic devices. *Macromol. Rapid Commun.* **30**, 1203–1231 (2009).
 45. R. Wyckoff, *Crystal structures, Vol. 1* (New York, 1963).
 46. L. . Hung, C. . Chen, Recent progress of molecular organic electroluminescent materials and devices. *Mater. Sci. Eng. R Reports.* **39**, 143–222 (2002).
 47. J. S. Kim, M. Granström, R. H. Friend, N. Johansson, W. R. Salaneck, R. Daik, W. J. Feast, F. Cacialli, Indium–tin oxide treatments for single- and double-layer polymeric light-emitting diodes: The relation between the anode physical, chemical, and morphological properties and the device performance. *J. Appl. Phys.* **84**, 6859–6870 (1998).
 48. Y. F. Liu, J. Feng, Y. F. Zhang, H. F. Cui, D. Yin, Y. G. Bi, J. F. Song, Q. D.

- Chen, H. B. Sun, Improved efficiency of indium-tin-oxide-free flexible organic light-emitting devices. *Org. Electron. physics, Mater. Appl.* **15**, 478–483 (2014).
49. T.-H. Han, Y. Lee, M.-R. Choi, S.-H. Woo, S.-H. Bae, B. H. Hong, J.-H. Ahn, T.-W. Lee, Extremely efficient flexible organic light-emitting diodes with modified graphene anode. *Nat. Photonics.* **6**, 105–110 (2012).
 50. X. Wu, F. Li, W. Wu, T. Guo, Flexible white phosphorescent organic light emitting diodes based on multilayered graphene/PEDOT:PSS transparent conducting film. *Appl. Surf. Sci.* **295**, 214–218 (2014).
 51. A. Andersson, N. Johansson, P. Bröms, N. Yu, D. Lupo, W. R. Salaneck, Fluorine Tin Oxide as an Alternative to Indium Tin Oxide in Polymer LEDs. *Adv. Mater.* **10**, 859–863 (1998).
 52. J. Zhao, S. Xie, S. Han, Z. Yang, L. Ye, T. Yang, Organic light-emitting diodes with AZO films as electrodes. *Synth. Met.* **114**, 251–254 (2000).
 53. J. Cui, A. Wang, N. L. Edleman, J. Ni, P. Lee, N. R. Armstrong, T. J. Marks, Indium Tin Oxide Alternatives-High Work Function Transparent Conducting Oxides as Anodes for Organic Light-Emitting Diodes. *Adv. Mater.* **13**, 1476–1480 (2001).
 54. M. A. Baldo, M. E. Thompson, S. R. Forrest, Phosphorescent materials for application to organic light emitting devices. *Pure Appl. Chem.* **71**, 2095–2106 (2007).
 55. S. L. Lai, S. L. Tao, M. Y. Chan, T. W. Ng, M. F. Lo, C. S. Lee, X. H. Zhang, S. T. Lee, Efficient white organic light-emitting devices based on phosphorescent iridium complexes. *Org. Electron. physics, Mater. Appl.* **11**, 1511–1515 (2010).
 56. T. Wakimoto, Y. Fukuda, K. Nagayama, A. Yokoi, H. Nakada, M. Tsuchida, Organic EL cells using alkaline metal compounds as electron injection materials. *IEEE Trans. Electron Devices.* **44**, 1245–1248 (1997).
 57. G. E. Jabbour, B. Kippelen, N. R. Armstrong, N. Peyghambarian, Aluminum based cathode structure for enhanced electron injection in electroluminescent organic devices. *Appl. Phys. Lett.* **73**, 1185–1187 (1998).
 58. S. J. Kang, D. S. Park, S. Y. Kim, C. N. Whang, K. Jeong, S. Im, Enhancing the electroluminescent properties of organic light-emitting devices using a thin NaCl layer. *Appl. Phys. Lett.* **81**, 2581–2583 (2002).
 59. N. C. Greenham, R. H. Friend, D. D. C. Bradley, Angular Dependence of the Emission from a Conjugated Polymer Light-Emitting Diode: Implications for efficiency calculations. *Adv. Mater.* **6**, 491–494 (1994).

60. I. D. Parker, Carrier tunneling and device characteristics in polymer light-emitting diodes. *J. Appl. Phys.* **75**, 1656–1666 (1994).
61. Ş. C. Cevher, D. Keles, G. Hizalan, L. Toppare, A. Cirpan, Alkyl-end phenanthroimidazole modification of benzotriazole based conjugated polymers for optoelectronic applications. *Synth. Met.* **244**, 1–9 (2018).
62. Q. Y. Zhang, K. Pita, S. Buddhudu, C. H. Kam, Luminescent properties of rare-earth ion doped yttrium silicate thin film phosphors for a full-colour display. *J. Phys. D. Appl. Phys.* **35**, 3085–3090 (2002).
63. Q. Y. Zhang, K. Pita, W. Ye, W. X. Que, Influence of annealing atmosphere and temperature on photoluminescence of Tb³⁺ or Eu³⁺-activated zinc silicate thin film phosphors via sol-gel method. *Chem. Phys. Lett.* **351**, 163–170 (2002).
64. D. Zhao, W. Huang, Z. Qin, Z. Wang, J. Yu, Emission spectral stability modification of tandem organic light-emitting diodes through controlling charge-carrier migration and outcoupling efficiency at intermediate/emitting unit interface. *ACS Omega.* **3**, 3348–3356 (2018).
65. Y. Yin, J. Yu, H. Cao, L. Zhang, H. Sun, W. Xie, Efficient non-doped phosphorescent orange, blue and white organic light-emitting devices. *Sci. Rep.* **4**, 1–7 (2014).
66. Y. Liu, L.-S. Cui, M.-F. Xu, X.-B. Shi, D.-Y. Zhou, Z.-K. Wang, Z.-Q. Jiang, L.-S. Liao, Highly efficient single-layer organic light-emitting devices based on a bipolar pyrazine/carbazole hybrid host material. *J. Mater. Chem. C.* **2**, 2488–2495 (2014).
67. L. Deng, T. Zhang, R. Wang, J. Li, Diphenylphosphorylpyridine-functionalized iridium complexes for high-efficiency monochromic and white organic light-emitting diodes. *J. Mater. Chem.* **22**, 15910–15918 (2012).
68. S. Wu, S. Li, Q. Sun, C. Huang, M. K. Fung, Highly efficient white organic light-emitting diodes with ultrathin emissive layers and a spacer-free structure. *Sci. Rep.* **6**, 4–11 (2016).
69. Y. Kawamura, S. Yanagida, S. R. Forrest, Energy transfer in polymer electrophosphorescent light emitting devices with single and multiple doped luminescent layers. *J. Appl. Phys.* **92**, 87–93 (2002).
70. Y. Zhang, S. L. Lai, Q. X. Tong, M. F. Lo, T. W. Ng, M. Y. Chan, Z. C. Wen, J. He, K. S. Jeff, X. L. Tang, W. M. Liu, C. C. Ko, P. F. Wang, C. S. Lee, High efficiency nondoped deep-blue organic light emitting devices based on imidazole- π -triphenylamine derivatives. *Chem. Mater.* **24**, 61–70 (2012).
71. H. Liu, Q. Bai, W. Li, Y. Guo, L. Yao, Y. Gao, J. Li, P. Lu, B. Yang, Y. Ma, Efficient deep-blue non-doped organic light-emitting diode with improved roll-off of efficiency based on hybrid local and charge-transfer excited state. *RSC*

- Adv.* **6**, 70085–70090 (2016).
72. W. C. Chen, Y. Yuan, S. F. Ni, Z. L. Zhu, J. Zhang, Z. Q. Jiang, L. S. Liao, F. L. Wong, C. S. Lee, Highly Efficient Deep-Blue Electroluminescence from a Charge-Transfer Emitter with Stable Donor Skeleton. *ACS Appl. Mater. Interfaces.* **9**, 7331–7338 (2017).
 73. S. Chen, Y. Wu, Y. Zhao, D. Fang, Deep blue organic light-emitting devices enabled by bipolar phenanthro[9,10-d]imidazole derivatives. *RSC Adv.* **5**, 72009–72018 (2015).
 74. A. Ivanauskaite, R. Lygaitis, S. Raisys, K. Kazlauskas, G. Kreiza, D. Volyniuk, D. Gudeika, S. Jursenas, J. V. Grazulevicius, Structure–property relationship of blue solid state emissive phenanthroimidazole derivatives. *Phys. Chem. Chem. Phys.* **19**, 16737–16748 (2017).
 75. J. R. Lakowicz, *Principles of fluorescence spectroscopy, 3rd Edition*, Joseph R. Lakowicz, editor (2006).
 76. H. Jin, W. Zhang, D. Wang, Z. Chu, Z. Shen, D. Zou, X. Fan, Q. Zhou, Dendron-jacketed electrophosphorescent copolymers: Improved efficiency and tunable emission color by partial energy transfer. *Macromolecules.* **44**, 9556–9564 (2011).
 77. B. Valderrama-García, E. Rodríguez-Alba, E. Morales-Espinoza, K. Moineau Chane-Ching, E. Rivera, Synthesis and Characterization of Novel Polythiophenes Containing Pyrene Chromophores: Thermal, Optical and Electrochemical Properties. *Molecules.* **21**, 172–190 (2016).
 78. C. Istanbuluoglu, S. Göker, G. Hizalan, S. O. Hacıoglu, Y. A. Udum, E. D. Yildiz, A. Cirpan, L. Toppare, Synthesis of a benzotriazole bearing alternating copolymer for organic photovoltaic applications. *New J. Chem.* **39**, 6623–6630 (2015).
 79. A. Tanimoto, T. Yamamoto, Nickel-2,2'-bipyridyl and palladium-triphenylphosphine complex promoted synthesis of new π -conjugated poly(2-hexylbenzotriazole)s and characterization of the polymers. *Adv. Synth. Catal.* **346**, 1818–1823 (2004).
 80. A. Tanimoto, T. Yamamoto, Synthesis of n-type poly(benzotriazole)s having p-conducting and polymerizable carbazole pendants. *Macromolecules.* **39**, 3546–3552 (2006).
 81. A. Balan, D. Baran, G. Gunbas, A. Durmus, F. Ozyurt, L. Toppare, One polymer for all: benzotriazole containing donor–acceptor type polymer as a multi-purpose material. *Chem. Commun.*, 6768–6770 (2009).
 82. Y. Ner, J. G. Grote, J. A. Stuart, G. A. Sotzing, White luminescence from multiple-dye-doped electrospun DNA nanofibers by fluorescence resonance

- energy transfer. *Angew. Chemie - Int. Ed.* **48**, 5134–5138 (2009).
83. E. Kaya, A. Balan, D. Baran, A. Cirpan, L. Toppare, Electrochromic and optical studies of solution processable benzotriazole and fluorene containing copolymers. *Org. Electron. physics, Mater. Appl.* **12**, 202–209 (2011).
 84. C. Q. Ma, M. Fonrodona, M. C. Schikora, M. M. Wienk, R. A. J. Janssen, P. Bäuerle, Solution-processed bulk-heterojunction solar cells based on monodisperse dendritic oligothiophenes. *Adv. Funct. Mater.* **18**, 3323–3331 (2008).
 85. A. Sadana, N. Sadana, *Handbook of Biosensors and Biosensor Kinetics* (Elsevier, 2011).
 86. R. S. Marks, D. C. Cullen, I. Karube, C. R. Lowe, H. H. Weetall, Eds., *Handbook of Biosensors and Biochips* (John Wiley & Sons, Ltd, Chichester, UK, 2008).
 87. S. Li, J. Singh, H. Li, I. A. Banerjee, Eds., *Biosensor Nanomaterials* (Wiley-VCH Verlag GmbH & Co. KGaA, Weinheim, Germany, 2011).
 88. C. Zhu, A. Chortos, Y. Wang, R. Pfattner, T. Lei, A. C. Hinckley, I. Pochorovski, X. Yan, J. W. F. To, J. Y. Oh, J. B. H. Tok, Z. Bao, B. Murmann, Stretchable temperature-sensing circuits with strain suppression based on carbon nanotube transistors. *Nat. Electron.* **1**, 183–190 (2018).
 89. X.-Y. Liu, F. Cheng, Y. Liu, W.-G. Li, Y. Chen, H. Pan, H.-J. Liu, Thermoresponsive gold nanoparticles with adjustable lower critical solution temperature as colorimetric sensors for temperature, pH and salt concentration. *J. Mater. Chem.* **20**, 278–284 (2010).
 90. B. Davaji, H. D. Cho, M. Malakoutian, J.-K. Lee, G. Panin, T. W. Kang, C. H. Lee, A patterned single layer graphene resistance temperature sensor. *Sci. Rep.* **7**, 8811–8821 (2017).
 91. D. J. Wales, J. Grand, V. P. Ting, R. D. Burke, K. J. Edler, C. R. Bowen, S. Mintova, A. D. Burrows, Gas sensing using porous materials for automotive applications. *Chem. Soc. Rev.* **44**, 4290–4321 (2015).
 92. G. Chen, T. M. Paronyan, E. M. Pigos, A. R. Harutyunyan, Enhanced gas sensing in pristine carbon nanotubes under continuous ultraviolet light illumination. *Sci. Rep.* **2**, 343–350 (2012).
 93. S. Thakur, P. Patil, Enhanced LPG sensing-performance at room temperature of poly(o-anisidine)–CeO₂ nanocomposites. *RSC Adv.* **6**, 45768–45782 (2016).
 94. T. Yamada, Y. Hayamizu, Y. Yamamoto, Y. Yomogida, A. Izadi-Najafabadi, D. N. Futaba, K. Hata, A stretchable carbon nanotube strain sensor for human-

- motion detection. *Nat. Nanotechnol.* **6**, 296–301 (2011).
95. H. Xu, Y. F. Lu, J. X. Xiang, M. K. Zhang, Y. J. Zhao, Z. Y. Xie, Z. Z. Gu, A multifunctional wearable sensor based on a graphene/inverse opal cellulose film for simultaneous, in situ monitoring of human motion and sweat. *Nanoscale.* **10**, 2090–2098 (2018).
 96. H. Li, Q. Yang, J. Li, H. Gao, P. Li, H. Zhou, The impact of temperature on microbial diversity and AOA activity in the Tengchong Geothermal Field, China. *Sci. Rep.* **5**, 17056–17068 (2015).
 97. L. L. Lavery, G. L. Whiting, A. C. Arias, All ink-jet printed polyfluorene photosensor for high illuminance detection. *Org. Electron.* **12**, 682–685 (2011).
 98. G. Yu, Y. Cao, J. Wang, J. McElvain, A. J. Heeger, High sensitivity polymer photosensors for image sensing applications. *Synth. Met.* **102**, 904–907 (1999).
 99. T. Manouras, M. Vamvakaki, Field responsive materials: photo-, electro-, magnetic- and ultrasound-sensitive polymers. *Polym. Chem.* **8**, 74–96 (2017).
 100. S. Chun, I. Hwang, W. Son, J.-H. Chang, W. Park, Recognition, classification, and prediction of the tactile sense. *Nanoscale.* **10**, 10545–10553 (2018).
 101. M. Xu, J. Qi, F. Li, X. Liao, S. Liu, Y. Zhang, Ultra-thin, transparent and flexible tactile sensors based on graphene films with excellent anti-interference. *RSC Adv.* **7**, 30506–30512 (2017).
 102. J. Engel, J. Chen, Z. Fan, C. Liu, Polymer micromachined multimodal tactile sensors. *Sensors Actuators A Phys.* **117**, 50–61 (2005).
 103. S. Singh, “Biosensors Market worth \$31.5 billion by 2024” (2019), (available at <https://www.marketsandmarkets.com/PressReleases/biosensors.asp>).
 104. L. S. B. Upadhyay, N. Verma, in *Environmental Microbial Biotechnology*, L. B. Sukla, N. Pradhan, S. Panda, B. K. Mishra, Eds. (Springer International Publishing, Cham, 2015), pp. 77–90.
 105. N. Cennamo, A. Varriale, A. Pennacchio, M. Staiano, D. Massarotti, L. Zeni, S. D’Auria, An innovative plastic optical fiber-based biosensor for new bio/applications. The case of celiac disease. *Sensors Actuators B Chem.* **176**, 1008–1014 (2013).
 106. M. H. Mat Zaid, J. Abdullah, N. A. Yusof, Y. Sulaiman, H. Wasoh, M. F. Md Noh, R. Issa, PNA biosensor based on reduced graphene oxide/water soluble quantum dots for the detection of Mycobacterium tuberculosis. *Sensors Actuators B Chem.* **241**, 1024–1034 (2017).
 107. D. Yu, B. Blankert, J. Viré, J. Kauffmann, Biosensors in Drug Discovery and Drug Analysis. *Anal. Lett.* **38**, 1687–1701 (2005).

108. L. A. Mercante, V. P. Scagion, F. L. Migliorini, L. H. C. Mattoso, D. S. Correa, Electrospinning-based (bio)sensors for food and agricultural applications: A review. *TrAC Trends Anal. Chem.* **91**, 91–103 (2017).
109. G. Kaur, R. Adhikari, P. Cass, M. Bown, P. Gunatillake, Electrically conductive polymers and composites for biomedical applications. *RSC Adv.* **5**, 37553–37567 (2015).
110. L. C. Clark, C. Lyons, Electrode Systems for Continuous Monitoring in Cardiovascular Surgery. *Ann. N. Y. Acad. Sci.* **102**, 29–45 (1962).
111. M. Frasconi, C. Tortolini, F. Botr. , F. Mazzei, Multifunctional Au Nanoparticle Dendrimer-Based Surface Plasmon Resonance Biosensor and Its Application for Improved Insulin Detection. *Anal. Chem.* **82**, 7335–7342 (2010).
112. Y. Amano, Q. Cheng, Detection of influenza virus: traditional approaches and development of biosensors. *Anal. Bioanal. Chem.* **381**, 156–164 (2005).
113. R. L. Caygill, G. E. Blair, P. A. Millner, A review on viral biosensors to detect human pathogens. *Anal. Chim. Acta.* **681**, 8–15 (2010).
114. J.-M. Moon, N. Thapliyal, K. K. Hussain, R. N. Goyal, Y.-B. Shim, Conducting polymer-based electrochemical biosensors for neurotransmitters: A review. *Biosens. Bioelectron.* **102**, 540–552 (2018).
115. A. Kausaite-Minkstimiene, A. Ramanaviciene, A. Ramanavicius, Surface plasmon resonance biosensor for direct detection of antibodies against human growth hormone. *Analyst.* **134**, 2051–2057 (2009).
116. B. Pejcic, R. De Marco, G. Parkinson, The role of biosensors in the detection of emerging infectious diseases. *Analyst.* **131**, 1079–1090 (2006).
117. S. Neethirajan, S. R. Ahmed, R. Chand, J. Buoziš, É. Nagy, Recent Advances in Biosensor Development for Foodborne Virus Detection. *Nanotheranostics.* **1**, 272–295 (2017).
118. J. Wang, X. Cai, G. Rivas, H. Shiraishi, P. A. M. Farias, N. Dontha, DNA Electrochemical Biosensor for the Detection of Short DNA Sequences Related to the Human Immunodeficiency Virus. *Anal. Chem.* **68**, 2629–2634 (1996).
119. Y. Braham, H. Barhoumi, A. Maaref, Urease capacitive biosensors using functionalized magnetic nanoparticles for atrazine pesticide detection in environmental samples. *Anal. Methods.* **5**, 4898–4904 (2013).
120. S. Hideshima, M. Kobayashi, T. Wada, S. Kuroiwa, T. Nakanishi, N. Sawamura, T. Asahi, T. Osaka, A label-free electrical assay of fibrous amyloid β based on semiconductor biosensing. *Chem. Commun.* **50**, 3476–3479 (2014).
121. K. Mondal, A. Sharma, Recent advances in electrospun metal-oxide nanofiber based interfaces for electrochemical biosensing. *RSC Adv.* **6**, 94595–94616

- (2016).
122. Z. Wang, Z. Dai, Carbon nanomaterial-based electrochemical biosensors: an overview. *Nanoscale*. **7**, 6420–6431 (2015).
 123. D. Kai, M. P. Prabhakaran, G. Jin, S. Ramakrishna, Biocompatibility evaluation of electrically conductive nanofibrous scaffolds for cardiac tissue engineering. *J. Mater. Chem. B*. **1**, 2305–2314 (2013).
 124. A. Pron, P. Rannou, Processible conjugated polymers: from organic semiconductors to organic metals and superconductors. *Prog. Polym. Sci.* **27**, 135–190 (2002).
 125. K. Jen, G. G. Miller, R. L. Elsenbaumer, Highly conducting, soluble, and environmentally-stable poly(3-alkylthiophenes). *J. Chem. Soc. Chem. Commun.* **5**, 1346–1347 (1986).
 126. S. Bhandari, N. K. Singha, D. Khastgir, Electrochemical synthesis of nanostructured polyaniline: Heat treatment and synergistic effect of simultaneous dual doping. *J. Appl. Polym. Sci.* **129**, 1264–1273 (2013).
 127. Z. Q. Gao, S. Rafea, L. H. Lim, Detection of Nucleic Acids Using Enzyme-Catalyzed Template-Guided Deposition of Polyaniline. *Adv. Mater.* **19**, 602–606 (2007).
 128. E. Komarova, M. Aldissi, A. Bogomolova, Direct electrochemical sensor for fast reagent-free DNA detection. *Biosens. Bioelectron.* **21**, 182–189 (2005).
 129. K. Krishnamoorthy, R. S. Gokhale, A. Q. Contractor, A. Kumar, Novel label-free DNA sensors based on poly(3,4-ethylenedioxythiophene). *Chem. Commun.* **10**, 820–821 (2004).
 130. I. Willner, E. Katz, *Bioelectronics: From Theory to Applications* (Wiley, 2005; <https://onlinelibrary.wiley.com/doi/book/10.1002/352760376X>).
 131. H. Wu, C.-J. Lee, H. Wang, Y. Hu, M. Young, Y. Han, F.-J. Xu, H. Cong, G. Cheng, Highly sensitive and stable zwitterionic poly(sulfobetaine-3,4-ethylenedioxythiophene) (PSBEDOT) glucose biosensor. *Chem. Sci.* **9**, 2540–2546 (2018).
 132. M. Bilgi, E. Ayranci, Development of amperometric biosensors using screen-printed carbon electrodes modified with conducting polymer and nanomaterials for the analysis of ethanol, methanol and their mixtures. *J. Electroanal. Chem.* **823**, 588–592 (2018).
 133. M. David, M. M. Barsan, C. M. A. Brett, M. Florescu, Improved glucose label-free biosensor with layer-by-layer architecture and conducting polymer poly(3,4-ethylenedioxythiophene). *Sensors Actuators B Chem.* **255**, 3227–3234 (2018).

134. Y. Liu, A. P. F. Turner, M. Zhao, W. C. Mak, Processable enzyme-hybrid conductive polymer composites for electrochemical biosensing. *Biosens. Bioelectron.* **100**, 374–381 (2018).
135. D. R. Thévenot, K. Toth, R. A. Durst, G. S. Wilson, ELECTROCHEMICAL BIOSENSORS: RECOMMENDED DEFINITIONS AND CLASSIFICATION. *Anal. Lett.* **34**, 635–659 (2001).
136. V. Perumal, U. Hashim, Advances in biosensors: Principle, architecture and applications. *J. Appl. Biomed.* **12**, 1–15 (2014).
137. D. G. Prajapati, B. Kandasubramanian, Progress in the Development of Intrinsically Conducting Polymer Composites as Biosensors. *Macromol. Chem. Phys.* **220**, 1–26 (2019).
138. D. O’Hare, in *Body Sensor Networks*, G.-Z. Yang, Ed. (Springer London, London, 2014; <https://linkinghub.elsevier.com/retrieve/pii/S0166526X1730034X>), vol. 77, pp. 55–115.
139. M. Gerard, Application of conducting polymers to biosensors. *Biosens. Bioelectron.* **17**, 345–359 (2002).
140. P. D’Orazio, Biosensors in clinical chemistry. *Clin. Chim. Acta.* **334**, 41–69 (2003).
141. D. Grieshaber, R. MacKenzie, J. Vörös, E. Reimhult, Electrochemical Biosensors - Sensor Principles and Architectures. *Sensors.* **8**, 1400–1458 (2008).
142. D. R. Thévenot, K. Toth, R. A. Durst, G. S. Wilson, Electrochemical biosensors: recommended definitions and classification | International Union of Pure and Applied Chemistry: Physical Chemistry Division, Commission I.7 (Biophysical Chemistry); Analytical Chemistry Division, Commission V.5 (Electroanalytical. *Biosens. Bioelectron.* **16**, 121–131 (2001).
143. G. Sauerbrey, Use of Quartz Crystal Vibrator for Weighting Thin Films on a Microbalance. *Zeitschrift fur Phys.* **155**, 206–222 (1959).
144. A. Janshoff, H.-J. Galla, C. Steinem, Piezoelectric Mass-Sensing Devices as Biosensors—An Alternative to Optical Biosensors? *Angew. Chemie.* **39**, 4004–4032 (2000).
145. B. Ebarvia, S. Cabanilla, F. Sevilla III, Biomimetic properties and surface studies of a piezoelectric caffeine sensor based on electrosynthesized polypyrrole. *Talanta.* **66**, 145–152 (2005).
146. D. D. Borole, U. R. Kapadi, P. P. Mahulikar, D. G. Hundiwale, Conducting polymers: an emerging field of biosensors. *Des. Monomers Polym.* **9**, 1–11

- (2006).
147. P. Ripka, A. Tipek, *Modern Sensors Handbook* (ISTE, London, UK, 2007; <http://doi.wiley.com/10.1002/9780470612231>).
 148. K. Ramanathan, B. Danielsson, Principles and applications of thermal biosensors. *Biosens. Bioelectron.* **16**, 417–423 (2001).
 149. Y. Zhou, C.-W. Chiu, H. Liang, Interfacial Structures and Properties of Organic Materials for Biosensors: An Overview. *Sensors.* **12**, 15036–15062 (2012).
 150. W. Xie, L. Bülow, B. Xie, Pyrroloquinoline quinone glucose dehydrogenase adopted in thermometric analysis for enhancement of glucose determination. *J. Therm. Anal. Calorim.* **134**, 1913–1919 (2018).
 151. P. Damborsky, J. Vitel, J. Katrlík, Optical biosensors. *Essays Biochem.* **60**, 91–100 (2016).
 152. R. S. Sethi, Transducer aspects of biosensors. *Biosens. Bioelectron.* **9**, 243–264 (1994).
 153. B. Kuswandi, R. Andres, R. Narayanaswamy, Optical fibre biosensors based on immobilised enzymes. *Analyst.* **126**, 1469–1491 (2001).
 154. I. Z. Mohamad Ahad, S. Wadi Harun, S. N. Gan, S. W. Phang, Polyaniline (PANI) optical sensor in chloroform detection. *Sensors Actuators B Chem.* **261**, 97–105 (2018).
 155. A. Domínguez-Aragón, J. A. Olmedo-Martínez, E. A. Zaragoza-Contreras, Colorimetric sensor based on a poly(ortho-phenylenediamine-co-aniline) copolymer for the monitoring of tilapia (*Oreochromis niloticus*) freshness. *Sensors Actuators B Chem.* **259**, 170–176 (2018).
 156. R. C. Rodrigues, C. Ortiz, Á. Berenguer-Murcia, R. Torres, R. Fernández-Lafuente, Modifying enzyme activity and selectivity by immobilization. *Chem. Soc. Rev.* **42**, 6290–6307 (2013).
 157. T. Itoh, Y. Shibuya, A. Yamaguchi, Y. Hoshikawa, O. Tanaike, T. Tsunoda, T. Hanaoka, S. Hamakawa, F. Mizukami, A. Hayashi, T. Kyotani, G. D. Stucky, High-performance bioelectrocatalysts created by immobilization of an enzyme into carbon-coated composite membranes with nano-tailored structures. *J. Mater. Chem. A.* **5**, 20244–20251 (2017).
 158. D. E. Koshland, The Key–Lock Theory and the Induced Fit Theory. *Angew. Chemie Int. Ed. English.* **33**, 2375–2378 (1995).
 159. E. Fischer, Einfluss der Configuration auf die Wirkung der Enzyme. *Berichte der Dtsch. Chem. Gesellschaft.* **27**, 2985–2993 (1894).
 160. F.-G. Bănică, *Chemical Sensors and Biosensors* (John Wiley & Sons, Ltd,

- Chichester, UK, 2012; <http://doi.wiley.com/10.1002/9781118354162>).
161. F. R. R. Teles, L. P. Fonseca, Applications of polymers for biomolecule immobilization in electrochemical biosensors. *Mater. Sci. Eng. C.* **28**, 1530–1543 (2008).
 162. S. Singh, D. V. S. Jain, M. L. Singla, One step electrochemical synthesis of gold-nanoparticles–polypyrrole composite for application in catechin electrochemical biosensor. *Anal. Methods.* **5**, 1024–1032 (2013).
 163. A. Dwevedi, *Enzyme Immobilization* (Springer International Publishing, Cham, 2016; <http://link.springer.com/10.1007/978-3-319-41418-8>).
 164. S. Chawla, R. Rawal, Shabnam, R. C. Kuhad, C. S. Pundir, An amperometric polyphenol biosensor based on laccase immobilized on epoxy resin membrane. *Anal. Methods.* **3**, 709–714 (2011).
 165. Y. Li, G. Huang, X. Zhang, B. Li, Y. Chen, T. Lu, T. J. Lu, F. Xu, Magnetic Hydrogels and Their Potential Biomedical Applications. *Adv. Funct. Mater.* **23**, 660–672 (2013).
 166. H. Zejli, J. L. Hidalgo-Hidalgo de Cisneros, I. Naranjo-Rodriguez, B. Liu, K. R. Temsamani, J. L. Marty, Phenol biosensor based on Sonogel-Carbon transducer with tyrosinase alumina sol–gel immobilization. *Anal. Chim. Acta.* **612**, 198–203 (2008).
 167. Q. Fan, D. Shan, H. Xue, Y. He, S. Cosnier, Amperometric phenol biosensor based on laponite clay–chitosan nanocomposite matrix. *Biosens. Bioelectron.* **22**, 816–821 (2007).
 168. F. Selampinar, U. Akbulut, M. Y. Özden, L. Toppare, Immobilization of invertase in conducting polymer matrices. *Biomaterials.* **18**, 1163–1168 (1997).
 169. B. D. Malhotra, A. Chaubey, S. P. Singh, Prospects of conducting polymers in biosensors. *Anal. Chim. Acta.* **578**, 59–74 (2006).
 170. P. K. H. Ho, J. Kim, J. H. Burroughes, H. Becker, S. F. Y. Li, T. M. Brown, F. Cacialli, R. H. Friend, Molecular-scale interface engineering for polymer light-emitting diodes. *Nature.* **404**, 481–484 (2000).
 171. A. Michalska, Optimizing the analytical performance and construction of ion-selective electrodes with conducting polymer-based ion-to-electron transducers. *Anal. Bioanal. Chem.* **384**, 391–406 (2005).
 172. J. Bobacka, Conducting Polymer-Based Solid-State Ion-Selective Electrodes. *Electroanalysis.* **18**, 7–18 (2006).
 173. L. Xia, Z. Wei, M. Wan, Conducting polymer nanostructures and their application in biosensors. *J. Colloid Interface Sci.* **341**, 1–11 (2010).

174. K. Mosbach, *Immobilized Enzymes* (Academic Press, 1976; <http://www.sciencedirect.com/science/article/pii/S007668797644003X>), vol. 44.
175. P. Cuatrecasas, Immobilized Enzymes. *Science* (80-.). **184**, 56–56 (1974).
176. G. B. Broun, in *Immobilized Enzymes* (Academic Press, 1976; <http://www.sciencedirect.com/science/article/pii/S0076687976440223>), vol. 44, pp. 263–280.
177. T. H. Ji, The application of chemical crosslinking for studies on cell membranes and the identification of surface reporters. *Biochim. Biophys. Acta - Rev. Biomembr.* **559**, 39–69 (1979).
178. A. F. Collings, F. Caruso, Biosensors: recent advances. *Reports Prog. Phys.* **60**, 1397–1445 (1997).
179. L. D. Bowers, P. W. Carr, (Springer Berlin Heidelberg, Berlin, Heidelberg, 1980; http://link.springer.com/10.1007/3540096868_4), pp. 89–129.
180. F. E. Kanik, E. Rende, S. Timur, L. Toppare, A novel functional conducting polymer: synthesis and application to biomolecule immobilization. *J. Mater. Chem.* **22**, 22517–22525 (2012).
181. S. Cosnier, in *Handbook of Biosensors and Biochips* (John Wiley & Sons, Ltd, Chichester, UK, 2008; <https://doi.org/10.1002/9780470061565.hbb025>), *Major Reference Works*.
182. S. Cosnier, Biosensors based on electropolymerized films: new trends. *Anal. Bioanal. Chem.* **377**, 507–520 (2003).
183. M. M. Rodríguez-Delgado, G. S. Alemán-Nava, J. M. Rodríguez-Delgado, G. Dieck-Assad, S. O. Martínez-Chapa, D. Barceló, R. Parra, Laccase-based biosensors for detection of phenolic compounds. *TrAC Trends Anal. Chem.* **74**, 21–45 (2015).
184. S. Sukhonthara, K. Kaewka, C. Theerakulkait, Inhibitory effect of rice bran extracts and its phenolic compounds on polyphenol oxidase activity and browning in potato and apple puree. *Food Chem.* **190**, 922–927 (2016).
185. P. Baldrian, Fungal laccases – occurrence and properties. *FEMS Microbiol. Rev.* **30**, 215–242 (2006).
186. K. Riedel, B. Beyersdorf-Radeck, B. Neumann, F. Schaller, Microbial sensors for determination of aromatics and their chloro derivatives. Part III: Determination of chlorinated phenols using a biosensor containing *Trichosporon beigelii* (cutaneum). *Appl. Microbiol. Biotechnol.* **43**, 7–9 (1995).
187. D. Luthria, A. P. Singh, T. Wilson, N. Vorsa, G. S. Banuelos, B. T. Vinyard, Influence of conventional and organic agricultural practices on the phenolic

- content in eggplant pulp: Plant-to-plant variation. *Food Chem.* **121**, 406–411 (2010).
188. E. Meulenberg, Phenolics: Occurrence and Immunochemical Detection in Environment and Food. *Molecules.* **14**, 439–473 (2009).
 189. A. Gardziella, L. A. Pilato, A. Knop, *Phenolic Resins* (Springer Berlin Heidelberg, Berlin, Heidelberg, 2000; <http://link.springer.com/10.1007/978-3-662-04101-7>).
 190. A. A. Makarenko, I. P. Bezverbnaya, I. A. Kosheleva, T. N. Kuvichkina, Development of Biosensors for Phenol Determination from Bacteria Found in Petroleum Fields of West Siberia. **38**, 23–27 (2002).
 191. J. KULYS, I. BRATKOVSKAJA, Antioxidants determination with laccase. *Talanta.* **72**, 526–531 (2007).
 192. A. P. Annachhatre, S. H. Gheewala, Biodegradation of chlorinated phenolic compounds. *Biotechnol. Adv.* **14**, 35–56 (1996).
 193. N. Nakada, T. Tanishima, H. Shinohara, K. Kiri, H. Takada, Pharmaceutical chemicals and endocrine disrupters in municipal wastewater in Tokyo and their removal during activated sludge treatment. *Water Res.* **40**, 3297–3303 (2006).
 194. S. Suárez, M. Carballa, F. Omil, J. M. Lema, How are pharmaceutical and personal care products (PPCPs) removed from urban wastewaters? *Rev. Environ. Sci. Bio/Technology.* **7**, 125–138 (2008).
 195. S. Zhang, Q. Zhang, S. Darisaw, O. Ehie, G. Wang, Simultaneous quantification of polycyclic aromatic hydrocarbons (PAHs), polychlorinated biphenyls (PCBs), and pharmaceuticals and personal care products (PPCPs) in Mississippi river water, in New Orleans, Louisiana, USA. *Chemosphere.* **66**, 1057–1069 (2007).
 196. X. Wang, M. Wu, H. Li, Q. Wang, P. He, Y. Fang, Simultaneous electrochemical determination of hydroquinone and catechol based on three-dimensional graphene/MWCNTs/BMIMPF₆ nanocomposite modified electrode. *Sensors Actuators B Chem.* **192**, 452–458 (2014).
 197. Q. Guo, J. Huang, P. Chen, Y. Liu, H. Hou, T. You, Simultaneous determination of catechol and hydroquinone using electrospun carbon nanofibers modified electrode. *Sensors Actuators B Chem.* **163**, 179–185 (2012).
 198. L. Wang, Y. Zhang, Y. Du, D. Lu, Y. Zhang, C. Wang, Simultaneous determination of catechol and hydroquinone based on poly(diallyldimethylammonium chloride) functionalized graphene-modified glassy carbon electrode. *J. Solid State Electrochem.* **16**, 1323–1331 (2012).

199. S. Chandra, H. Lang, D. Bahadur, Polyaniline-iron oxide nanohybrid film as multi-functional label-free electrochemical and biomagnetic sensor for catechol. *Anal. Chim. Acta.* **795**, 8–14 (2013).
200. D. C. Topping, L. G. Bernard, J. L. O'Donoghue, J. C. English, Hydroquinone: Acute and subchronic toxicity studies with emphasis on neurobehavioral and nephrotoxic effects. *Food Chem. Toxicol.* **45**, 70–78 (2007).
201. S. Canofeni, S. Di Sario, J. Mela, R. Pilloton, Comparison of Immobilisation Procedures for Development of an Electrochemical PPO-Based Biosensor for on Line Monitoring of a Depuration Process. *Anal. Lett.* **27**, 1659–1669 (1994).
202. Y. Tan, X. Guo, J. Zhang, J. Kan, Amperometric catechol biosensor based on polyaniline–polyphenol oxidase. *Biosens. Bioelectron.* **25**, 1681–1687 (2010).
203. S.-Y. Seo, V. K. Sharma, N. Sharma, Mushroom Tyrosinase: Recent Prospects. *J. Agric. Food Chem.* **51**, 2837–2853 (2003).
204. J. S. Chen, D. J. Charest, M. R. Marshall, C. I. Wei, Comparison of two treatment methods on the purification of shrimp polyphenol oxidase. *J. Sci. Food Agric.* **75**, 12–18 (1997).
205. E. Ziyar, Ş. Pekyarımcı, Characterization of Polyphenol Oxidase from Jerusalem Artichoke (*Helianthus tuberosus*). *Turkish J. Chem.* **27**, 217–225 (2003).
206. Ş. Şimşek, A. Yemenicioğlu, Partial purification and kinetic characterization of mushroom stem polyphenoloxidase and determination of its storage stability in different lyophilized forms. *Process Biochem.* **42**, 943–950 (2007).
207. T. Aydemir, Partial purification and characterization of polyphenol oxidase from artichoke (*Cynara scolymus* L.) heads. *Food Chem.* **87**, 59–67 (2004).
208. N. Durán, E. Esposito, Potential applications of oxidative enzymes and phenoloxidase-like compounds in wastewater and soil treatment: a review. *Appl. Catal. B Environ.* **28**, 83–99 (2000).
209. O. V Morozova, G. P. Shumakovich, M. A. Gorbacheva, S. V Shleev, A. I. Yaropolov, “Blue” laccases. *Biochem.* **72**, 1136–1150 (2007).
210. H. Huang, G. Zoppellaro, T. Sakurai, Spectroscopic and Kinetic Studies on the Oxygen-centered Radical Formed during the Four-electron Reduction Process of Dioxygen by *Rhus vernicifera* Laccase. *J. Biol. Chem.* **274**, 32718–32724 (1999).
211. G. Zoppellaro, T. Sakurai, H. -w. Huang, A Novel Mixed Valence Form of *Rhus vernicifera* Laccase and Its Reaction with Dioxygen to Give a Peroxide Intermediate Bound to the Trinuclear Center. *J. Biochem.* **129**, 949–953 (2001).
212. A. T. Martinez, M. Speranza, F. J. Ruiz-Duenas, P. Ferreira, S. Camarero, F.

- Guillen, M. J. Martinez, A. Gutierrez, J. C. del Rio, Biodegradation of lignocellulosics: microbial, chemical, and enzymatic aspects of the fungal attack of lignin. *Int. Microbiol.* **8**, 195–204 (2005).
213. S. Lee, S. D. George, W. E. Antholine, B. Hedman, K. O. Hodgson, E. I. Solomon, Nature of the Intermediate Formed in the Reduction of O₂ to H₂O at the Trinuclear Copper Cluster Active Site in Native Laccase. *J. Am. Chem. Soc.* **124**, 6180–6193 (2002).
214. A. E. Palmer, S. K. Lee, E. I. Solomon, Decay of the Peroxide Intermediate in Laccase: Reductive Cleavage of the O–O Bond. *J. Am. Chem. Soc.* **123**, 6591–6599 (2001).
215. D. W. S. Wong, Structure and Action Mechanism of Ligninolytic Enzymes. *Appl. Biochem. Biotechnol.* **157**, 174–209 (2009).
216. B. Haghighi, L. Gorton, T. Ruzgas, L. J. Jönsson, Characterization of graphite electrodes modified with laccase from *Trametes versicolor* and their use for bioelectrochemical monitoring of phenolic compounds in flow injection analysis. *Anal. Chim. Acta.* **487**, 3–14 (2003).
217. H. Lineweaver, D. Burk, The Determination of Enzyme Dissociation Constants. *J. Am. Chem. Soc.* **56**, 658–666 (1934).
218. J. Abdullah, M. Ahmad, L. Heng, N. Karuppiah, H. Sidek, An Optical Biosensor based on Immobilization of Laccase and MBTH in Stacked Films for the Detection of Catechol. *Sensors.* **7**, 2238–2250 (2007).
219. E. Esen, I. Yazgan, D. O. Demirkol, S. Timur, Laccase assay based on electrochemistry and fluorescence detection via anthracene sequestered poly(amic acid) films. *React. Funct. Polym.* **131**, 36–43 (2018).
220. A. Boujakhrou, S. Jimenez-Falcao, P. Martínez-Ruiz, A. Sánchez, P. Díez, J. M. Pingarrón, R. Villalonga, Novel reduced graphene oxide–glycol chitosan nanohybrid for the assembly of an amperometric enzyme biosensor for phenols. *Analyst.* **141**, 4162–4169 (2016).
221. C. Sarika, K. Rekha, B. N. Murthy, Laccase based amperometric biosensor for industrial waste waters: A comparative study on covalent immobilization methods on gold electrode. *IOSR J. Appl. Chem.* **7**, 20–27 (2014).
222. J. Fu, H. Qiao, D. Li, L. Luo, K. Chen, Q. Wei, Laccase Biosensor Based on Electrospun Copper/Carbon Composite Nanofibers for Catechol Detection. *Sensors.* **14**, 3543–3556 (2014).
223. M. C. Scharber, N. S. Sariciftci, Efficiency of bulk-heterojunction organic solar cells. *Prog. Polym. Sci.* **38**, 1929–1940 (2013).
224. D. L. Morel, E. . Stogryn, A. K. Ghosh, T. Feng, P. E. Purwin, R. F. Shaw, C.

- Fishman, G. . Bird, A. P. Piechowski, Organic Photovoltaic Cells. Correlations between Cell Performance and Molecular Structure. *J. Phys. Chem.* **88**, 923–933 (1984).
225. C. W. Tang, Two-layer organic photovoltaic cell. *Appl. Phys. Lett.* **48**, 183–185 (1986).
 226. N. S. Sariciftci, L. Smilowitz, A. J. Heeger, F. Wudl, Photoinduced Electron Transfer from a Conducting Polymer to Buckminsterfullerene. *Science (80-.)*. **258**, 1474–1476 (1992).
 227. P. A. Troshin, R. N. Lyubovskaya, V. F. Razumov, Organic solar cells: Structure, materials, critical characteristics, and outlook. *Nanotechnologies Russ.* **3**, 242–271 (2008).
 228. M. A. Uddin, H. P. Chan, B. M. A. Rahman, Structural improvement of organic photovoltaic cell (OPVC) towards higher efficiency. *Rev. Adv. Mater. Sci.* **26**, 58–66 (2010).
 229. W. Geens, T. Aernouts, J. Poortmans, G. Hadziioannou, Organic co-evaporated films of a PPV-pentamer and C60: model systems for donor/acceptor polymer blends. *Thin Solid Films.* **403–404**, 438–443 (2002).
 230. D. Cheyns, J. Poortmans, H. Gommans, M. Odijk, P. Heremans, Stacked organic solar cells based on pentacene and C60C60. *Sol. Energy Mater. Sol. Cells.* **91**, 399–404 (2007).
 231. F. C. Krebs, Fabrication and processing of polymer solar cells: A review of printing and coating techniques. *Sol. Energy Mater. Sol. Cells.* **93**, 394–412 (2009).
 232. E. D. Glowacki, N. S. Sariciftci, *Solar Energy* (Springer New York, New York, NY, 2013; <http://link.springer.com/10.1007/978-1-4614-5806-7>).
 233. M. Brumbach, P. A. Veneman, F. S. Marrikar, T. Schulmeyer, A. Simmonds, W. Xia, P. Lee, N. R. Armstrong, Surface Composition and Electrical and Electrochemical Properties of Freshly Deposited and Acid-Etched Indium Tin Oxide Electrodes. *Langmuir.* **23**, 11089–11099 (2007).
 234. T. Aernouts, P. Vanlaeke, W. Geens, J. Poortmans, P. Heremans, S. Borghs, R. Mertens, R. Andriessen, L. Leenders, Printable anodes for flexible organic solar cell modules. *Thin Solid Films.* **451–452**, 22–25 (2004).
 235. J. Nelson, Polymer:fullerene bulk heterojunction solar cells. *Mater. Today.* **14**, 462–470 (2011).
 236. J. B. Kim, S. Lee, M. F. Toney, Z. Chen, A. Facchetti, Y. S. Kim, Y.-L. Loo, Reversible Soft-Contact Lamination and Delamination for Non-Invasive Fabrication and Characterization of Bulk-Heterojunction and Bilayer Organic

- Solar Cells. *Chem. Mater.* **22**, 4931–4938 (2010).
237. J.-Y. Lee, S. T. Connor, Y. Cui, P. Peumans, Semitransparent Organic Photovoltaic Cells with Laminated Top Electrode. *Nano Lett.* **10**, 1276–1279 (2010).
 238. J. J. M. Halls, K. Pichler, R. H. Friend, S. C. Moratti, A. B. Holmes, Exciton diffusion and dissociation in a poly(p-phenylenevinylene)/C 60 heterojunction photovoltaic cell. *Appl. Phys. Lett.* **68**, 3120–3122 (1996).
 239. M. Theander, A. Yartsev, D. Zigmantas, V. Sundström, W. Mammo, M. Andersson, O. Inganäs, Photoluminescence quenching at a polythiophene/C-60 heterojunction. *Phys. Rev. B (Condensed Matter Mater. Physics)*. **61**, 12957–12963 (2000).
 240. A. Haugeneder, M. Neges, C. Kallinger, W. Spirkel, U. Lemmer, J. Feldmann, U. Scherf, E. Harth, A. Gügel, K. Müllen, Exciton diffusion and dissociation in conjugated polymer/fullerene blends and heterostructures. *Phys. Rev. B*. **59**, 15346–15351 (1999).
 241. T. Stübinger, W. Brütting, Exciton diffusion and optical interference in organic donor–acceptor photovoltaic cells. *J. Appl. Phys.* **90**, 3632–3641 (2001).
 242. D. E. Markov, E. Amsterdam, P. W. M. Blom, A. B. Sieval, J. C. Hummelen, Accurate Measurement of the Exciton Diffusion Length in a Conjugated Polymer Using a Heterostructure with a Side-Chain Cross-Linked Fullerene Layer. *J. Phys. Chem. A*. **109**, 5266–5274 (2005).
 243. P. M. Allemand, A. Koch, F. Wudl, Y. Rubin, F. Diederich, M. M. Alvarez, S. J. Anz, R. L. Whetten, Two different fullerenes have the same cyclic voltammetry. *J. Am. Chem. Soc.* **113**, 1050–1051 (1991).
 244. C. J. Brabec, G. Zerza, G. Cerullo, S. De Silvestri, S. Luzzati, J. C. Hummelen, S. Sariciftci, Tracing photoinduced electron transfer process in conjugated polymer/fullerene bulk heterojunctions in real time. *Chem. Phys. Lett.* **340**, 232–236 (2001).
 245. R. Abbassi, A. Abbassi, M. Jemli, S. Chebbi, Identification of unknown parameters of solar cell models: A comprehensive overview of available approaches. *Renew. Sustain. Energy Rev.* **90**, 453–474 (2018).
 246. E. Q. B. Macabebe, C. J. Sheppard, E. Ernest Van Dyk, Parameter extraction from I-V characteristics of PV devices. *29th ISES Bienn. Sol. World Congr. 2009, ISES 2009*. **2**, 1149–1155 (2009).
 247. A. M. Humada, M. Hojabri, S. Mekhilef, H. M. Hamada, Solar cell parameters extraction based on single and double-diode models: A review. *Renew. Sustain. Energy Rev.* **56**, 494–509 (2016).

248. A. R. Jordehi, Parameter estimation of solar photovoltaic (PV) cells: A review. *Renew. Sustain. Energy Rev.* **61**, 354–371 (2016).
249. K. Ishaque, Z. Salam, S. Mekhilef, A. Shamsudin, Parameter extraction of solar photovoltaic modules using penalty-based differential evolution. *Appl. Energy.* **99**, 297–308 (2012).
250. K. Ishaque, Z. Salam, An improved modeling method to determine the model parameters of photovoltaic (PV) modules using differential evolution (DE). *Sol. Energy.* **85**, 2349–2359 (2011).
251. M. U. Siddiqui, M. Abido, Parameter estimation for five- and seven-parameter photovoltaic electrical models using evolutionary algorithms. *Appl. Soft Comput. J.* **13**, 4608–4621 (2013).
252. S. xian Lun, S. Wang, G. hong Yang, T. ting Guo, A new explicit double-diode modeling method based on Lambert W-function for photovoltaic arrays. *Sol. Energy.* **116**, 69–82 (2015).
253. D. H. Muhsen, A. B. Ghazali, T. Khatib, I. A. Abed, Parameters extraction of double diode photovoltaic module's model based on hybrid evolutionary algorithm. *Energy Convers. Manag.* **105**, 552–561 (2015).
254. Q. Niu, L. Zhang, K. Li, A biogeography-based optimization algorithm with mutation strategies for model parameter estimation of solar and fuel cells. *Energy Convers. Manag.* **86**, 1173–1185 (2014).
255. C. Clavero, Plasmon-induced hot-electron generation at nanoparticle/metal-oxide interfaces for photovoltaic and photocatalytic devices. *Nat. Photonics.* **8**, 95–103 (2014).
256. M. Raugei, E. Leccisi, A comprehensive assessment of the energy performance of the full range of electricity generation technologies deployed in the United Kingdom. *Energy Policy.* **90**, 46–59 (2016).
257. M. A. Green, K. Emery, Y. Hishikawa, W. Warta, E. D. Dunlop, Solar cell efficiency tables (version 47). *Prog. Photovoltaics Res. Appl.* **24**, 3–11 (2016).
258. D. Bonkougou, Z. Koalaga, D. Njomo, Modelling and Simulation of photovoltaic module considering single-diode equivalent circuit model in MATLAB. *Int. J. Emerg. Technol. Adv. Eng.* **3**, 493–502 (2013).
259. M. Carbajales-Dale, C. J. Barnhart, A. R. Brandt, S. M. Benson, A better currency for investing in a sustainable future. *Nat. Clim. Chang.* **4**, 524–527 (2014).
260. F. Rasool, M. Driberg, N. Badruddin, B. S. Mahinder Singh, PV panel modeling with improved parameter extraction technique. *Sol. Energy.* **153**, 519–530 (2017).

261. N. A. Zainal, Ajisman, A. R. Yusoff, Modelling of Photovoltaic Module Using Matlab Simulink. *IOP Conf. Ser. Mater. Sci. Eng.* **114**, 012137–012146 (2016).
262. N. Rajasekar, N. Krishna Kumar, R. Venugopalan, Bacterial Foraging Algorithm based solar PV parameter estimation. *Sol. Energy.* **97**, 255–265 (2013).
263. B. Romero, G. del Pozo, B. Arredondo, Exact analytical solution of a two diode circuit model for organic solar cells showing S-shape using Lambert W-functions. *Sol. Energy.* **86**, 3026–3029 (2012).
264. H.-L. Tsai, C.-S. Tu, Y.-J. Su, Development of generalized photovoltaic model using MATLAB/SIMULINK. *Proceed World Congr. Eng Comput Sci. 2008*, 6 (2008).
265. J. Gilot, M. M. Wienk, R. A. J. Janssen, Double and triple junction polymer solar cells processed from solution. *Appl. Phys. Lett.* **90**, 1–4 (2007).
266. W. Shockley, H. J. Queisser, Detailed Balance Limit of Efficiency of p-n Junction Solar Cells. *J. Appl. Phys.* **32**, 510–519 (1961).
267. M. C. Scharber, D. Mühlbacher, M. Koppe, P. Denk, C. Waldauf, A. J. Heeger, C. J. Brabec, Design Rules for Donors in Bulk-Heterojunction Solar Cells—Towards 10 % Energy-Conversion Efficiency. *Adv. Mater.* **18**, 789–794 (2006).
268. B. Fan, D. Zhang, M. Li, W. Zhong, Z. Zeng, L. Ying, F. Huang, Y. Cao, Achieving over 16% efficiency for single-junction organic solar cells. *Sci. China Chem.* **62**, 746–752 (2019).
269. L. Meng, Y. Zhang, X. Wan, C. Li, X. Zhang, Y. Wang, X. Ke, Z. Xiao, L. Ding, R. Xia, H.-L. Yip, Y. Cao, Y. Chen, Organic and solution-processed tandem solar cells with 17.3% efficiency. *Science (80-.)*. **361**, 1094–1098 (2018).
270. L. G. Kaake, Towards the Organic Double Heterojunction Solar Cell. *Chem. Rec.* **19**, 1131–1141 (2019).
271. K. Nayak, D. S. Marynick, The interplay between geometric and electronic structures in polyisothianaphthene, polyisophonothiothiophene, polythieno(3,4-b)pyrazine, and polythieno(3,4-b)quinoxaline. *Macromolecules.* **23**, 2237–2245 (1990).
272. F. Wudl, M. Kobayashi, A. J. Heeger, Poly(isothianaphthene). *J. Org. Chem.* **49**, 3382–3384 (1984).
273. J. Roncali, Molecular engineering of the band gap of π -conjugated systems: Facing technological applications. *Macromol. Rapid Commun.* **28**, 1761–1775 (2007).
274. T. Zheng, L. Lu, N. E. Jackson, S. J. Lou, L. X. Chen, L. Yu, Roles of Quinoidal

- Character and Regioregularity in Determining the Optoelectronic and Photovoltaic Properties of Conjugated Copolymers. *Macromolecules*. **47**, 6252–6259 (2014).
275. F. He, W. Wang, W. Chen, T. Xu, S. B. Darling, J. Strzalka, Y. Liu, L. Yu, Tetrathienoanthracene-based copolymers for efficient solar cells. *J. Am. Chem. Soc.* **133**, 3284–3287 (2011).
276. H. Feng, M. Li, W. Ni, F. Liu, X. Wan, B. Kan, Y. Wang, Y. Zhang, Q. Zhang, Y. Zuo, X. Yang, Y. Chen, Investigation of the effect of large aromatic fusion in the small molecule backbone on the solar cell device fill factor. *J. Mater. Chem. A*. **3**, 16679–16687 (2015).
277. X. Song, N. Gasparini, M. M. Nahid, H. Chen, S. M. Macphée, W. Zhang, V. Norman, C. Zhu, D. Bryant, H. Ade, I. McCulloch, D. Baran, A Highly Crystalline Fused-Ring n-Type Small Molecule for Non-Fullerene Acceptor Based Organic Solar Cells and Field-Effect Transistors. *Adv. Funct. Mater.* **28**, 1–9 (2018).
278. K. Yang, Q. Liao, C. W. Koh, J. Chen, M. Su, X. Zhou, Y. Tang, Y. Wang, Y. Zhang, H. Y. Woo, X. Guo, Improved photovoltaic performance of a nonfullerene acceptor based on a benzo[b]thiophene fused end group with extended π -conjugation. *J. Mater. Chem. A*. **7**, 9822–9830 (2019).
279. L. Lu, T. Zheng, Q. Wu, A. M. Schneider, D. Zhao, L. Yu, Recent Advances in Bulk Heterojunction Polymer Solar Cells. *Chem. Rev.* **115**, 12666–12731 (2015).
280. B. Jia, S. Dai, Z. Ke, C. Yan, W. Ma, X. Zhan, Breaking 10% Efficiency in Semitransparent Solar Cells with Fused-Undecacyclic Electron Acceptor. *Chem. Mater.* **30**, 239–245 (2018).
281. S. Rajaram, R. Shivanna, S. K. Kandappa, K. S. Narayan, Nonplanar perylene diimides as potential alternatives to fullerenes in organic solar cells. *J. Phys. Chem. Lett.* **3**, 2405–2408 (2012).
282. H. Lin, S. Chen, H. Hu, L. Zhang, T. Ma, J. Y. L. Lai, Z. Li, A. Qin, X. Huang, B. Tang, H. Yan, Reduced Intramolecular Twisting Improves the Performance of 3D Molecular Acceptors in Non-Fullerene Organic Solar Cells. *Adv. Mater.* **28**, 8546–8551 (2016).
283. Q. Wu, D. Zhao, A. M. Schneider, W. Chen, L. Yu, Covalently Bound Clusters of Alpha-Substituted PDI-Rival Electron Acceptors to Fullerene for Organic Solar Cells. *J. Am. Chem. Soc.* **138**, 7248–7251 (2016).
284. J. Zhang, Y. Li, J. Huang, H. Hu, G. Zhang, T. Ma, P. C. Y. Chow, H. Ade, D. Pan, H. Yan, Ring-Fusion of Perylene Diimide Acceptor Enabling Efficient Nonfullerene Organic Solar Cells with a Small Voltage Loss. *J. Am. Chem. Soc.*

- 139**, 16092–16095 (2017).
285. H. Zhong, C. H. Wu, C. Z. Li, J. Carpenter, C. C. Chueh, J. Y. Chen, H. Ade, A. K. Y. Jen, Rigidifying Nonplanar Perylene Diimides by Ring Fusion Toward Geometry-Tunable Acceptors for High-Performance Fullerene-Free Solar Cells. *Adv. Mater.* **28**, 951–958 (2016).
286. Q. Wu, D. Zhao, J. Yang, V. Sharapov, Z. Cai, L. Li, N. Zhang, A. Neshchadin, W. Chen, L. Yu, Propeller-Shaped Acceptors for High-Performance Non-Fullerene Solar Cells: Importance of the Rigidity of Molecular Geometry. *Chem. Mater.* **29**, 1127–1133 (2017).
287. J. Chen, Q. Liao, G. Ye, D. He, X. Du, W. Zhu, J. Liao, Z. Xiao, L. Ding, D-A conjugated polymers based on tetracyclic acceptor units: Synthesis and application in organic solar cells. *Macromol. Chem. Phys.* **214**, 2054–2060 (2013).
288. T. Wang, N. W. Scarratt, H. Yi, I. F. Coleman, Y. Zhang, R. T. Grant, J. Yao, M. W. A. Skoda, A. D. F. Dunbar, R. A. L. Jones, A. Iraqi, D. G. Lidzey, Vertical stratification and its impact on device performance in a polycarbazole based copolymer solar cells. *J. Mater. Chem. C.* **3**, 4007–4015 (2015).
289. B. Behramand, F. Molin, H. Gallardo, 2,1,3-Benzoxadiazole and 2,1,3-benzothiadiazole-based fluorescent compounds: Synthesis, characterization and photophysical/electrochemical properties. *Dye. Pigment.* **95**, 600–605 (2012).
290. F. Livi, N. K. Zawacka, D. Angmo, M. Jørgensen, F. C. Krebs, E. Bundgaard, Influence of Side Chain Position on the Electrical Properties of Organic Solar Cells Based on Dithienylbenzothiadiazole- alt -phenylene Conjugated Polymers. *Macromolecules.* **48**, 3481–3492 (2015).
291. W. Tang, X. Chen, Y. Zou, B. Liu, H. Zhong, C. Pan, 5,6-bis(tetradecyloxy)-2,1,3-benzoselenadiazole-based polymers for photovoltaic applications. *J. Appl. Polym. Sci.* **128**, 3678–3686 (2013).
292. T. Umeyama, Y. Watanabe, E. Douvogianni, H. Imahori, Effect of Fluorine Substitution on Photovoltaic Properties of Benzothiadiazole–Carbazole Alternating Copolymers. *J. Phys. Chem. C.* **117**, 21148–21157 (2013).
293. J. Sun, Y. Zhu, X. Xu, L. Lan, L. Zhang, P. Cai, J. Chen, J. Peng, Y. Cao, High Efficiency and High V_{oc} Inverted Polymer Solar Cells Based on a Low-Lying HOMO Polycarbazole Donor and a Hydrophilic Polycarbazole Interlayer on ITO Cathode. *J. Phys. Chem. C.* **116**, 14188–14198 (2012).
294. P. Ding, C.-C. Chu, Y. Zou, D. Xiao, C. Pan, C.-S. Hsu, New low bandgap conjugated polymer derived from 2, 7-carbazole and 5, 6-bis(octyloxy)-4, 7-di(thiophen-2-yl) benzothiadiazole: Synthesis and photovoltaic properties. *J.*

- Appl. Polym. Sci.* **123**, 99–107 (2011).
295. P. Shen, H. Bin, Y. Zhang, Y. Li, Synthesis and optoelectronic properties of new D–A copolymers based on fluorinated benzothiadiazole and benzoselenadiazole. *Polym. Chem.* **5**, 567–577 (2014).
296. D. A. M. Egbe, L. H. Nguyen, H. Hoppe, D. Mühlbacher, N. S. Sariciftci, Side chain influence on electrochemical and photovoltaic properties of Yne-containing poly(phenylene vinylene)s. *Macromol. Rapid Commun.* **26**, 1389–1394 (2005).
297. J. Hou, M. H. Park, S. Zhang, Y. Yao, L. M. Chen, J. H. Li, Yang, Bandgap and molecular energy level control of conjugated polymer photovoltaic materials based on benzo[1,2-b:4,5-b']dithiophene. *Macromolecules.* **41**, 6012–6018 (2008).
298. E. Wang, M. Wang, L. Wang, C. Duan, J. Zhang, W. Cai, C. He, H. Wu, Y. Cao, Donor polymers containing benzothiadiazole and four thiophene rings in their repeating units with improved photovoltaic performance. *Macromolecules.* **42**, 4410–4415 (2009).
299. E. Zhou, J. Cong, K. Hashimoto, K. Tajima, A Benzoselenadiazole-Based Low Band Gap Polymer: Synthesis and Photovoltaic Application. *Macromolecules.* **46**, 763–768 (2013).
300. G. L. Gibson, T. M. McCormick, D. S. Seferos, Atomistic band gap engineering in donor-acceptor polymers. *J. Am. Chem. Soc.* **134**, 539–547 (2012).
301. G. Li, R. Zhu, Y. Yang, Polymer solar cells. *Nat Phot.* **6**, 153–161 (2012).
302. P. M. Beaujuge, J. M. J. Fréchet, Molecular design and ordering effects in π -functional materials for transistor and solar cell applications. *J. Am. Chem. Soc.* **133**, 20009–20029 (2011).
303. H. Zhou, L. Yang, W. You, Rational design of high performance conjugated polymers for organic solar cells. *Macromolecules.* **45**, 607–632 (2012).
304. F. He, L. Yu, How far can polymer solar cells go? in need of a synergistic approach. *J. Phys. Chem. Lett.* **2**, 3102–3113 (2011).
305. I. Y. Kanal, S. G. Owens, J. S. Bechtel, G. R. Hutchison, Efficient computational screening of organic polymer photovoltaics. *J. Phys. Chem. Lett.* **4**, 1613–1623 (2013).
306. B. Qi, J. Wang, Open-circuit voltage in organic solar cells. *J. Mater. Chem.* **22**, 24315–24325 (2012).
307. S. F. Hoefler, T. Rath, N. Pastukhova, E. Pavlica, D. Scheunemann, S. Wilken, B. Kunert, R. Resel, M. Hobisch, S. Xiao, G. Bratina, G. Trimmel, The effect of polymer molecular weight on the performance of PTB7-Th:O-IDTBR non-

- fullerene organic solar cells. *J. Mater. Chem. A*. **6**, 9506–9516 (2018).
308. C. Duan, Z. Peng, F. J. M. Colberts, S. Pang, L. Ye, O. M. Awartani, K. H. Hendriks, H. Ade, M. M. Wienk, R. A. J. Janssen, Efficient Thick-Film Polymer Solar Cells with Enhanced Fill Factors via Increased Fullerene Loading. *ACS Appl. Mater. Interfaces*. **11**, 10794–10800 (2019).
 309. H. Akpınar, Ş. C. Cevher, L. Wei, A. Cirpan, B. M. Wong, D. Venkataraman, P. M. Lahti, Poly((2-alkylbenzo[1,2,3]triazole-4,7-diyl)vinylene)s for organic solar cells. *J. Polym. Sci. Part B Polym. Phys.* **53**, 1539–1545 (2015).
 310. R. Yuksel, S. C. Cevher, A. Cirpan, L. Toppare, H. E. Unalan, All-Organic Electrochromic Supercapacitor Electrodes. *J. Electrochem. Soc.* **162**, A2805–A2810 (2015).
 311. M. Kesik, H. Akbulut, S. Söylemez, Ş. C. Cevher, G. Hizalan, Y. Arslan Udum, T. Endo, S. Yamada, A. Çırpan, Y. Yağcı, L. Toppare, Synthesis and characterization of conducting polymers containing polypeptide and ferrocene side chains as ethanol biosensors. *Polym. Chem.* **5**, 6295–6306 (2014).
 312. M. Kesik, B. Demir, F. B. Barlas, C. Geyik, S. C. Cevher, D. Odaci Demirkol, S. Timur, A. Cirpan, L. Toppare, A multi-functional fluorescent scaffold as a multi-colour probe: design and application in targeted cell imaging. *RSC Adv.* **5**, 83361–83367 (2015).
 313. I. Onk, G. Hizalan, S. C. Cevher, S. O. Hacıoglu, L. Toppare, A. Cirpan, Multipurpose selenophene containing conjugated polymers for optoelectronic applications. *J. Macromol. Sci. Part A*. **54**, 133–139 (2017).
 314. Ö. Karagaçtı, S. C. Cevher, G. Hizalan, S. O. Hacıoglu, L. Toppare, A. Cirpan, Enhancing the power conversion efficiency of polymer solar cells via selection of quinoxaline substituents. *New J. Chem.* **41**, 14635–14645 (2017).
 315. Ö. Azeri, E. Aktas, C. Istanbuluoglu, S. O. Hacıoglu, S. C. Cevher, L. Toppare, A. Cirpan, Efficient benzodithiophene and thienopyrroledione containing random polymers as components for organic solar cells. *Polymer (Guildf)*. **133**, 60–67 (2017).
 316. A. Cetin, C. Istanbuluoglu, S. O. Hacıoglu, S. C. Cevher, L. Toppare, A. Cirpan, Synthesis of bistrisphenylamine- and benzodithiophene-based random conjugated polymers for organic photovoltaic applications. *J. Polym. Sci. Part A Polym. Chem.* **55**, 3705–3715 (2017).
 317. S. C. Cevher, G. Hizalan, C. Temiz, Y. A. Udum, L. Toppare, A. Cirpan, Effect of substituent groups on quinoxaline-based random copolymers on the optoelectronic and photovoltaic properties. *Polymer (Guildf)*. **101**, 208–216 (2016).
 318. D. Keles, M. C. Erer, E. Bolayir, S. C. Cevher, G. Hizalan, L. Toppare, A.

Cirpan, Conjugated polymers with benzothiadiazole and benzotriazole moieties for polymer solar cells. *Renew. Energy*. **139**, 1184–1193 (2019).

APPENDICES

A. Supporting Figures

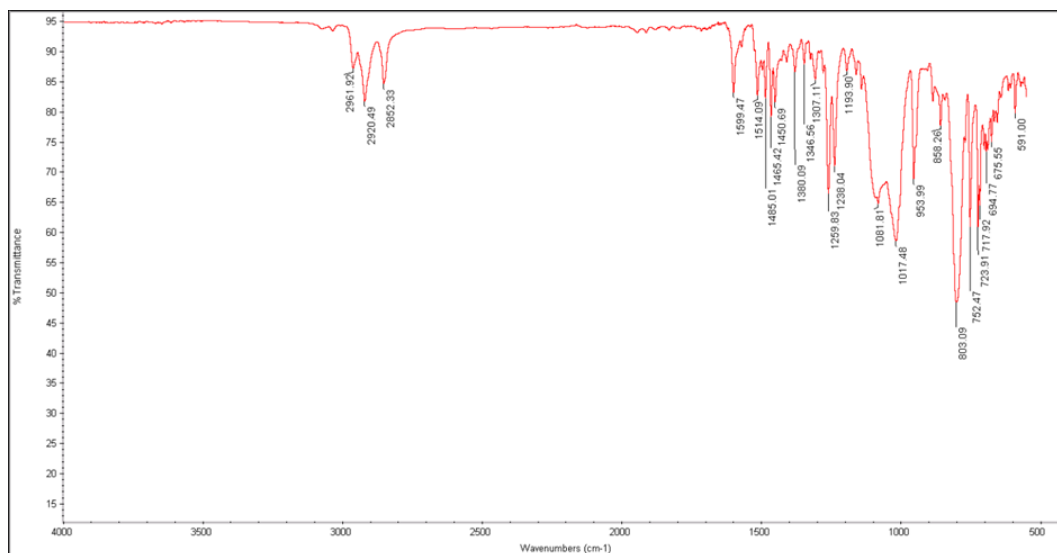


Figure 0.1. FTIR spectra of 2-(3-((10-(4,7-dibromo-2H-benzo[d][1,2,3]triazol-2-yl)decyl)oxy)phenyl)-1-(4-hexylphenyl)-1H-phenanthro[9,10-d]imidazole (IV) (ATR).

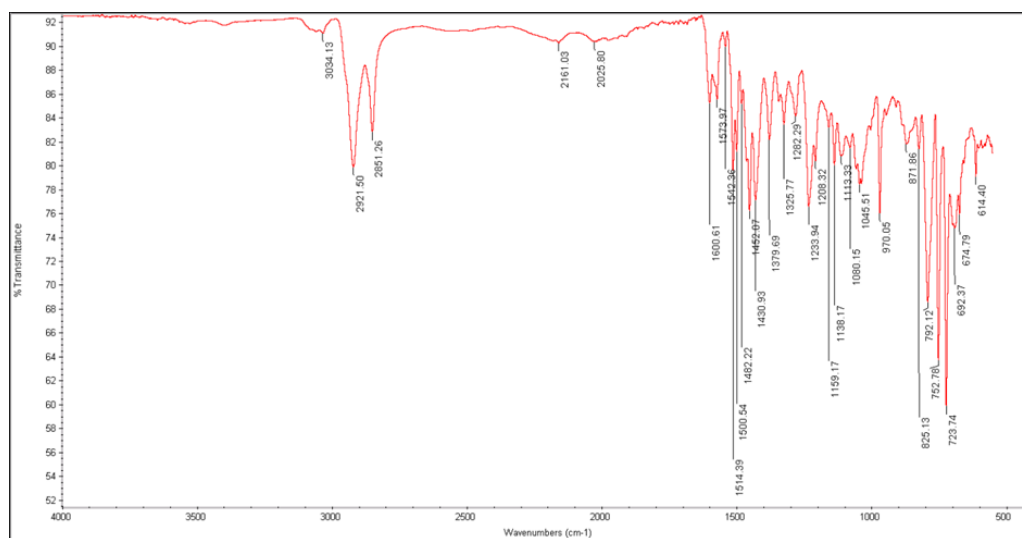


Figure 0.2. FTIR Spectra of 2-(3-((10-(4,7-di(thiophen-2-yl)-2H-benzo[d][1,2,3]triazol-2-yl)decyl)oxy)phenyl)-1-(4-hexylphenyl)-1H-phenanthro[9,10-d]imidazole (VI) (ATR).

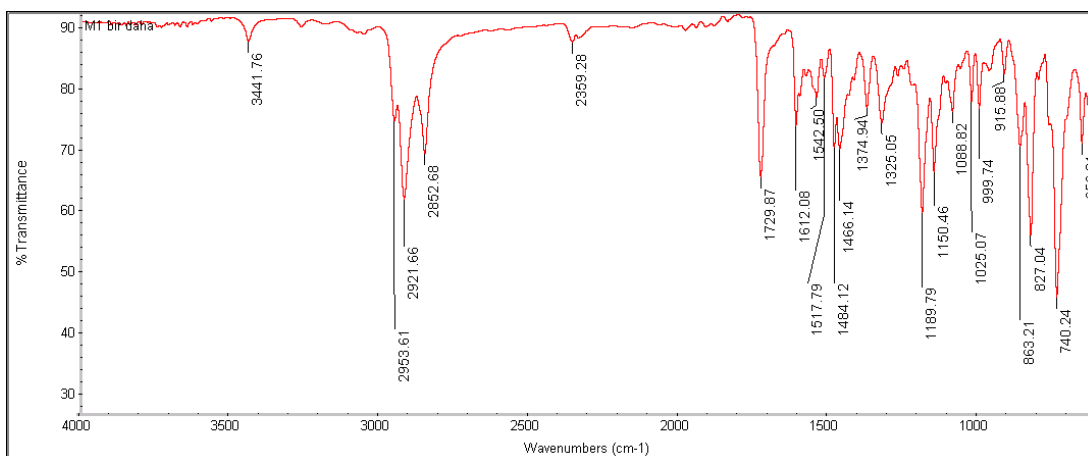


Figure 0.3. FTIR spectrum of monomer M1 (ATR).

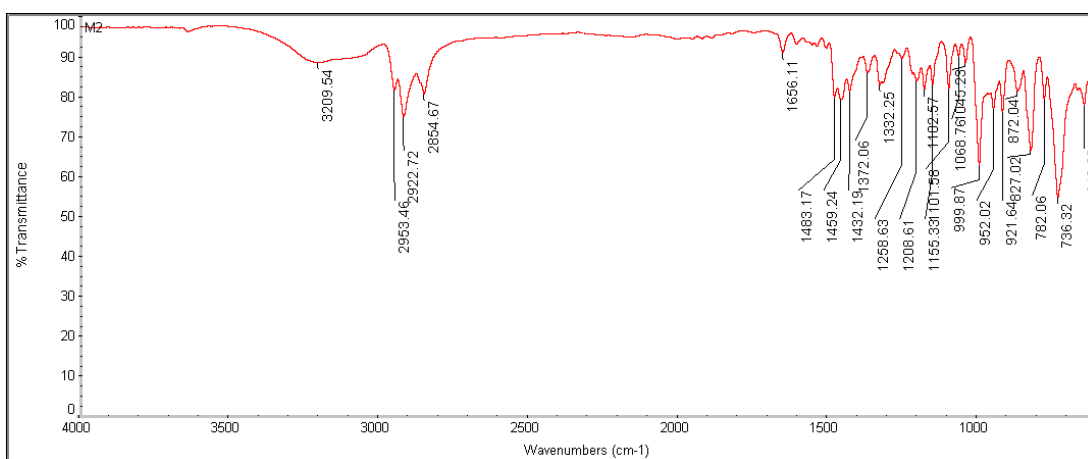


Figure 0.4. FTIR spectrum of monomer M2 (ATR).

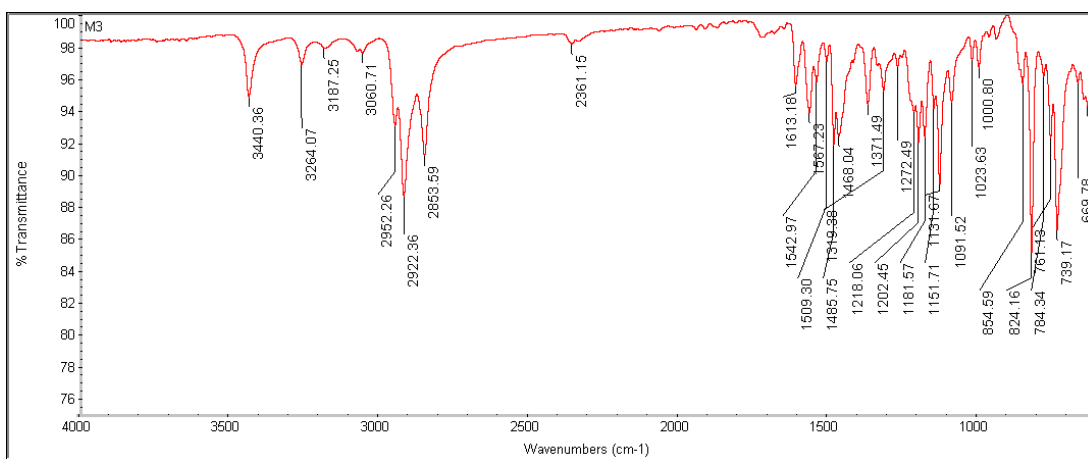


Figure 0.5. FTIR spectrum of monomer M3 (ATR).

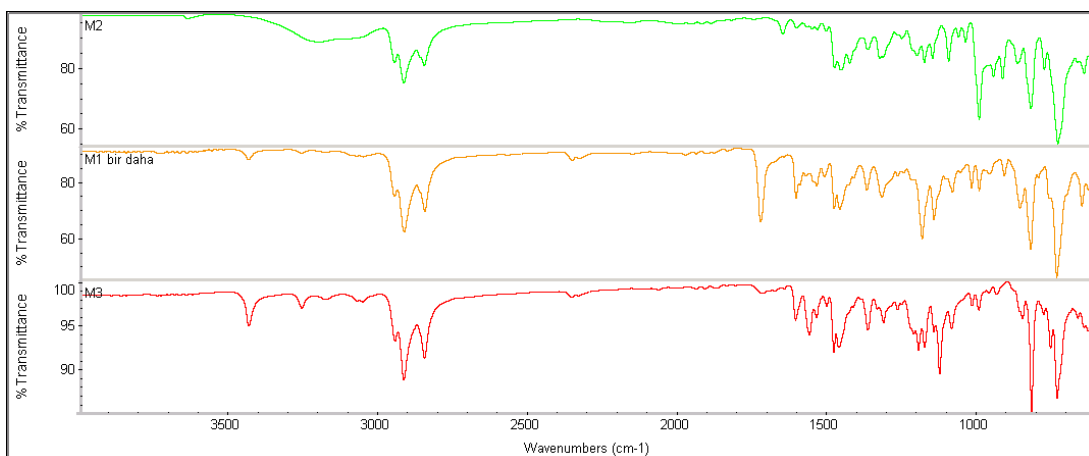


Figure 0.6. Stacked FTIR spectrum of monomers M1, M2 and M3 (ATR).

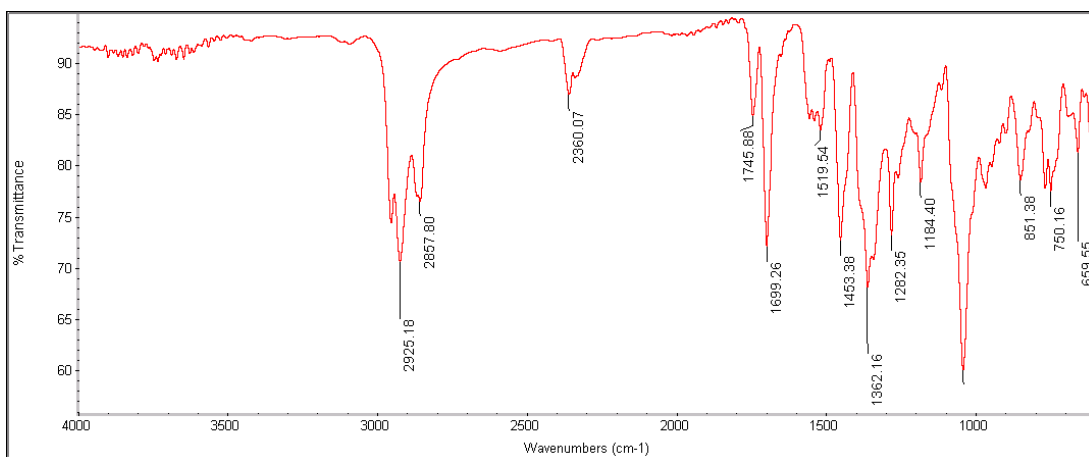


Figure 0.7. FTIR spectrum of polymers PS (ATR).

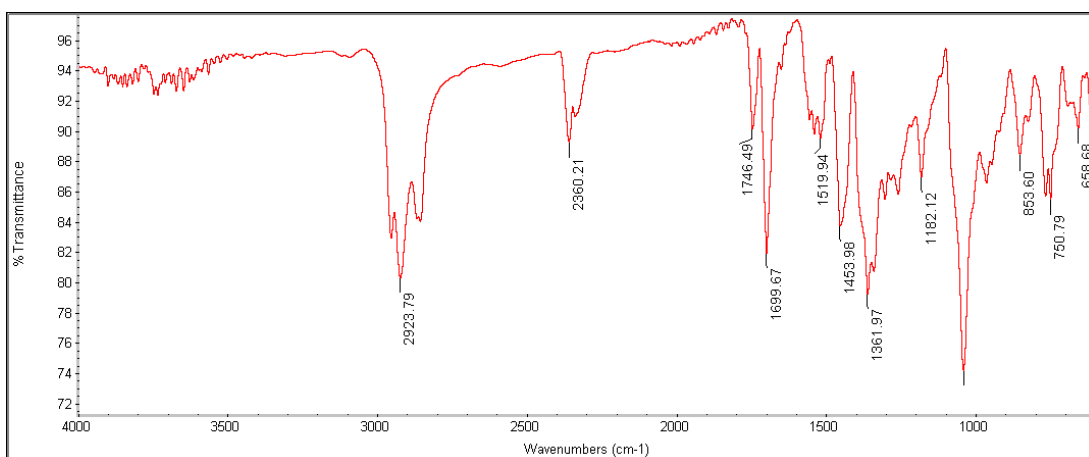


Figure 0.8. FTIR spectrum of polymers PSe (ATR).

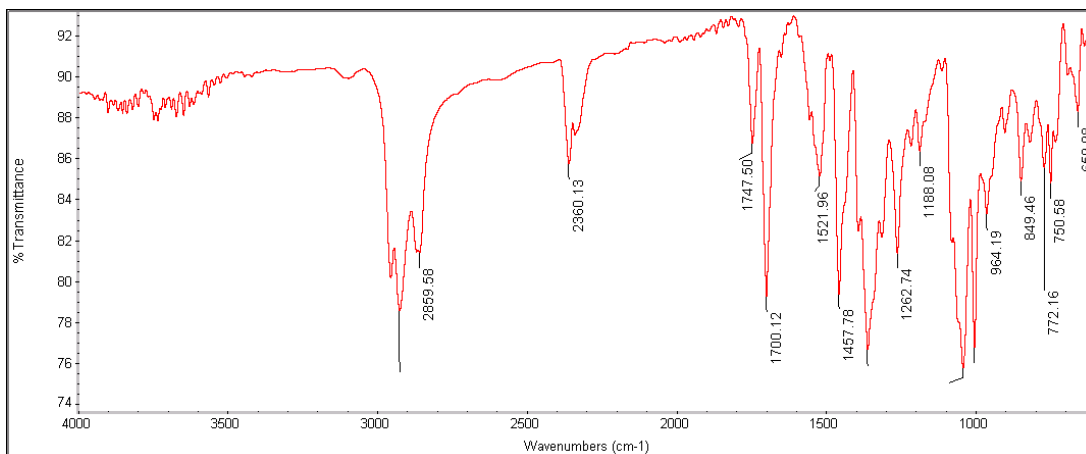


Figure 0.9. FTIR spectrum of polymers PO (ATR).

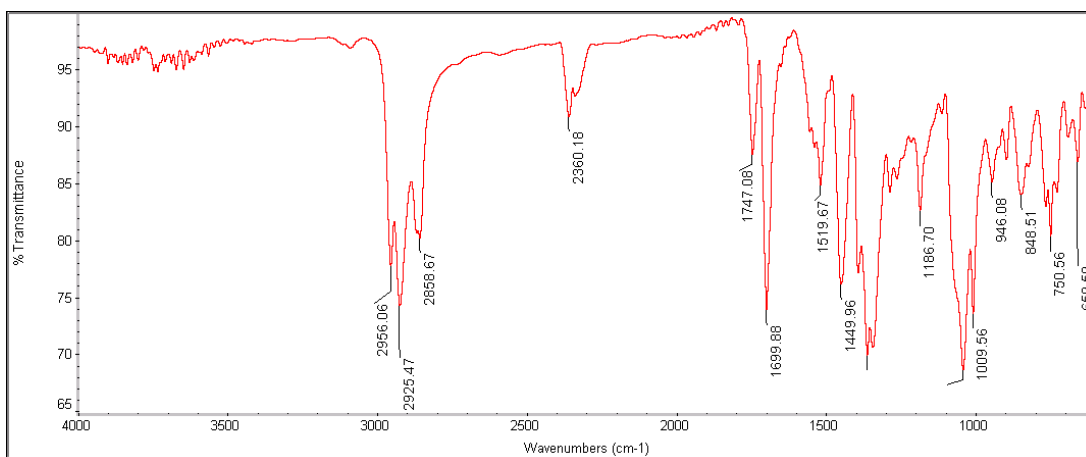


Figure 0.10. FTIR spectrum of polymers PF (ATR).

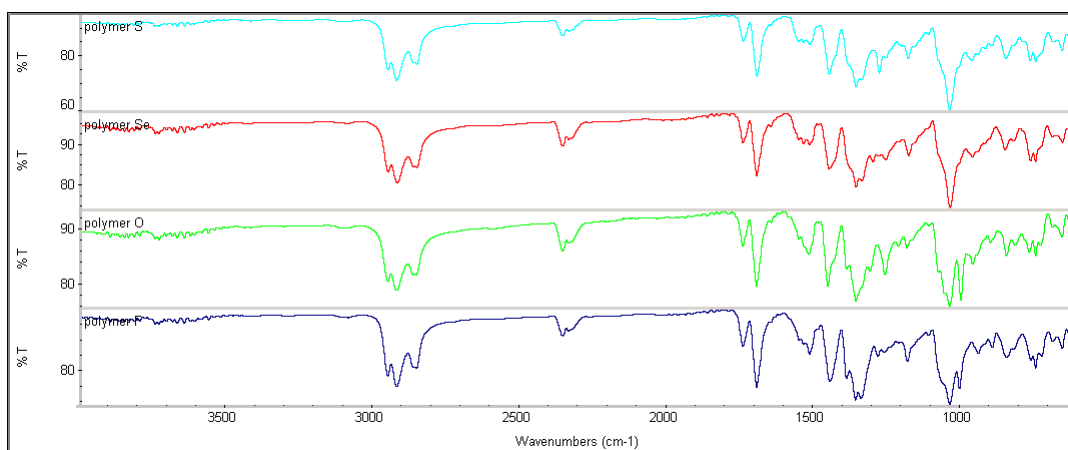


Figure 0.11. Stacked FTIR spectrum of polymers PS, PSe, PO and PF (ATR).

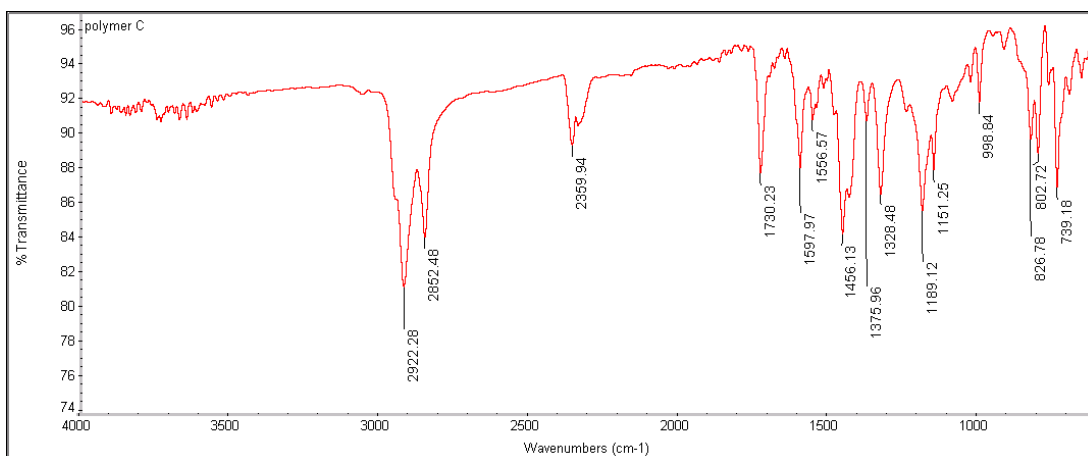


Figure 0.12. FTIR spectrum of PIQCAR (polymer C) (ATR).

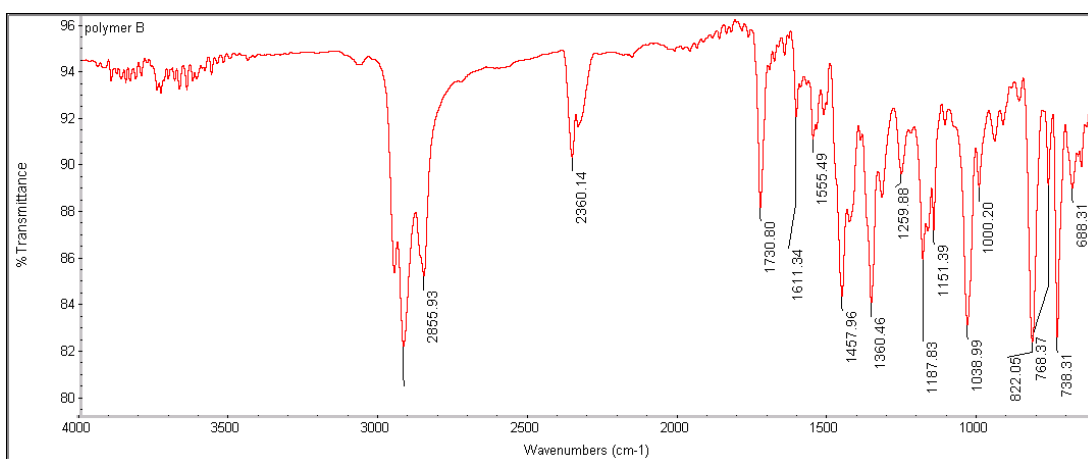


Figure 0.13. FTIR spectrum of PIQBDT (polymer B) (ATR).

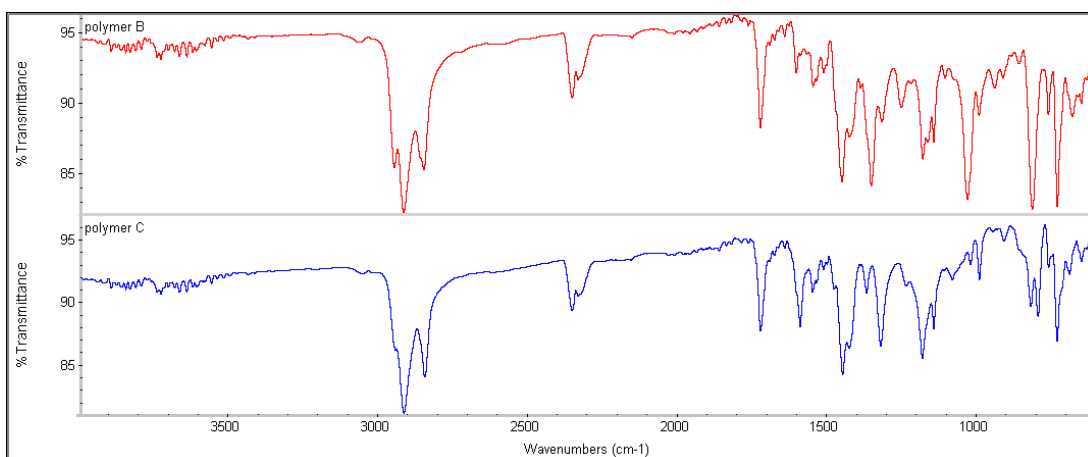


Figure 0.14. Stacked FTIR spectrum of PIQCAR (polymer C) and PIQBDT (polymer B) (ATR).



Figure 0.15. ^1H NMR spectrum of 1,2-dimethoxy-4,5-dinitrobenzene (in CDCl_3).

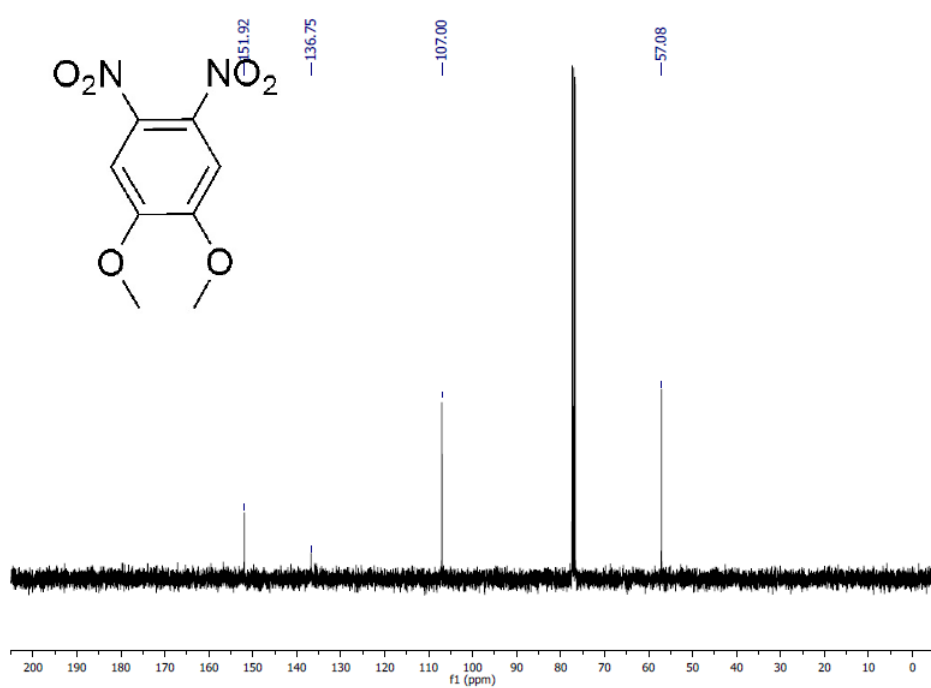


Figure 0.16. ^{13}C NMR spectrum of 1,2-dimethoxy-4,5-dinitrobenzene (in CDCl_3).

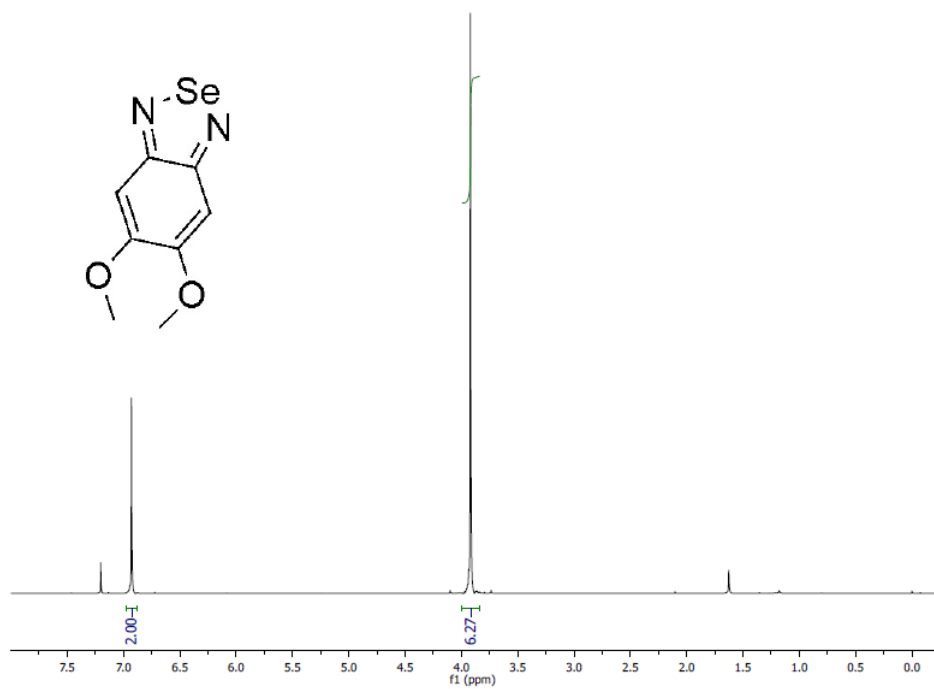


Figure 0.17. ^1H NMR spectrum of 5,6-dimethoxybenzo[*c*][1,2,5]selenadiazole (in CDCl_3).

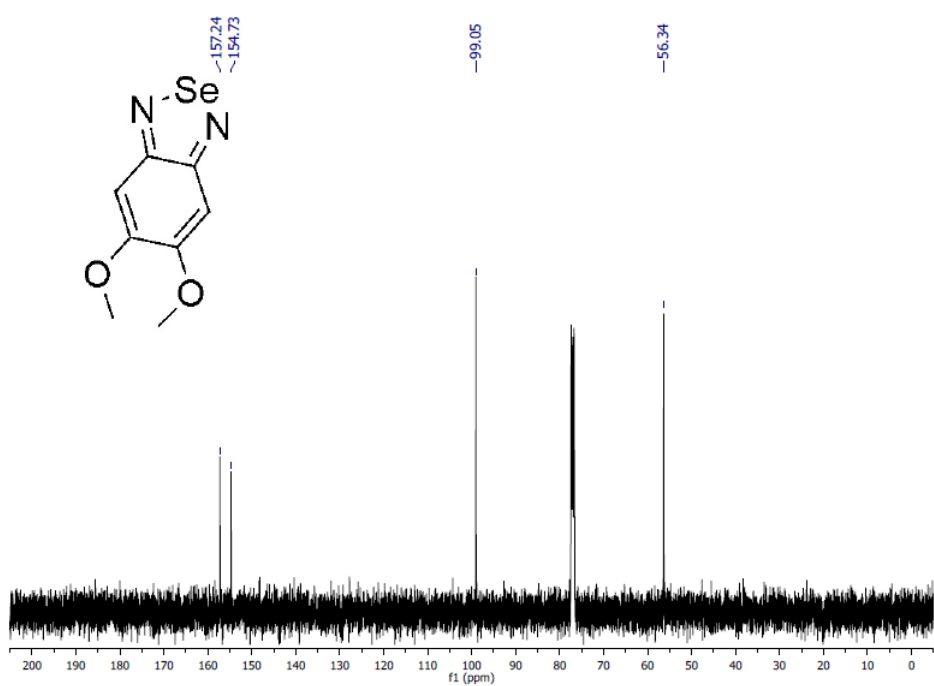


Figure 0.18. ^{13}C NMR spectrum of 5,6-dimethoxybenzo[*c*][1,2,5]selenadiazole (in CDCl_3).

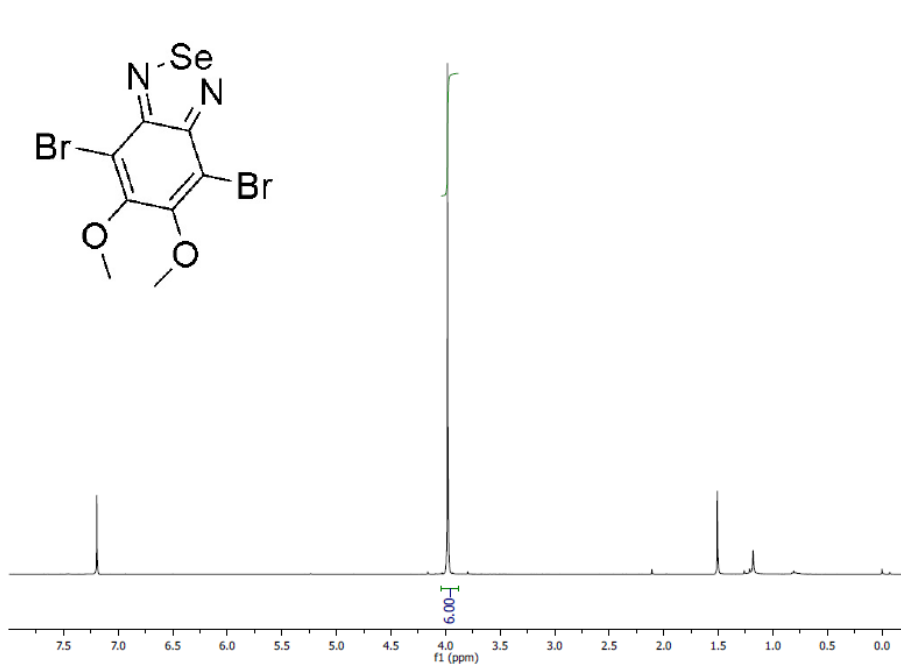


Figure 0.19. ^1H NMR spectrum of 4,7-Dibromo-5,6-dimethoxybenzo[*c*][1,2,5]selenadiazole (in CDCl_3).

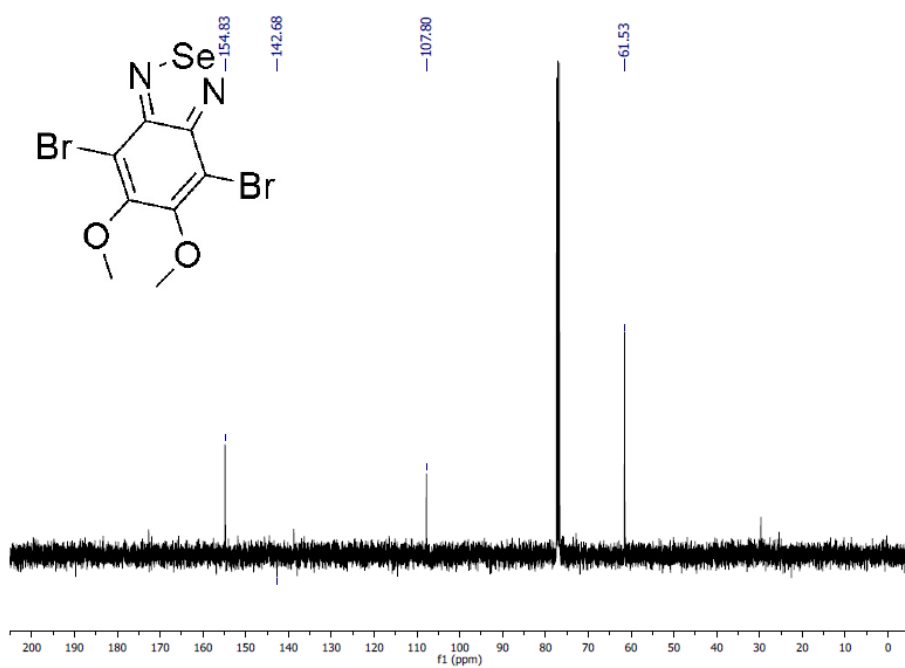


Figure 0.20. ^{13}C NMR spectrum of 4,7-Dibromo-5,6-dimethoxybenzo[*c*][1,2,5]selenadiazole (in CDCl_3).

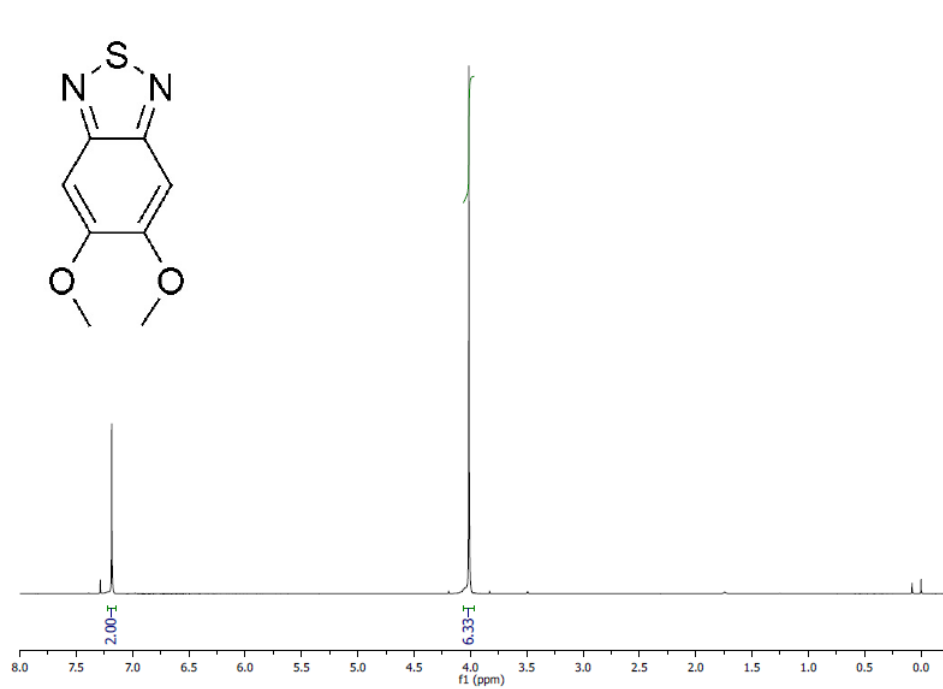


Figure 0.21. ^1H NMR spectrum of 5,6-dimethoxybenzo[*c*][1,2,5]thiadiazole (in CDCl_3).

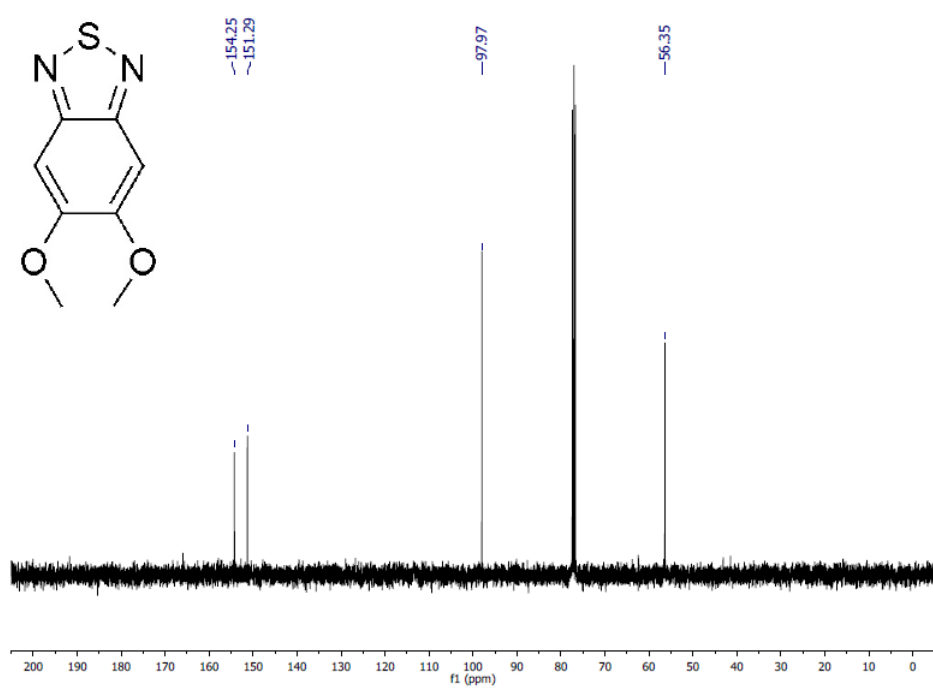


Figure 0.22. ^{13}C NMR spectrum of 5,6-dimethoxybenzo[*c*][1,2,5]thiadiazole (in CDCl_3).

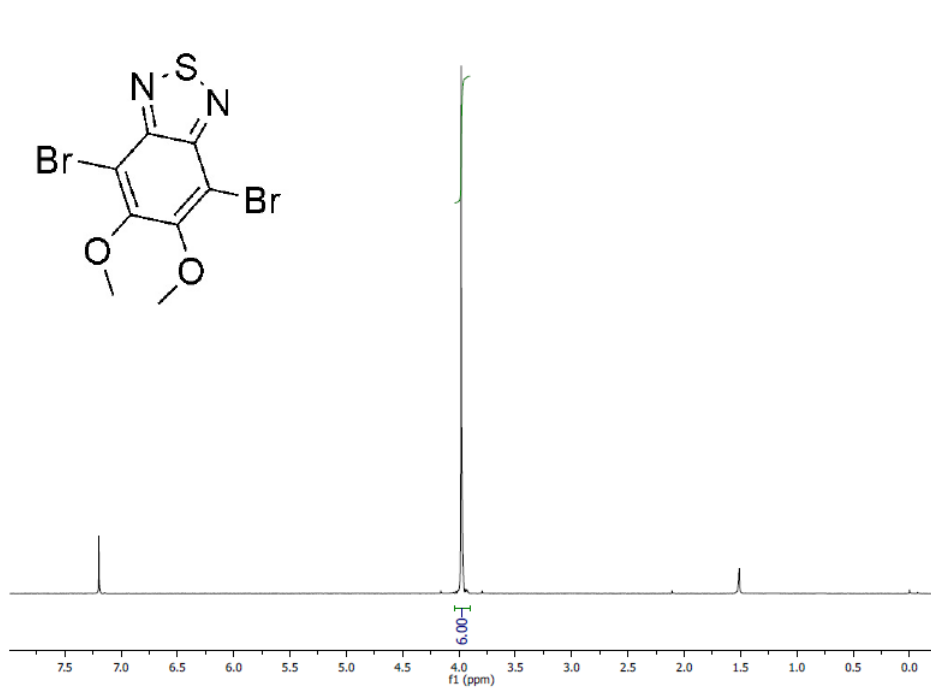


Figure 0.23. ^1H NMR spectrum of 4,7-Dibromo-5,6-dimethoxybenzo[*c*][1,2,5]thiadiazole (in CDCl_3).

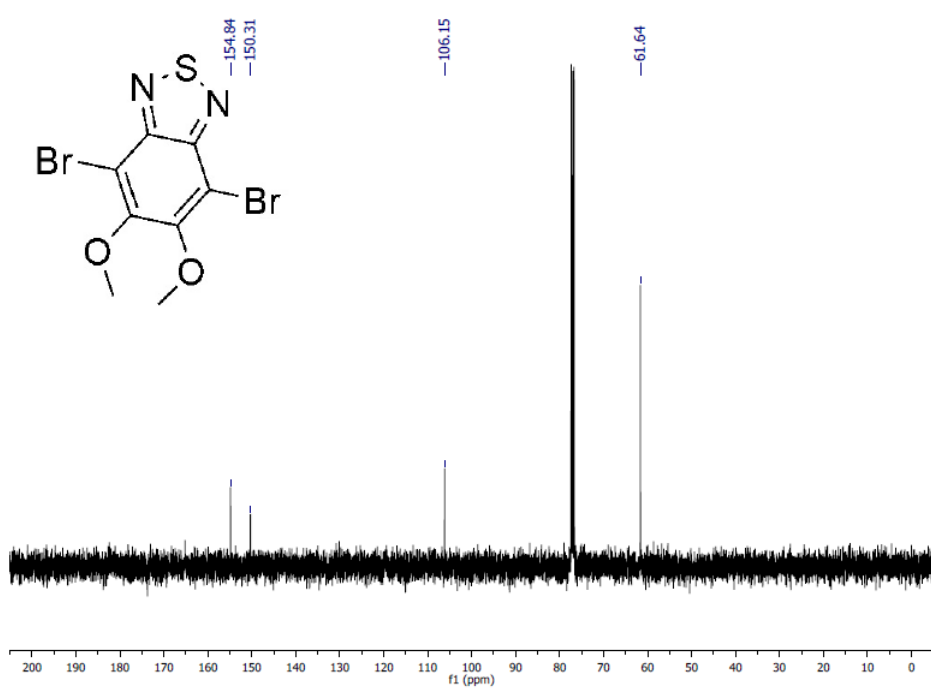


Figure 0.24. ^{13}C NMR spectrum of 4,7-Dibromo-5,6-dimethoxybenzo[*c*][1,2,5]thiadiazole (in CDCl_3).

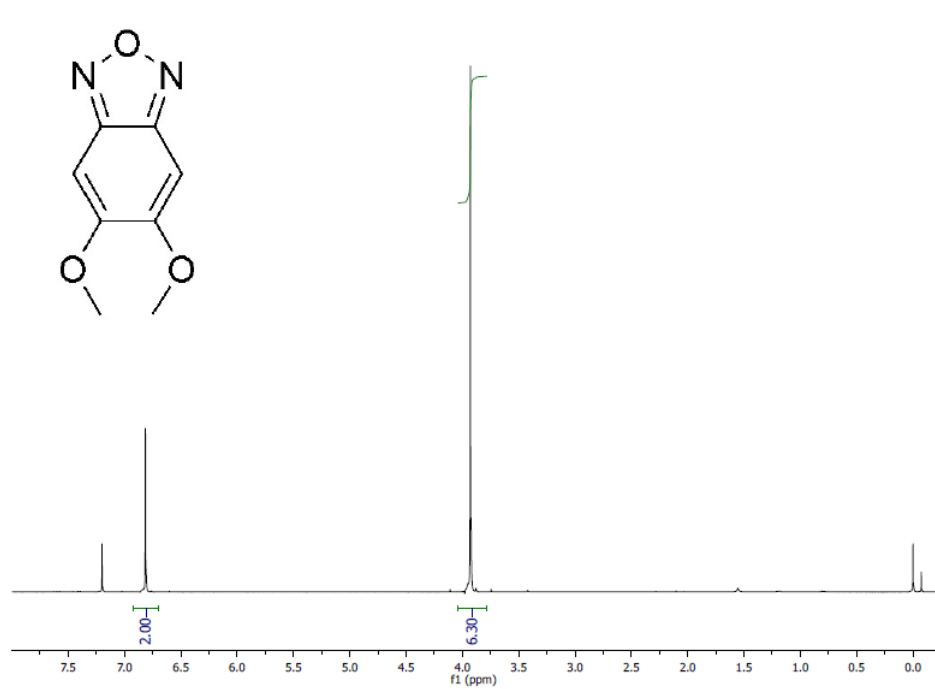


Figure 0.25. ¹H NMR spectrum of 5,6-dimethoxybenzo[*c*][1,2,5]oxadiazole (in CDCl₃).

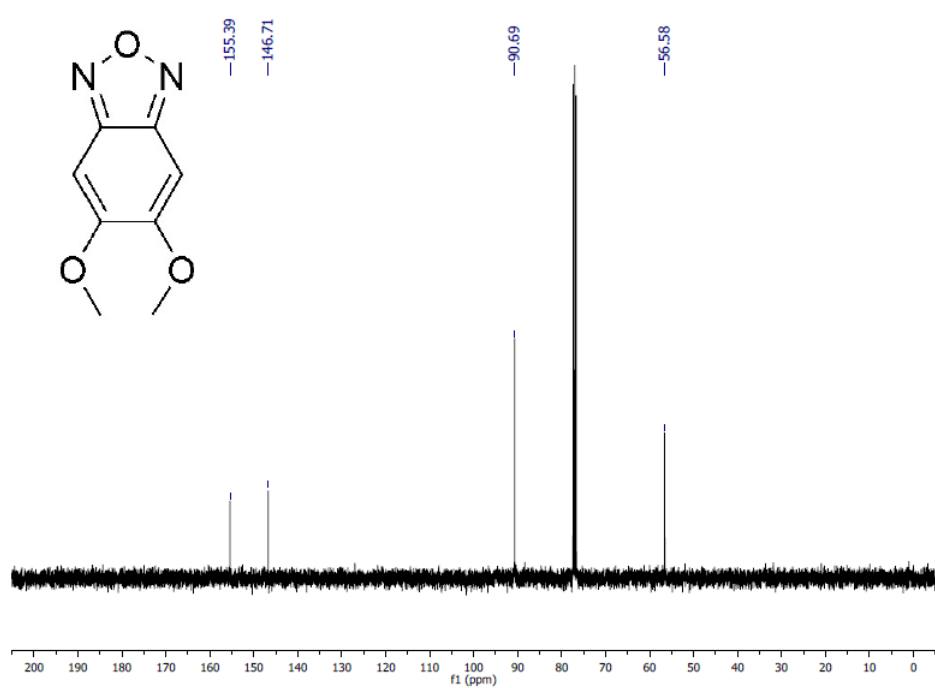


Figure 0.26. ¹³C NMR spectrum of 5,6-dimethoxybenzo[*c*][1,2,5]oxadiazole (in CDCl₃).

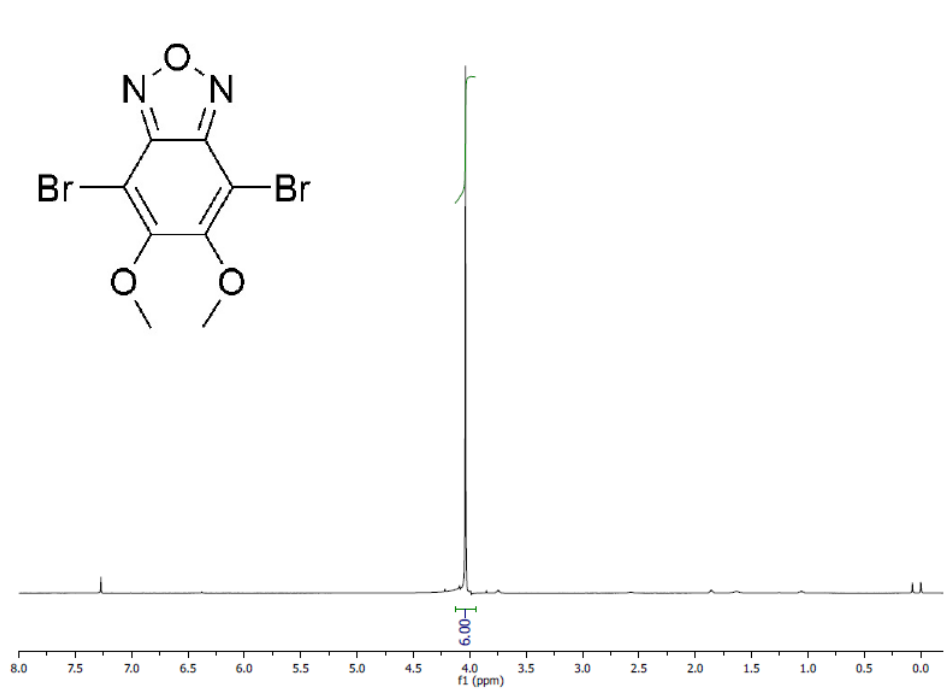


Figure 0.27. ¹H NMR spectrum of 4,7-dibromo-5,6-dimethoxybenzo[*c*][1,2,5]oxadiazole (in CDCl₃).

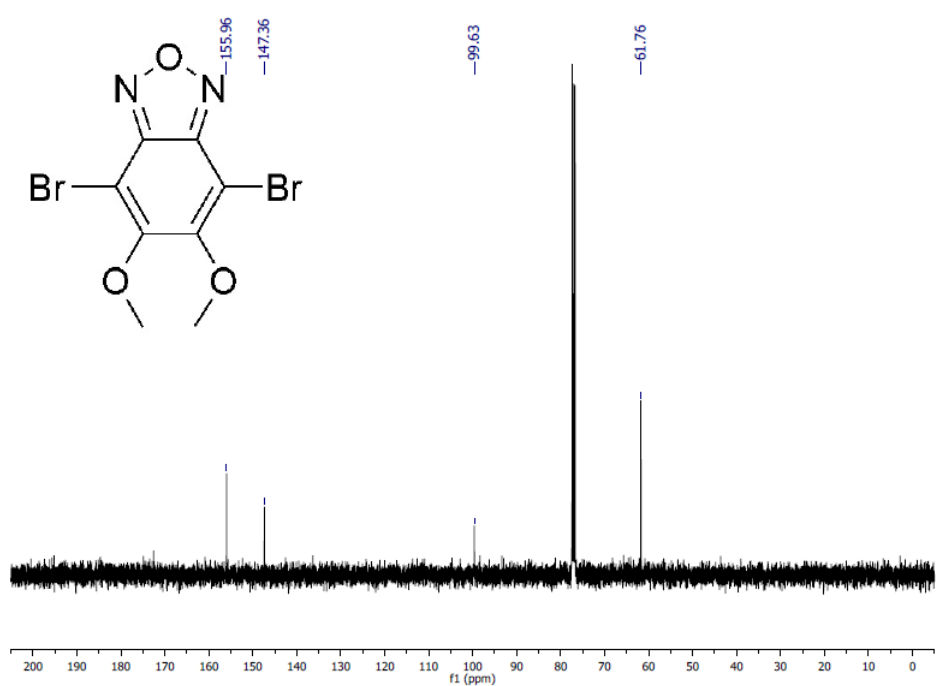


Figure 0.28. ¹³C NMR spectrum of 4,7-dibromo-5,6-dimethoxybenzo[*c*][1,2,5]oxadiazole (in CDCl₃).

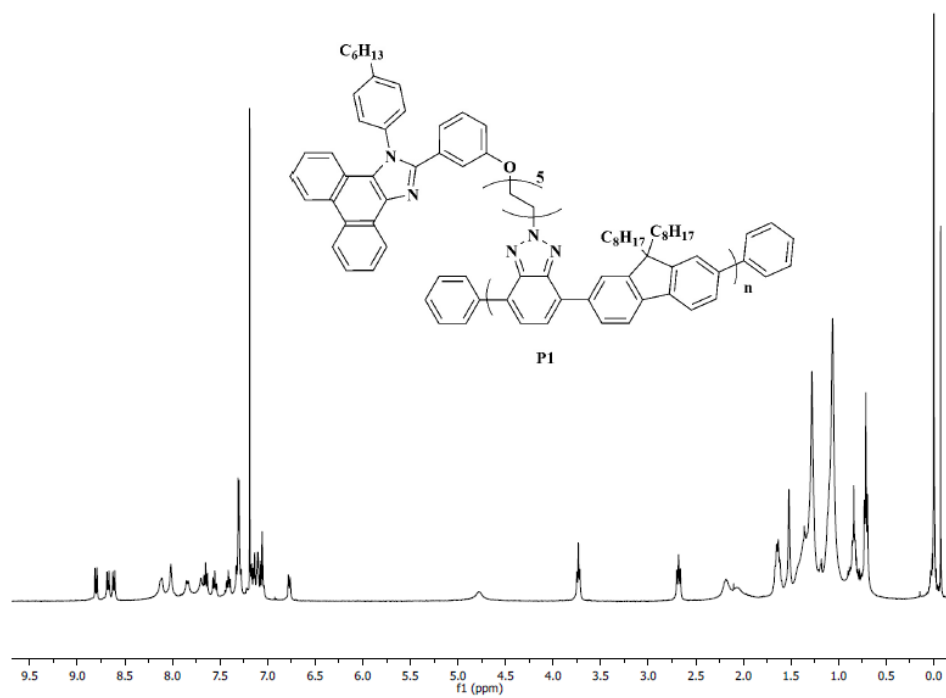


Figure 0.29. ¹H NMR spectrum of P1 (in CDCl₃).

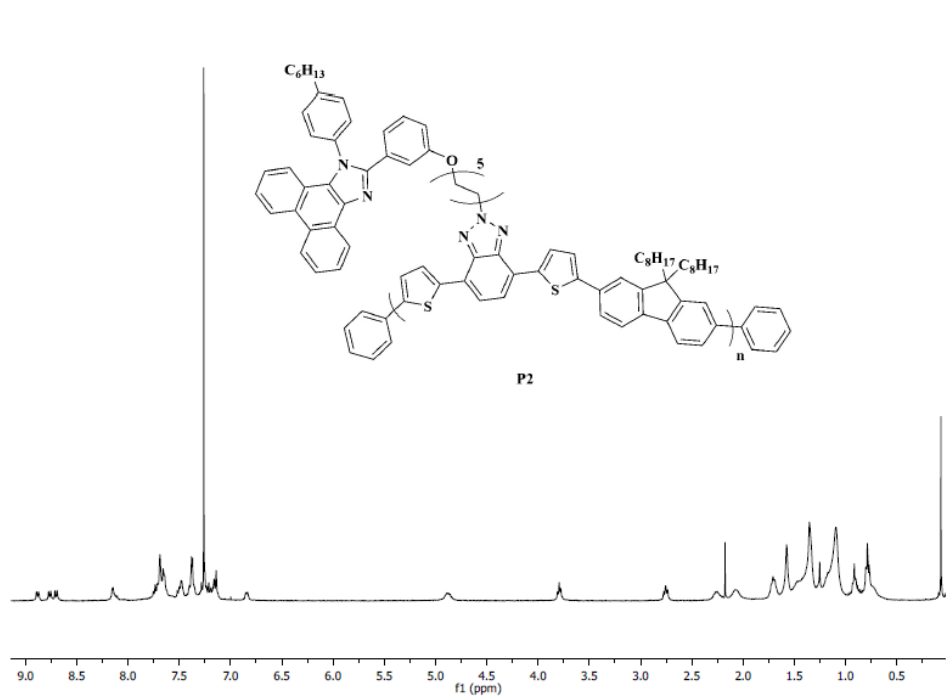


Figure 0.30. ¹H NMR spectrum of P2 (in CDCl₃).

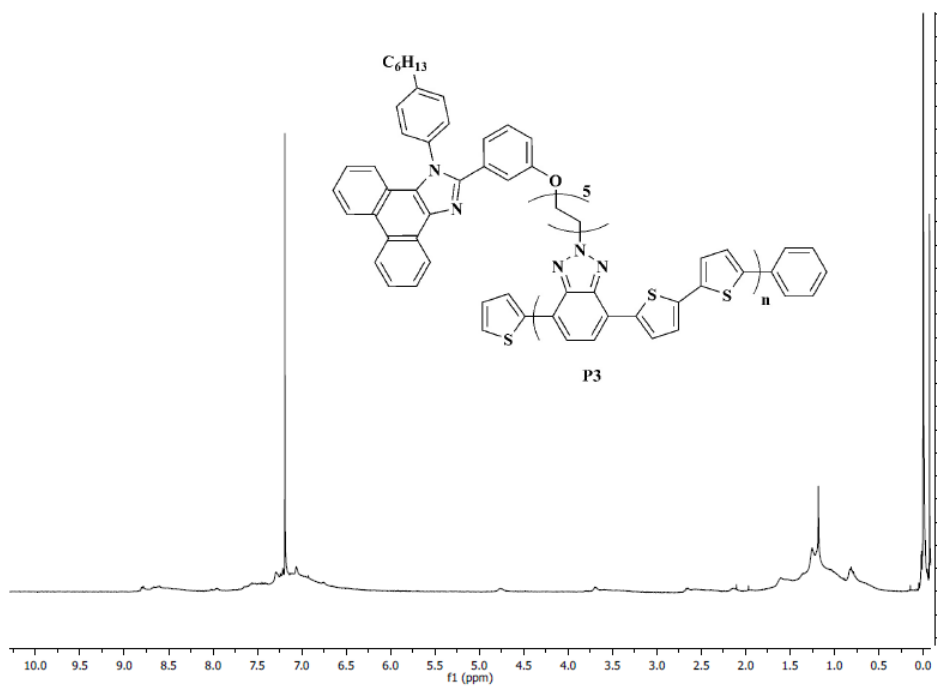


Figure 0.31. ^1H NMR spectrum of P3 (in CDCl_3).

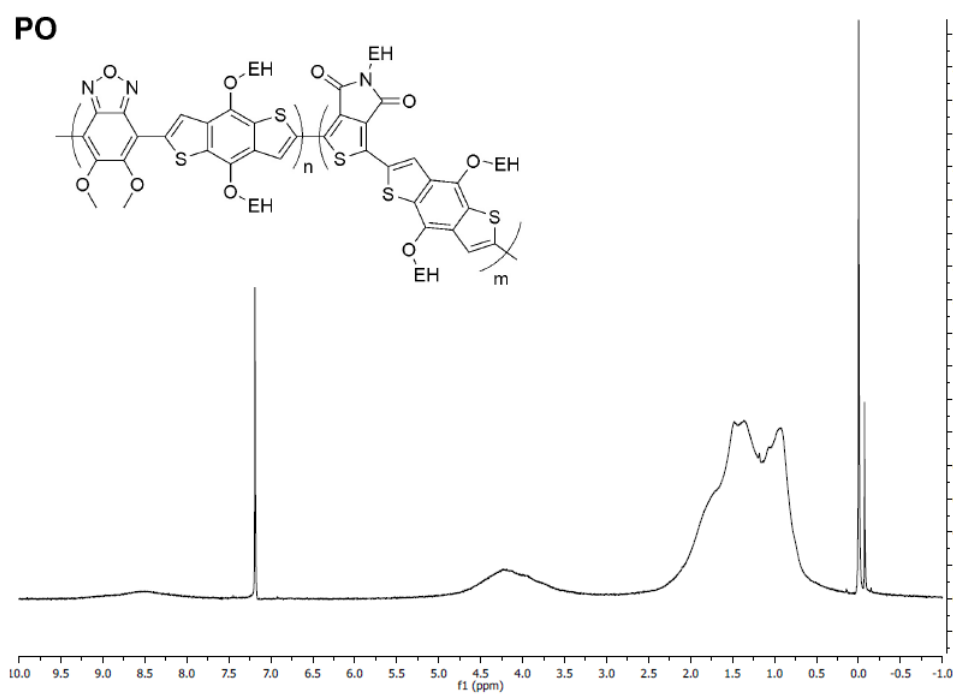


Figure 0.32. ^1H NMR spectrum of PO (in CDCl_3).

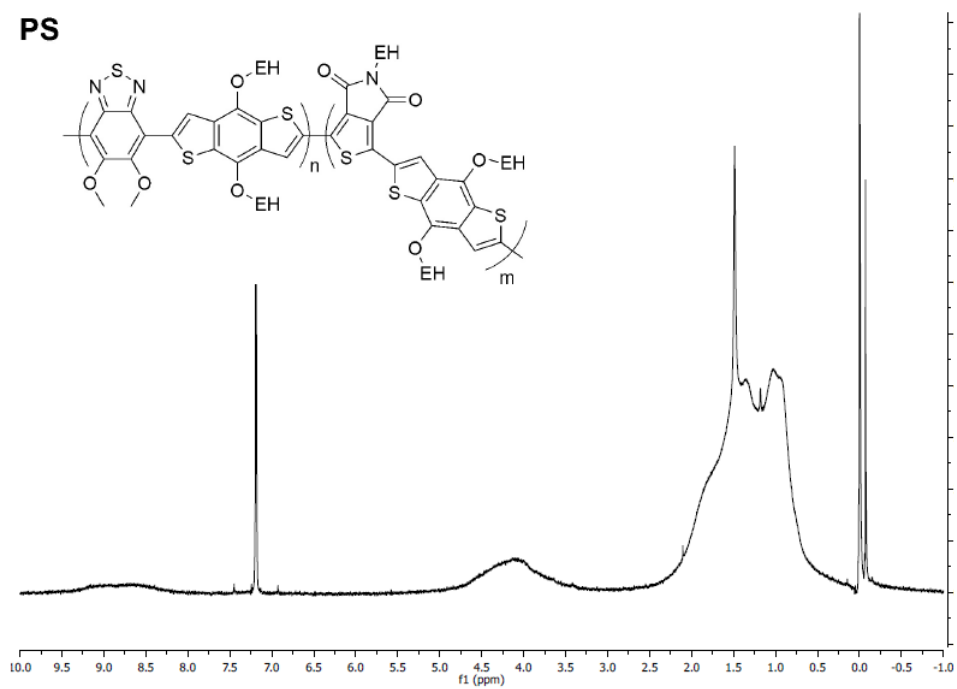


Figure 0.33. ^1H NMR spectrum of PS (in CDCl_3).

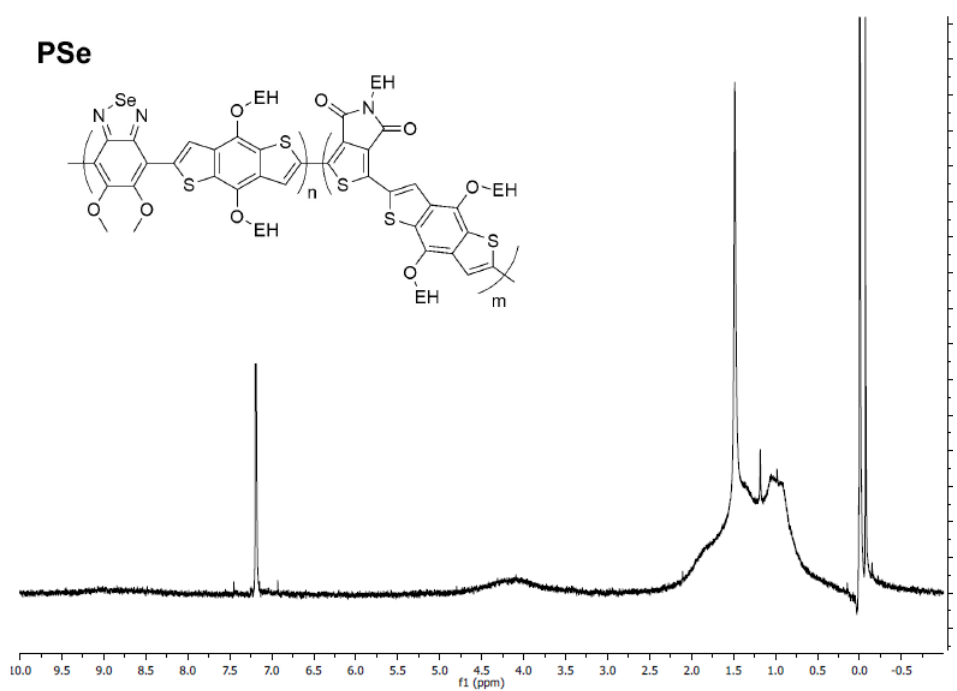


Figure 0.34. ^1H NMR spectrum of PSe (in CDCl_3).

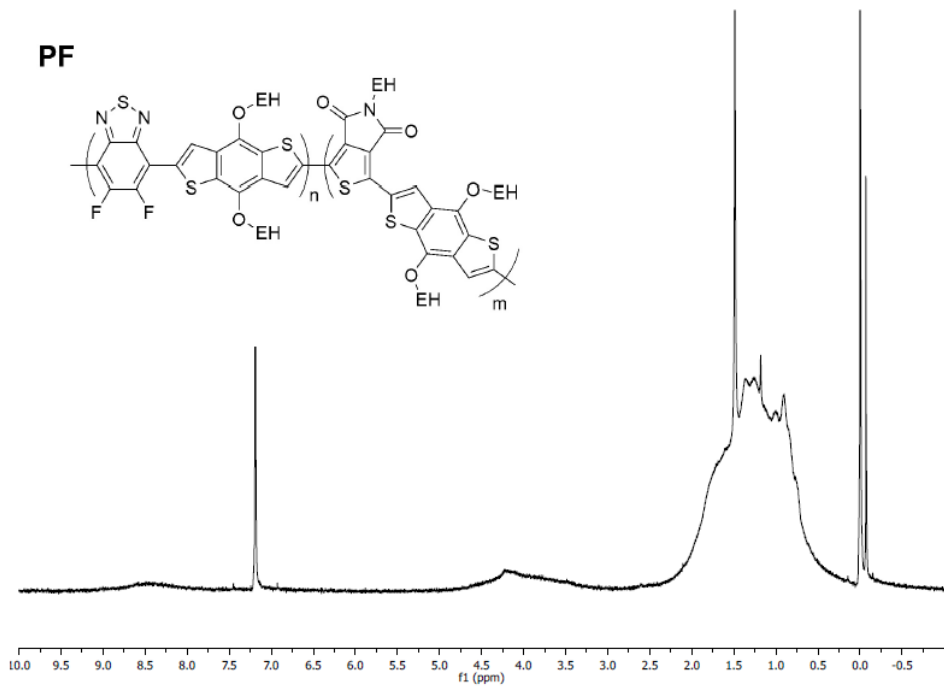


Figure 0.35. ^1H NMR spectrum of PF (in CDCl_3).

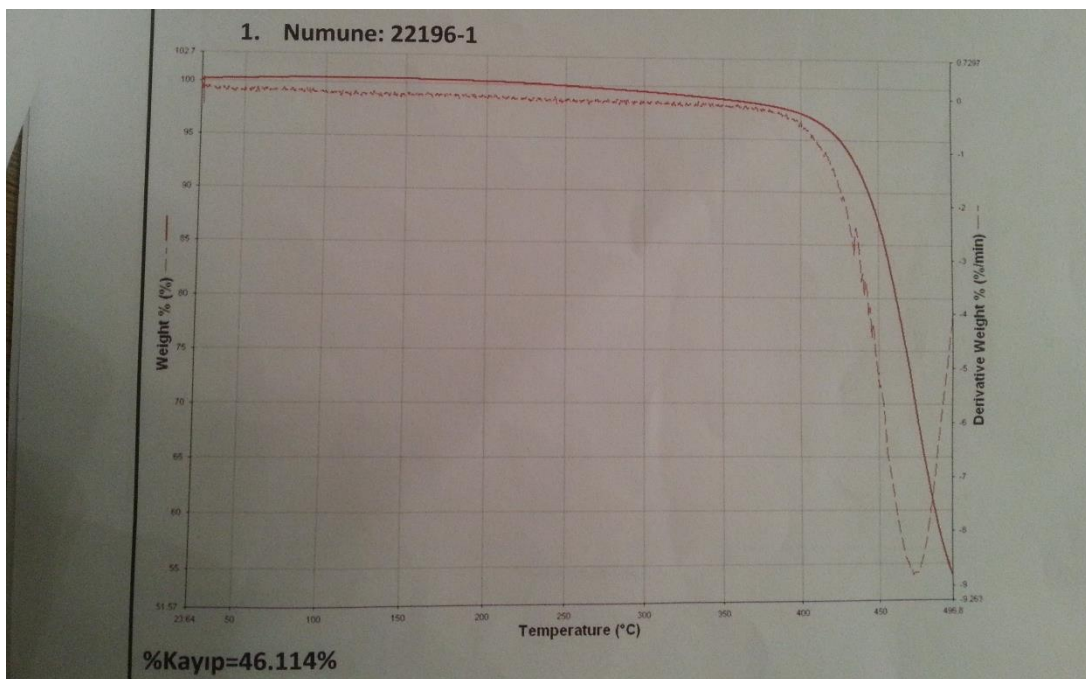


Figure 0.36. TGA result of P1

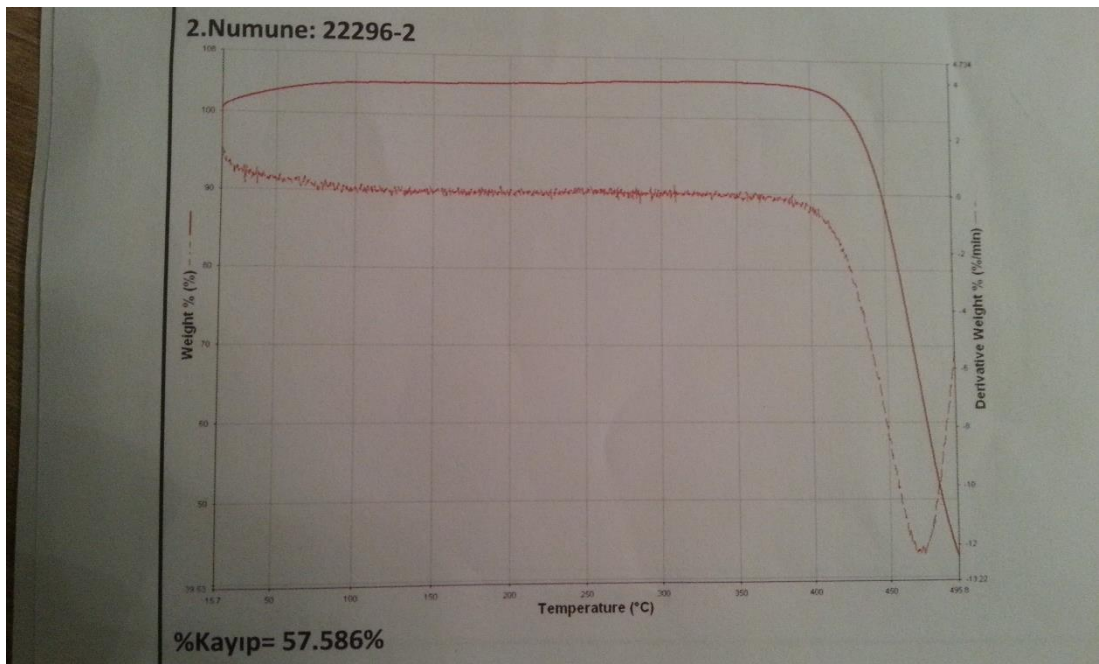


Figure 0.37. TGA result of P2



Figure 0.38. TGA result of P3

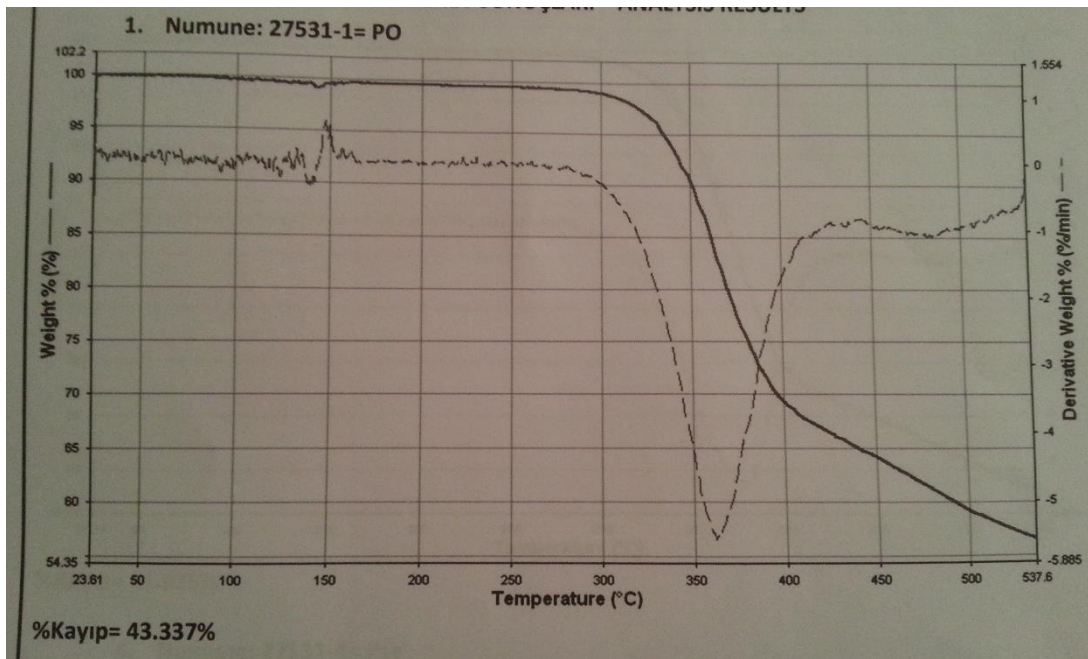


Figure 0.39. TGA result of PO

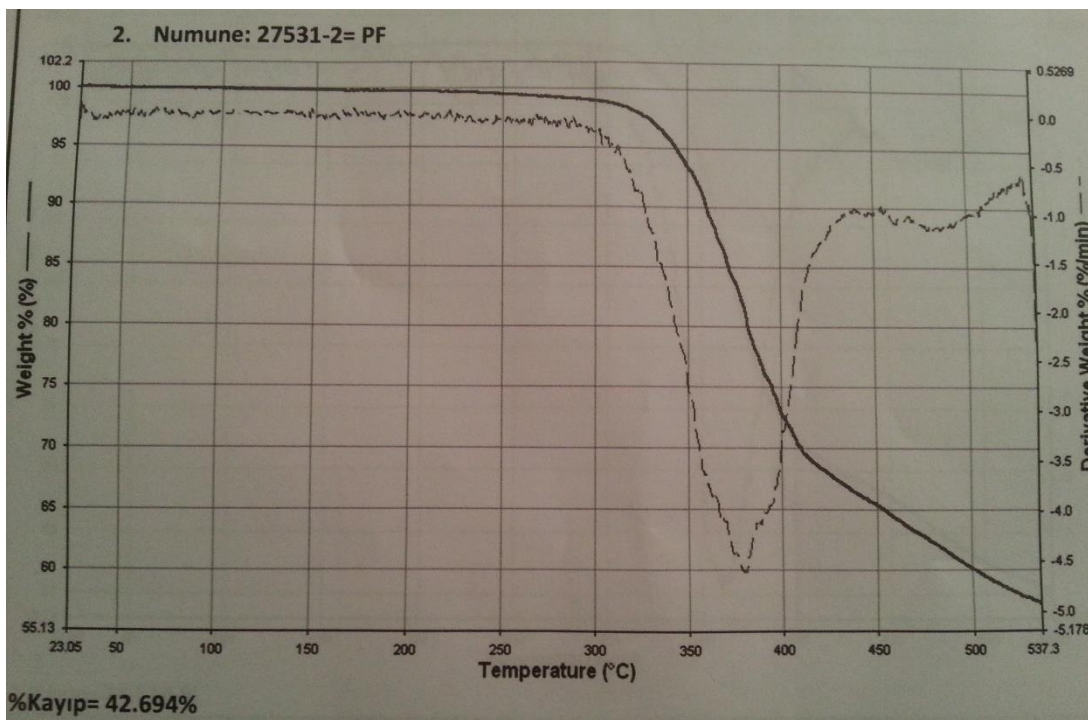


Figure 0.40. TGA result of PF

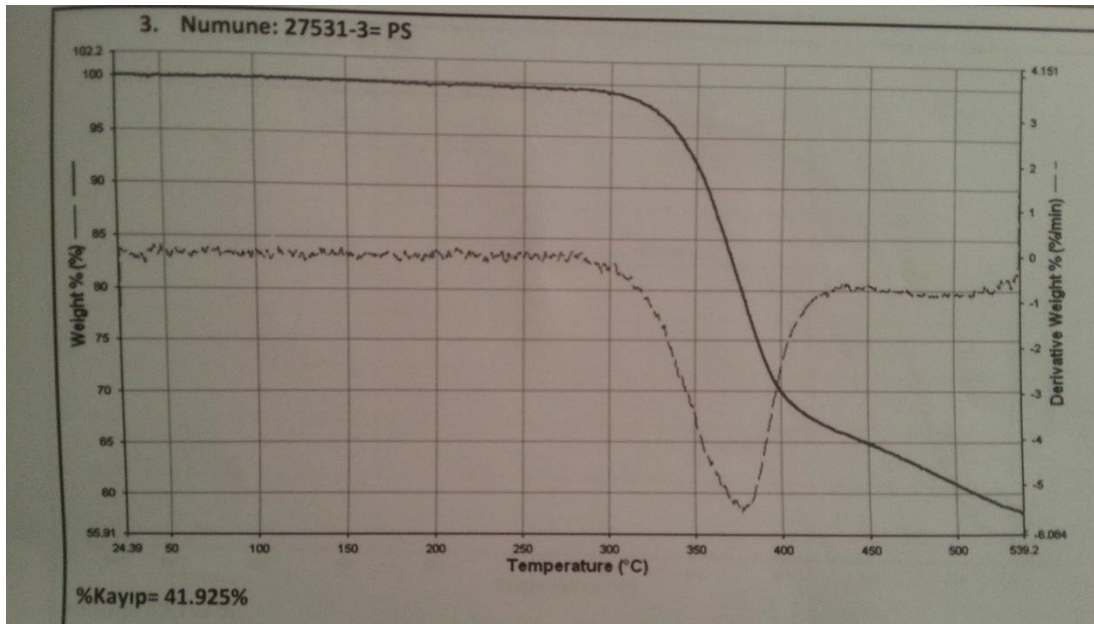


Figure 0.41. TGA result of PS

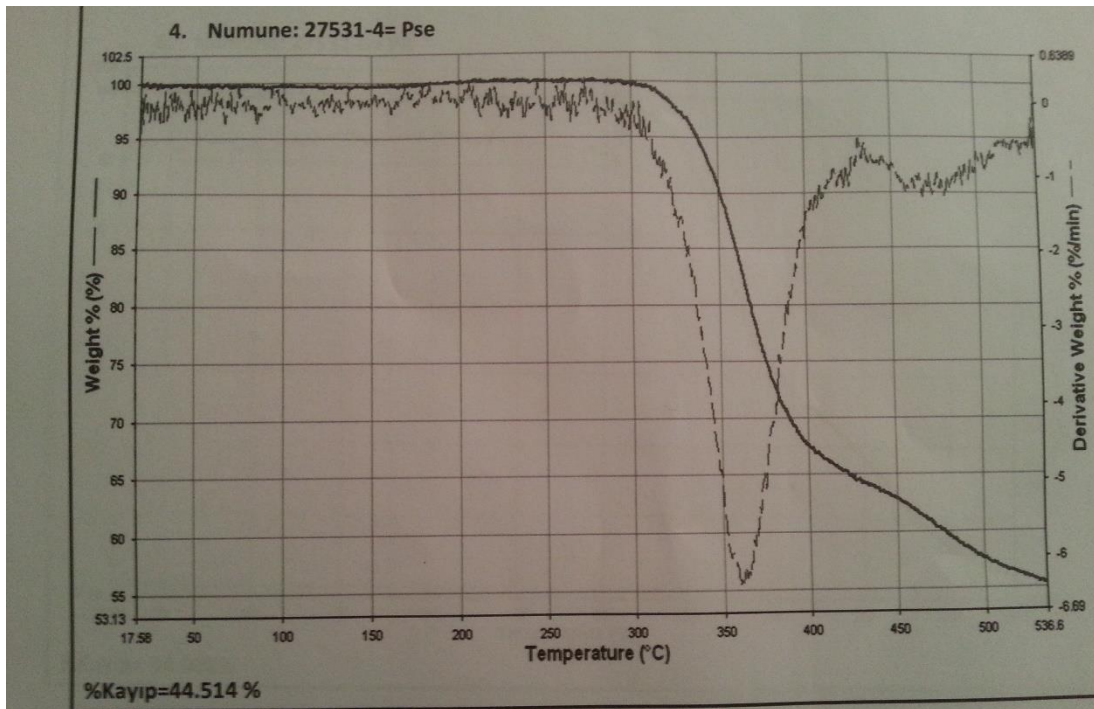


Figure 0.42. TGA result of PSe

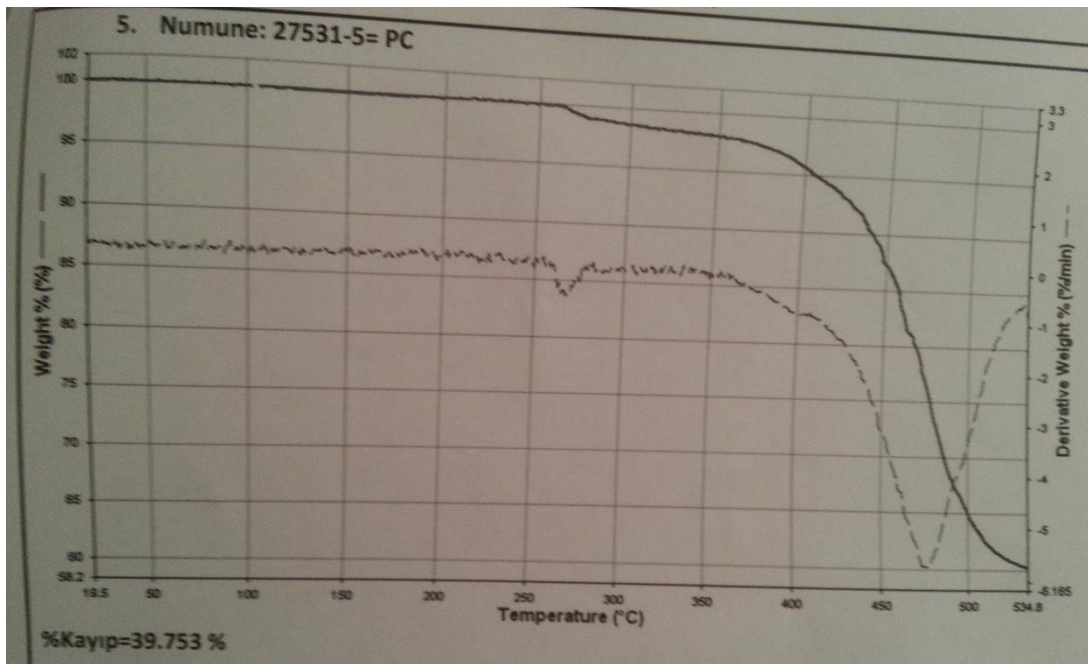


Figure 0.43. TGA result of PIQCAR

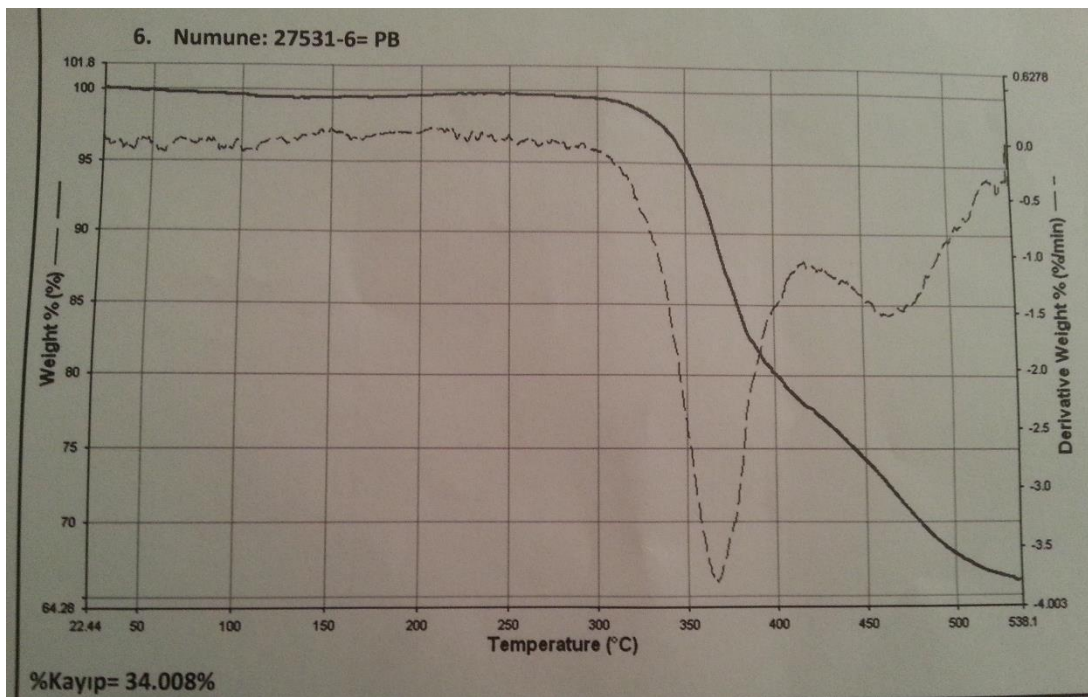


Figure 0.44. TGA result of PIQBDT

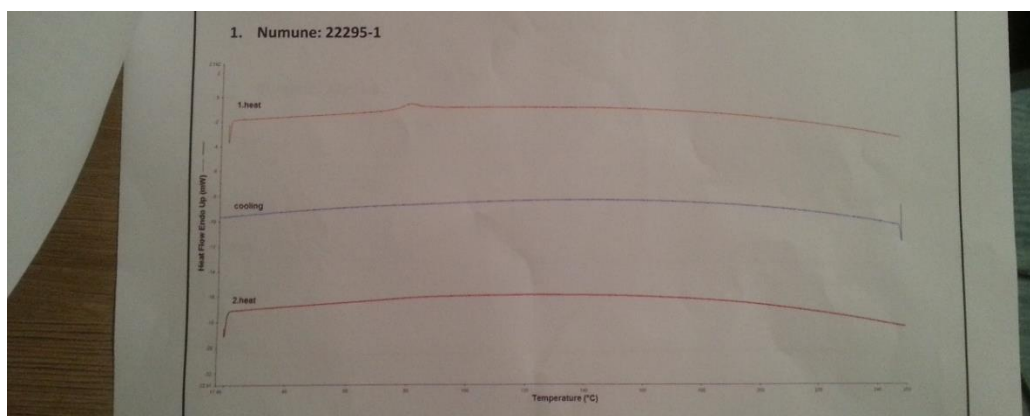


Figure 0.45. DSC result of P1

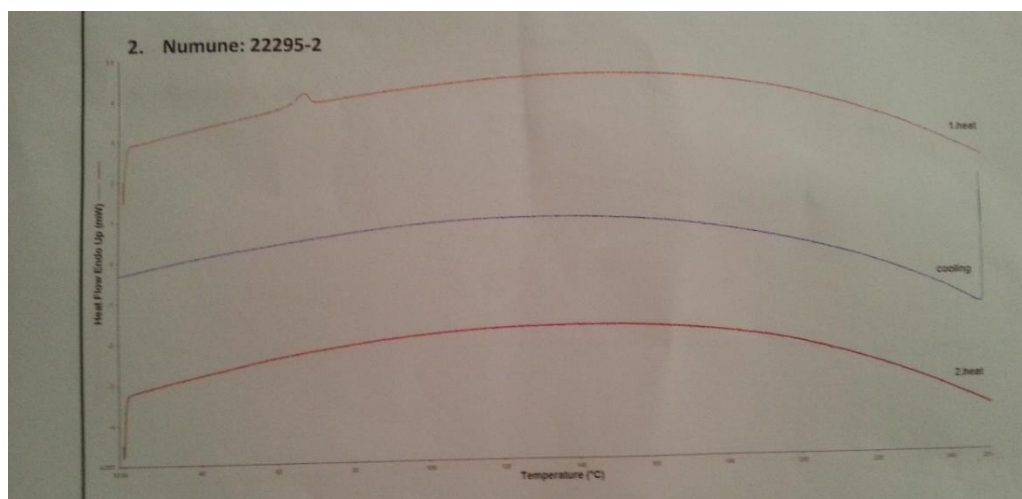


Figure 0.46. DSC result of P2

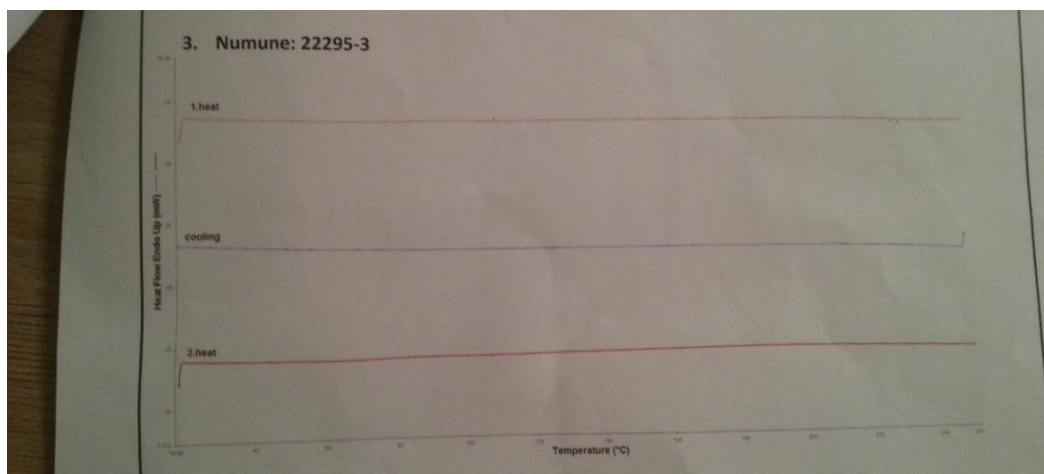


Figure 0.47. DSC result of P3

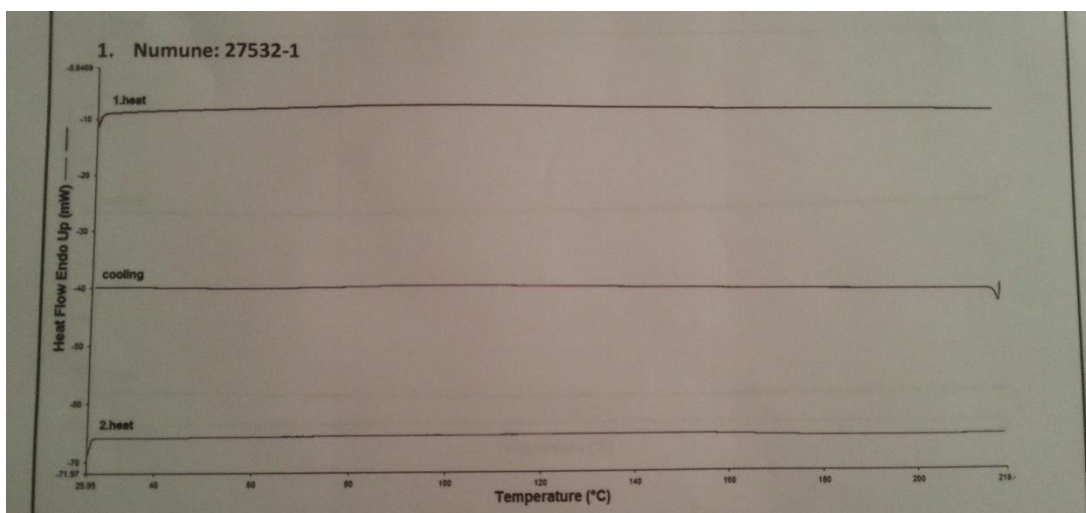


Figure 0.48. DSC result of PO

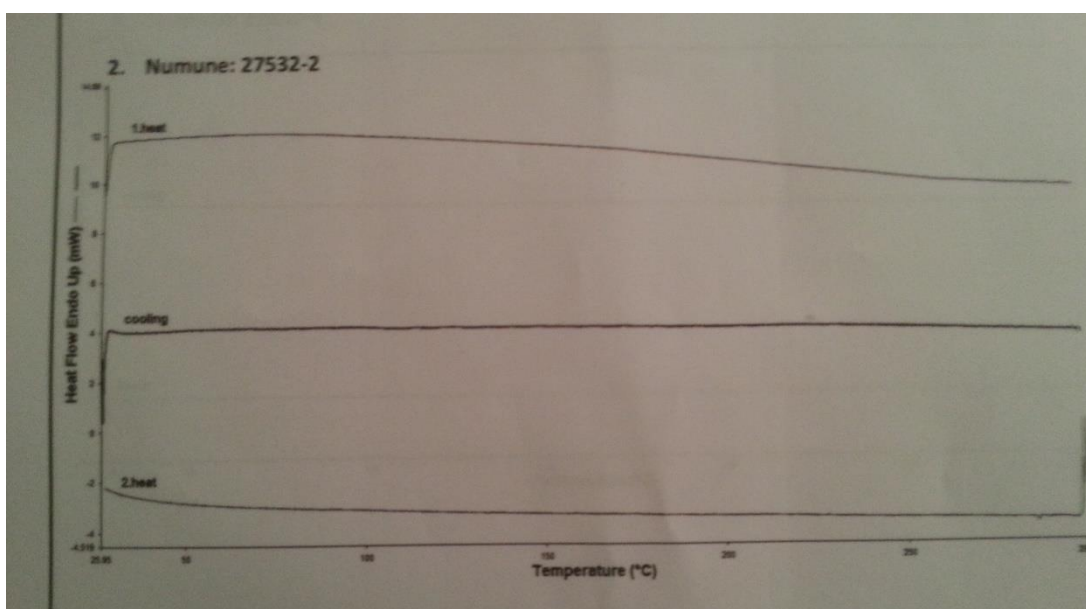


Figure 0.49. DSC result of PF

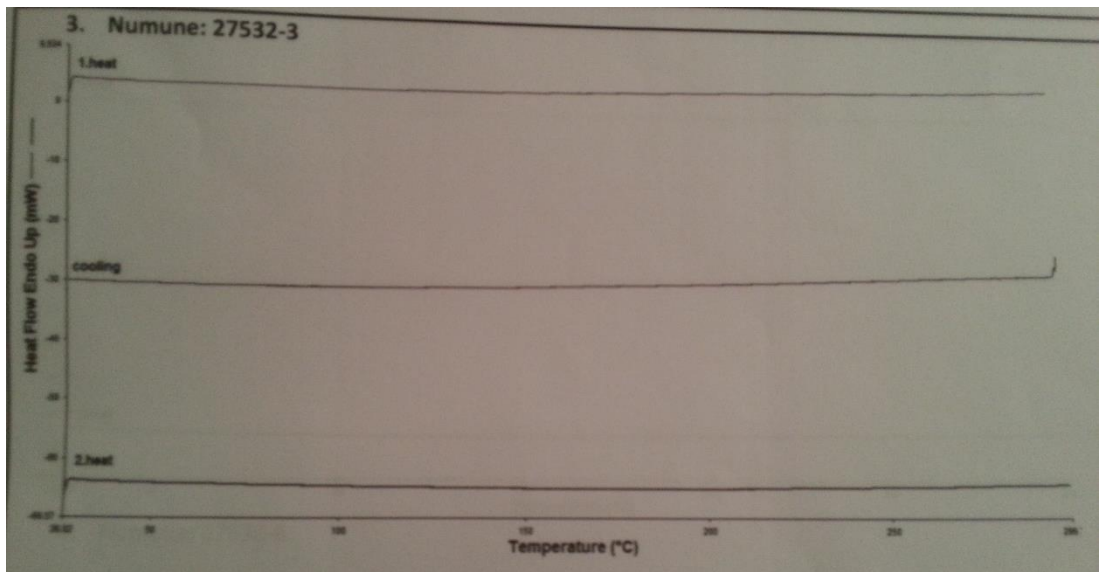


Figure 0.50. DSC result of PS

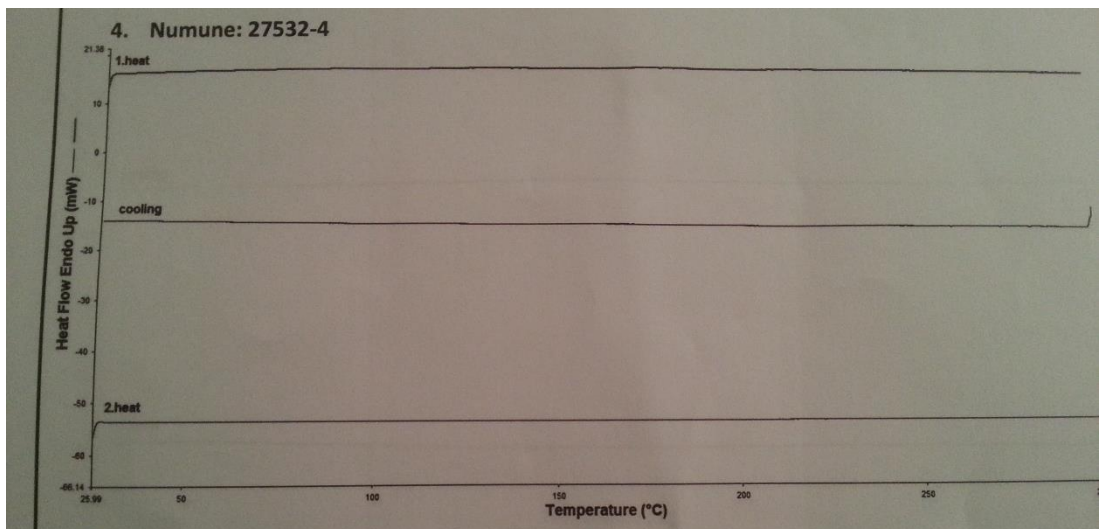


Figure 0.51. DSC result of PSe

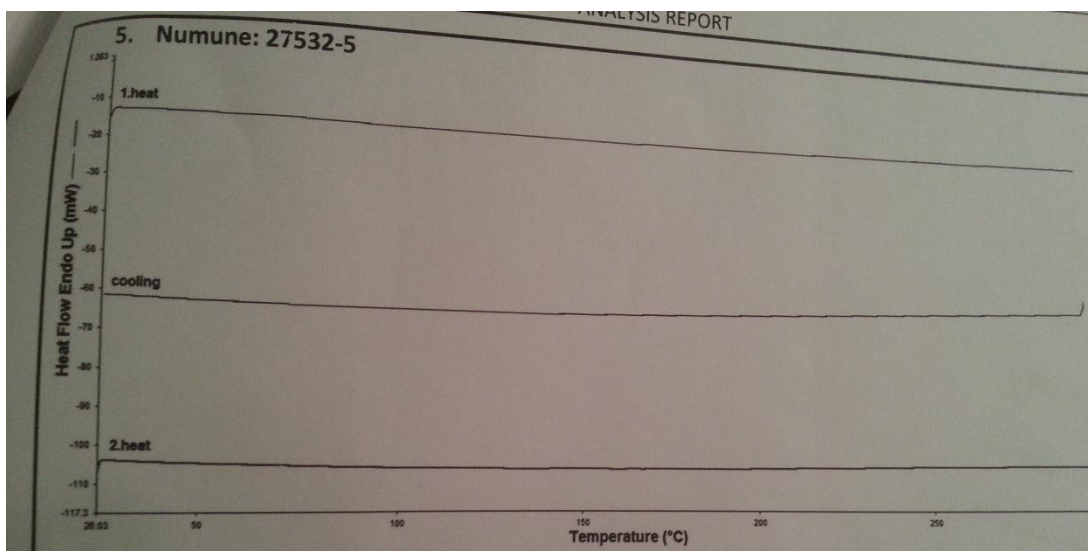


Figure 0.52. DSC result of PIQCAR

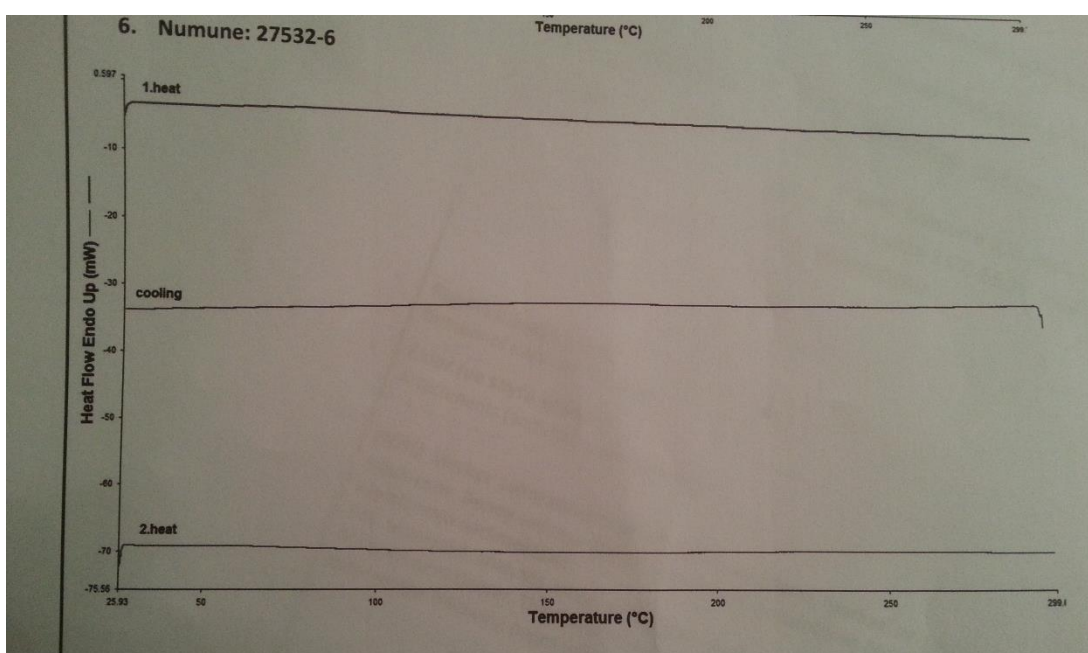


Figure 0.53. DSC result of PIQBDT

CURRICULUM VITAE

PERSONAL INFORMATION

Surname, Name : Cevher, Şevki Can
Nationality : Turkish (TC)
Date and Place of Birth : 22 August 1988, Ankara
Phone : +90 312 210 51 02
E-mail : e153399@metu.edu.tr

EDUCATION

Degree	Institution	Year of Graduation
MS	METU Department of Chemistry	2013
BS	METU Department of Chemistry	2011
High School	Mehmet Emin Resulzade Anadolu High School, Ankara	2006

WORK EXPERIENCE

Year	Place	Enrollment
2011-Present	METU-Department of Chemistry	Research Asistant
2010 Summer	PETKİM	Summer-Intern

FOREIGN LANGUAGES

Advanced English, Beginner French, Beginner Spanish

PUBLICATIONS

- 1) Keles Duygu, Erer Mert Can, Bolayır Eda, **CEVHER ŞEVKİ CAN**, Hizalan Gönül, Toppare Levent, Cirpan Ali, (2019) Conjugated polymers with benzothiadiazole and benzotriazole moieties for polymer solar cells, Renewable Energy 139, 1184-1193

- 2) **CEVHER ŐEVKİ CAN**, Keles Duygu, Hizalan Gonul, Toppare Levent, Cirpan Ali (2018) Alkyl-End Phenanthroimidazole Modification Of Benzotriazole Based Conjugated Polymers For Optoelectronic Applications, Synthetic Metals, 244, 1-9.
- 3) Çetin Aslı, İstanbulluođlu Çađla, Özdemir Haciođlu Őerife, **CEVHER ŐEVKİ CAN**, Toppare Levent Kamil, Çirpan Ali (2017). Synthesis Of Bistriphenylamine And Benzodithiophene Based Random Conjugated Polymers For Organic Photovoltaic Applications. Journal of Polymer Science, Part A: Polymer Chemistry, 55, 3705-3715.
- 4) Karagaçtı Özge, **CEVHER ŐEVKİ CAN**, Hizalan Özsoy Gönül, Özdemir Haciođlu Őerife, Toppare Levent Kamil, Çirpan Ali (2017). Enhancing Power Conversion Efficiency of Polymer Solar Cells via Selection of Quinoxaline Substituents. New Journal of Chemistry, 41, 14635-14645.
- 5) Azeri Özge, Aktaş Ece, İstanbulluođlu Çađla, Özdemir Haciođlu Őerife, **CEVHER ŐEVKİ CAN**, Toppare Levent Kamil, Çirpan Ali (2017). Efficient Benzodithiophene and Thienopyrroledione Containing Random Polymers as Components for Organic Solar Cells. Polymer, 133, 60-67.
- 6) Önk İpek, Hizalan Gönül, **CEVHER ŐEVKİ CAN**, Hacıđlu Özdemir Őerife, Toppare Levent, Çirpan Ali (2017). Multipurpose selenophene containing conjugated polymers for optoelectronic applications. Journal of Macromolecular Science, Part A Pure and Applied Chemistry, 54 (3), 133-139.
- 7) **CEVHER ŐEVKİ CAN**, Hizalan Gönül, Temiz Cansel, Udum Arslan Yasemin, Toppare Levent, Çirpan Ali (2016). Effect of substituent groups on quinoxaline-based random copolymers on the optoelectronic and photovoltaic properties. Polymer, 101, 208–216.
- 8) Yuksel Recep, **CEVHER ŐEVKİ CAN**, Çirpan Ali, Toppare Levent Kamil, Ünalın Hüsnü Emrah (2015). All-Organic Electrochromic Supercapacitor Electrodes. Journal of The Electrochemical Society, 162(14), 2805-2810.

- 9) Kesik Melis, Demir B, Barlas F B, Geyik C, **CEVHER ŞEVKİ CAN**, Odaci Demirkol, Çırpan Ali, Toppare Levent Kamil (2015). A multi-functional fluorescent scaffold as a multi-colour probe: design and application in targeted cell imaging. RSC Adv., 5(101), 83361-83367.
- 10) Akpınar Handan, **CEVHER ŞEVKİ CAN**, Wei Lang, Çırpan Ali, Wong Bryan M, Venkataraman Dhandapani, Lahti Paul M (2015). Poly((2-alkylbenzo[1,2,3]triazole-4,7-diyl)vinylene)s for organic solar cells. Journal of Polymer Science Part B: Polymer Physics, 53(21), 1539-1545.
- 11) Kesik Melis, Huseyin Akbulut, Söylemez Saniye, **CEVHER ŞEVKİ CAN**, Hızalan Özsoy Gönül, Udum Yasemin, Endo Takeshi, Shuhei Yamada, Çırpan Ali, Yağcı Yusuf, Toppare Levent Kamil (2014). Synthesis and characterization of conducting polymers containing polypeptide and ferrocene side chains as ethanol biosensors. Polym. Chem., 5(21), 6295-6306.
- 12) **CEVHER ŞEVKİ CAN**, Unlu Naime Akbasoglu, Ozeltaglayan Ali Can, Apaydin Dogukan Hazar, Udum Yasemin Arslan, Toppare Levent Kamil, Çırpan Ali (2013). Fused structures in the polymer backbone to investigate the photovoltaic and electrochromic properties of donor-acceptor-type conjugated polymers. Journal of Polymer Science Part A: Polymer Chemistry, 51(9), 1933-1941.

ACADEMIC CONFERENCES

- 1) May 2016, **Poster**, European Materials Research Society (e-MRS), Lille/ France
S.C. Cevher, C. Temiz, G. Hizalan, Y.A. Udum, L. Toppare, A. Çırpan, *Modifications Of Quinoxaline On The Polymeric Materials For Optoelectronic Devices*
- 2) May 2016, **Poster**, European Materials Research Society (e-MRS), Lille/ France
N. Sohrabnia, **S.C. Cevher**, G. Hizalan, L. Toppare, A. Çırpan, *Optoelectronic Application of Phenanthrenyl-Imidazole Derivatives*

- 3) May 2016, **Poster**, European Materials Research Society (e-MRS), Lille/ France
I. Onk, C. Istanbuluoglu, G. Hizalan, S. Hacıoglu, **S.C. Cevher**, A. Cirpan, L. Toppare, *Carbazole Based Alternating Copolymer For Electrochromic And Organic Photovoltaic Applications*
- 4) May 2015, **Poster**, 5. Fiziksel Kimya Kongresi, Konya/ Turkey
C. Temiz, N. A. Unlu, **S.C. Cevher**, S.O. Hacıoglu, L. Toppare, A. Cirpan *Organik güneş pili uygulamaları için benzotriazol ve kuinokzalin yapıları içeren konjuge polimer*
- 5) September 2014, **Poster**, V.Ulusal Polimer Bilim ve Teknolojisi Kongresi, Tokat/ Turkey
C. Temiz, N.A. Unlu, **S.C. Cevher**, S.O. Hacıoglu, L. Toppare, A. Cirpan, *Organik Işık Yayan Diyotlar İçin Benzotriazol İçeren Konjuge Polimerler*
- 6) September 2014, **Poster**, V.Ulusal Polimer Bilim ve Teknolojisi Kongresi, Tokat/ Turkey
O. Azeri, **S.C. Cevher**, S.O. Hacıoglu, A. Cirpan, *Organik güneş pilleri için bitişik thiazolo-thiazole halkası içeren konjuge polimer*
- 7) September 2014, **Poster**, V.Ulusal Polimer Bilim ve Teknolojisi Kongresi, Tokat/ Turkey
A.O. Saf, N.A. Unlu, **S.C. Cevher**, A. Cirpan *Farklı miktarda piridin türevi içeren konjüge polimerlerin sentezi, karakterizasyonu ve güneş pili uygulamaları*
- 8) June 2014 **Poster**, IV. Fiziksel Kimya Kongresi, Denizli/ Turkey
S.C. Cevher, Y.A. Udum, L. Toppare, A. Cirpan *Ferrosen İçeren Konjüge Polimerin Elektrokromik ve Optik Özellikleri*
- 9) January 2014 **Poster**, International Semiconductor Science and Technology Conference (ISSTC-2014), İstanbul/Turkey
D. E. Yıldız, G. Hizalan, **S. C. Cevher**, L. Toppare, A. Cirpan *Effect of Thickness on the Electrical and Optical Properties of Organic Solar Cell*
- 10) August 2013 **Poster**, 44th World Chemistry Congress (IUPAC 2013), İstanbul/ Turkey
S. C. Cevher, N. A. Unlu, L. Toppare, A. Cirpan, *Electrochromic properties of a dithieneothiophene and benzotriazole containg conjugated polymer.*
- 11) June 2012 **Poster**, 8th Nanoscience & Nanotechnology Congress, Ankara/ Turkey

S. C. Cevher, N. A. Unlu, L. Toppare, A. Cirpan, *Synthesis of Dithienothiophene and Benzotriazole Containing Conjugated Polymers and Photovoltaic Applications.*

SCHOLARSHIPS

- 1) **Visiting Scholar** research project was funded by **Turkish Council of Higher Education (YOK)** under the supervision of **Prof. Dr. Paul M. Lahti (University of Massachusetts, Amherst)** (2013).
- 2) Volunteer activity in **Hungary** was supported by **The Youth in Action Programme of The European Commission** (2009).